Mechanical Behaviour and Durability of FRP-to-steel Adhesively-bonded Joints

Xu Jiang

Mechanical Behaviour and Durability of FRP-to-steel Adhesively-bonded joints

Proefschrift

ter verkrijging van de graad van doctor
aan de Technische Universiteit Delft,
op gezag van de Rector Magnificus prof. ir. K.C.A.M. Luyben,
voorzitter van het College voor Promoties,
in het openbaar te verdedigen
op woensdag 23 oktober 2013 om 12:30 uur

door

Xu JIANG

Master of Science in Structural Engineering, Tongji University, China

geboren te Shenyang, China

Dit proefschrift is goedgekeurd door de promotoren:

Prof. ir. F.S.K. Bijlaard

Copromotor:

Dr. M.H. Kolstein

Samenstelling promotiecommissie:

Rector Magnificus	voorzitter
Prof. ir. F.S.K. Bijlaard	Technische Universiteit Delft, promotor
Dr. M.H. Kolstein	Technische Universiteit Delft, copromotor
Prof. dr. Airong Chen	Tongji University
Prof. dr.ir. P. van Bogaert	University of Gent
Prof. dr.ir. D.A. Hordijk	Technische Universiteit Delft
Prof. ir. A.C.W.M. Vrouwenvelder	Technische Universiteit Delft
Prof. dr. I.M. Richardson	Technische Universiteit Delft

ISBN 978-90-5335-747-7

Copyright © 2013 by Xu Jiang

All rights reserved. No part of the material protected by this copyright notice may be reproduced or utilized in any form or by any means, electronica or mechanical, including photocopying, recording or by any information storage and retrieval system, without the prior permission of the author.

Printed by Ridderprint in the Netherlands

For my parents

Summary

During the last two decades, fiber-reinforced polymer (FRP) bridge decks have been increasingly used as a competitive alternative for wood, concrete and orthotropic steel decks, due to their various advantages: light-weight, good corrosion resistance, low maintenance cost and rapid installation for minimizing the traffic disturbing time. These advantages meet critical needs for rehabilitation and new construction of pedestrian and highway bridges. To be cost effective, FRP decks are usually supported by steel girders. For the connection between FRP decks and steel girders, adhesive bonding technique is usually considered as a preferable connecting method, which can reduce construction time, save weight by eliminating fasteners, allow more uniform load transfer, achieve better adaption to the brittle and anisotropic nature of FRP materials and provide higher joint efficiency.

Despite the fact that FRP bridge decks and adhesive joints are already in service in many FRP-steel composite bridges, mechanical behaviour and long-term performance are still not clearly understood, which results in more conservative designs of the FRP-steel composite bridges. To compensate this lack, the overall aim of this project is to investigate mechanical behaviours (in terms of strength and stiffness) of adhesively-bonded joints between FRP bridge decks and steel girders, as well as durability of these adhesively-bonded joints. As to the first aspect, considering the distribution of traffic loads in the longitudinal and transverse directions of bridges, the adhesive-bonded joints have been experimentally studied under six loading conditions, including tensile loading, shear loading and four combining ratios of tensile and shear loading. A specific tensile-shear loading device was designed and then employed to offer six different angle loading conditions. Different surface pretreatment methods (acetone (AC), sand paper (SP) and sand blasting (SB)) were compared with regard to influences on the stiffness, load-bearing capacity, failure mode and interfacial bonding quality of adhesive joints. A Finite Element (FE) model was developed to simulate the stress distribution throughout the adhesive joints under different loading conditions, which proved that the failure of joints was induced by combination of both tensile and shear stress peaks. The edge zone

(approximately 10mm from the ends of the adhesive layer) was the most sensitive area to initiate the failure, where both the shear stress peak and the tensile stress singularity were located.

Another critical aspect of this research is to characterize the durability of FRP-to-steel adhesively-bonded joints under both temperature and moisture effects. The influence of hydrothermal environmental aging on the mechanical behaviours of adhesive joints has been studied and compared with the un-aged adhesive joints. The shear-tensile failure criterions of hydrothermal aged and un-aged adhesive joints were addressed. To better understand the moisture effects, the moisture diffusion process in FRP composite materials was characterized. Subsequently, the hydrothermal degradation on the flexural and interlaminar properties of FRP laminates was addressed. A coupled hygro-mechanical FE model was developed to analyse the enviroment-dependent mechanical behaviours of FRP lanimates. This FE model was first validated by test results of flexural tests and subsequently employed in an inverse parameter identification method to determine the elastic interlaminar shear modulus of FRP laminates. Predictive equations for environment-dependent mechanical properties (flexural and interlaminar) of FRP laminates were sustained by using the least square method for the curve fitting.

Results of this research can contribute to the development of a design code of FRP-steel composite bridges. They can also be used as a reference information for understanding mechanical behaviours and durability of FRP-to-steel adhesively bonded joints for other applications in civil engineering field, such as strengthening of steel structures using FRP composite materials.

Contents

Part II Joint level research

List of notations

A	adhesive-bonding area
b	plate (specimen) width
c	moisture concentration
c_∞	maximum equilibrium moisture concentration
D	equivalent moisture diffusion coefficient
D_{max}	maximum deflection of the center of the beam
D_1	moisture diffusion coefficients along the direction of length
D_2	moisture diffusion coefficients along the direction of width
D_3	moisture diffusion coefficients along the direction of thickness
d	depth of FRP beam tested
E	modulous
e	plate thickness
F^{sbs}	short-beam strength
F_{shear}	shear load applied on the adhesive joint
$F_{tension}$	tensile load applied on the adhesive joint
G_{13} (G_{23})	interlaminar shear modulus
h	specimen thickness
K_n	characteristic fractile factor
L	support span
l	plate length
M_t	moisture absorption content at the time t
M_∞	equilibrium amount of absorption
P	load at the midspan on the load-deflection curve
P_m	maximum load observed during the short-beam test
R	rate of crosshead motion
R^2	R-square value
S	strength
t	time
w_0	specimen's weight before exposure
w_t	specimen's weight after exposure
x	space coordinate measured parallel to the diffusion
Z	rate of straining of the outer fiber
σ	stress in the outer fibers at midpoint
σ_v	Von Mises stress
ε	strain in the outer fibers at midpoint
$\tau_{average}$	average shear stress
$\sigma_{average}$	average tensile stress

List of abbreviations

1D	one dimensional
2D	two dimensional
3D	three dimensional
AC	acetone
ASTM	American Society for Testing and Materials
DS	displacement sensor
FE	finite element
FEA	finite element analysis
FRP	fiber reinforced polymer
GFRP	glass fibre-reinforced polymer
ISO	International Organization for Standardization
LVDT	linear variable differential transformer
PC	personal computer
RC	reinforced concrete
RH	relative humidity
SB	sand blasting
SP	sand paper
Tg	glass transition temperature

Chapter 1
Introduction

1.1 Background

The deteriorating state of the bridge infrastructure in many countries is well documented all over the world. Conventional concrete decks, timber decks as well as orthotropic steel decks are usually the major cause of structurally deficient bridges. To address this issue, Fiber Reinforced Polymer (FRP) bridge decks were developed to be a light-weight and durable alternative as a means of deck replacement for older and deteriorated bridges, particularly for bridges with steel girders. Due to the light-weight of FRP decks, the reduced deck load may permit increased traffic loading without altering the original state of the bridge. Moreover, the rapid installation of an FRP deck also reduces bridge closure time for a rehabilitation project and minimizes inconvenience to the daily traffic. Also, for new bridges, steel girder with an FRP deck is a realistic option.

For the connection between the FRP decks and the steel girders, the adhesive bonding technique is usually considered as a preferable connecting method, which can reduce construction time, save weight by eliminating fasteners, allow more uniform load transfer, achieve better adaption to the brittle and anisotropic nature of FRP materials and provide higher joint efficiency. Despite the fact that adhesive joints are already in service in many FRP-steel composite bridges, the long-term performance, gluing technique and design method are still not clearly understood. Literature review shows that the adhesive joints have been intensively investigated over the past 70 years. However, most researches are related to the applications in aerospace and aircraft engineering. Only during the last two decades, the adhesive joints have been increasingly used in civil infrastructures, especially applied together with FRP composite materials. But the adhesively-bonded joints utilized in civil infrastructures show essential differences, including bond geometries (adhesive and adherent thicknesses), fabrication processes, loading, curing conditions and service environments. The FRP composite profiles and adhesive layers for aerospace/aircraft structures are usually thin (0.1–1 mm), while in bridge and building structures adherents and adhesive layers are comparatively much thicker (2–20 mm). Furthermore, the design requirements and service conditions of adhesive joints for infrastructures differ from those employed in aerospace/aircraft structures. For instance, the service life of a bridge or building is much longer than that of an aircraft. In many countries, 70 years or more is expected to be the service life of bridges. Furthermore, curing conditions are also different. Adhesives used in the civil engineering industry are usually cured in ambient environments, but for aerospace applications the temperatures of curing conditions are usually over 100ºC, which leads to higher glass transition temperatures and the joints tend to be more durable. Thus, researches conducted in aerospace engineering can only be applied to the civil engineering field with limitations.

1.2 Aim of the research

The overall aim of this project is to investigate the mechanical behaviour (in terms of strength and stiffness) of adhesively-bonded joints between FRP bridge decks and steel girders, as well as the durability of these adhesively-bonded joints. As to the first aspect, considering the distribution of traffic loads in the longitudinal and transverse directions of bridges, the adhesive-bonded joints have been experimentally studied under six loading conditions, including tensile loading, shear loading and four combining ratios of tensile and shear loading. Shear stress occurring in adhesive joints is due to the composite action between FRP decks and steel girders in the longitudinal direction of the bridge. The deck and steel girder tend to bend together to carry the traffic load. Thus, the adhesive joint is in the shear stress state to transfer the loading from FRP deck to steel beam, see Fig. 1.1 a). As shown in Fig. 1.1 b), in the transverse direction of the bridge, loading on left traffic lanes causes up-lift forces locally on the adhesive joint at the right side of the bridge, which results in the through-thickness tensile stress in the adhesive joints between FRP decks and steel girders. The above two phenomenon can also take place simultaneously resulting in a combination of shear and tensile stress in the adhesively-bonded joint.

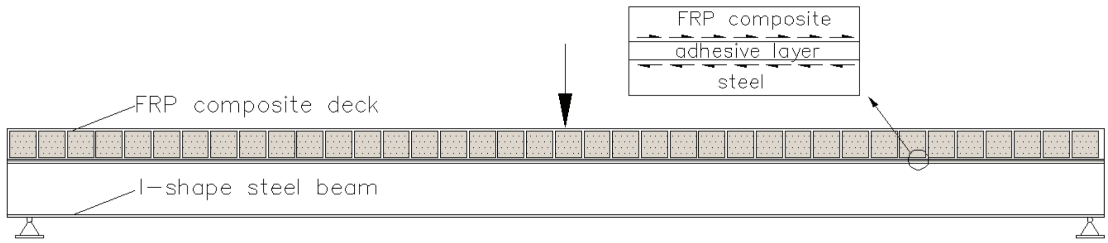

a) Shear stress in the longitudinal direction

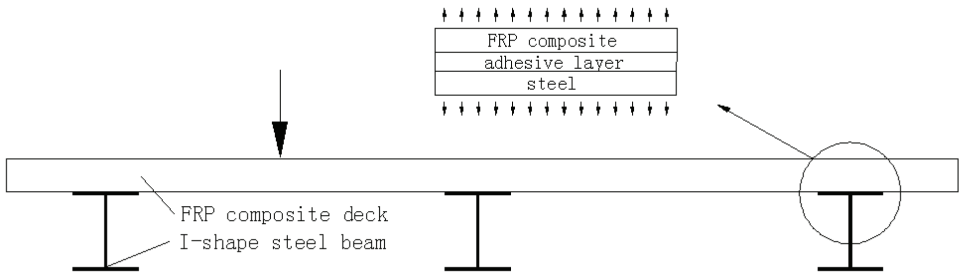

b) Tensile stress in the transverse direction

Fig. 1.1. Typical stress states in an adhesively-bonded joint of an FRP-steel composite bridge

Different surface pretreatment methods are compared with regard to the influence on the stiffness, load-bearing capacity, failure mode and interfacial bonding quality of adhesive joints. A Finite Element (FE) model is developed to simulate the stress distribution throughout the adhesive joints under different loading conditions. Another critical aspect of this research is to characterize the durability of FRP-to-steel adhesively-bonded joints under temperature and moisture effects. The influence of hydrothermal environmental aging on the mechanical behaviours of adhesive joints has been studied. To better understand the moisture effects, the moisture diffusion process in FRP composite materials is characterized. Subsequently, the hydrothermal degradation on the flexural and interlaminar properties of FRP laminates is addressed. Results of this research can contribute to the development of a design code on FRP composite materials and structures for application in the civil engineering field, particularly for the FRP-steel composite bridge.

1.3 Outline

This thesis contains six chapters, as illustrated in Fig. 1.2. After the first introductory chapter, a literature review is provided in Chapter 2, which gives a brief state-of-the-art in FRP bridge decks, the FRP-steel composite bridge deck system, adhesively-bonded joints and environmental effects.

The research work mainly consists of two parts: Part I - material level research (Chapter 3 and Chapter 4) and Part II - joint level research (Chapter 5).

In Chapter 3, the moisture diffusion characteristic of two types of FRP composite materials (pultrusion and resin-infusion) are studied by gravimetric experiments in four environmental conditions. Based on the moisture diffusion theory, the moisture diffusion coefficients are determined. Subsequently, the FE model for simulating the moisture diffusion process in the FRP composites is developed and validated by the experimental results, which provides a numerical technical basis for coupling the moisture diffusion and mechanical analysis of FRP composites. Chapter 4 investigates the influence of moisture and temperature on the mechanical properties (flexural and interlaminar shear) of FRP laminates by employing the three-point bending tests. One cycle of the moisture absorption-desorption process is considered. The environment-dependent degradation of flexural modulus and strength as well as shear strength is experimentally addressed. Furthermore, the coupled hydro-mechanical FE model is developed and employed to determine the environment-dependent interlaminar shear modulus by an inverse parameter identification approach. Finally, the predictive equations of mechanical degradation of FRP composite properties (flexural and interlaminar shear) are presented.

In Chapter 5, firstly, the mechanical behaviour (in terms of load-deformation and stress-deformation) of FRP-to-steel adhesively-bonded joints is experimentally and numerically studied. A specific tensile-shear loading device is designed and then employed to offer six different angle loading conditions, including the pure tensile, 18°, 36°, 54°, 72° and pure shear loading. The 18°, 36°, 54°, 72° angle loading conditions are considered as the combination of tensile and shear loads in four different ratios. The influence of different surface pretreatment methods on the mechancial performance of adhesive joints is also investigated under tensile and shear loading. By experimental investigations, a tensile/shear failure criterion of adhesively-bonded joints is addressed. Furthermore, a three-dimensional FE model of the adhesive joint is developed and validated by experimental results. Subsequently, linear elastic simulations are performed to characterize the stress distribution in the adhesive joint under six different loading conditions. The mesh-dependency of the FE model is also addressed in the longitudinal, transverse and through-thickness direction of the adhesive joint. Subsequently, further research is focused on mechanical behaviours of the FRP-steel adhesively-bonded joint after hydrothermal aging. The previous tensile/shear loading device is employed again to offer the six different loading angles for testing the four-month aged adhesive joints. A tensile/shear failure criterion of four-month aged adhesively-bonded joints is obtained. To better understand the influence of hydrothermal aging on mechanical behaviours of the adhesively-bonded joint, a comparison between the experimental results of un-aged joints and hydrothermal aged joints is conducted with regard to the ultimate failure load, failure criterion, failure mode and stiffness. Furthermore, the post curing mechanism induced by the elevated temperature of hydrothermal aging environment is discussed.

Finally, Chapter 6 gives the overall conclusions of this research, as well as recommendations for future research work.

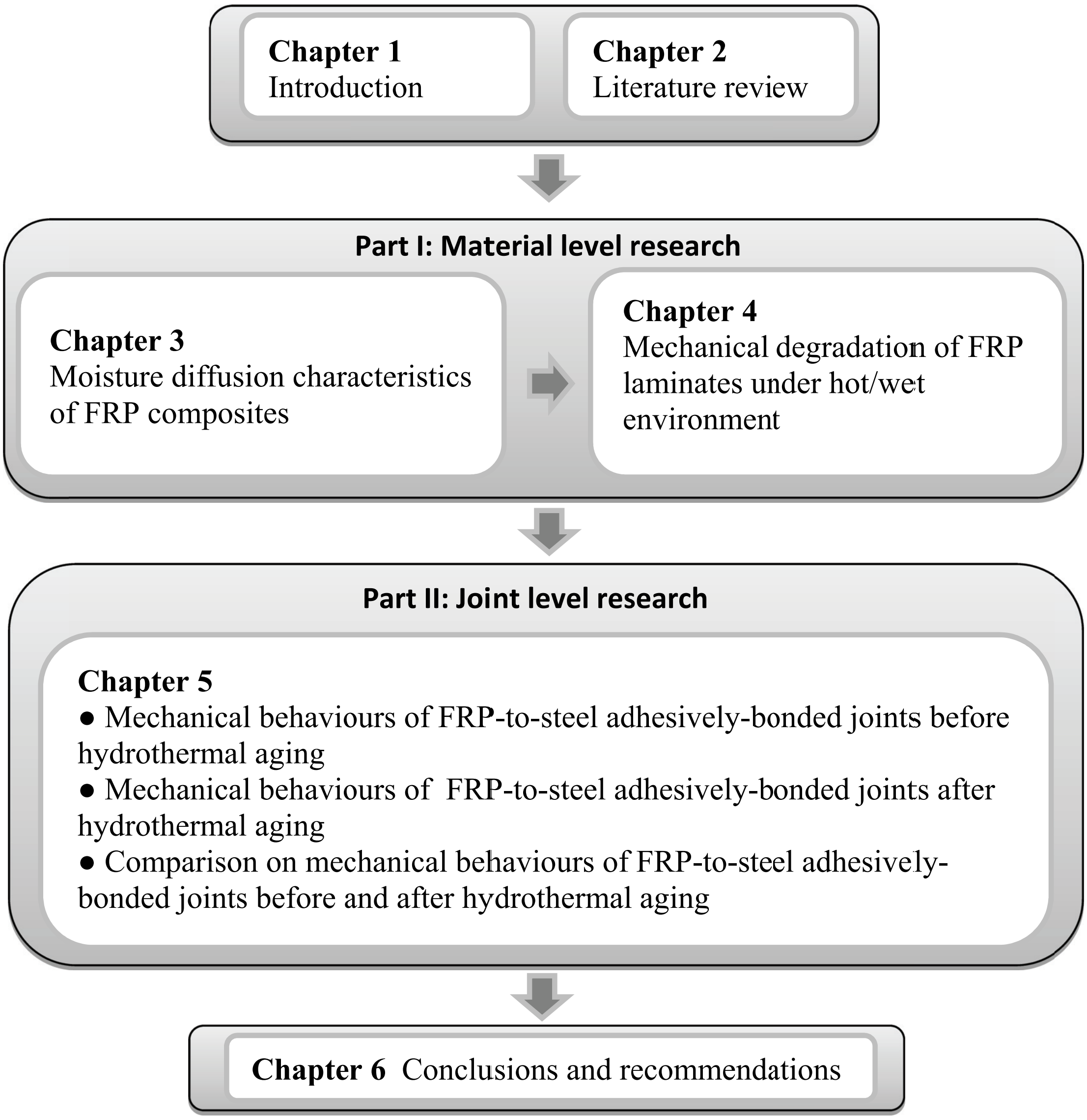

Fig. 1.2. Outline of the thesis

Chapter 2
Literature review

2.1 FRP bridge decks

Fibre reinforced polymer (FRP) materials, especially glass-fibre-reinforced polymer (GFRP) composites are being increasingly applied in civil engineering as a competitive alternative to traditional materials, such as concrete, timber and steel [1-5]. From a review of FRP composites for construction [1], FRP composites were firstly commercialized to meet the higher performance challenges of space exploration and air travel in the 1960s and 1970s. Thanks to cost reduction of the continued growth of the FRP industry, FRP composites finally found their acceptance in the conservative infrastructure construction industry during the late 1980s and throughout the 1990s. For the design of FRP structures, optimization design methods were introduced and compared in literature [2], which compensated for the lack of design standards for FRP infrastructure. Throughout the past two decades, one conspicuous application of FRP materials in civil engineering is FRP bridge decks for rehabilitation of old bridges and the construction of new bridges [3-8]. Current commercially available FRP decks can be classified into two categories according to the types of assembly and construction [9]: sandwich panels (Fig. 2.1 a) and b)) and multi-cellular type panels (Fig. 2.1 c) and d)). The sandwich decks are mainly manufactured by the resin vacuum infusion technique, and the cellular decks are made by the pultrusion technique.


(a) ECOSAFE (Infra Composites, Netherlands) (b) Honeycomb Deck (Kansas, USA)


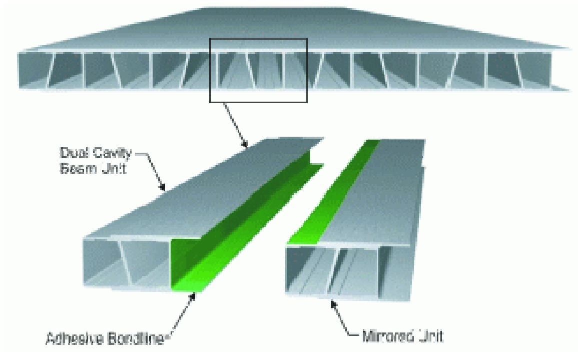

(c) ASSET (Fiberline, Denmark) (d) DuraSpan (Martin Marietta Composite, USA)

Fig. 2.1. FRP bridge decks

The growing acceptance of FRP bridge decks can be attributed to their pronounced advantages [10]:

• Light weight. FRP bridge decks weigh about 10-20% of a reinforced concrete deck. Consequently, using an FRP deck to replace a concrete deck reduces the dead load significantly. A lighter dead load can be translated into savings throughout the structure and the foundations are reduced for new structures.

• Corrosion resistance. Corrosion of the reinforcing steel is the main cause of premature deterioration of RC bridge decks. The use of road de-icing salts accelerates this corrosion. FRP composites possess a higher tolerance for frost and de-icing salts.

• Rapid installation with minimum traffic disruption and factory making. Factory made FRP deck panels offer several advantages over cast-in-place concrete decks. These are:

1) Quality of the product can be closely monitored in the controlled factory environment.

2) During manufacturing the potential for inclement weather is eliminated.

3) Once the superstructure is prepared, the fabricated deck structure can be installed quickly with light lifting cranes.

- High strength to weight ratio.
- Longer service life and lower maintenance cost. Life cycle cost savings have been shown to more than offset the relatively high initial cost of the FRP materials compared to conventional materials. The service life of the FRP deck can be about three times larger than concrete decks. However, few public agencies select materials based on projected life-cycle costs, most materials are chosen on the experience and judgement of the engineer, agency preferences and industry standard practice, generally with a strong bias towards minimizing initial construction costs.

2.2 FRP-steel composite bridge deck system

To be cost effective, the FRP decks are usually supported by steel girders, as shown in Fig. 2.2. Steel girders enhance the ductility of this composite bridge system after failure loading achieved, which compensates for the brittle characteristics of FRP composites. Between the FRP decks and steel girders, the adhesive bonding technique is usually employed as a preferable connection method. In recent years, this kind of FRP composite girder system was utilized [3, 4, 11]. In Knippers's research [3], it was employed as a flyover across the federal road B3 in Germany. The high durability of FRP composites and the fast assembly of the bridge were decisive factors for this application. Through Cassity et al.'s experimental investigation [11], the degree of composite action between cellular FRP decks and steel girders was studied and subsequently adopted in a rehabilitation project of an old and deteriorated bridge. Through these projects, valuable experience was gathered concerning in-situ constructions, and the good performance of FRP-steel composite deck system was confirmed.

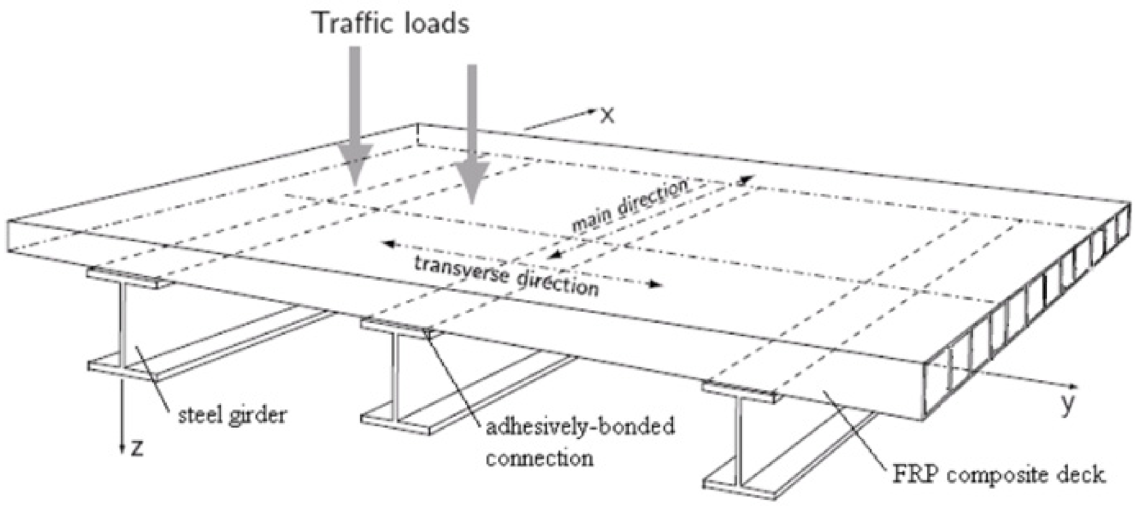

Fig. 2.2. FRP-to-Steel composite girder system [12]

In most cases, FRP decks have to compete with concrete decks. For the widely used concrete-steel composite bridge, concrete decks are usually designed to behave as the top chord of the composite girder in the longitudinal direction of the bridge, and the stiffness and load-bearing capacity of the bridge can be significantly increased. To be competitive, FRP decks also need to be capable to contribute as part of the longitudinal top chord for maintaining the full composite action. To achieve this, the adhesively-bonded joint between FRP decks and steel girders must obtain the full loading transfer capacity, which implies a linear strain distribution through the depth of the hybrid cross-section. In literature, some researches [7, 11-15] highlighted that the composite action between FRP decks and steel girders is of great importance. In the research of Keller and Gurtler [14], a 30% decrease in deflection and a 56% increase in load-bearing capacity were experimentally identified, both relative to a single steel I-shape beam acting alone, for a 7.5m span simple-supported composite specimen with the FRP deck adhesively bonded to the steel beam. The full load transfer capacity was evident through the adhesive joint between the FRP deck and the steel beam, as shown in Fig. 2.3.

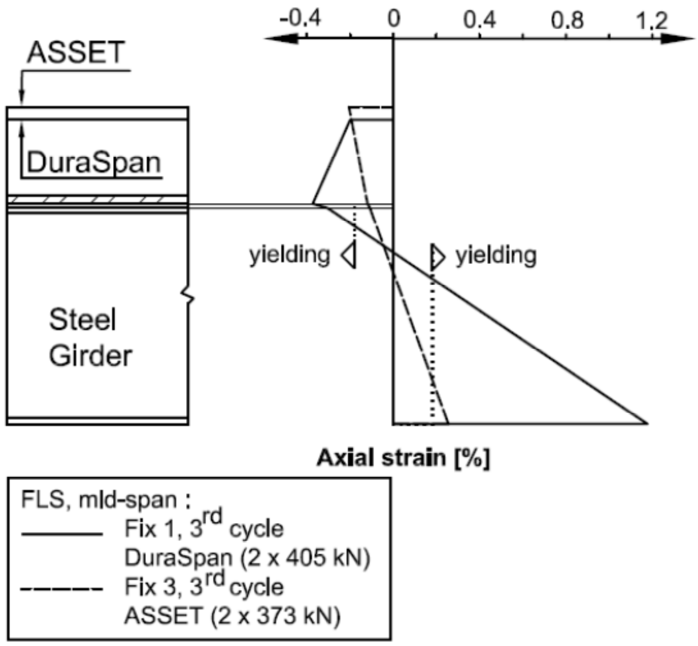

Fig. 2.3. Axial strain distribution in the mid-span cross-section of the Asset and DuraSpan hybrid Girders [16]

The plate-bending behaviour of a pultruded GFRP bridge deck system was investigated by full-scale experiments and numerical modeling [12], as shown in Fig. 2.4. Particularly, the through-thickness performance of adhesive joints between FRP bridge decks and steel girders was studied. Tensile stress distribution in the adhesive joint is non-uniform with high stress concentrations underneath the FRP webs of the cellular deck, attaining stress concentration factors higher than 12, see Fig. 2.5 and 2.6.

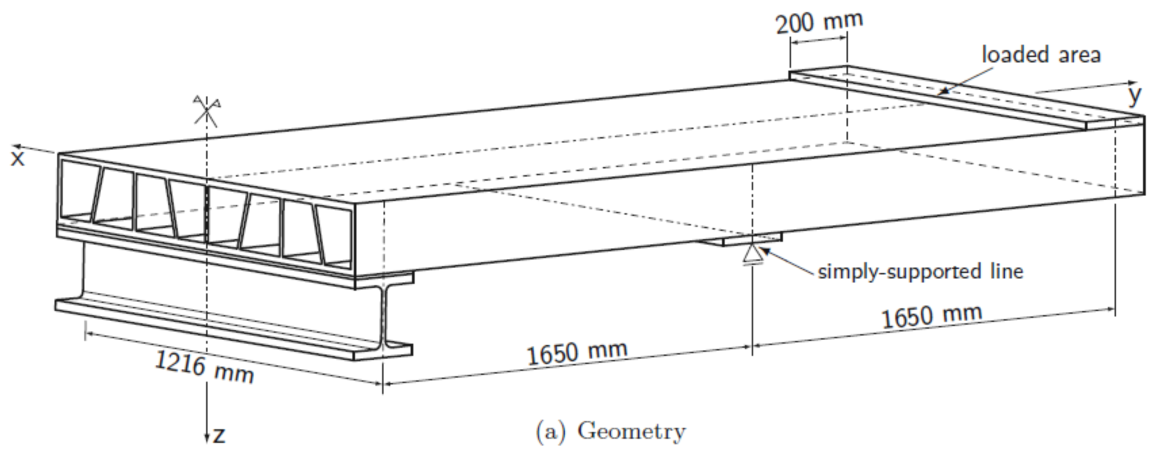

Fig. 2.4. FE model of test set-up

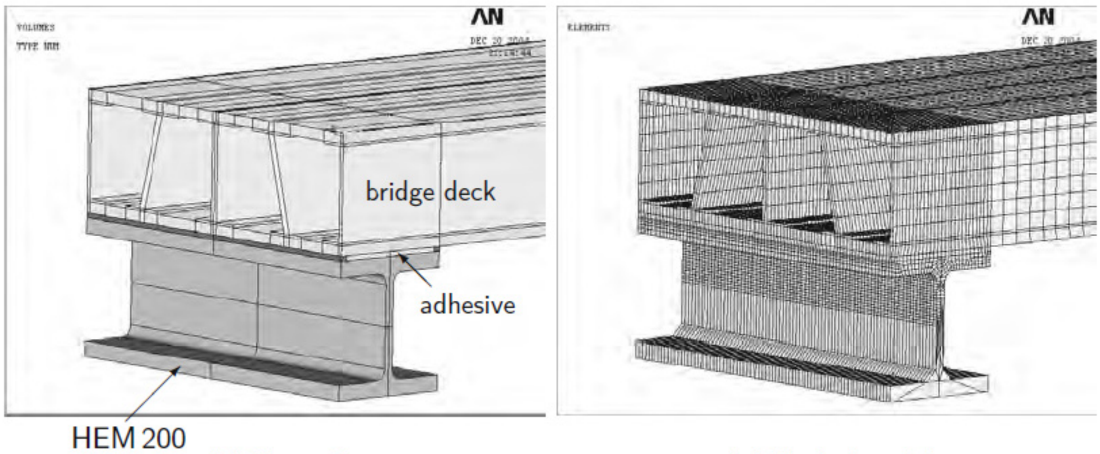

(b) Materials (c) Meshed model

Fig. 2.4. FE model of test set-up

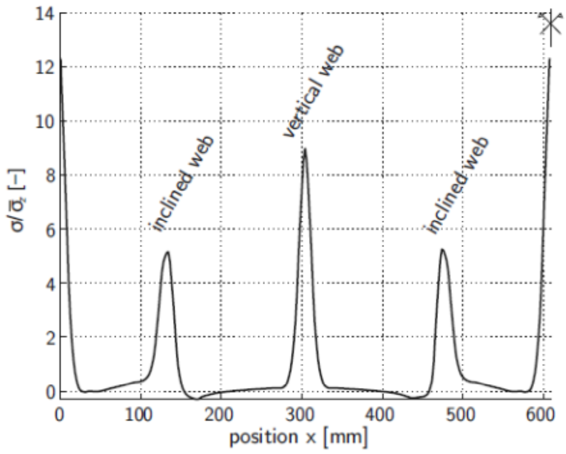

Fig. 2.5. Normalized through-thickness tensile stress distribution in adhesive layer/bridge deck interface (x-direction) over center of steel girder

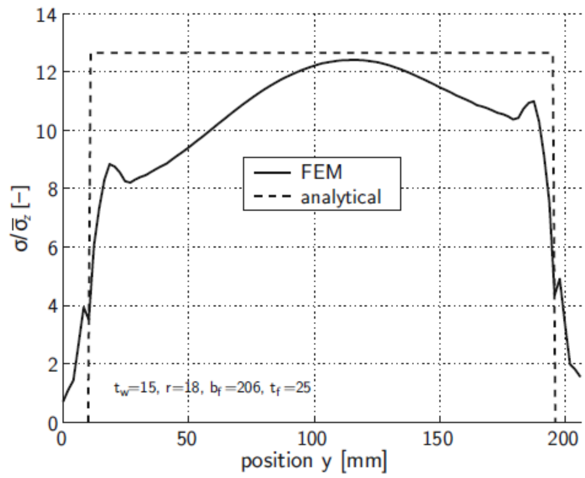

Fig. 2.6. Normalized through-thickness tensile stress distribution in adhesive layer/bridge deck interface (y-direction) below vertical web at x=608 mm

2.3 Adhesively-bonded joint

As mentioned in reference [9], the load carrying connections in an FRP composite bridge include component–component connections to form modular FRP bridge deck panels (henceforth referred as component level connection), panel–panel connections to form FRP bridge deck systems (henceforth referred as panel level connection), and FRP deck-to-support connections to form bridge superstructures (including deck-girder, deck-abutment and deck-barrier connections, etc., henceforth referred as system level connection). For these connections, the adhesive bonding technique is usually considered to be an excellent alternative. As compared to bolted or stud connections, adhesively-bonded connections can reduce construction time, save weight by eliminating fasteners, introduce more uniform load transferring and provide better long-term performance. Bolted connections usually result in much higher stress concentrations where cracks occur. Furthermore cutouts of FRP plates can provide path for moisture penetration. Adhesive connections, however, are more material-adapted, since larger surfaces can be glued together and no holes are made, thus reducing concentrated stresses.

As mentioned above, lots of studies on FRP composite adhesive joints were conducted in the aerospace engineering field [17-20]. But these experiences and knowledge cannot be directly applied to civil engineering applications because of essential differences in geometries, types of fibres and matrix, fabrication methods, curing processes and service environmental conditions. Recently, some researches [21-23] were conducted for civil engineering applications, focusing on the mechanical performance of adhesively-bonded single-lap joints and double-lap joints. These adhesive joints were composed of pultruded GFRP composite profiles glued by epoxy adhesives, as illustrated in Fig. 2.7.

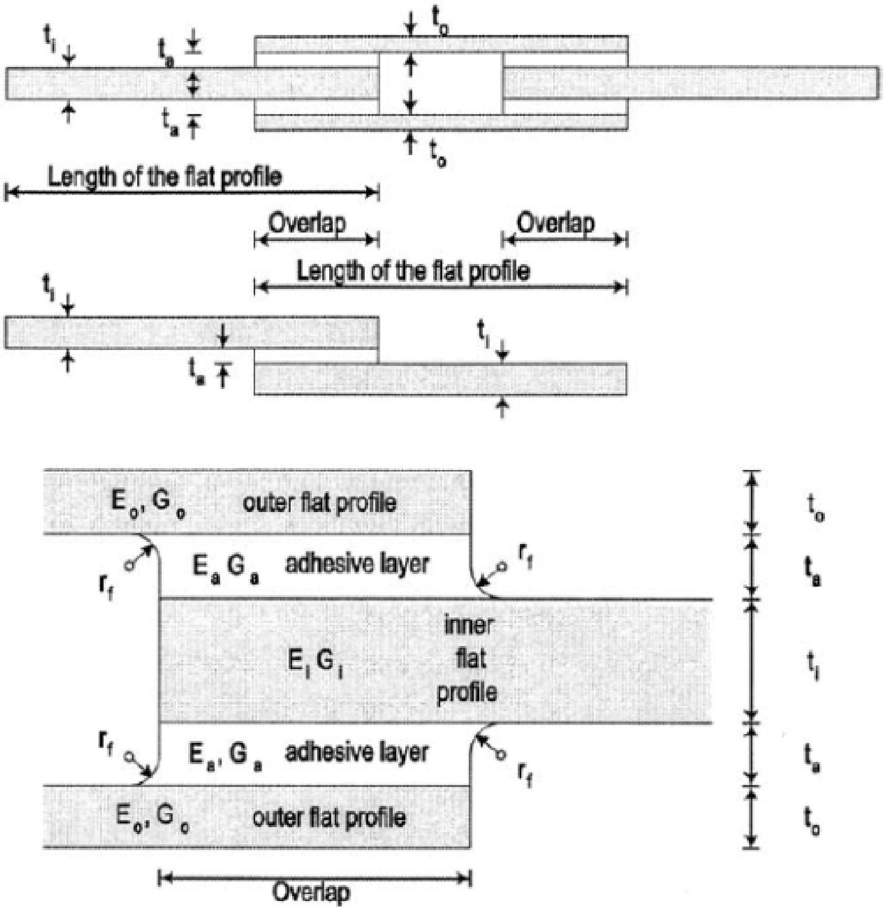

Fig. 2.7. Geometry of lap joint specimens (not to scale)

Parametric studies were conducted experimentally and numerically on the overlap length, the adhesive layer thickness, the adherent thickness and the degree of chamfering of the adherents. The results (Fig. 2.8) indicated that the combination of local through-thickness tensile (peeling) and shear stresses was the most severe stress-state and usually initiated the failures in the adhesive fillet and in the outer fibre-mat layers of the adherents below the joint edges. Further researches [24, 25] offered a probabilistic strength prediction method on the adhesive joints under quasi-static axial tensile loading.

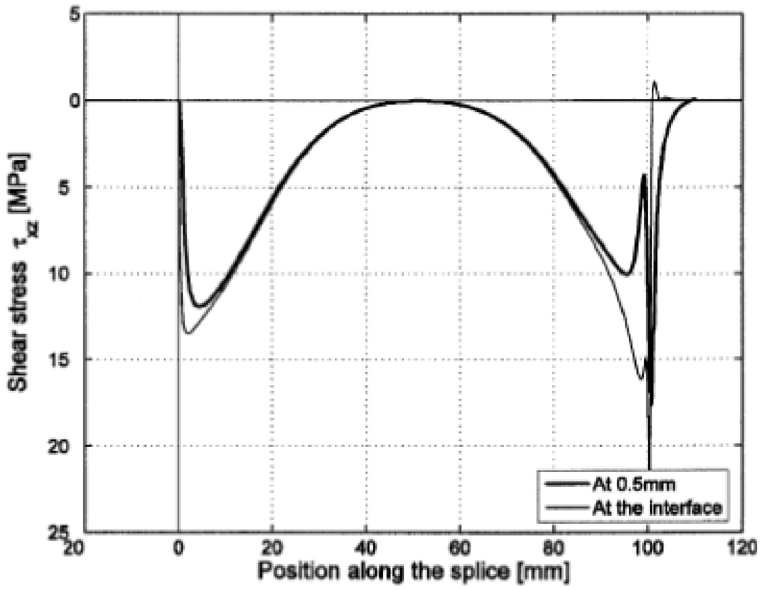

a) Shear stress distribution

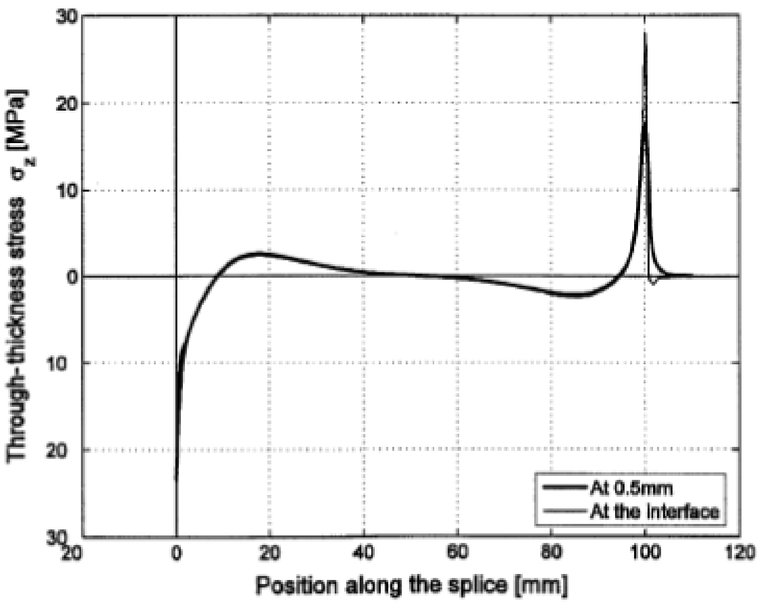

b) Through-thickness stress distribution

Fig. 2.8. Stress distribution at 100kN for DN 100.1/5 specimen (100mm overlap, inner profile)

The stress analysis on the adhesively-bonded joints is usually approached by a closed-form analytical model or a finite element analysis (FEA). For a fast and easy answer, a closed-form analysis is preferable. A review [17] on analytical models of adhesively-bonded joints shows that almost all analytical models for adhesively-bonded lap joints are two-dimensional, which are generally sufficient because the variation of stresses in the width direction are significantly lower than that in the direction of the loading. The linear elastic analysis is supposed to be more appropriate for both adherents and adhesive, because the inclusion of material non-linearity renders the solution too complex. However, for the complex geometries and elaborate material models, an FEA is more suitable, which allows many tests to be simulated that would take too long to perform or be too expensive in practice, such as a geometrical parametric study or selection of appropriate material properties. In recent years, by improving the computational power of present machines, three-dimensional FE models [19, 26, 27] are more preferable for the stress-strain analysis on the adhesive joint than a two-dimensional FE model. By employing the three-dimensional FE models, the behaviour out of the plane can be addressed in a more trustworthy way.

2.4 Environmental effects

Although FRP composites are increasingly being used in civil infrastructure applications, their durability and long-term performance are still not comprehensively understood. More comprehensive understanding and accurate experimental data are required, since the service life of infrastructures is generally expected to be more than 50 years. With a view to the fact that most FRP infrastructures were constructed in the last two decades, the research correlating to the effects of environmental degradation on the mechanical behaviour and long-term performance of FRP structures are very limited in literature. In the natural life of such applications, the FRP composites are usually exposed to harsh and changing environments, involving large variations in temperature and humidity. In Ashcroft et al.'s research [28], three typical outdoor environments were selected and considered as hot/wet environment (Innisfail, Australia), hot/dry environment (Cloncurry, Australia) and temperate environment (Farnborough, UK). Average temperature and relative humidity of these three places are listed and shown in Table 2.1 and Fig. 2.9 respectively.

Table 2.1. Average climatic conditions at outdoor environments

Environment	Hot/wet	Hot/dry	Temperate
Temperature	23°C	25°C	10°C
Relative humidity	83%	55%	78%
Monthly rainfall	297mm	39mm	49mm

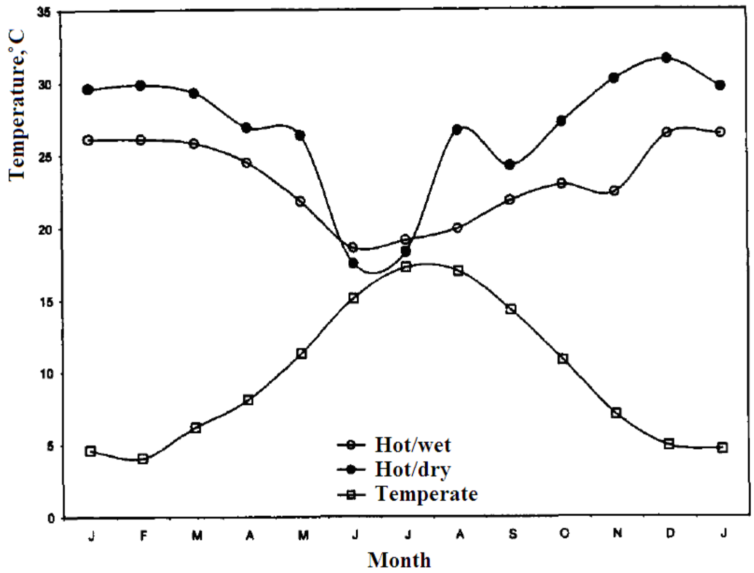

(a) Temperature

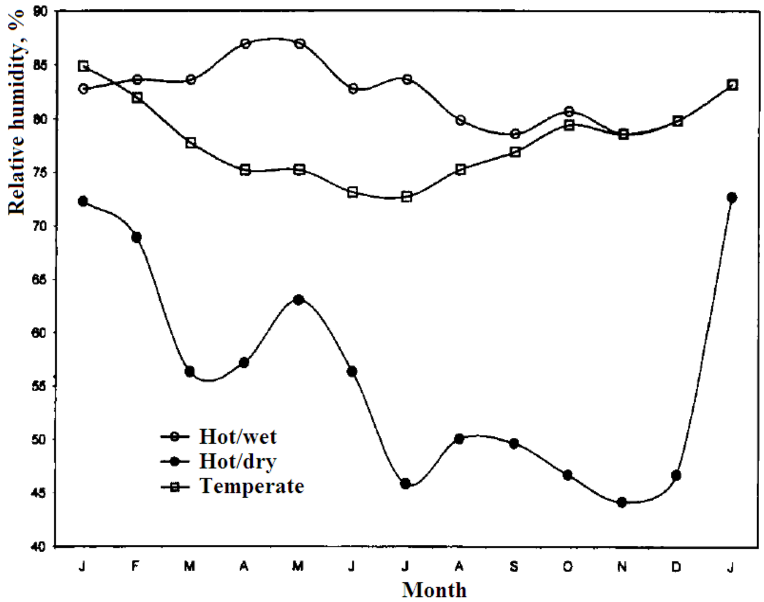

(b) Relative humidity

Fig. 2.9. Average monthly temperature and relative humidity in outdoor environments

The “hot/wet” exposure is supposed to be the severest environmental condition to degrade the performance of FRP composites [29-37], which will decrease the service life of FRP composite structures. The absorbed moisture will cause plasticization, saponification or hydrolysis that will induce both reversible and irreversible changes in the micro structure of the polymer, which will lead to degradation in their mechanical, chemical and thermo-physical characteristics [38-40]. Degradation due to moisture absorption may significantly reduce the service life of FRP structures. The elevated temperature usually accelerates this process. Thus, moisture diffusion in FRP composites is considered to be one of the major reliability concerns for the long-term performance of FRP structures.

In the aerospace engineering field, the influence of moisture absorption on mechanical properties of FRP composites and adhesive material is well documented in literature [29-34, 41-53]. Absorbed moisture can cause pronounced changes in modulus, strength and ultimate strain [50]. Moisture content of submerged FRP composites increases by diffusion. The research of Garcia et al. [47] indicates that the absorbed moisture can cause matrix cracking, fibre-matrix debonding, and corrosion of glass fibres, which results in a reduction of strength and stiffness of the FRP composite. Phifer [49] recorded that tensile strength and stiffness reductions are 60 percent and 10 percent, respectively, for E-glass/vinyl ester composites submerged in fresh water for a period of about 2 years. Doxsee et al. [51] correlated the interlaminar shear strength with the moisture concentration at the plane of failure in aramid/epoxy composites. In the research of Hu et al. [53] on fibre/polylactide composites, after 24 hour aging under 70°C in saturated water vapour condition, the tensile strength of uncoated fibre/polylactide composite specimen was 85.4% of the specimens without aging. After 72 hour aging, the tensile strength has badly deteriorated both for coated and uncoated specimens, less than 30% of unaged specimens. Interlaminar shear and flexural properties of FRP composites are generally more sensitive to moisture effects than tensile properties, since tensile properties are dominated by the fibres. But the glass and carbon fibre reinforcement does not absorb moisture. Only the fibre-matrix interface offers a preferential pathway for moisture ingression [45, 46]. For FRP bridge decks, the mechanical degradation of FRP composites will result in reduction of effective deck widths and the degree of composite action between decks and supporting girders, as well as overall stiffness of FRP bridges.

Consequently, the residual strength and service life of bridges will be less than expected.

Given the strong correlation between the rate of mechanical degradation and moisture absorption, it is of immense importance to understand the moisture diffusion process in polymers. The research [33] suggested that moisture diffuses into composite materials by three different mechanisms: (1) diffusion of water molecules inside the micro-gaps between polymer chains, (2) capillary transport into the gaps and flaws at the interfaces between fibres and polymer, and (3) transport by micro-cracks in the matrix, formed during the compounding process. Understanding the whole diffusion process by which moisture enters an FRP composite is critical to identify the location of damage, analyse the mechanical degradation as well as predict the residual strength and service life of FRP structures. Hence, it is important to know that moisture concentration distribution throughout sections of FRP composites as a function of time. As it is difficult to measure moisture concentration distribution throughout structural sections by experimental methods, gravimetric experiments [54-61] on the thin sections of FRP material are usually employed to obtain the moisture diffusion coefficients by recording the weight of absorbed water in a specimen as a function of aging time. Post et al. [57] obtained the higher diffusion rates and maximum moisture uptakes of a pultruded polyester/E-glass profile than typically reported for this class of material, which may be attributable to a larger microscopic void volume in the matrix resulting from rapid cure during pultrusion. Pierron [54] proposed a novel method for the identification of 3D moisture diffusion parameters on an epoxy resin reinforced by a glass fibre cloth. An optimization solution was employed to get the moisture saturation level only based on the slope of the initial linear part of the gravimetric curve, since the saturation of thick FRP specimens usually lead to very long conditioning times. For the case of Kevlar epoxy composite [60], the moisture diffusion was two orders of magnitude more rapid in the composite than in the base resin and the solubility was three to four times more than that accommodated by the base resin. It was speculated that the rapid diffusion in the composite was due to preferential diffusion of moisture along the matrix/fibre interface. This conclusion was confirmed by the research of Leman [61] on sugar palm fibre reinforced epoxy composites.

Generally, the moisture diffusion experiments for FRP composites are limited to a fairly short time, normally no more than 5 years. But the expected service life of infrastructures such as bridges is more than 50 years. Thus, the short-term experimental investigations are not sufficient to estimate the long-term performance of FRP structures. To achieve this aim, some accelerated experimental methods were developed by the researches [30, 37, 62, 63], in which the temperature or atmospheric pressure of the environmental aging conditions were raised beyond the normal service conditions to accelerate the moisture diffusion and degradation process. These accelerating experimental methods were confirmed to be useful and time-effective to investigate the durability of FRP composites and adhesive materials. But some researches indicated that the high aging temperatures approaching the glass transition temperature of specimens would improve the mechanical performance by post-cure or deteriorate the materials by inducing thermal cracks, which do not occur in the real utilisation of FRP composite structures. Another method for studying the long-term moisture diffusion behaviour in FRP structures is the Finite Element (FE) Method. Using the moisture diffusion coefficients determined by short-term gravimetric experiments, the moisture diffusion process in real FRP structures can be predicted by FE analysis [64]. The research [65] investigated the moisture diffusion in an adhesively-bonded composite connection under two environmental conditions (45°C-85%RH and 90°C-97%RH) by FE analysis, parametrically studying the unidirectional and multidirectional composites as well as two different fillet shapes, i.e., a rectangular and a triangular fillet.

References:

[1] Bakis CE, Bank LC, Brown VL, Cosenza E, Davalos JF, Lesko JJ, et al. Fiber-reinforced polymer composites for construction-state-of-the-art review. J Compos Constr. 2002;6(2):73-87.
[2] Awad ZK, Aravinthan T, Yan ZG, Gonzalez F. A review of optimization techniques used in the design of fibre composite structures for civil engineering applications. Mater Design. 2012;33:534-44.
[3] Knippers J, Pelke E, Gabler M, Berger D. Bridges with Glass Fibre-Reinforced Polymer Decks: The Road Bridge in Friedberg, Germany Structural Engineering International. 2010;20(4):400-4.
[4] Luke S, Canning L, Collins S, Knudsen E, Brown P, Taljsten B, et al. Advanced composite bridge decking system—project ASSET. Structural Engineering International. 2002;12(2):76-9.
[5] Reising RMW, Shahrooz BM, Hunt VJ, Neumann AR, Helmicki AJ, Hastak M. Close look at construction issues and performance of four fiber-reinforced polymer composite bridge decks. J Compos Constr. 2004;8(1):33-42.
[6] Hejll A, Taljsten B, Motavalli M. Large scale hybrid FRP composite girders for use in bridge structures - theory, test and field application. Compos Part B-Eng. 2005;36(8):573-85.
[7] Moses JP, Harries KA, Earls CJ, Yulismana W. Evaluation of effective width and distribution factors for GFRP bridge decks supported on steel girdersl. J Bridge Eng. 2006;11(4):401-9.
[8] King L, Toutanji H, Vuddandam R. Load and resistance factor design of fiber reinforced polymer composite bridge deck. Compos Part B-Eng. 2012;43(2):673-80.
[9] Zhou A, Keller T. Joining techniques for fiber reinforced polymer composite bridge deck systems. Compos Struct. 2005;69(3):336-45.
[10] Hollaway LC. A review of the present and future utilisation of FRP composites in the civil infrastructure with reference to their important in-service properties. Constr Build Mater. 2010;24(12):2419-45.
[11] Cassity P, Richards D, Gillespie J. Compositely Acting FRP Deck and Girder System. Structural Engineering International. 2002;2:71-5.
[12] Schollmayer M. Through-Thickness Performance of Adhesive Connections Between FRP Bridge Decks and Steel Main Girders. Lausanne: Ecole Polytechnique Federale de Lausanne; 2009.
[13] Park KT, Kim SH, Lee YH, Hwang YK. Degree of composite action verification of bolted GFRP bridge deck-to-girder connection system. Compos Struct. 2006;72(3):393-400.
[14] Keller T, Gurtler H. Composite action and adhesive bond between fiber-reinforced polymer bridge decks and main girders. J Compos Constr. 2005;9(4):360-8.
[15] Keelor DC, Luo Y, Earls CJ, Yulismana W. Service load effective compression flange width in fiber reinforced polymer deck systems acting compositely with steel stringers. J Compos Constr. 2004;8(4):289-97.
[16] Gurtler HW. Composite action of FRP bridge decks adhesively bonded to steel main girders Lausanne: Ecole Polytechnique Federale de Lausanne; 2004.
[17] da Silva LFM, das Neves PJC, Adams RD, Spelt JK. Analytical models of adhesively bonded joints-Part I: Literature survey. Int J Adhes Adhes. 2009;29(3):319-30.
[18] da Silva LFM, das Neves PC, Adams RD, Wang A, Spelt JK. Analytical models of adhesively bonded joints-Part II: Comparative study. Int J Adhes Adhes. 2009;29(3):331-41.

[19] Diaz J, Romera L, Hernandez S, Baldomir A. Benchmarking of three-dimensional finite element models of CFRP single-lap bonded joints. Int J Adhes Adhes. 2010;30(3):178-89.
[20] Wahab MMA, Crocombe AD, Beevers A, Ebtehaj K. Coupled stress-diffusion analysis for durability study in adhesively bonded joints. Int J Adhes Adhes. 2002;22(1):61-73.
[21] Keller T, Vallee T. Adhesively bonded lap joints from pultruded GFRP profiles. Part I: stress-strain analysis and failure modes. Compos Part B-Eng. 2005;36(4):331-40.
[22] Keller T, Vallee T. Adhesively bonded lap joints from pultruded GFRP profiles. Part II: joint strength prediction. Compos Part B-Eng. 2005;36(4):341-50.
[23] Vallee T, Keller T. Adhesively bonded lap joints from pultruded GFRP profiles. Part III: Effects of chamfers. Compos Part B-Eng. 2006;37(4-5):328-36.
[24] Vallee T, Correia JR, Keller T. Probabilistic strength prediction for double lap joints composed of pultruded GFRP profiles part I: Experimental and numerical investigations. Compos Sci Technol. 2006;66(13):1903-14.
[25] Vallee T, Correia JR, Keller T. Probabilistic strength prediction for double lap joints composed of pultruded GFRP profiles - Part II: Strength prediction. Compos Sci Technol. 2006;66(13):1915-30.
[26] Ichikawa K, Shin Y, Sawa T. A three-dimensional finite-element stress analysis and strength evaluation of stepped-lap adhesive joints subjected to static tensile loadings. Int J Adhes Adhes. 2008;28(8):464-70.
[27] Goncalves JPM, de Moura MFSF, de Castro PMST. A three-dimensional finite element model for stress analysis of adhesive joints. Int J Adhes Adhes. 2002;22(5):357-65.
[28] Ashcroft IA, Digby RP, Shaw SJ. A comparison of laboratory-conditioned and naturally-weathered bonded joints. J Adhesion. 2001;75(2):175-201.
[29] Shao YX, Kouadi S. Durability of fiberglass composite sheet piles in water. J Compos Constr. 2002;6(4):280-7.
[30] Bank LC, Gentry TR, Barkatt A. Accelerated Test Methods to Determine the Long-Term Behavior of Frp Composite Structures - Environmental-Effects. J Reinf Plast Comp. 1995;14(6):559-87.
[31] Nogueira P, Ramirez C, Torres A, Abad MJ, Cano J, Lopez J, et al. Effect of water sorption on the structure and mechanical properties of an epoxy resin system. J Appl Polym Sci. 2001;80(1):71-80.
[32] Earl JS, Shenoi RA. Hygrothermal ageing effects on FRP laminate and structural foam materials. Compos Part a-Appl S. 2004;35(11):1237-47.
[33] Robert M, Roy R, Benmokrane B. Environmental Effects on Glass Fiber Reinforced Polypropylene Thermoplastic Composite Laminate for Structural Applications. Polym Composite. 2010;31(4):604-11.
[34] Karbhari VM. E-glass/vinylester composites in aqueous environments: Effects on short-beam shear strength. J Compos Constr. 2004;8(2):148-56.
[35] Daly HB, Brahim HB, Hfaied N, Harchay M, Boukhili R. Investigation of water absorption in pultruded composites containing fillers and low profile additives. Polym Composite. 2007;28(3):355-64.
[36] Karbhari VM, Xian GJ. Hygrothermal effects on high V(F) pultruded unidirectional carbon/epoxy composites: Moisture uptake. Compos Part B-Eng. 2009;40(1):41-9.
[37] Muliana A, Nair A, Khan KA, Wagner S. Characterization of thermo-mechanical and long-term behaviors of multi-layered composite materials. Compos Sci Technol. 2006;66(15):2907-24.
[38] Levy RL, Fanter DL, Summers CJ. Spectroscopic Evidence for Mechanochemical Effects of Moisture in Epoxy-Resins. J Appl Polym Sci. 1979;24(7):1643-64.

[39] Birger S, Moshonov A, Kenig S. The Effects of Thermal and Hygrothermal Aging on the Failure Mechanisms of Graphite-Fabric Epoxy Composites Subjected to Flexural Loading. Composites. 1989;20(4):341-8.
[40] Mikols WJ, Seferis JC, Apicella A, Nicolais L. Evaluation of Structural-Changes in Epoxy Systems by Moisture Sorption-Desorption and Dynamic Mechanical Studies. Polym Composite. 1982;3(3):118-24.
[41] Springer GS. Enivormental effects on composite materials, vol.1. Lancaster, PA: Technomic Pubnishing company; 1981.
[42] Springer GS. Enivormental effects on composite materials, vol.2. Lancaster, PA: Technomic Pubnishing company; 1984.
[43] Springer GS. Enivormental effects on composite materials, vol.3. Lancaster, PA: Technomic Pubnishing company; 1987.
[44] Loh WK, Crocombe AD, Wahab MMA, Ashcroft IA. Modelling anomalous moisture uptake, swelling and thermal characteristics of a rubber toughened epoxy adhesive. Int J Adhes Adhes. 2005;25(1):1-12.
[45] Haque A, Mahmood S, Walker L, Jeelani S. Moisture and Temperature Induced Degradation in Tensile Properties of Kevlar Graphite Epoxy Hybrid Composites. J Reinf Plast Comp. 1991;10(2):132-45.
[46] Akay M, Mun SKA, Stanley A. Influence of moisture on the thermal and mechanical properties of autoclaved and oven-cured Kevlar-49/epoxy laminates. Compos Sci Technol. 1997;57(5):565-71.
[47] Garcia K, Hayes MD, Verghese N, Lesko JJ. The effects of cycling moisture aging on glass/vinyl ester composite system. Proceedings of 3rd International Conference on Progress in Durability Analysis of Composite Systems1998. p. 173-9.
[48] Phifer SP. Hygrothermal evaluation of pultruded polymer composite laminates-Experimentation, analysis, and prediction. Blacksburg, VA: Virginia Tech; 2003.
[49] Phifer SP. Hygrothermal evaluation of pultruded polymer composite laminates-Experimentation, analysis, and prediction. Blacksburg, VA: Virginia Tech; 2003.
[50] Shen CH, Springer GS. Moisture absorption and desorption of composite materials, environmental effects on composite materials: Technomic Publishing Company, Westport, CT; 1981.
[51] Doxsee LE, Janssens W, Verpoest I, Demeester P. Strength of Aramid-Epoxy Composites during Moisture Absorption. J Reinf Plast Comp. 1991;10(6):645-55.
[52] Arun KV, Basavarajappa S, Sherigara BS. Damage characterisation of glass/textile fabric polymer hybrid composites in sea water environment. Mater Design. 2010;31(2):930-9.
[53] Hu RH, Sun MY, Lim JK. Moisture absorption, tensile strength and microstructure evolution of short jute fiber/polylactide composite in hygrothermal environment. Mater Design. 2010;31(7):3167-73.
[54] Pierron F, Poirette Y, Vautrin A. A novel procedure for identification of 3D moisture diffusion parameters on thick composites: Theory, validation and experimental results. J Compos Mater. 2002;36(19):2219-43.
[55] Bao LR, Yee AF. Moisture diffusion and hygrothermal aging in bismaleimide matrix carbon fiber composites - Part I: uni-weave composites. Compos Sci Technol. 2002;62(16):2099-110.
[56] Bao LR, Yee AF. Moisture diffusion and hygrothermal aging in bismaleimide matrix carbon fiber composites: part II - woven and hybrid composites. Compos Sci Technol. 2002;62(16):2111-9.

[57] Post NL, Riebel F, Zhou A, Keller T, Case SW, Lesko JJ. Investigation of 3D Moisture Diffusion Coefficients and Damage in a Pultruded E-glass/Polyester Structural Composite. J Compos Mater. 2009;43(1):75-96.
[58] Barjastech E, Nutt SR. Moisture absorption of unidirectional hybrid composites Compos Part a-Appl S. 2012;43:158-64.
[59] Katzman HA, Castaneda RM, Lee HS. Moisture diffusion in composite sandwich structures. Compos Part a-Appl S. 2008;39(5):887-92.
[60] Aronhime MT, Neumann S, Marom G. The Anisotropic Diffusion of Water in Kevlar Epoxy Composites. J Mater Sci. 1987;22(7):2435-46.
[61] Leman Z, Sapuan SM, Saifol AM, Maleque MA, Ahmad MMHM. Moisture absorption behavior of sugar palm fiber reinforced epoxy composites. Mater Design. 2008;29(8):1666-70.
[62] Davies P, Evrard G. Accelerated ageing of polyurethanes for marine applications. Polym Degrad Stabil. 2007;92(8):1455-64.
[63] Moulzakis DE, Zoga H, Galiotis C. Accelerated environmental ageing study of polyester/glass fiber reinforced composites (GFRPCs). Compos Part B-Eng. 2008;39(3):467-75.
[64] Jiang X, Kolstein H, Bijlaard FSK. Moisture diffusion in glass-fiber-reinforced polymer composite bridge under hot/wet environment. Compos Part B-Eng. 2013;45(1):407-16.
[65] Abdelwahab MM, Ashcroft IA, Crocombe AD, Shaw SJ. Diffusion of moisture in adhesively bonded joints. J Adhesion. 2001;77(1):43-80.

Chapter 3

Moisture diffusion characteristics of FRP composites*

3.1 Introduction

The subject of this chapter is to study the moisture diffusion process in FRP composites (pultrusion and resin-infusion). By gravimetric experiments, the moisture diffusion in FRP composites has been characterized under four environmental conditions. Based on the analytical solution from the one-dimensional and the three-dimensional moisture diffusion theory, the diffusion coefficients were determined by the least-square curve fitting to the experimental data. The FE models with the same dimensions as test specimens were developed and validated against the experimental results. By employing the FE model, the three dimensional diffusion coefficients were also validated. This research provides a numerical technical basis for coupling the moisture diffusion and mechanical analysis of FRP composites to predict the residual strength of FRP structures exposed to hot/wet environments.

3.2 Moisture diffusion theory

Most of the studies on moisture diffusion in FRP composites rely on the one-dimensional Fickian process, the equation of which is expressed as [3, 4]:

$$\frac{\partial c}{\partial t} = D\frac{\partial^2 c}{\partial x^2} \tag{3.1}$$

where *c* represents the moisture concentration, *x* the space coordinate measured parallel to the diffusion, and *D* the moisture diffusion coefficient in

* The content of this chapter is partially published in [1] Jiang X, Kolstein H, Bijlaard FSK. Moisture diffusion in glass-fiber-reinforced polymer composite bridge under hot/wet environment. Compos Part B-Eng. 2013;45(1):407-16. and [2] Jiang X, Kolstein H, Bijlaard FSK, Qiang X. Effects of hygrothermal aging on glass-fibre reinforced polymer laminates and adhesive of FRP composite bridge: Moisture diffusion characteristics Composites Part A: Applied Science and Manufacturing. 2014, 57: 49 – 58.

the *x* direction. *D* is supposed to be independent of the spatial and temporal coordinates. For a plate of infinite dimensions, the boundary conditions are:

$$\begin{cases} c = c_i & 0 \le x \le e \qquad t < 0 \\ c = c_\infty & x < 0;\ x > e \qquad t \ge 0 \end{cases} \tag{3.2}$$

where *e* is the plate thickness. The analytical solution [3], giving the moisture concentration *c* at time *t*, is expressed as:

$$\frac{c}{c_\infty} = 1 - \frac{4}{\pi}\sum_{n=0}^{\infty}\frac{(-1)^n}{(2n+1)}\exp\left[-\frac{Dt}{e^2}\pi^2(2n+1)^2\right] \tag{3.3}$$

where c_∞ is the maximum equilibrium moisture concentration. The expression is integrated, giving the moisture absorption content M_t as a function of time, in Equation (3.4):

$$M_t = M_\infty\left\{1 - \frac{8}{\pi^2}\sum_{n=0}^{\infty}\frac{1}{(2n+1)^2}\exp\left[-\frac{Dt}{e^2}\pi^2(2n+1)^2\right]\right\} \tag{3.4}$$

where M_∞ is the equilibrium amount of absorption. The theoretical Fickian diffusion process is shown in Fig. 3.1.

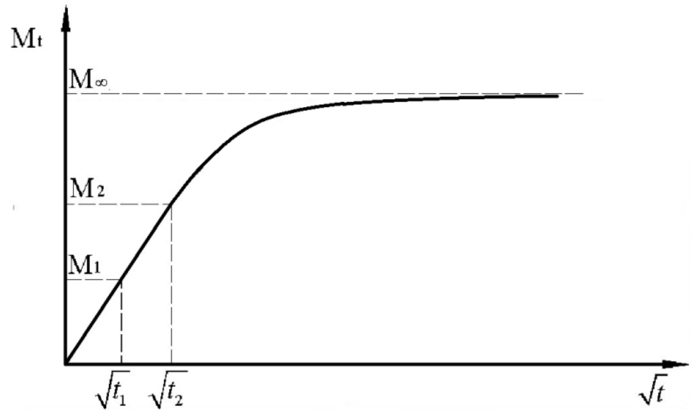

Fig. 3.1. Fickian diffusion process.

For the initial linear part of the Fickian diffusion curve ($\sqrt{Dt}/e \le 0.28$), the identification of the moisture diffusion coefficient *D* is performed as follows. The total gravimetric curve (Fig. 3.1) is used to determine M_∞. Then, *D* is calculated from the linear part using two points at times t_1 and t_2.

$$D = \pi\left(\frac{e}{4M_\infty}\right)^2\left(\frac{M_1 - M_2}{\sqrt{t_1} - \sqrt{t_2}}\right)^2 \tag{3.5}$$

In practice, this simple procedure is mostly used for the thin-section of an FRP composite plate in the through-thickness direction, although the hypothesis on which it relies, i.e., the fact that the plate is infinite in the plane directions, is incorrect for the generally small specimens used in the climate chambers.

For a thick plate of FRP composites, to satisfy the above assumption "infinite" plate, the use of very large specimens is unavoidable to achieve the required surface-to-thickness ratio. But these large specimens are inconvenient to store in environmental chambers and weight measuring. Thus, other approaches need to be developed to analytically depict three-dimensional moisture diffusion process in the thick plate of FRP composites.

Firstly, due to the simplicity and mathematical tractability, the equivalent diffusion coefficient method is usually used [3]. It assumes that the total mass of moisture absorbed is equal to the total amount of moisture absorbed from the six surfaces independently. According to this assumption, the moisture uptake can be expressed as:

$$M_t = 4c_\infty \sqrt{\frac{t}{\pi}} \left(eb\sqrt{D_1} + el\sqrt{D_2} + bl\sqrt{D_3} \right) \tag{3.6}$$

where l and b are the length and width of the plate and D_1, D_2 and D_3 are the moisture diffusion coefficients along the direction of length, width and thickness, respectively.

As $c_\infty = m_\infty lbe$, then Eq. 3.6 comes to be:

$$M_t = \frac{4m_\infty}{e} \sqrt{\frac{t}{\pi}} \left(\frac{e}{l}\sqrt{D_1} + \frac{e}{b}\sqrt{D_2} + \sqrt{D_3} \right) \tag{3.7}$$

By analogy to the infinite plate solution, for the three dimensional moisture diffusion it is possible to define an equivalent moisture diffusion coefficient D by:

$$D = D_3 \left(\frac{e}{l}\sqrt{\frac{D_1}{D_3}} + \frac{e}{b}\sqrt{\frac{D_2}{D_3}} + 1 \right)^2 \tag{3.8}$$

Employing the gravimetric curve (Fig. 3.1) obtained from experiments, the equivalent D can be addressed by Eq.3.5. Then three groups of FRP specimens with different aspect ratios fully enable the identification of the three dimensional diffusion coefficients: D_1, D_2 and D_3, from Eq.3.8. However, this approach has limits, which will be discussed hereafter in further detail.

The other method to obtain the D_1, D_2 and D_3 is depending on the full three-dimensional moisture diffusion theory [3]. The three-dimensional Fickian differential equation is written as:

$$\frac{\partial c}{\partial t} = D_1 \frac{\partial^2 c}{\partial {x_1}^2} + D_2 \frac{\partial^2 c}{\partial {x_2}^2} + D_3 \frac{\partial^2 c}{\partial {x_3}^2} \tag{3.9}$$

With the boundary conditions as:

$$\begin{cases} c = c_i & 0 \le x_1 \le l\,; 0 \le x_2 \le b\,; 0 \le x_3 \le e & t < 0 \\ c = c_\infty & x_1 < 0, x_2 < 0, x_3 < 0;\; x_1 > l, x_2 > b, x_3 > e & t \ge 0 \end{cases} \tag{3.10}$$

A closed-form solution to the above is given as:

$$\begin{aligned} \frac{c_t - c_i}{c_\infty - c_i} = 1 - \frac{64}{\pi^3} \sum_{m=0}^{\infty} \sum_{n=0}^{\infty} \sum_{p=0}^{\infty} \frac{(-1)^m (-1)^n (-1)^p}{(2m+1)(2n+1)(2p+1)} \exp(-Qt) \cos\frac{(2m+1)\pi x_1}{l} \\ \times \cos\frac{(2n+1)\pi x_2}{b} \cos\frac{(2p+1)\pi x_3}{e} \end{aligned} \tag{3.11}$$

With

$$Q = \pi^2 \left[D_1 \left(\frac{2m+1}{l}\right)^2 + D_2 \left(\frac{2n+1}{b}\right)^2 + D_3 \left(\frac{2p+1}{e}\right)^2 \right] \tag{3.12}$$

By integrating on the space variables, the moisture uptake content can be expressed as:

$$M_t = M_\infty \left[1 - \left(\frac{8}{\pi^2}\right)^3 \sum_{m=0}^{\infty} \sum_{n=0}^{\infty} \sum_{p=0}^{\infty} \frac{1}{(2m+1)^2 (2n+1)^2 (2p+1)^2} \exp(-Qt) \right] \tag{3.13}$$

It is noted that the three-dimensional moisture diffusion analytical expression is rather complicated. There is no analogical equation like Eq. 3.5 to directly identify the moisture diffusion coefficients D_1, D_2 *and* D_3 from the experimental gravimetric curve (Fig. 3.1). A novel method for identification of three-dimensional moisture diffusion coefficients on thick

FRP plates was developed by Pierron [5], which is based on an optimization scheme. The idea is to build up an objective function q as:

$$q = \sum_{i} \left[M_t(t_i) - M_i \right]^2 \tag{3.14}$$

where $M_t(t_i)$ is the moisture content calculated from Eq.3.13 at time t_i and M_i the moisture content experimentally obtained from the gravimetric curve at time t_i. Minimizing q with respect to D_1, D_2 *and* D_3 enables the identification. This process is realized by fitting the best Fickian least-square curve to the experimental data points.

3.3 Experiments

3.3.1 Specimen preparation

Two typical FRP composites are selected for this research: pultrusion profile and resin-infusion laminates. For the pultruded FRP composites, specimens are cut from the ASSET FRP bridge deck element (Fig. 3.2) produced by Fiberline Composites A/S [6].

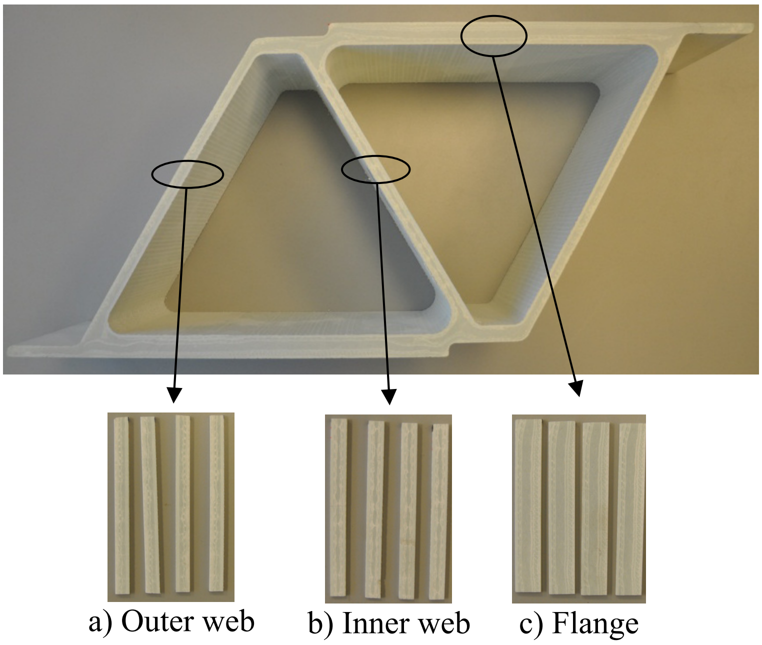

Fig. 3.2. FRP ASSET bridge deck element and test specimens

These triangular shape profiles are manufactured by the pultrusion process, and then bonded together to form the bridge deck. The lay-up consists of longitudinal rovings, surrounded by a continuous strand mat and a surfacing veil, as shown in Fig. 3.3. In the roving part, fibres are unidirectional oriented in the direction of pultrusion. The surfacing veil is added outside the mat part to protect against environmental attacks. The shapes consist of an average 62% E-glass fibres (volume fraction) embedded in an isophthalic polyester matrix.

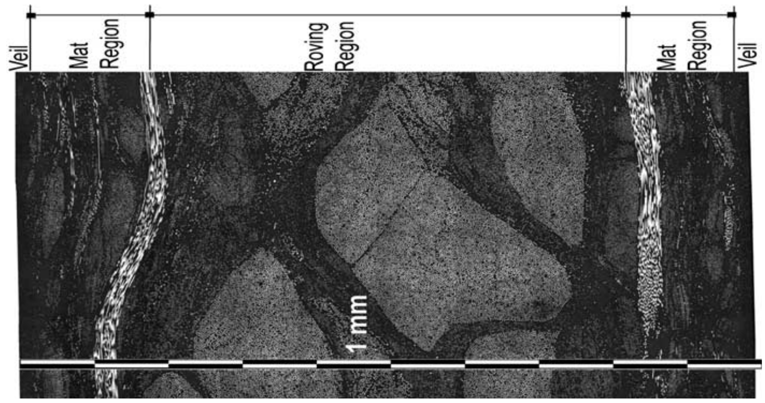

Fig. 3.3. Typical cross-section view of pultruded FRP composites [7]

It is obvious from Fig. 3.2 that specimens from different parts (inner web, outer web and flange) of the ASSET bridge deck element are composed of different volume fractions of roving and mat layer. It can be expected that deviations of moisture diffusion properties can occur on different parts of the cross-section. Thus, it is of great interest to conduct separate moisture diffusion experiments on the inner web, outer web and flange parts. Nominal dimensions of pultruded FRP specimens are listed in Table 3.1.

Table 3.1 Nominal dimension of FRP specimens

Pultrusion profile	Length (mm)	Width (mm)	Thickness (mm)
Inner web	100	9.80	2.80
Outer web	100	7.80	2.80
Flange	100	15.6	2.80
Resin-infusion Laminate	Length (mm)	Width (mm)	Thickness (mm)
Square	100	100	2.82
Rectangular	100	50	2.82
Small square	50	50	5.64

For resin-infusion FRP laminates, specimens are manufactured by resin vacuum infusion (Infra Composite BV [8]) and then cut into specific dimensions (see Fig. 3.4). The resin used is polyester. In order to obtain the three-dimensional moisture diffusion coefficients D_1, D_2 *and* D_3, specimens were deliberately prepared with three different aspect ratios, as listed in Table 1. The 2.82mm thickness specimens are made up of three plies of standard 0.94mm EQX1200, which is a glass-fibre reinforced polymer composites (54% glass content by weight). Layup configuration of EQX1200 is listed in Table 3.2. The 5.64mm thickness specimen is made up of six plies of standard 0.94mm EQX1200.

a) Square

b) Rectangular

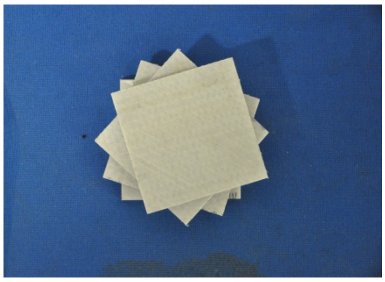

c) Small square

Fig. 3.4. FRP laminate specimens

Table 3.2. Properties of FRP laminates (supplied by manufacturer [9])

Product name	Total weight (g/m^2)	Weight uniformity (g/m^2)				
		Yarn roving				Knit yarn
		0^o	$+45^o$	90^o	-45^o	
EQX 1200	1193	283	300	300	300	10

3.3.2 Gravimetric test process

Generally, the moisture diffusion process in FRP composite materials is investigated by gravimetric tests [10-15]. The whole experiment process follows the test code ASTM D5229/D5229M-92 [16]. For both pultruded FRP composites and resin-infusion FRP laminates, four replicates are tested in each specific aging condition. Four environmental aging conditions are selected with regard to normal service environments of bridge decks, which are 20°C-50% RH (relative humidity), 20°C-water, 40°C-96% RH and 40°C-water. The 40°C-96% RH and 40°C-water conditions are considered as typical hot/wet environments for the application of an FRP composite bridge. The temperature and relative humidity of each aging condition is kept constant during the whole process of testing. The 20°C-50% RH condition is obtained by putting specimens in a climate room, with constant temperature and relative humidity at 20°C and 50% RH. The 20°C-water condition is obtained by putting specimens in a water filled glass container, which is also kept in the same climate room. The 40°C-96% RH is provided in a climate chamber, of which the temperature and relative humidity are controlled to be 40°C and 96% RH. 40°C-water condition is obtained by putting specimens in a water filled glass container, which is kept in the same chamber at stable temperature 40°C. Prior to putting specimens into the environmental conditions, all the specimens are dried in an oven at 40°C and the weight of specimens is periodically checked until no changes in weight occur. This status is assumed to be the original stage of the whole moisture diffusion process. For tracking the change of weight, after each specific time interval, each specimen is removed from the environmental conditioning chamber, weighed quickly using a precise balance with the accuracy of 0.00001g and then returned to the chamber. For the water immersed aging conditions, before measuring the self-weight, the residual liquid water trapped on the surface of the specimens must be wiped away. The procedure is repeated until the samples reach a saturation level. The moisture uptake content (M_t) absorbed by each specimen is calculated according to its weight before exposure (w_0) and after exposure (w_t) as follows:

$$M_t = \frac{w_t - w_0}{w_0} \tag{3.15}$$

3.4 Experimental results and discussion

3.4.1 Pultruded FRP composites

After a 24-day aging period in water and vapour environmental conditions, the moisture uptake curves of the pultruded FRP specimens are presented in Fig. 3.5, where M_t is plotted vs. $\sqrt{t}$ to show the initial linear diffusion curve. All the detailed test data can be found in the Stevin II lab report.

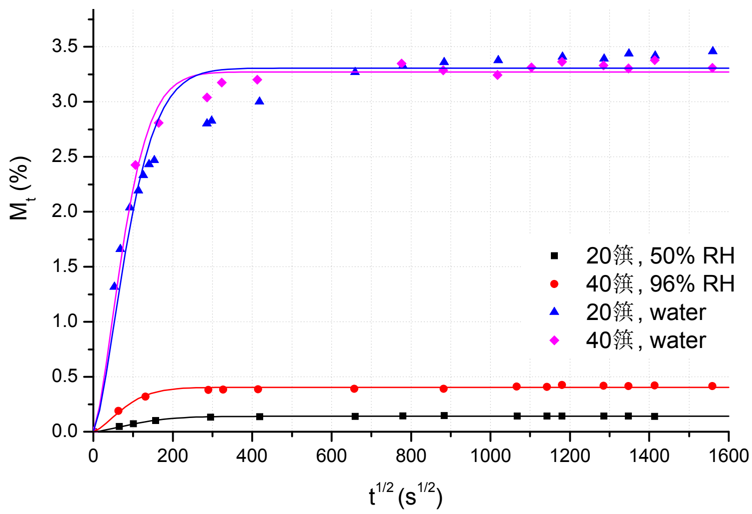

a) Inner web

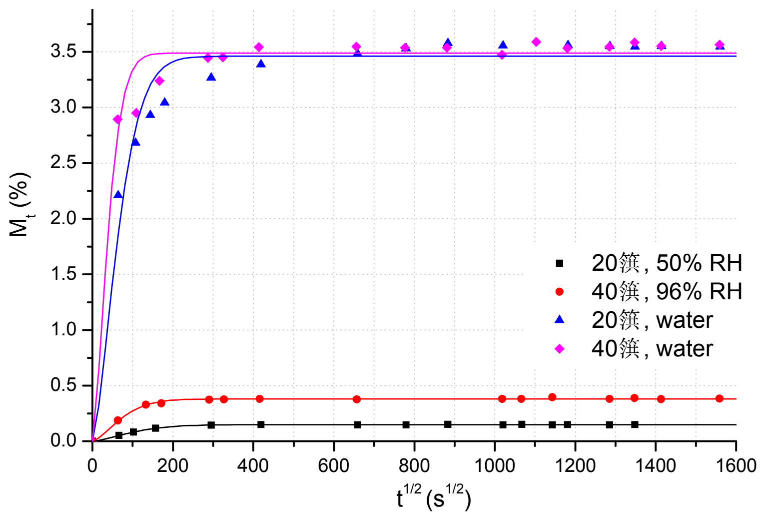

b) Outer web

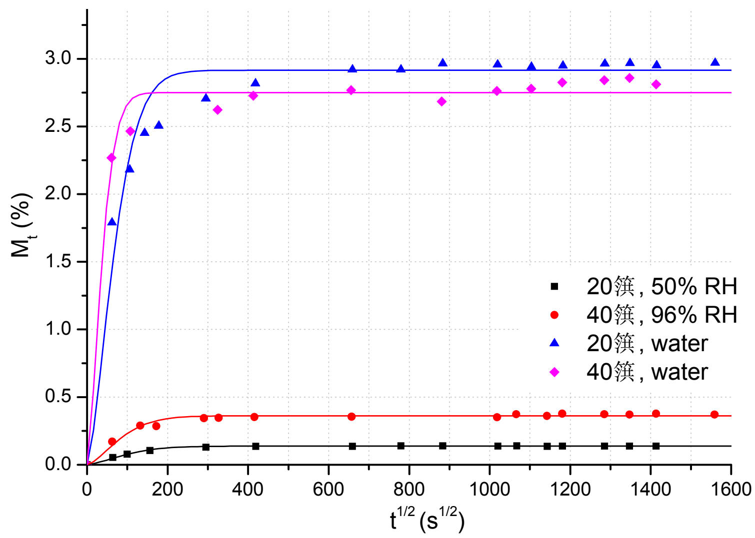

c) Flange

Fig. 3.5. Moisture absorption process of pultruded FRP specimens from different parts

For the initial part of all curves, moisture uptakes of the pultruded FRP specimens increase abruptly. All the FRP specimens aged in the specific environmental condition reached the moisture saturation level within two days. To analytically model this moisture diffusion process, the one-dimensional Fickian model is employed due to its simplicity and mathematical tractability [3, 4]. As aforementioned, it is assumed that the FRP plate is infinite and the moisture only diffuses in the through-thickness direction. But for this study, only small scale specimens could be prepared due to the limited geometry of the ASSET bridge deck element. It is generally noted that in continuous fibre composites, the bulk diffusion properties are orthotropic due to the material heterogeneity difference along and transverse to the fibre direction. Results of Aronhime et al.'s experiments [17] showed that the moisture diffusion rates along the fibre direction were much higher than those transverse to the fibre direction, and they were in a different order of magnitude. In this study, the pultruded FRP specimens are cut in the vertical direction of pultrusion, which means the cutting surfaces (XY plane in Fig. 3.6) of FRP specimens are vertical to the fibre direction of the roving part. Thus, the amount of moisture content diffused through the cutting surfaces of FRP specimens is much larger than that through the edge surfaces of FRP specimens. Moreover, the edge surfaces of FRP specimens are protected from environmental attacks by the surfacing veil. So, the moisture absorption from the edge surfaces of specimens can be neglected. Therefore, in this study, the moisture diffusion process in FRP specimens can be assumed to be essentially one-dimensional through the thickness direction (Z direction in Fig. 3.6) of FRP specimens.

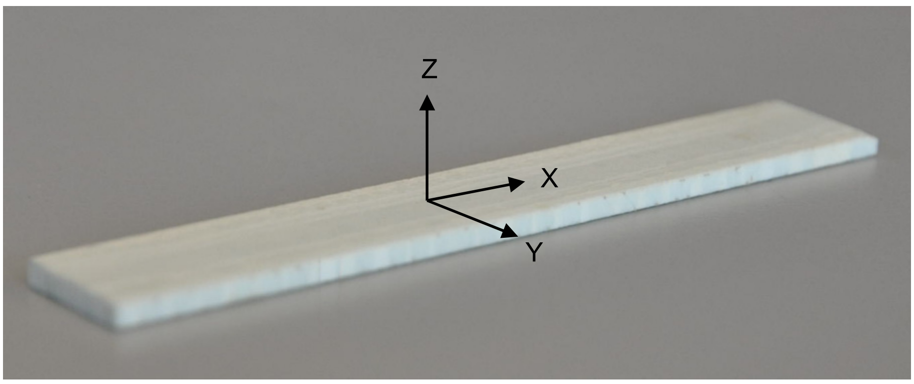

Fig. 3.6. Illustration of coordinates in the pultruded FRP specimen

For the pultruded FRP composites, the initial moisture diffusion process is too fast to get enough data points to comply the assumption ($\sqrt{D_z t} / e \leq 0.28$) of the Fickian diffusion theory. In order to get the accurate value of Fickian diffusion coefficient *D,* the analytical model (Eq. 3.4) is employed to fit the experimental data points by the least-square method. After the analytical curve fitting, the Fickian diffusion coefficients and maximum moisture contents at equilibrium are obtained and summarized in Table 3.3, and analytical curves are plotted in Fig. 3.5.

Table 3.3 Moisture diffusion coefficients of pultruded FRP composites

Specimen	Aging condition	D ($\times 10^{-5}$ mm^2/s)	M_∞ (%)
Inner web	20°C , 50% RH	3.164	0.141
	40°C , 96% RH	6.105	0.403
	20°C , water	4.717	3.306
	40°C , water	6.022	3.272
Outer web	20°C , 50% RH	3.804	0.149
	40°C , 96% RH	7.365	0.380
	20°C , water	9.278	3.461
	40°C , water	24.92	3.489
Flange	20°C , 50% RH	4.425	0.137
	40°C , 96% RH	5.750	0.361
	20°C , water	8.847	2.915
	40°C , water	29.38	2.751

Comparing with the gravimetric experiments in the vapour aging conditions, experiments conducted in water result in higher moisture saturation levels, around 3% of the initial self-weight of FRP materials. Specimens immersed in water at temperatures of 20°C and 40°C develop almost identical moisture uptakes to each other. Only for the initial linear phase, the moisture diffusion into FRP specimens under 40°C is faster than that of 20°C. The moisture saturation levels for both aging temperatures are close to each other. Results (Table 3.3) show that the rates of moisture uptake are more sensitive to temperature and the moisture saturation levels of FRP material are only dominated by humidity of aging conditions. For the vapour environmental conditions, the comparison of the mass variation exhibited by both FRP profiles depicts significant differences, with the moisture uptake for 20°C -50% RH aging condition being considerably slower and lower in moisture equilibrium than that exhibited by the 40°C -96% RH aging condition, which is reasonable according to the aforementioned conclusion. Comparing the results of different part specimens, it is found that there is no considerable variability in the value of maximum equilibrium moisture contents, where the flange absorbs about 2.8% in water and the inner and outer webs absorb about 3.3% in water. Only the moisture diffusion rates of inner web specimens in water conditions are considerably lower than the other two parts.

It is noted that analytical solutions for moisture diffusion prediction are limited to simple geometry. It is not feasible to predict the moisture diffusion process in the complex shaped FRP composite profiles, such as the ASSET bridge element (Fig. 3.2). Thus, it is of great interest to develop the Finite Element (FE) method to simulate the moisture diffusion process in FRP composites. As we know, the moisture diffusion process is a transient phenomenon, which relates to the moisture concentration distribution throughout the profiles as a function of exposure time. So the transient field analysis is the most appropriate form for FE based diffusion analysis. The commercial FE analysis package ABAQUS 6.8 is employed for the moisture diffusion analysis. In ABAQUS 6.8, the governing equations for mass diffusion are an extension of Fickian equations: they allow for non-uniform solubility of the diffusing substance in the base material and for mass diffusion driven by gradients of temperature and pressure. The basic solution variable (used as the degree of freedom at the nodes of the mesh) is the “normalized concentration”, which is the mass concentration of the diffusing material divided by its solubility in the base material. Therefore, when the mesh includes dissimilar materials that share nodes, the normalized concentration is continuous across the interface between the different materials [18]. The mass diffusion element DC3D8 is used in FE analysis, which is a 8-node linear brick element. The FE model is built with the same dimensions as the test specimens (see Fig. 3.7).

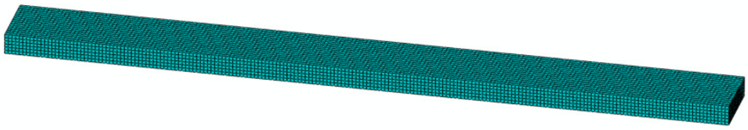

a) Inner web

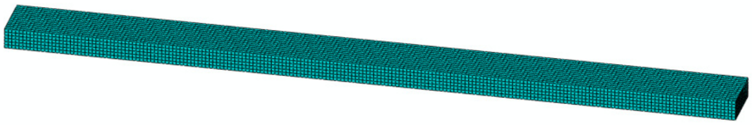

b) Outer web

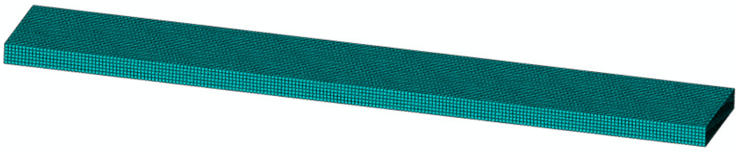

c) Flange

Fig. 3.7. FE models of pultruded FRP specimens

Herein, only the moisture diffusion in the 40°C-water aging condition is simulated by FE analysis, depending on which the coupled hygro-thermal mechanical analysis can be conducted. The moisture diffusion coefficients obtained from tests (see Table 3.3) are used as input parameters for material properties in the FE model. The typical Fickian diffusion is considered for the pultruded FRP composites. All of these parameters are assumed to be constant during the whole diffusion analysis. Small integration time steps are inevitably needed to achieve the convergence and enhance the accuracy, especially at the initial stage of FE diffusion analysis. Integration time steps are automatically controlled. The moisture concentration of six surfaces of FE models are set to be fully saturated as the boundary conditions to active the kinetics of the diffusion process. Because the specimens are fully immersed in water, the variation in the moisture boundary concentration with time is assumed to be negligible. The results of mass concentration at integration points (CONC) are output to a .fil result file. The specific post-processing subroutine is developed and performed by FORTRAN to get the moisture absorption curves as a function of time. The subroutine realizes: 1) calculating the moisture content of each element (at the time *t*) by using the mass concentration (conc) of the element multiplied by this element volume; 2) summarising the moisture content (M_t) of each element to obtain the amount of moisture content in the FE model.

Fig. 3.8 shows the comparison of analytical solutions and FE analysis results together with experimental data for moisture diffusion in pultruded FRP composite specimens under the 40°C -water condition.

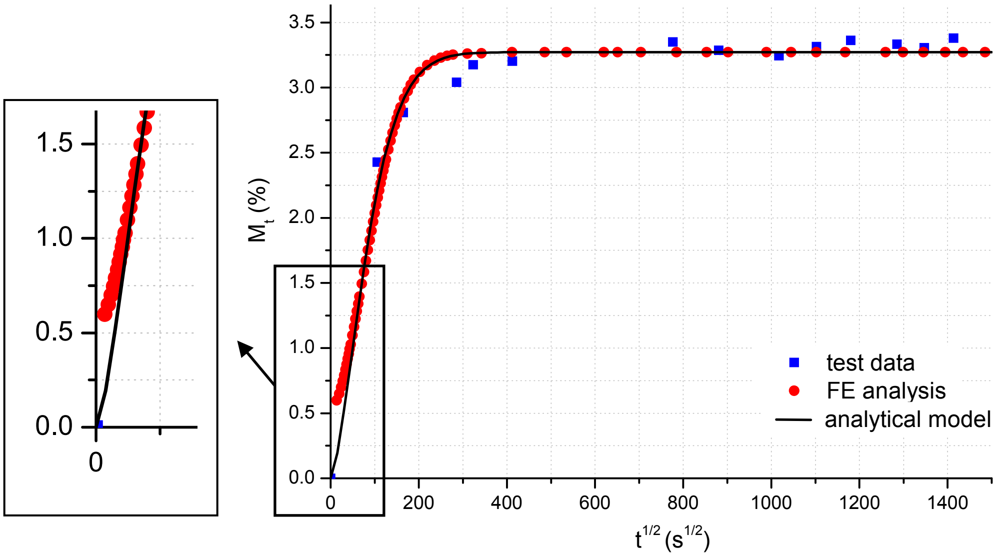

Fig. 3.8. a) inner web FRP composites

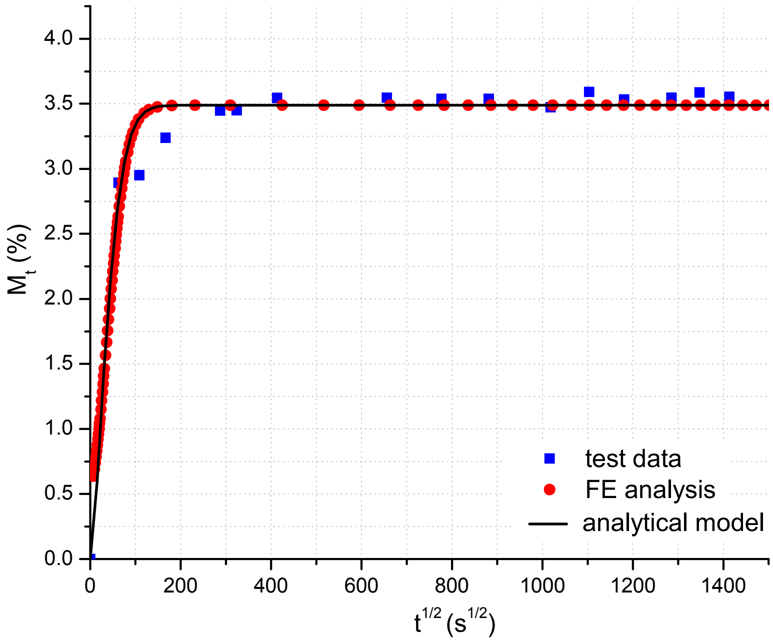

Fig. 3.8. b) outer web FRP composites

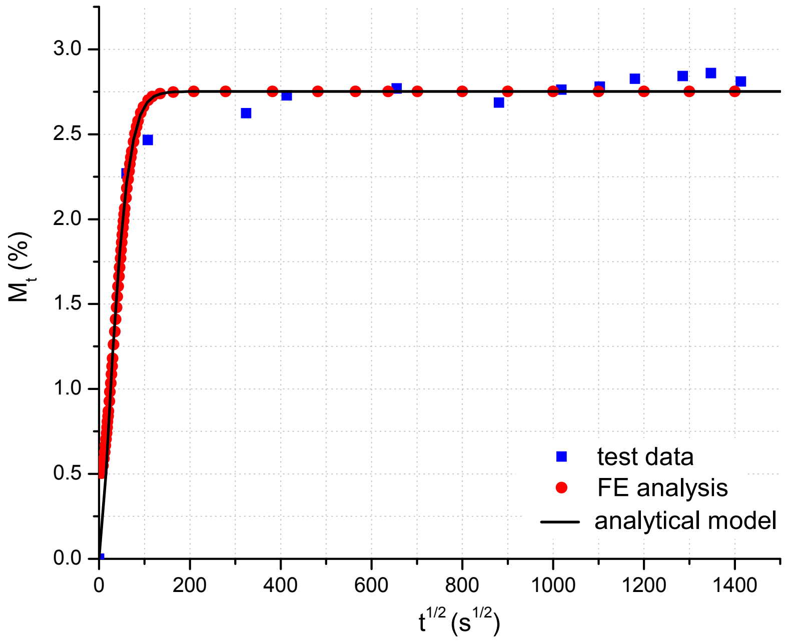

c) flange FRP composites

Fig. 3.8. Comparison of FE results, analytical models and experimental data

It is manifest from Fig. 3.8 a) - c) that analytical curves and FE results agree very well with each other. Only for the initial diffusion stage, deviation from two curves takes place, which is due to boundary conditions of the FE model. At time=0, the moisture concentration of edge surfaces of FE models is fully saturated, which means the total moisture content before running the FE analysis is not zero. As the diffusion analysis is going on, the FE results gradually approach analytical curves and finally they superpose each other. Thus, the FE model is validated by analytical curves and experimental data. It can be used in future work to predict the moisture diffusion in the pultruded FRP composites with complex geometry and longer aging times.

3.4.2 Resin-infusion FRP laminates

After about 250-day aging in water and vapour environmental conditions, the average moisture uptake curves of FRP laminate specimens are presented in Fig. 3.9. All the detailed test data can be found in the Stevin II lab report.

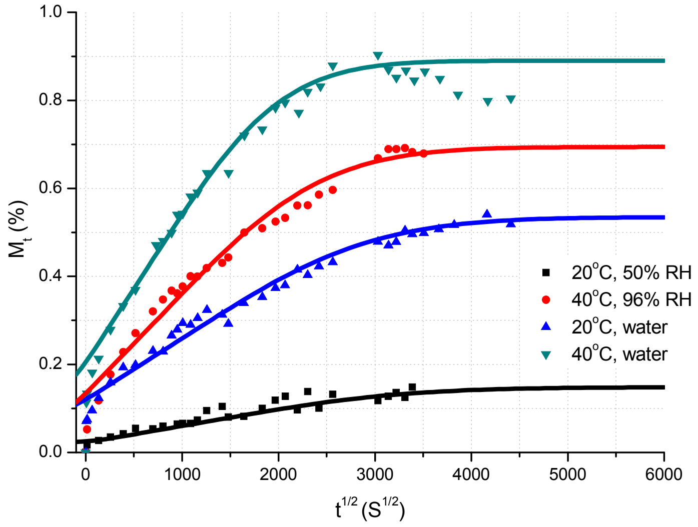

a) 100mm×100mm×2.82mm

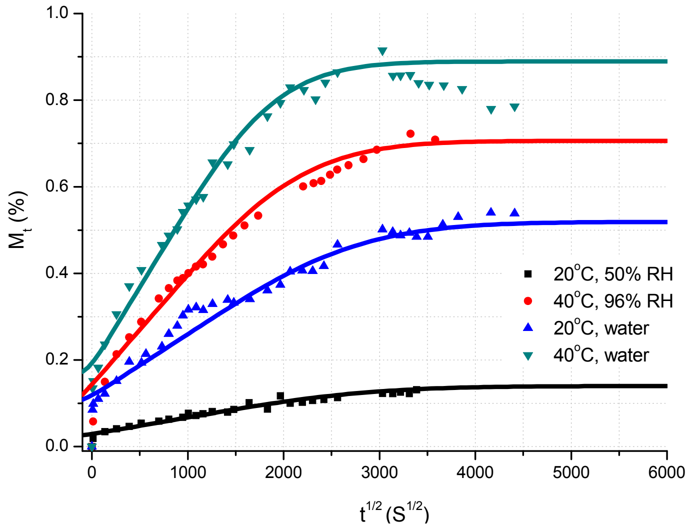

b) 100mm×50mm×2.82mm

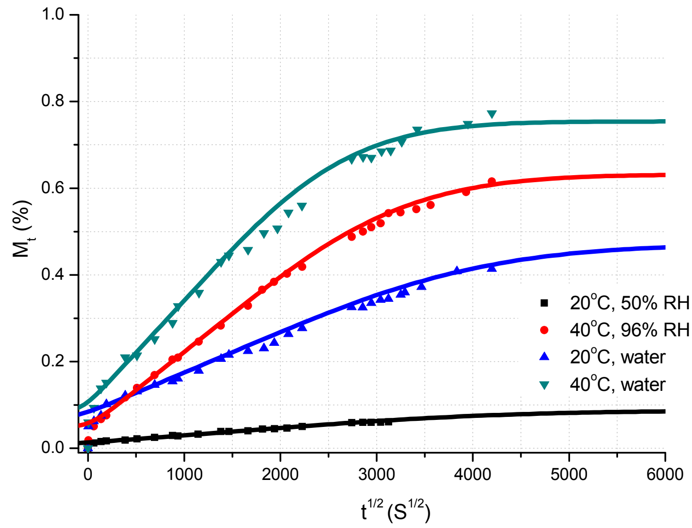

c) 50mm×50mm×5.64mm

Fig. 3.9. Moisture absorption process of FRP laminate specimens

Similar to the pultruded FRP composites, in the initial part of all curves, moisture uptakes increase linearly and then regularly slow down until reaching the moisture saturation level. Moisture absorption content varies significantly in four aging conditions.

Table 3.4 Moisture diffusion coefficients of FRP laminates based on one dimensional diffusion theory

Specimen	Aging condition	D($\times 10^{-7}$mm^2/s)	M_∞ (%)
Square	20°C, 50%RH	1.347	0.148
	40°C, 96%RH	1.963	0.694
	20°C, water	1.438	0.535
	40°C, water	3.040	0.890
Rectangular	20°C, 50%RH	1.542	0.140
	40°C, 96%RH	2.380	0.706
	20°C, water	1.676	0.519
	40°C, water	3.602	0.889
Small square	20°C, 50%RH	2.830	0.087
	40°C, 96%RH	5.198	0.632
	20°C, water	3.101	0.471
	40°C, water	7.330	0.754

As listed in Table 3.4, the specimens aged in the 40°C-water condition result in the highest moisture saturation level (M_∞), which is more than six times of that in the 20°C-50% aging condition. It is confirmed once more that the hot/wet environment can accelerate the moisture-induced deterioration process of FRP materials. As compared to the maximum moisture uptakes of pultruded FRP composites addressed above, the M_∞ of FRP laminates are considerably lower. Moreover, for the last part of the moisture diffusion process of the Square and Rectangular specimens under the 40°C-water aging condition, the curves drop from the moisture equilibrium content, which means the mechanism of mass loss took place. The same phenomenon is also found in other researches [19, 20], when the environmental temperature approach the glass transition temperature (Tg) of FRP composites. It indicates that the material has experienced some form of physical and/or chemical degradation: hydrolysis of the matrix, chain breakage, creation of small molecules and extraction (leaching) out of these molecules from the composite. From Table 3.4, it can be also found that the moisture saturation levels of Square and Rectangular specimens are much close to each other for the four aging conditions, but deviate a bit from that of Small square specimens. This can be attributed to the manufacture and curing process of FRP laminates, which could influence the microstructure of FRP composite materials. In this research, the Square and Rectangular specimens are cut from the same FRP plate, while the Small square specimens are cut from another thicker plate. This could be the reason to explain the deviation of moisture saturation levels. Moreover, mass loss can also influence the saturation level, since they could occur to different extents in the different sample types.

Firstly, for the purpose of convenience, the experimental results are fitted to one dimensional moisture diffusion theory (Eq.3.4) by using the least-square method. The equivalent diffusion rates D and maximum moisture contents (M_∞) at equilibrium of different aspect ratio specimens in four aging conditions are obtained. For comparison, the analytical curves are drawn in Fig. 3.9. Good agreement is achieved between experimental results and analytical fitting curves. Subsequently, by employing Eq.3.8, three dimensional Fickian diffusion coefficients D_1, D_2 and D_3 are obtained and summarized in Table 3.5.

Table 3.5 Moisture diffusion coefficients of FRP laminates in three directions from Eq. 3.8

Aging condition	D_1 ($\times10^{-6}$mm^2/s)	D_2 ($\times10^{-6}$mm^2/s)	D_3 ($\times10^{-6}$mm^2/s)
20C 50%RH	1.121	0.786	0.097
40C 96%RH	2.829	2.547	0.123
20C water	1.071	1.132	0.102
40C water	3.501	3.021	0.202

To validate the above three dimensional Fickian diffusion coefficients, FE analysis are used herein. The whole FE modeling process is the same as mentioned above for the pultruded FRP composites. The typical three-dimensional Fickian diffusion analysis is considered for resin-infusion FRP laminates. The D_1, D_2 and D_3 (from Table 3.5) are used as input parameters for the FE model. Subsequently, the FE results are obtained and shown in Fig. 3.10 (indicated as 1D FE diffusion curve), together with the analytical model and experimental data for FRP laminates with three aspect ratios under the 40°C–water environmental condition. It is manifest that the moisture uptake of 1D FE analysis is relatively slower than that of experimental results. It can be explained that, due to the assumption of the equivalent diffusion coefficient method (Eq. 3.6), the amount of moisture absorption is equal to the one dimensional moisture uptake from six surfaces independently. However, in tests, specimens absorb moisture from six surfaces homogeneously, which means in the corner between two adjacent surfaces, moisture uptake from one direction can interact with that from the other direction. This interaction mechanism can disturb the typical one-dimensional moisture diffusion process and correspondingly “decrease” the diffusion rate. Eq. 3.6 does not take this mechanism into account, so the three directional moisture diffusion coefficients D_1, D_2 and D_3 derived from Eq. 3.8 are lower than the real values. Thus, the conclusion can be drawn that only at the initial moisture diffusion stage, the assumption of Eq. 3.6 can be satisfied by neglecting the interaction mechanism on moisture absorption at the corner area between adjacent surfaces.

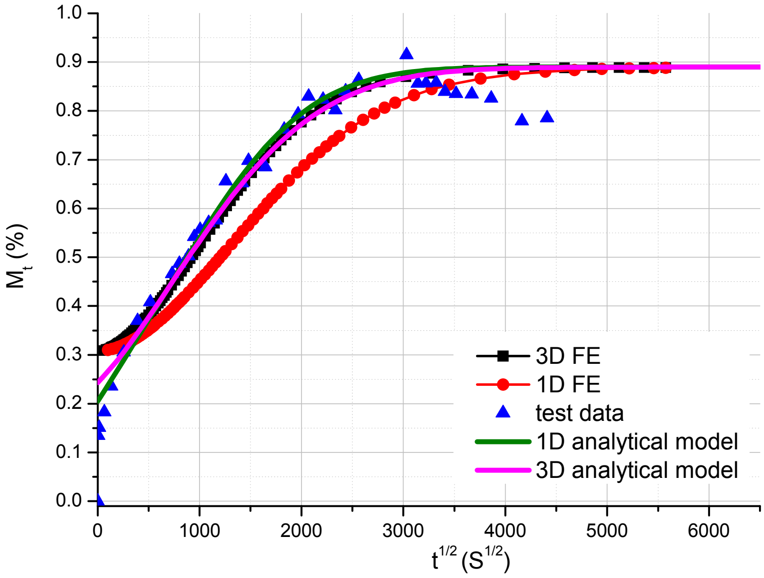

Fig. 3.10. a) Square

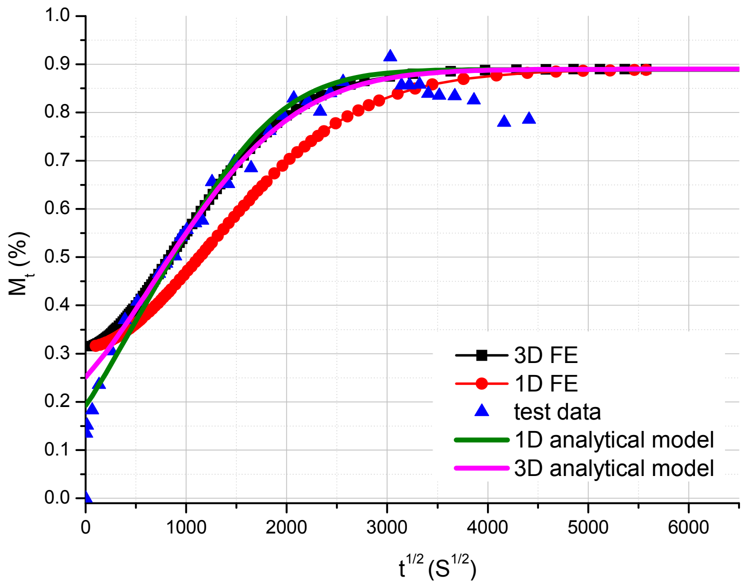

Fig. 3.10. b) Rectangular

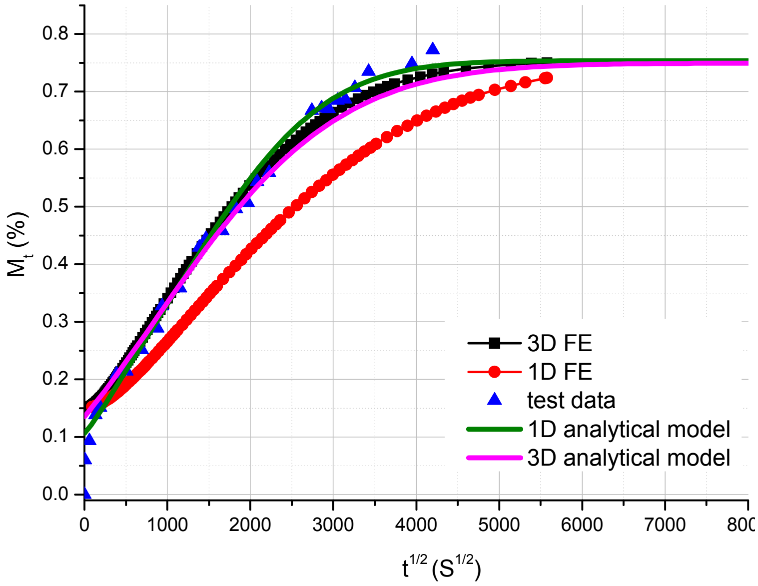

c) Small square

Fig. 3.10. Comparison of FE results, analytical models and experimental data of FRP laminate specimens aged at the 40°C–water condition

In order to obtain the accurate three directional moisture diffusion coefficients, the full three-dimensional diffusion theory needs to be employed. Eq. 3.13 indicates the moisture uptake as the function of time based on three dimensional coordinates. As mentioned before, an optimization routine is developed to minimize the least squared error, between test data and the equation prediction for all the specimens with different aspect ratios. As the results of this optimized solution, D_1, D_2 and D_3 of FRP laminates in four aging conditions are listed in Table 3.6, of which the values differ significantly from those in Table 3.5. Fig. 3.10 shows the FE diffusion curves based on the three-dimensional diffusion theory, indicated as 3D FE. Perfect agreement is achieved between FE results, analytical solution and test data. Thus, the FE analysis suggests that Eq. 3.8 is not reliable for determination of moisture diffusion coefficients of anisotropic polymeric materials. The three-dimensional moisture diffusion theory is inevitably needed. What's more, development of FE model is confirmed to be useful to simulate and validate the moisture diffusion process. With these moisture diffusion coefficients (D_1, D_2 , D_3 and M_∞), the moisture diffusion process in FRP laminates with other complex geometries can be easily modeled by FE analysis, even for thicker sections or much longer environmental aging durations.

Table 3.6 Moisture diffusion coefficients of FRP laminates in three directions from Eq. 3.13

Aging condition	D_1 ($\times 10^{-6}mm^2/s$)	D_2 ($\times 10^{-6}mm^2/s$)	D_3 ($\times 10^{-6}mm^2/s$)
20C 50%RH	0.869	1.081	0.125
40C 96%RH	9.243	9.403	0.187
20C water	0.862	0.927	0.182
40C water	9.607	9.631	0.318

From Table 3.6 it can be found that, for each aging condition, the moisture diffusion rate through the thickness of FRP laminates (D_3) is lower than D_1 and D_2, especially for the aging conditions of 40°C temperature. Meanwhile, the D_1 and D_2 are close to each other. This implies that the moisture is inclined to diffuse along the fibre direction, and with a view to the layup configuration of FRP laminates (Table 3.2), it is reasonable that D_1 and D_2 achieve approximately the identical value. Furthermore, comparing the moisture diffusion coefficients between different aging conditions, the maximum values of D_1 and D_2 are obtained almost simultaneously in both 40°C-96%RH and 40°C-water conditions, which indicates that the environmental temperature dominates the moisture diffusion rates along the fibre direction. For the moisture diffusion transverse to the fibre direction, the influence of temperature is not that significant, since the absolute value of D_3 is too low to be sensitive to the various aging conditions. However, no matter moisture diffusion rates (D_1, D_2 and D_3) or saturated content (M_∞), the 40°C-water condition always leads to the highest values, in comparison with the other three aging conditions. It confirms that the hot/wet condition should be considered to be a hostile service environment for the utilization of FRP structures.

3.5 Conclusions

By gravimetric experiments, the moisture diffusion characteristics of pultruded FRP composites and resin-infusion FRP laminates under four environments were studied. For the pultruded FRP specimens, the moisture saturation levels were reached under four aging conditions within only two days. The one-dimensional Fickian diffusion analytical model was employed to fit the experimental data by the least-square method. Subsequently, the moisture diffusion coefficients were determined. In comparison with the vapour aging conditions, FRP composites immersed in water result in much higher moisture uptake levels, around 3% of the initial self-weight. The experimental data and fitted analytical curves confirm that elevated temperatures could accelerate the moisture diffusion process, and the maximum moisture equilibrium contents are dominated by the humidity of aging environments. No significant variations on moisture diffusion characteristics of pultruded FRP specimens from different parts of the FRP deck profile exist. The FE modelling for simulating the moisture diffusion process in pultruded FRP composites were developed, and validated against the gravimetric experimental data and analytical solution.

For resin-infusion FRP laminate specimens, more aging time was needed for specimens to achieve the moisture saturated levels. In comparison with the pultruded FRP composites, the FRP laminates obtained much lower values for both moisture diffusion rate and saturated content, which indicates good corrosion resistance to environmental effects. Consequently, the surfacing veil is not necessary to be added to lay-ups of FRP laminates for protection against environmental attacks. The experimental results confirmed once more that the hot/wet environment can accelerate the moisture-induced deterioration process of FRP materials. Furthermore, the mass loss mechanism was observed for Square and Rectangular specimens under 40°C-water aging condition. For identification of three-dimensional moisture diffusion coefficients of anisotropic FRP materials, the equivalent diffusion coefficient method has proven to be unreliable by employing the three-dimensional FE diffusion analysis. The three-dimensional moisture diffusion theory is inevitably needed for developing the optimization scheme. The research described in this chapter can be attributable for the coupled hygro-thermal stress-strain analysis on FRP structures, which develops a step towards the prediction of long-term performance and life-time estimation of FRP-steel composite bridges.

References:

[1] Jiang X, Kolstein H, Bijlaard FSK. Moisture diffusion in glass-fiber-reinforced polymer composite bridge under hot/wet environment. Compos Part B-Eng. 2013;45(1):407-16.
[2] Jiang X, Kolstein H, Bijlaard FSK, Qiang X. Effects of hygrothermal aging on glass-fibre reinforced polymer laminates and adhesive of FRP composite bridge: Moisture diffusion characteristics Composites Part A: Applied Science and Manufacturing. 2014, 57: 49-58.
[3] Springer GS. Enivormental effects on composite materials, vol.1. Lancaster, PA: Technomic Pubnishing company; 1981.
[4] Crank J. The mathematics of diffusion. 2nd editon. Oxford: Clarendon Press; 1975.
[5] Pierron F, Poirette Y, Vautrin A. A novel procedure for identification of 3D moisture diffusion parameters on thick composites: Theory, validation and experimental results. J Compos Mater. 2002;36(19):2219-43.
[6] http://www.fiberline.dk/.
[7] Zhou A, Keller T. Joining techniques for fiber reinforced polymer composite bridge deck systems. Compos Struct. 2005;69(3):336-45.
[8] http://www.infracomposites.com.
[9]http://pdf.nauticexpo.com/pdf/vetrotex-ocv-reinforcements/quadraxial-fabrics/27891-13674-_2.html.
[10] Shao YX, Kouadi S. Durability of fiberglass composite sheet piles in water. J Compos Constr. 2002;6(4):280-7.
[11] Post NL, Riebel F, Zhou A, Keller T, Case SW, Lesko JJ. Investigation of 3D Moisture Diffusion Coefficients and Damage in a Pultruded E-glass/Polyester Structural Composite. J Compos Mater. 2009;43(1):75-96.
[12] Robert M, Roy R, Benmokrane B. Environmental Effects on Glass Fiber Reinforced Polypropylene Thermoplastic Composite Laminate for Structural Applications. Polym Composite. 2010;31(4):604-11.
[13] Karbhari VM, Xian GJ. Hygrothermal effects on high V(F) pultruded unidirectional carbon/epoxy composites: Moisture uptake. Compos Part B-Eng. 2009;40(1):41-9.
[14] Bao LR, Yee AF. Moisture diffusion and hygrothermal aging in bismaleimide matrix carbon fiber composites: part II - woven and hybrid composites. Compos Sci Technol. 2002;62(16):2111-9.
[15] Bao LR, Yee AF. Moisture diffusion and hygrothermal aging in bismaleimide matrix carbon fiber composites - Part I: uni-weave composites. Compos Sci Technol. 2002;62(16):2099-110.
[16] D5229/D5229M-92 A. Standard Test Method for Moisture Absorption Properties and Equilibrium Conditioning of Polymer Matrix Composite Materials. PA, United States: ASTM International; 1992.
[17] Aronhime MT, Neumann S, Marom G. The Anisotropic Diffusion of Water in Kevlar Epoxy Composites. J Mater Sci. 1987;22(7):2435-46.
[18] Abaqus Analysis User's Manual, 6.8 version.
[19] Daly HB, Brahim HB, Hfaied N, Harchay M, Boukhili R. Investigation of water absorption in pultruded composites containing fillers and low profile additives. Polym Composite. 2007;28(3):355-64.
[20] Liao K, Schultheisz CR, Hunston DL, Brinson LC. Long-term durability of fiber-reinforced polymer-matrix composite materials for infrastructure applications: A review. J Adv Mater-Covina. 1998;30(4):3-40.

Chapter 4

Mechanical degradation of FRP laminates under hot/wet environment

4.1 Introduction

In the present chapter, the influence of moisture and temperature on the mechanical properties of Glass-Fiber-Reinforced polymer (GFRP) laminates is investigated. In the use of GFRP bridge decks, the GFRP laminates are mainly loaded by the wheel load in the through-thickness direction. Therefore, it is of great importance that the flexural and interlaminar shear properties are studied. For this study, three point bending tests were performed with different support spans to study the flexural and shear properties of FRP laminates by varying the thickness to support span ratio. The mechanical properties of dry (0%M_t/M_∞), moisture unsaturated (30%M_t/M_∞ and 50%M_t/M_∞) and moisture saturated specimens (100%M_t/M_∞) under both 20°C and 40°C test temperatures are compared. One cycle of moisture absorption-desorption process is also included in this study to investigate how the residual damage induced by the moisture diffusion degrades the mechanical properties of FRP laminates. Furthermore, to better understand the environment-dependent mechanical performance of FRP laminates, a coupled hygro-mechanical FE model was developed by writing a specific postprogressing subroutine to work together with the FEM software ABAQUS, and subsequently validated by the flexural test results. Based on this coupled hygro-mechanical FE model, an inverse parameter identification approach to short-beam shear tests was developed and then employed to determine the environment-dependent interlaminar shear modulus of FRP laminates by minimizing the difference between the numerically predicted material response and experimental measured data.

4.2 Flexural property

4.2.1 Experiment

To investigate the flexural property of FRP laminates, three point bending tests are employed. The whole test procedure follows the standard test code ASTM D790-10 [1]. FRP laminates studied in this chapter are the same as those used in Chapter 3, which are manufactured by resin vacuum infusion (Infra Composite BV) and then cut into specific dimensions with the principal axis parallel to the warp direction of the woven roving (as shown in Fig. 4.1). The 5.64mm thick specimen is composed of six layers of standard 0.94mm EQX1200. The layup configuration of each piece of the standard 0.94mm EQX1200 is illustrated in Table 4.1. The mechanical properties of FRP laminates supplied by the manufacturer are shown in Table 4.2. The nominal length and width of the specimens are selected to be 150mm and 20mm respectively. According to the standard test code ASTM D790-10 [1], the specimen length shall be sufficient to allow for overhanging on each end of at least 10% of the support span. The specimen width shall not exceed one fourth of the support span for specimens greater than 3.2mm in depth.

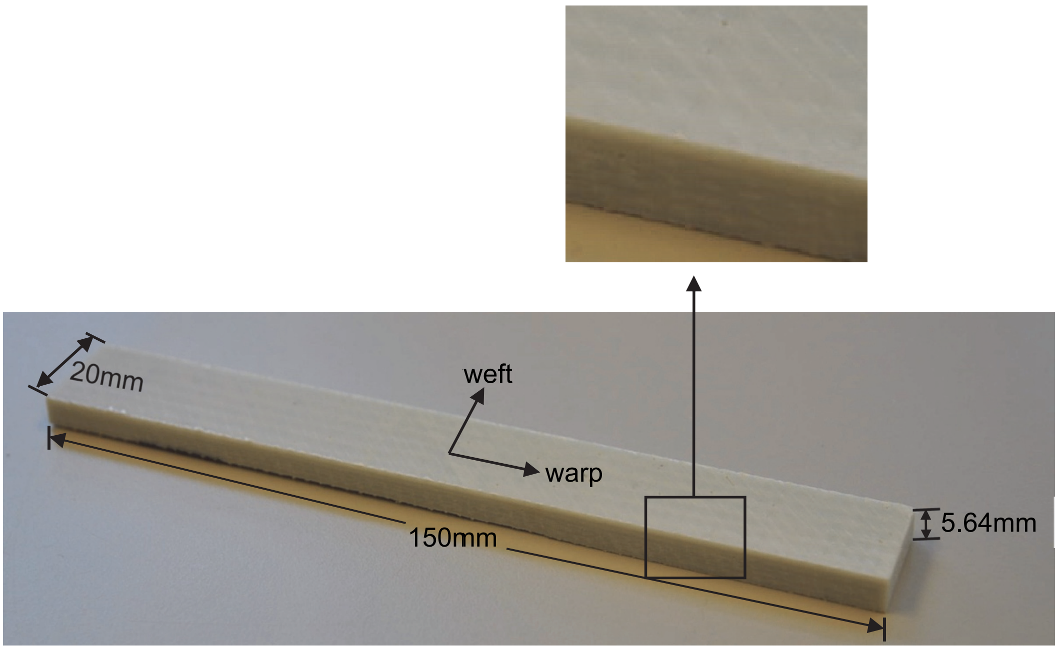

Fig. 4.1. FRP laminate specimen for flexural tests

Table 4.1. FRP laminate properties of EQX1200 (supplied by manufacturer)

Product name	Total weight (g/m^2)	Weight uniformity (g/m^2)				
		Yarn roving				Knit yarn
		0^o(warp)	$+45^o$	90^o(Weft)	-45^o	
EQX 1200	1193	283	300	300	300	10

Table 4.2. Mechanical properties of FRP laminates (supplied by manufacturer)

Property	Tensile (ISO 527-4)		Compression (ISO 8515)		Flexural (ISO 14.125)	
Mean value	Warp	Weft	Warp	Weft	Warp	Weft
Strength	331 MPa	314 MPa	220 MPa	200 MPa	473 MPa	433MPa
Modulus	18 GPa	17 GPa	14 GPa	14 GPa	13 GPa	11 GPa

The numbering of the specimens is given in Table 4.3, with regard to the moisture uptake content, test temperature, absorption/desorption process and replicated number. Two test temperatures 20°C and 40°C are selected for the three point bending tests, which are controlled by the climate chamber with the tolerance of ±2°C, as shown in Fig. 4.2.

Fig. 4.2. Climate chamber

Table 4.3. FRP laminate specimens for flexural tests

Specimen identification		Test	M_t/M_∞	Test temperature	After desorption	Numder of specimens
Set-1	F-0%-20°C	flexural	0	20°C	no	5
	F-0%-40°C	flexural	0	40°C	no	5
Set-2	F-30%-20°C	flexural	30%	20°C	no	5
	F-30%-40°C	flexural	30%	40°C	no	5
Set-3	F-50%-20°C	flexural	50%	20°C	no	5
	F-50%-40°C	flexural	50%	40°C	no	5
Set-4	F-100%-20°C	flexural	100%	20°C	no	5
	F-100%-40°C	flexural	100%	40°C	no	5
Set-5	F-50%-20°C-D	flexural	50%	20°C	yes	5
	F-50%-40°C-D	flexural	50%	40°C	yes	5
Set-6	F-30%-20°C-D	flexural	30%	20°C	yes	5
	F-30%-40°C-D	flexural	30%	40°C	yes	5
Set-7	F-0%-20°C-D	flexural	0	20°C	yes	5
	F-0%-40°C-D	flexural	0	40°C	yes	5

As listed in Table 4.3, the test in each condition is repeated five times to investigate the spread of test results. The hydrothermal aging condition is 40°C-water, which is supposed to be a severe hot/wet condition for FRP laminates, as discussed in Chapter 3. In total, 70 pieces of specimens are prepared. During the hydrothermal aging process, all the specimens are immersed in the water at the temperature of 40°C, except for the F-0-20°C and F-0-40°C specimens, which are the as-received reference specimens (Set-1 in Table 4.3). The as-received specimens are stored in the laboratory environment. The moisture content of them is very low, and thus can be ignored. As illustrated in Table 4.3, the Set-2 specimens (F-30%-20°C and F-30%-40°C) are tested at 30% relative moisture uptake content. The Set-3 specimens (F-50%-20°C and F-50%-40°C) are tested at 50% relative moisture uptake content. The Set-4 specimens (F-50%-20°C and F-50%-40°C) are tested at the moisture saturation level (100% relative moisture uptake content). Until this point in time, the above test process is considered as the moisture absorption process. Then, the remaining specimens are all taken out of the hydrothermal aging environment, and put into an oven at a temperature of 42°C to dry them, which is considered as the moisture desorption process. In this way, the Set-5 specimens (F-50%-20°C-D and F-50%-40°C-D) are tested at 50% relative moisture uptake content after a certain time of moisture desorption. Subsequently, the Set-6 specimens (F-30%-20°C-D and F-30%-40°C-D) are tested at 30% relative moisture uptake content after the moisture desorption. The final Set-7 specimens (F-0-20°C-D and F-0-40°C-D) are the fully dry specimens after one cycle of moisture absorption-desorption process. Herein, the symbol “D” indicates the moisture desorption.

As shown in Fig. 4.3, the whole three point bending test set-up is put into the chamber. According to ASTM D790-10 [1], the support span-to-depth ratio is 16:1. Thus, the support span is proposed to be 90.24mm, but it varies between different groups of specimens, since the value of the support span is exactly calculated based on the average real thickness of each group of specimens. The radii of the loading nose and supports are 5.0 ± 0.1mm. The whole loading process employs the strain rate of 0.01mm/mm/min. Correspondingly, the rate of crosshead motion is 2.4 mm/min, which is calculated as follows [1]:

$$R = ZL^2 / 6d \tag{4.1}$$

R = rate of crosshead motion, mm/min,

L = support span, mm,

d = depth of FRP beam tested, mm,

Z = rate of straining of the outer fiber, mm/mm/min.

The specimen is deflected until the load drops to 30% of the maximum load or until a maximum displacement of mid-span reaches 10mm, whichever occurs first (as illustrated in Fig. 4.4). The experimental data is recorded per second. To track the moisture absorption process in FRP laminate specimens, gravimetric tests are also conducted, the test procedure of which can be found in section 3.3.2.

Fig. 4.3. Flexural test device

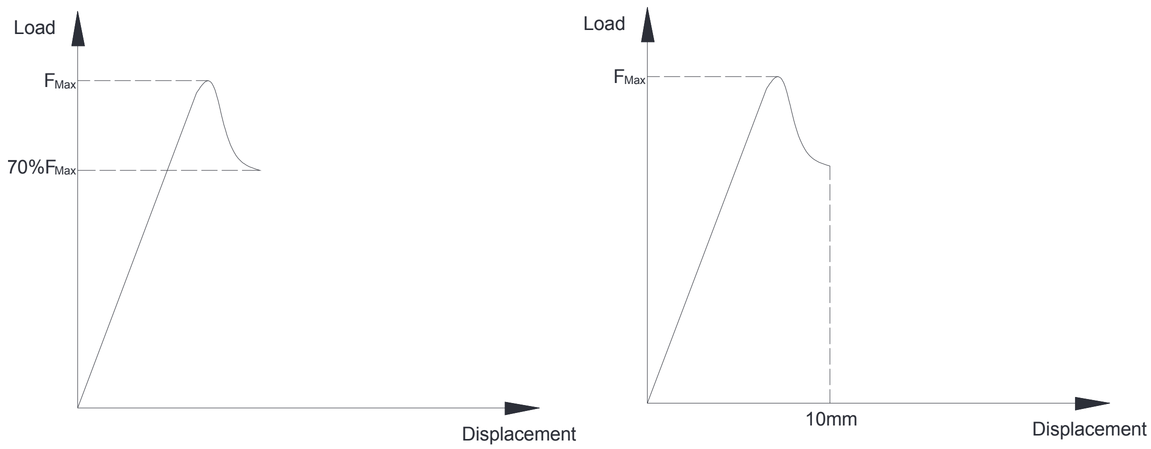

a) Drop to 30% of the maximum load b) Maximum displacement of 10mm

Fig. 4.4. Termination rule of the flexural test

4.2.2 Experimental results and discussion

Fig. 4.5 shows the moisture absorption process of FRP laminate flexural test specimens immersed in water of 40°C, compared with the FE moisture diffusion analysis. Moisture content (calculated from Eq. 3.15) is established as the function of the square root of time. It can be found that the moisture saturation level is about 0.77% (M_∞), which is in line with the gravimetric experimental results obtained in Chapter 3. The specimens developed a similar moisture diffusion curve as that simulated by the FE analysis, which confirms the accuracy of the FE moisture diffusion model.

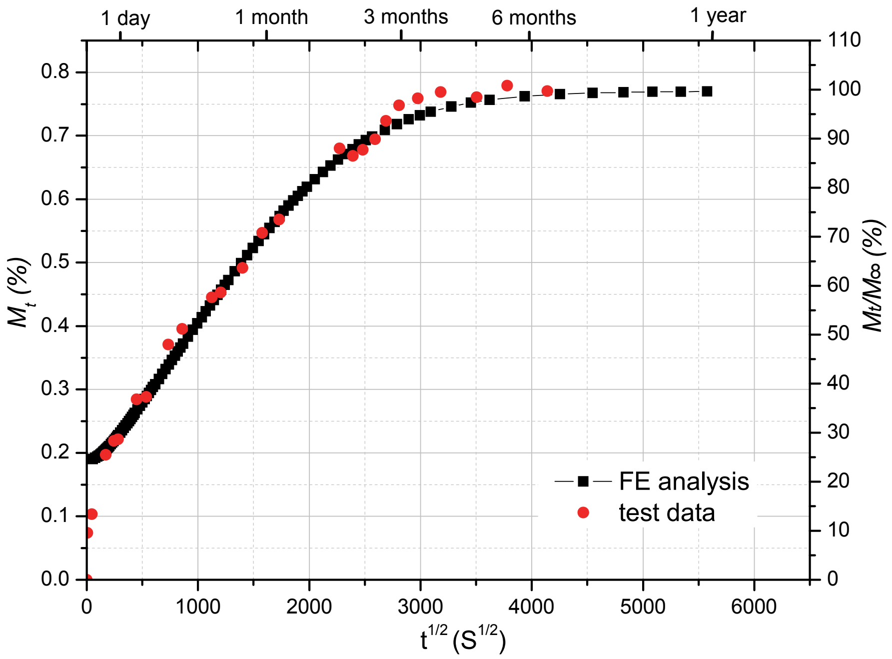

Fig. 4.5. Comparison of moisture uptake curve between test results and FE analysis on FRP specimens for flexural tests

The typical failure mode of specimens under flexural tests is shown in Fig. 4.6, where rupture occurs in the outer surface of the test specimen. All the detailed test data can be found in the Stevin II lab report. In order to obtain the E-modulus of FRP laminates, the stress and strain at the midspan of FRP specimens are calculated as follows.

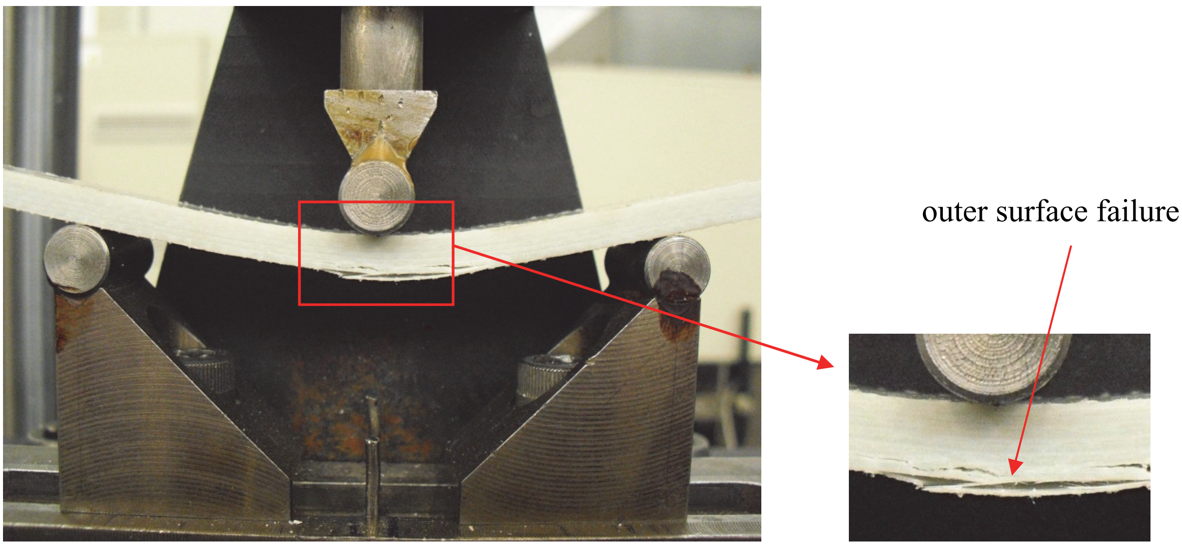

Fig. 4.6. Failure mode of the flexural test specimen

According to ASTM D790-10 [1], the flexural stress in the outer surface of the specimen at midpoint is calculated by means of the following equation:

$$\sigma = 3PL/2bd^2 \qquad (4.2)$$

where:

σ = stress in the outer fibers at midpoint, MPa,

P = load at the midspan on the load-deflection curve, N,

b = width of FRP beam tested, mm.

The flexural strain, that nominal fractional change in the length of an element of the outer surface of the test specimen at midspan, is calculated for any deflection using Eq. 4.3:

$$\varepsilon = 6D_{\max} d / L^2 \qquad (4.3)$$

where:

ε = strain in the outer fibers at midpoint, MPa,

D_{max} = maximum deflection of the center of the beam, mm

The stress-strain curves are presented in Fig. 4.7. To make the comparison more clear, the curve of only one specimen of each test condition is presented, which is selected visually as the average curve of the five specimens.

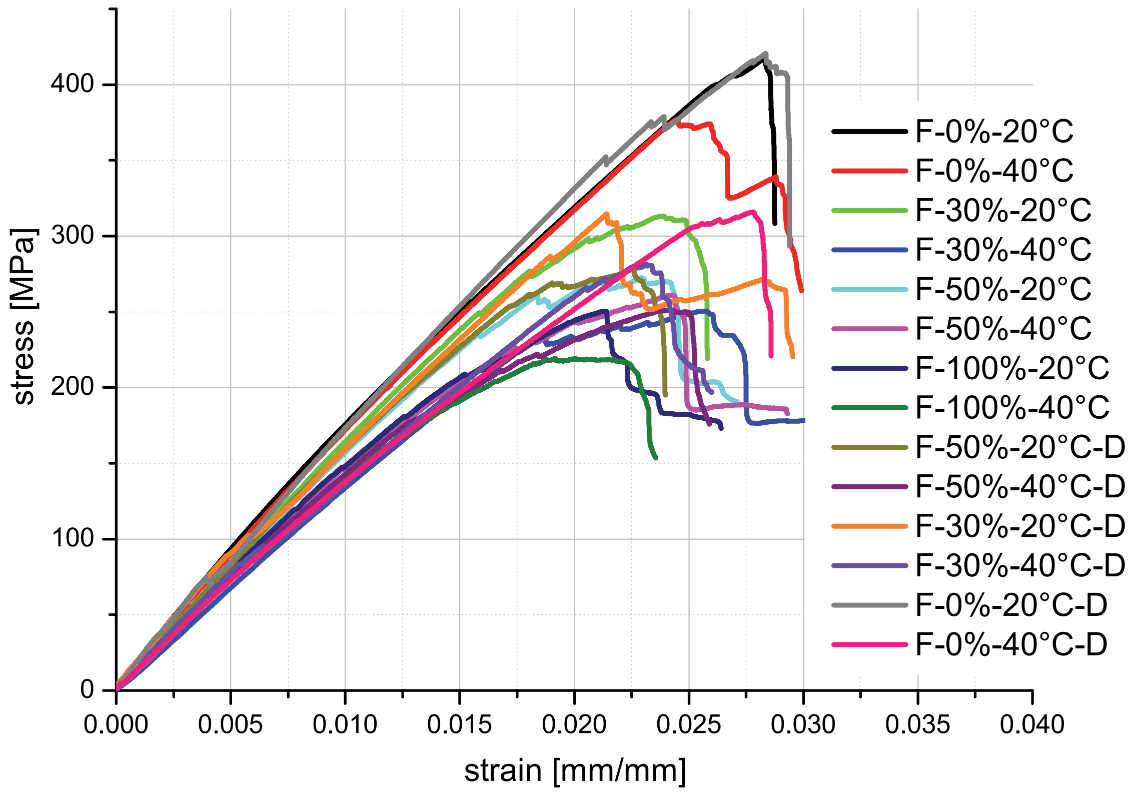

Fig. 4.7. Stress-strain curves of FRP specimens under flexural tests

The E-modulus is represented by the chord modulus, which is calculated from two discrete points on the load-deflection curve, using Eq. 4.4 [1]:

$$E = (\sigma_2 - \sigma_1)/(\varepsilon_2 - \varepsilon_1) \tag{4.4}$$

σ_1, ε_1 and σ_2, ε_2 are the flexural stress and strain selected at two points of stress-strain curves (Fig. 4.7) in the linear and stable range.

The flexural strength is the maximum flexural stress sustained by the test specimen during the flexural test. The environment-dependent flexural properties (including E-modulus and strength) are shown in Fig. 4.8 and Table 4.4. The R-square value for each curve is also present in Fig. 4.8, which indicates how well the curve fits test data points.

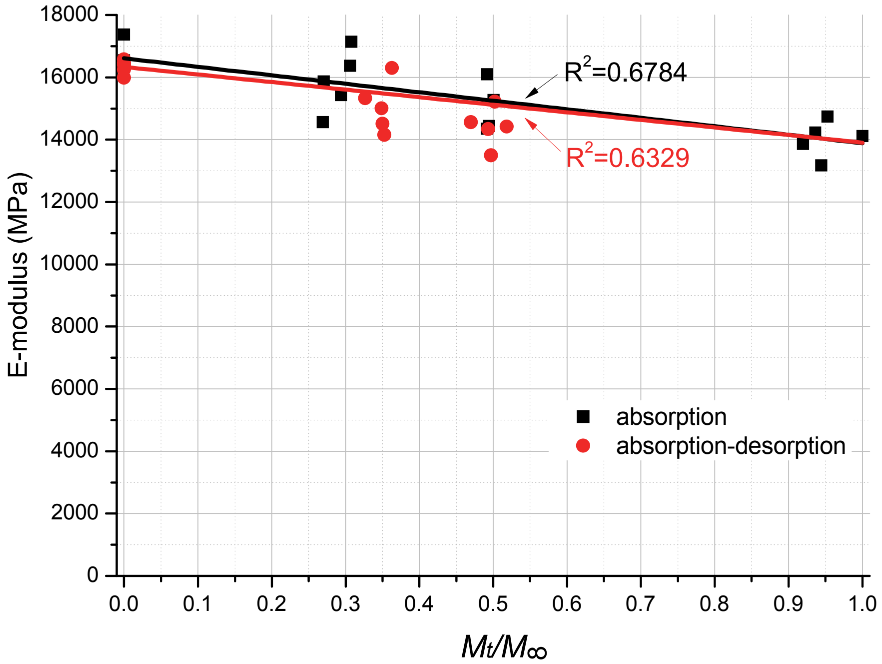

Fig. 4.8. a) E-modulus, 20°C

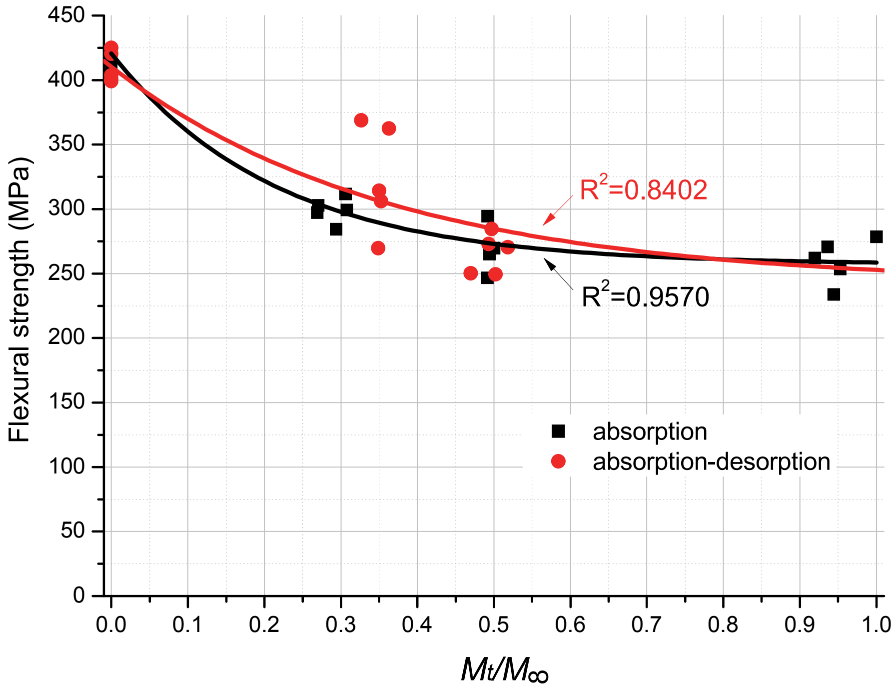

Fig. 4.8. b) Strength, 20°C

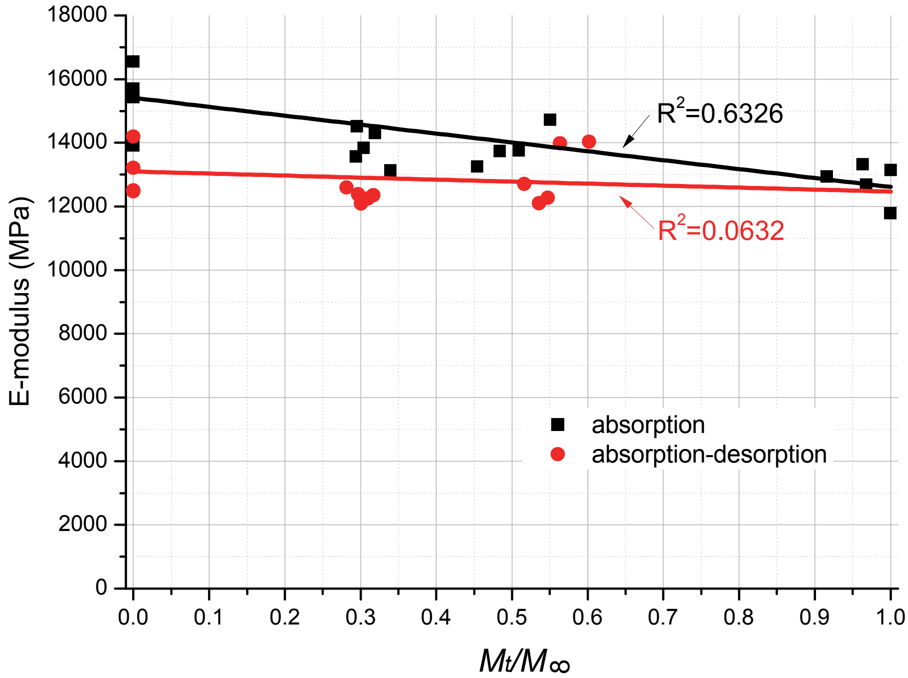

c) E-modulus, 40°C

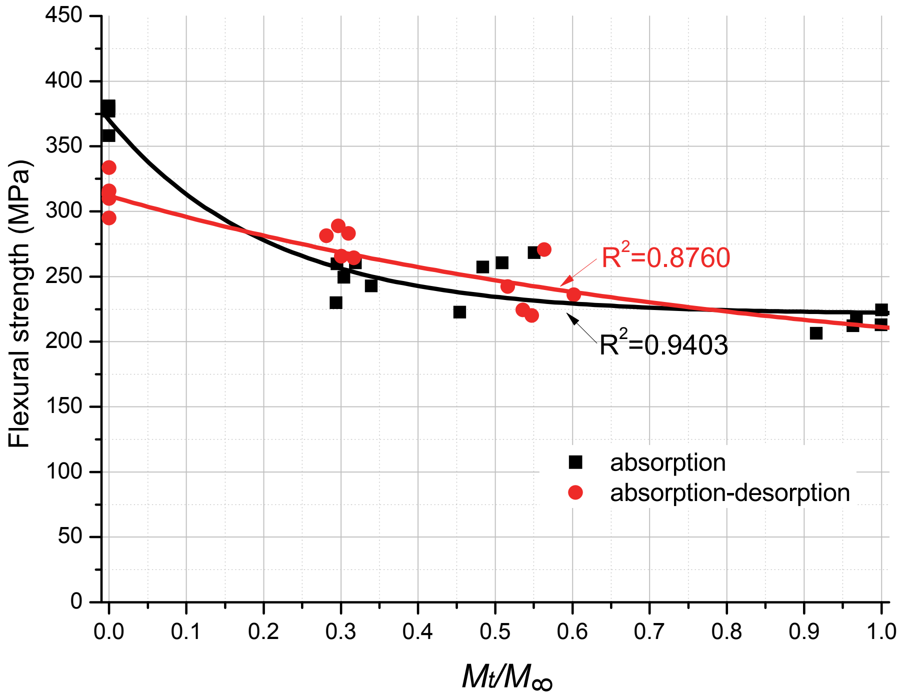

d) Strength, 40°C

Fig. 4.8 Environment-dependent flexural property degradation of FRP laminates

Table 4.4 Flexural property degradation of FRP laminates

Specimen identification	E-modulus* (MPa)	Standard Deviation(MPa)	Flexural strength* (MPa)	Standard Deviation(MPa)
F-0%-20°C	16609	386	411	6.89
F-0%-40°C	15409	852	375	8.49
F-30%-20°C	15873	867	299	8.88
F-30%-40°C	13874	500	249	11.42
F-50%-20°C	15038	710	269	17.03
F-50%-40°C	13870	535	252	17.57
F-100%-20°C	14022	514	265.	13.74
F-100%-40°C	12780	538	214	6.08
F-50%-20°C-D	14408	551	260	15.46
F-50%-40°C-D	13019	832	239	17.85
F-30%-20°C-D	15059	740	324	37.04
F-30%-40°C-D	12336	166	277	9.85
F-0%-20°C-D	16333	204	410	10.80
F-0%-40°C-D	13095	698	314	13.92

* mean value of five specimens

To be simplified, the predictive equation for the E-modulus degradation as the function of moisture content is curve fitted by the linear interpolant function, while for the flexural strength the exponential function is used. All the curve fitting processes are conducted by using the MATLAB R2011b software, employing the least square method. The obtained predictive equation is as follows:

E-modulus, 20°C, absorption process:

$$E= -2725\times M_t/M_\infty+16609 \tag{4.5}$$

E-modulus, 20°C, absorption-desorption process:

$$E= -2428\times M_t/M_\infty+16333 \tag{4.6}$$

Flexural strength, 20°C, absorption process:

$$S = 103^{-(\frac{M_t}{M_\infty}-1.1)} + 257 \tag{4.7}$$

Flexural strength, 20°C, absorption-desorption process:

$$S = 15.5^{-(\frac{M_t}{M_\infty}-1.87)} + 242 \tag{4.8}$$

E-modulus, 40°C, absorption process:

$$E= -2795\times M_t/M_\infty+15409 \tag{4.9}$$

E-modulus, 40°C, absorption-desorption process:

$$E= -628\times M_t/M_\infty+13095 \tag{4.10}$$

Flexural strength, 40°C, absorption process:

$$S=123^{-(\frac{M_t}{M_\infty}-1.04)}+221 \tag{4.11}$$

Flexural strength, 40°C, absorption-desorption process:

$$S=3.23^{-(\frac{M_t}{M_\infty}-4.25)}+166 \tag{4.12}$$

All the predictive curves are illustrated in Fig. 4.8 for comparison with the experimental results.

Considering firstly the specimens tested at 20°C (Fig. 4.8a)), the E-modulus of FRP laminates is decreasing gradually as the moisture content increases from fully dry to fully saturated. The E-modulus of the moisture saturated specimen is 14022 MPa (as shown in Table 4.4), which is 15.6% lower than that of the unconditioned dry specimen. For the specimens with the moisture content of 30% and 50% of the saturation level, the loss of E-modulus is 4.4% and 9.5% respectively. With regard to specimens in the moisture desorption process, the E-modulus does not decrease significantly as compared to the specimens at the same moisture uptake level. Accordingly, the slight loss of E-modulus is 1.7%, 5.1% and 4.2% at the moisture uptake level of 0%, 30% and 50% respectively. In terms of flexural strength (see Fig. 4.8b)), there is a general exacerbation of decreasing between the fully dry specimens and 30% moisture content specimens, regardless of the moisture absorption/desorption process. More than 20% loss of flexural strength is evident. After this, as the moisture uptake content increases, the flexural strength of specimens is slightly decreasing, until reaching 265MPa of the moisture fully saturated specimens. In the end, the total drop of flexural strength is 35.4% of the fully dry specimens. Similar to the E-modulus degradation, the difference of flexural strength between absorption process and desorption process is very limited.

With regard to the environment-dependent flexural properties of FRP laminates at 40°C, the E-modulus of FRP laminates is regularly decreasing from 15409 MPa (dry) to 12780 MPa (moisture fully saturated), and then slightly increases to 13095 MPa after fully drying in the moisture desorption process. Different from that under 20°C, there is a significant unrecoverable loss (15.0%) of the E-modulus for the dry specimens tested at 40°C. Accordingly, the loss of 11.1% and 6.1% of the E-modulus is evident for the specimens with 30% and 50% moisture content respectively in the desorption process. As to the flexural strength of specimens tested under 40°C, a rapid decrease is observed at a moisture content of about 30% of moisture saturation level, and then the flexural strength slightly decreases to 214 MPa of the moisture fully saturated specimens, which is the lowest value among the whole series of tests. It is 42.9% lower than that of the unconditioned dry specimens (375 MPa, as listed in Table 4.4) tested at 40°C, and 47.9% lower than that of the unconditioned dry specimens (410 MPa) tested at 20°C. This most severe loss of flexural strength indicates that the combination of moisture and temperature effects can significantly influence the mechanical properties of FRP laminates. Comparing the unconditioned dry specimens with the dry specimens after the moisture desorption, a decrease of 16.4% of the flexural strength is observed for the specimens tested at 40°C. However, for the specimens with a moisture content of 30% and 50%, the loss of flexural strength is not obvious. Even a slight increase is observed for the specimens with 30% moisture content in the moisture desorption process.

In conclusion, the hot and wet environment sincerely degrades the flexural properties of FRP laminates, and in turn influences the durability of FRP composite structures. As to the moisture effects, as stated in the researches [2, 3], the degradation of the mechanical properties of FRP composite materials was due to water plasticization during the moisture uptake process and the disruption of hydrogen bonds between the molecular chains in the polymer. Furthermore, the fibre/matrix debonding, matrix cracking due to the moisture/thermal cycle and ultimately fiber breaking would also contribute.

With regard to the temperature effects, when the test temperature was approaching the Tg (glass transition temperature) of FRP composite materials, the mechanical performance such as E-modulus, strength and fatigue resistance significantly decreased [4, 5]. The recommended working temperature for FRP composite structures should be at least 20°C lower than the Tg of FRP composite materials. Furthermore, the researches [5, 6] confirmed that a decrease of Tg was evident when the moisture uptake content increased in the FRP composite materials. Meanwhile, as already proven in Chapter 3, the high temperature can speed up the moisture diffusion process. Thus, the interaction between moisture and temperature effects accelerates the environmental degradation process on the FRP composite material, which in turn explains why the combination of moisture and temperature effects seriously deteriorates the mechanical properties of FRP materials.

4.2.3 Coupled hygro-mechanical FE analysis

Generally, the environmental degradation experiments (mainly concerning moisture and temperature effects) for FRP composite materials are limited to a fairly short time, normally no more than 5 years. But the expected service life of infrastructures such as bridges exceeds 50 years. Thus, the short-term experimental investigations are not sufficient to estimate the long-term performance of FRP structures. To achieve this aim, some accelerated experimental methods were developed by the researches [7-10], in which the temperature or atmospheric pressure of the environmental aging conditions were raised beyond the normal service conditions to accelerate the moisture diffusion and degradation process. These accelerating experimental methods were confirmed to be useful and time-effective to investigate the durability of FRP composites and adhesive materials. But researches indicated that the high aging temperatures approaching glass transition temperature of specimens would improve the mechanical performance by post-cure or deteriorate the materials by inducing thermal cracks, which do not occur in the real utilization of FRP composite structures. Another method for studying the environmental degradation of mechanical behaviour of FRP materials and structures is the predictive FE modeling [11]. The first step is modeling moisture transport through FRP structures in order to determine the moisture concentration distribution through the cross-sections as a function of time. The material parameters required for the transient diffusion FE analysis are the diffusion coefficient and the solubility coefficient, which can be obtained from the short term gravimetric experiments, as stated in Chapter 3. And then, based on the obtained moisture concentration distribution, the environment-dependent mechanical behaviour of FRP structures can be investigated using the coupled hygro-mechanical FE analysis. The input moisture-dependent material properties of FRP composites are obtained by the material level tests (such as flexural test, tensile test and short-beam shear test).

To develop the coupled hygro-mechanical FE modeling method, in this section, the FE model of the FRP flexural test specimen is built (see Fig. 4.9). The moisture diffusion process in the FRP specimen is modeled by the transient diffusion FE analysis (thoroughly described in Chapter 3) and validated previously by comparing with the gravimetric experimental results, as shown in Fig. 4.5. From the moisture diffusion analysis, the moisture concentration distribution across the FRP specimen section is obtained as a function of time, which can be read into the stress analysis as a predefined field variable. The predictive equations (Eq. 4.5, 4.6, 4.9 and 4.10) of environment-dependent material properties serve as the input of field-dependent material properties of FRP composites, which is obtained by the flexural tests. Hence, the E-modulus of each element is determined by the local moisture concentration distribution. Thus, the coupled hygro-mechanical FE modeling is realized on the flexural test specimen. Subsequently, it can be employed to simulate other material level tests (such as short-beam shear tests) and FRP structures.

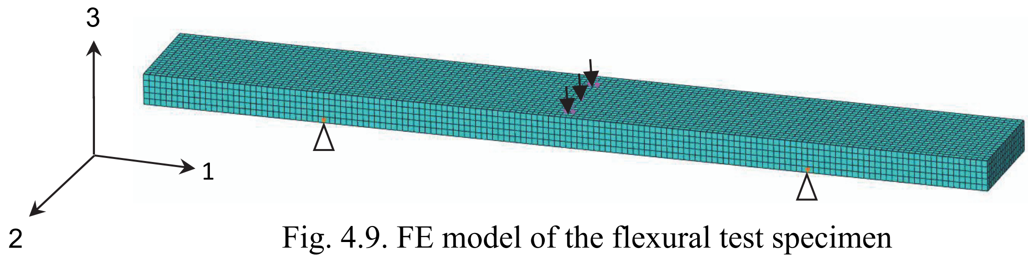

Fig. 4.9. FE model of the flexural test specimen

To validate this coupled hygro-mechanical FE modeling method, two groups of FRP specimens are selected: F-50%-20°C and F-30%-40°C-D. Firstly, the moisture concentration distribution in these two specimens is shown in Fig. 4.10 and Fig. 4.11. Based on this two predefined fields, the coupled hygro-mechanical FE analysis is conducted. The FE analysis is linear-elastic. The element used is C3D8R. In total 2000N load is applied at mid-span of the specimen.

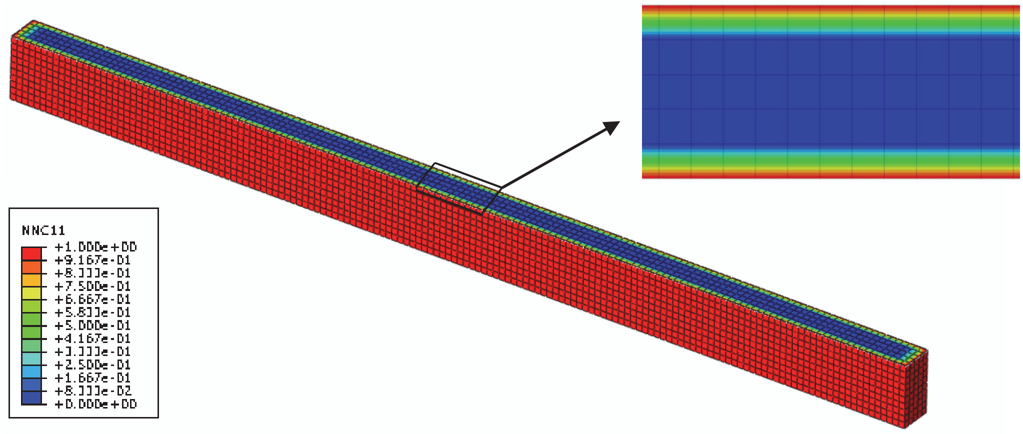

Fig. 4.10. Nominal moisture concentration distribution across the mid-plane of the FRP specimen with 30% moisture uptake content (time= 24 hours)

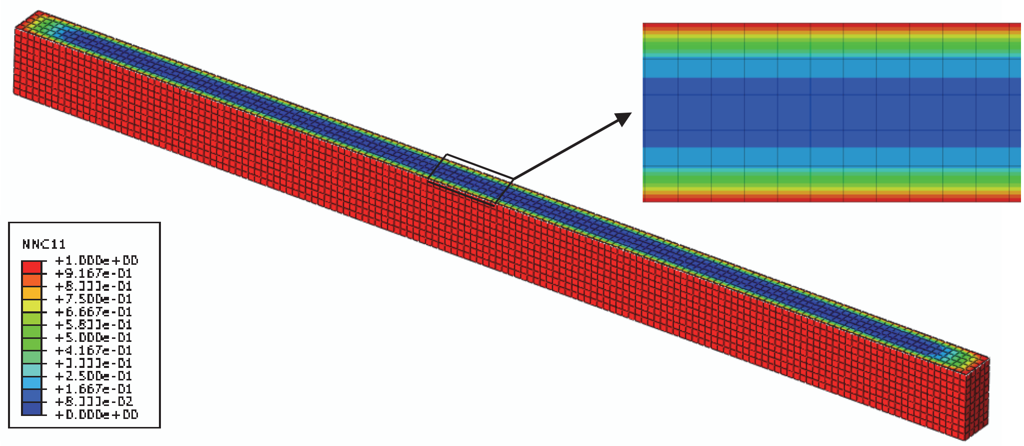

Fig. 4.11. Nominal moisture concentration distribution across the mid-plane of the FRP specimen with 50% moisture uptake content (time= 229 hours)

Comparison of experimental and FE results on the load-deflection curve of F-50%-20°C specimens and F-30%-40°C-D specimens are illustrated in Fig. 4.12 and Fig. 4.13 respectively. Good agreement is obtained in the linear stage, which means the environment-dependent stiffness of FRP specimens with different moisture uptake contents can be predicted by the coupled hygro-mechanical FE model. Hence, the accuracy of FE model is proven.

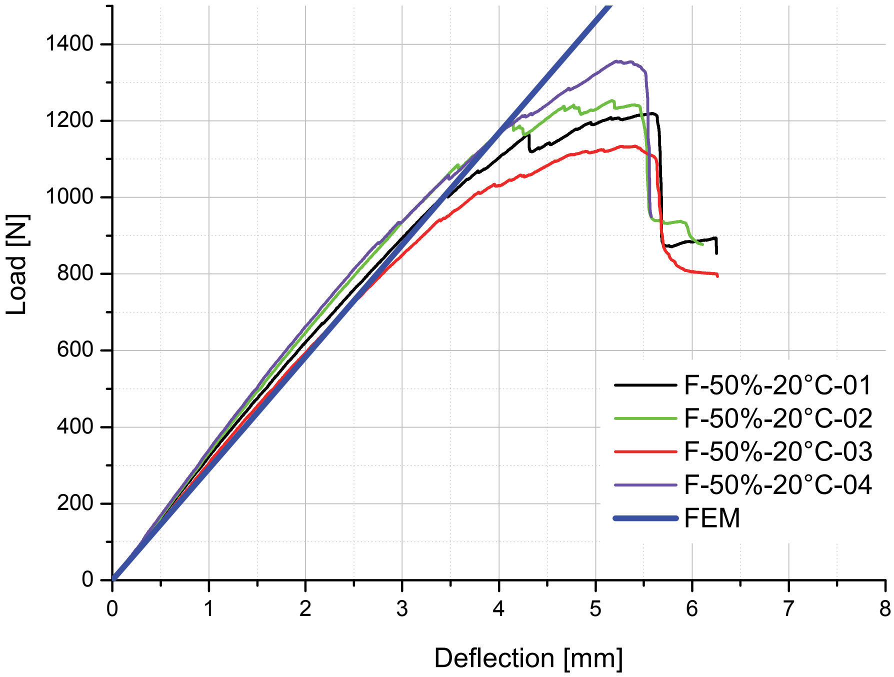

Fig. 4.12. Comparison of experimental and FE results on the load-deflection curve of F-50%-20°C specimens

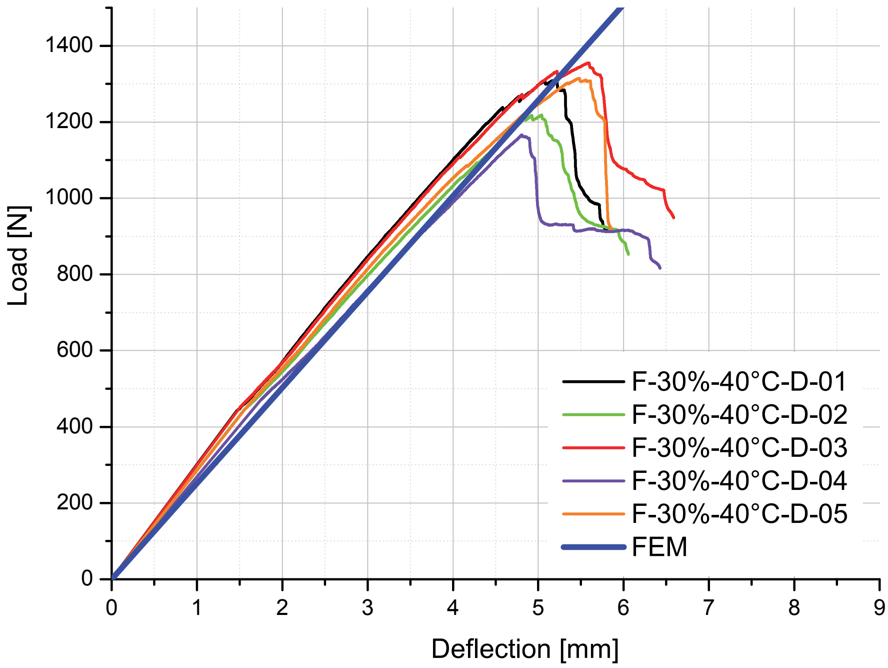

Fig. 4.13. Comparison of experimental and FE results on the load-deflection curve of F-30%-40°C-D specimens

4.3 Interlaminar shear property

4.3.1 Experiment

To investigate the interlaminar shear property of FRP laminates, three point bending tests of short-beam FRP specimens are employed. The whole test procedure follows the standard test code ASTM D2344/D2344M-00 [12]. FRP laminates studied in this section are the same as those discussed in Section 4.2.1. As shown in Fig. 4.14, the nominal thickness, width and length of the FRP short-beam specimen are 5.64mm, 12mm and 40mm. Numbering of specimens is shown in Table 4.5, with regard to the moisture uptake content, test temperature, absorption/desorption process and replicated number. The numbering method of short-beam shear specimens is similar to that of the flexural test specimens. Only the first character "F" (representing the flexural tests) is changed to "S", which represents the short-beam shear tests. The whole aging condition process is the same as that of the flexural tests. During the aging time, the moisture uptake content of each specimen is recorded by using the gravimetric test method.

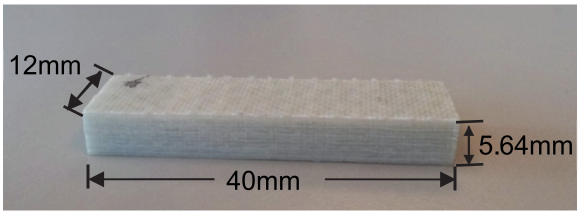

Fig. 4.14. FRP laminate short beam specimen

Table 4.5. FRP laminate specimens for the short-beam shear tests

Specimen identification		Test	M_t/M_∞	Test temperature	After desorption	Numder of specimens
Set-1	S-0%-20°C	shear	0	20°C	no	5
	S-0%-40°C	shear	0	40°C	no	5
Set-2	S-30%-20°C	shear	30%	20°C	no	5
	S-30%-40°C	shear	30%	40°C	no	5
Set-3	S-50%-20°C	shear	50%	20°C	no	5
	S-50%-40°C	shear	50%	40°C	no	5
Set-4	S-100%-20°C	shear	100%	20°C	no	5
	S-100%-40°C	shear	100%	40°C	no	5
Set-5	S-50%-20°C-D	shear	50%	20°C	yes	5
	S-50%-40°C-D	shear	50%	40°C	yes	5
Set-6	S-30%-20°C-D	shear	30%	20°C	yes	5
	S-30%-40°C-D	shear	30%	40°C	yes	5
Set-7	S-0%-20°C-D	shear	0	20°C	yes	5
	S-0%-40°C-D	shear	0	40°C	yes	5

The short-beam shear test device is shown in Fig. 4.15. According to ASTM D2344/D2344M-00 [12], the loading span length-to-specimen thickness ratio is 4. Consequently, the support span is proposed to be 22.56mm. It varies among different groups of specimens, since the value of the support span is exactly calculated based on the average real thickness of each group of specimens. The diameter of the loading nose and supports is 6.00mm and 3.00mm, respectively. The speed of testing is set at a rate of crosshead movement of 1.0mm/min. The specimen is deflected until the load drops to 30% of the maximum load or until a maximum displacement of mid-span reaches 4mm, whichever occurs first (see Fig. 4.16). The experimental data is recorded per second.

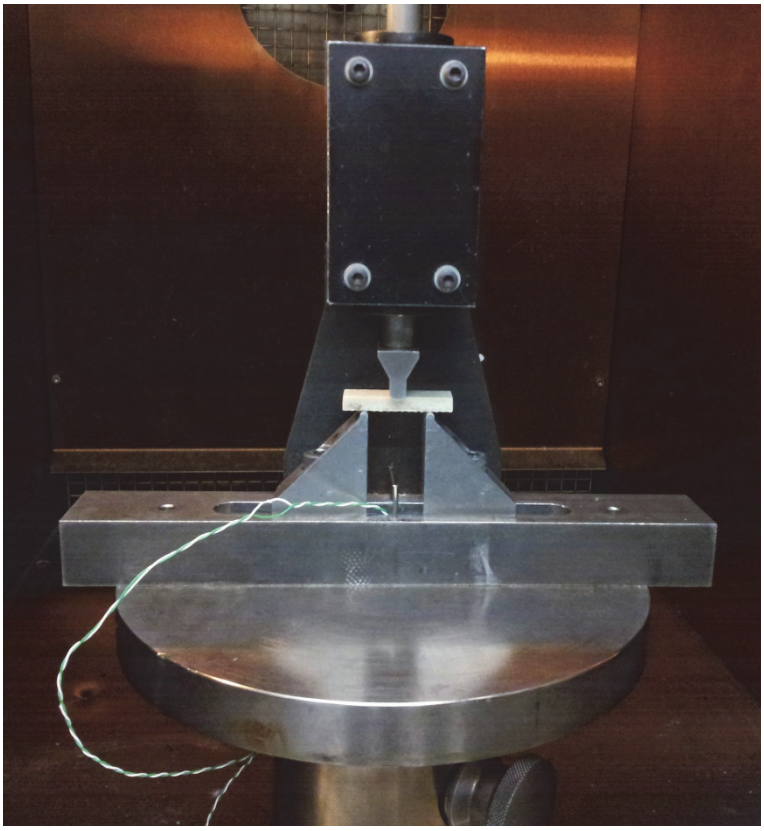

Fig. 4.15. Short-beam shear test device

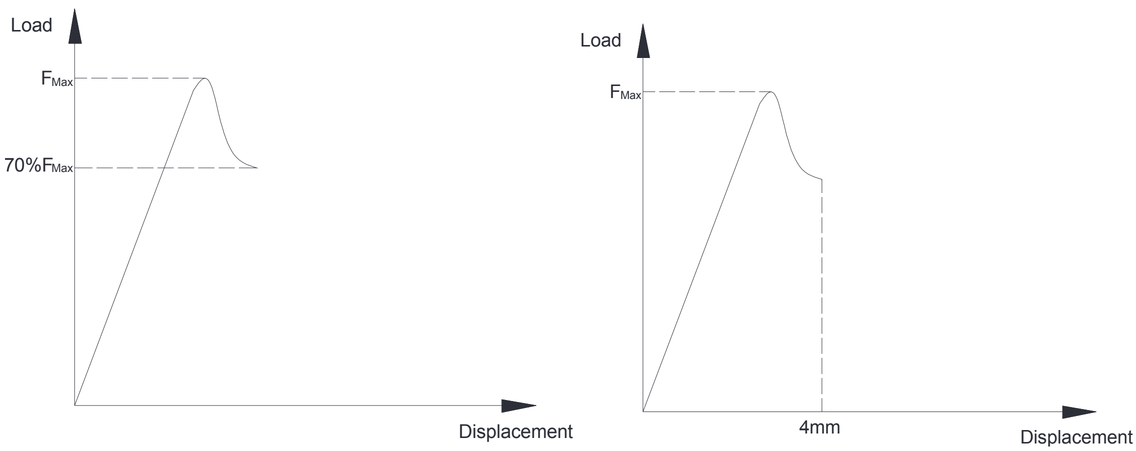

a) Drop to 30% of the maximum load b) Maximum displacement of 4mm

Fig. 4.16. Termination rule of the short-beam shear tests

4.3.2 Experimental results and discussion

Fig. 4.17 shows the moisture absorption process of FRP short-beam specimens immersed in water of 40°C. Moisture content (calculated from Eq. 3.15) is drawn as the function of square root of time. It can be found that the moisture saturation level is about 0.72%. Good agreement is obtained between experimental results and FE simulation.

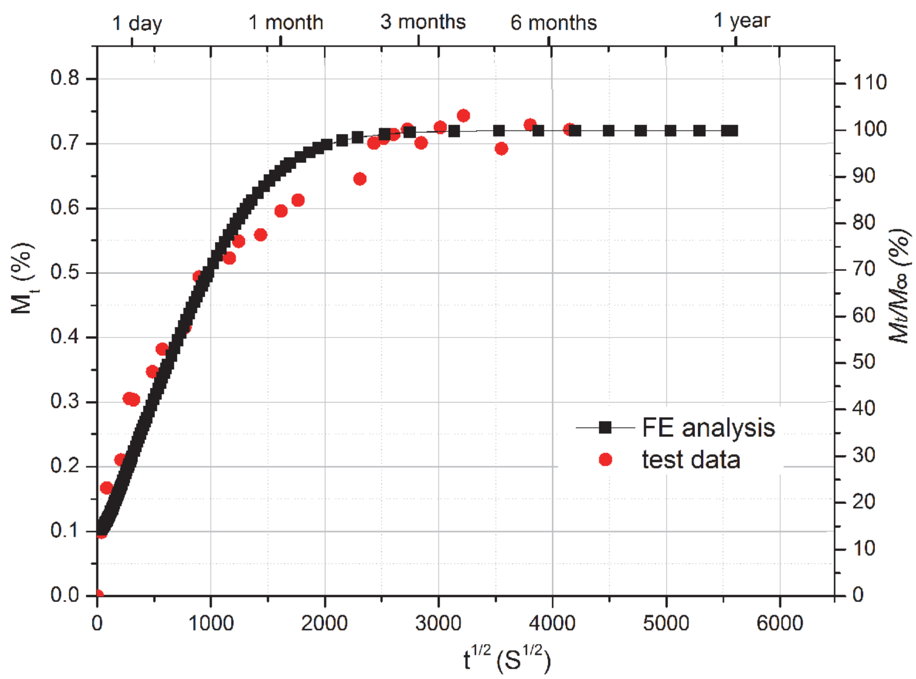

Fig. 4.17. Comparison of moisture uptake curve between test results and FE analysis on FRP specimens for short-beam shear tests

The typical failure mode of short-beam shear specimens is shown in Fig. 4.18, which is the interlaminar failure through the thickness of FRP laminates.

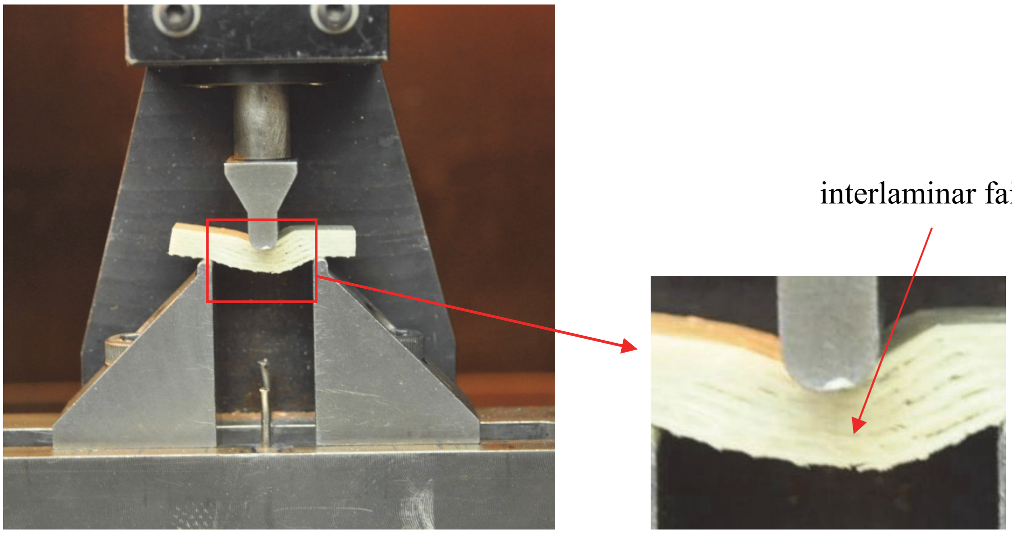

Fig. 4.18 The failure mode of the short-beam shear test specimen

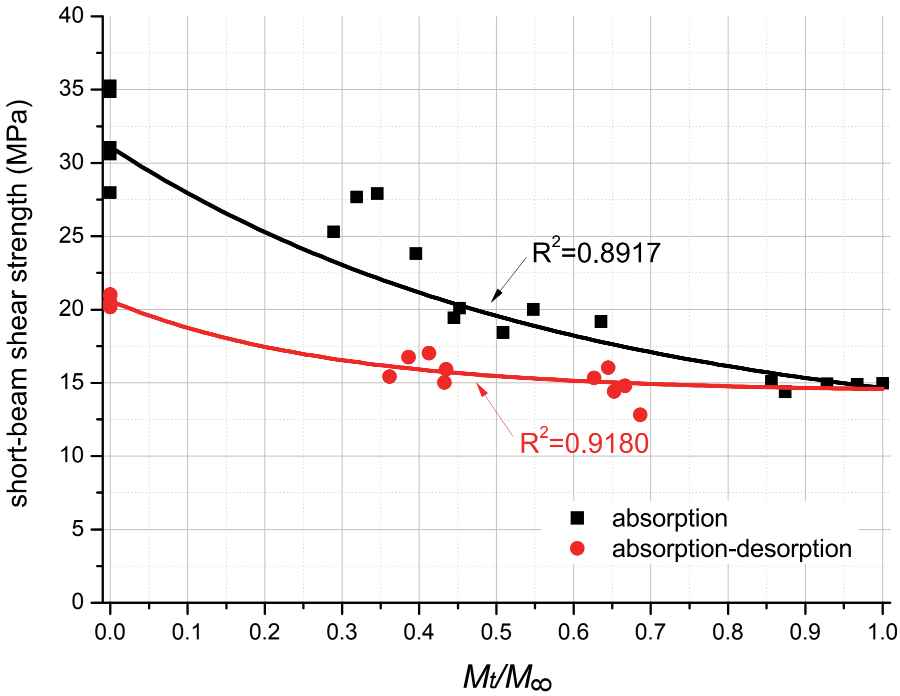

Fig. 4.19. a) 20°C

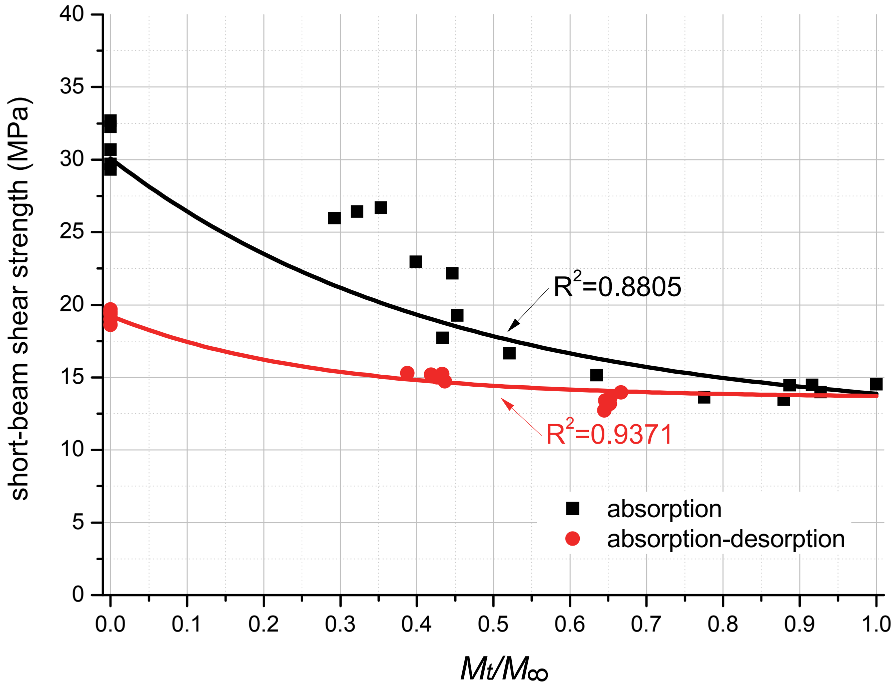

b) 40°C

Fig. 4.19. Degradation on the short-beam shear strength of FRP laminates

Fig. 4.19 shows the mechanical degradation of short-beam shear strength of FRP laminates as a function of moisture uptake content at 20°C and 40°C respectively. The R-square value for each curve is also present in Fig. 4.19, which indicates how well the curve fits test data points. The short-beam shear strength can be calculated as follows [12]:

$$F^{sbs} = 0.75 \times \frac{P_m}{b \times h} \tag{4.13}$$

where:

F^{sbs} = short-beam strength, MPa,

P_m = maximum load observed during the test, N,

b = measured specimen width, mm,

h = measured specimen thickness, mm.

The predictive equations for the short-beam shear strength degradation as the function of moisture content is curve fitted by the exponential function, using the least square method. The obtained predictive equation is as follows:

Shear strength, 20°C, absorption process:

$$S = 5.5^{-(\frac{M_t}{M_\infty}-1.76)} + 11 \tag{4.14}$$

Shear strength, 20°C, absorption-desorption process:

$$S = 34^{-(\frac{M_t}{M_\infty}-0.517)} + 14.4 \tag{4.15}$$

Shear strength, 40°C, absorption process:

$$S = 9.6^{-(\frac{M_t}{M_\infty}-1.28)} + 12 \tag{4.16}$$

Shear strength, 40°C, absorption-desorption process:

$$S = 46.8^{-(\frac{M_t}{M_\infty}-0.45)} + 13.6 \tag{4.17}$$

All the predictive curves are illustrated in Fig. 4.19 for comparison with the experimental results.

The interlaminar shear modulus of the FRP laminates cannot be determined experimentally via the short-beam three point bending. It is determined by the FE analysis using the inverse parameter identification approach, which is introduced in further detail hereafter.

As shown in Fig. 4.19a), in the moisture absorption process, the short-beam shear strength is quasi-linearly decreasing from the fully dry specimens to the specimens with about 75% moisture content of the saturated level. Then, the test data point is distributed stably until reaching the moisture fully saturated condition (100%M_∞). As listed in Table 4.6, the short-beam shear strength of the moisture fully saturated specimens is 15 MPa, which is 53.1% lower than that of the unconditioned dry specimens (32 MPa). Furthermore, in the moisture absorption process, the test data points are distributed more dispersively, since for the small scale short-beam specimens, the moisture uptake process deviates significantly. Thus, under the same water aging time, the moisture uptake content of the individual specimen varies in a certain range. With regard to the moisture desorption process, from fully saturated to dry, the short-beam shear strength is slightly increasing, ending at 21 MPa. It is 34.4% lower than that of the unconditioned dry specimens. This means that one cycle of moisture absorption-desorption process degrades the shear strength of FRP laminates by 34.4%.

Fig. 4.19b) presents the same tendency of degradation of the short-beam shear strength of FRP laminates at 40°C. As listed in Table 4.6, the higher temperature (40°C) only slightly deteriorates the shear strength of FRP specimens, which implies that the influence of temperature is not that significant as the influence of moisture.

Table 4.6 Short-beam shear strength degradation of FRP laminates

Specimen Identification	Shear Strength* (MPa)	Standard Deviation
S-0%-20°C	32	2.74
S-0%-40°C	31	1.34
S-30%-20°C	26	1.70
S-30%-40°C	25	1.89
S-50%-20°C	19	0.59
S-50%-40°C	16	2.10
S-100%-20°C	15	0.24
S-100%-40°C	14	0.41
S-50%-20°C-D	15	1.08
S-50%-40°C-D	13	0.41
S-30%-20°C-D	16	0.755
S-30%-40°C-D	15	0.21
S-0%-20°C-D	21	0.35
S-0%-40°C-D	19	0.36

* mean value of five specimens

4.3.3 Determining the interlaminar shear modulus of FRP laminates

Currently, standard test methods exist mostly for studies of the in-plane normal and shear modulus, and strength parameters of FRP composite materials [13]. However, the test method for obtaining the interlaminar shear modulus is limited. Failure always occurred through a combination of shear and transverse tension, indicating that a pure shear failure mode was not achievable in the test. It is, therefore, imperative that robust methodologies for determining the interlaminar material properties of FRP composite materials need to be developed. In this section, an inverse parameter identification approach for determining the interlaminar shear modulus G_{13}

(G_{23}) is employed, which is realized by minimizing the difference between an experimentally measured and numerically predicted material response by varying the interlaminar shear modulus of FE model. It has been confirmed by the sensitivity FE analysis of Chan's research [14], that the short-beam three-point bend test (rather than the standard Iosipesu test and off-axis tensile test) is sensitive to changes in the interlaminar shear modulus while remaining relatively insensitive to changes in the other unknown material properties. Hence, using the short-beam three-point bending test to study the interlaminar shear modulus is the most suitable.

To determine the environment-dependent interlaminar shear modulus of FRP composites, the coupled hygro-mechanical FE modeling is employed herein, which is already well developed and has been validated by the flexural tests in section 4.2.3. For instance, at the test temperature of 20°C and in the moisture absorption process, the flexural modulus (E_{11} and E_{22}, as indicated in Fig. 4.8a)) of FRP laminates with a nominal moisture content of 0% to 100% can be predicted using Eq. (4.6). It is used as the field-dependent input values for material properties of the FE model. Other material properties are used according to Table 4.7, which is supplied by the manufacturer. Depending on the sensitivity analysis, these data cannot significantly influence the determination of the interlaminar shear modulus of FRP laminates.

Table 4.7. Mechanical properties of materials for FE model

Property	FRP laminates
Elastic Modulus 33 (N·mm)	11000
Poisson Ratio 12	0.33
Poisson Ratio 23	0.3
Poisson Ratio 13	0.18
Shear Modulus 12 (N·mm)	6986

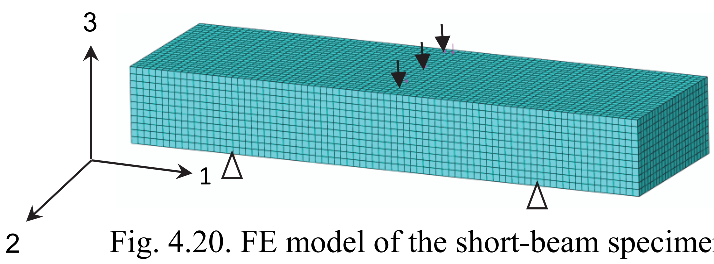

Fig. 4.20. FE model of the short-beam specimen

According to the test code ASTM D790-10 [1], as illustrated in Fig. 4.21, the initial non-linear stage of test results is an artifact caused by a takeup of slack and alignment or seating of the specimens, which does not represent the properties of the material. In order to obtain correct values of material properties, this curve must be offset to the corrected zero point (point B in Fig. 4.21). For each test, the initial non-linear regions are different from each other. To make easy comparisons, all the experimental curves are offset from B to A, to make the extension line of the linear CD region exactly through the zero point of coordinates. Original test results can be found in the Stevin II lab report.

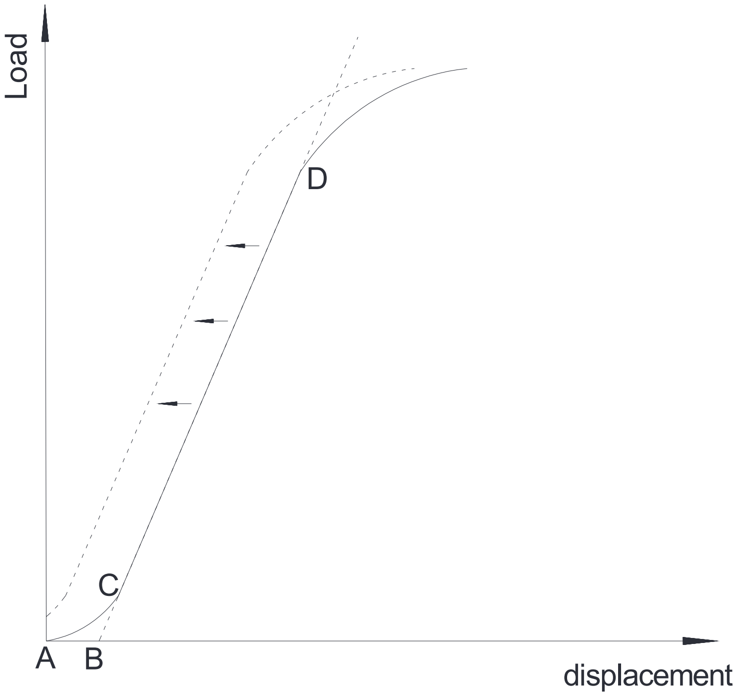

Fig. 4.21. Offset of the experimental load-displacement curve

It is assumed that the degradation of interlaminar shear modulus follows a linear relationship with the nominal moisture content, the same as obtained for the flexural modulus of FRP laminates. Thus, the interlaminar shear modulus of FRP specimens with the 0% moisture content (S-0%-20°C) is firstly determined by fitting the FE load-deflection curve to the test results, as shown in Fig. 4.22a). Accordingly, the shear modulus G_{13} (G_{23}) is numerically determined as 1200MPa. In the same way, the shear modulus G_{13} (G_{23}) of FRP specimens with the 100% moisture content (S-100%-20°C) is determined as 800MPa (Fig. 4.22b)). Subsequently, the predictive equation for the interlaminar shear modulus of FRP laminates at the test temperature of 20°C and in the moisture absorption process is as follows:

$$G_{23} = G_{13} = -400 \times M_t/M_\infty + 1200 \tag{4.18}$$

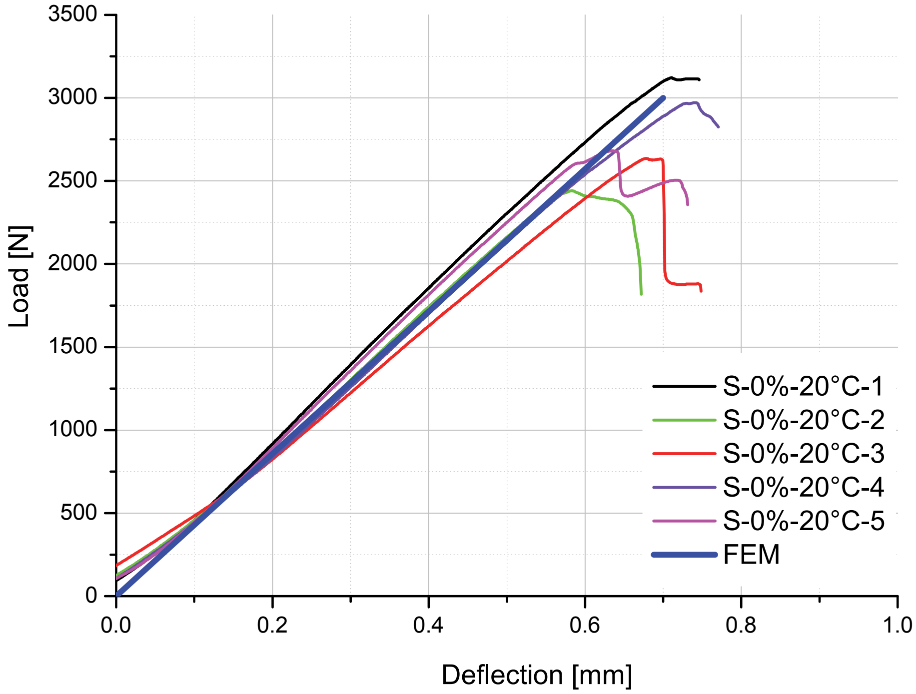

a) S-0%-20°C

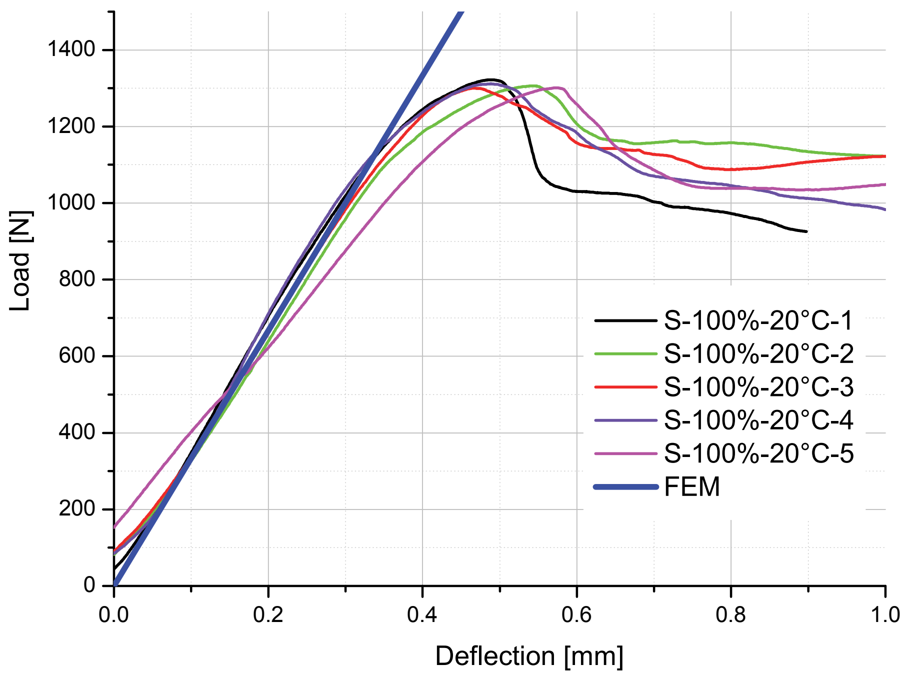

b) S-100%-20°C

Fig. 4.22. Comparison of load-deflection curves between FE analysis and test results of S-0%-20°C specimens and S-100%-20°C specimens

To validate Eq. 4.18, the other two exposure time intervals (30% M_t/M_∞ and 50% M_t/M_∞) are employed. From the moisture diffusion FE analysis, the moisture distributions across the mid-plane of the FRP specimens are shown in Fig. 4.23 and Fig. 4.24, which are used as the input field for the coupled stress analysis. The field-dependent shear modulus is input as presented by Eq. 4.18.

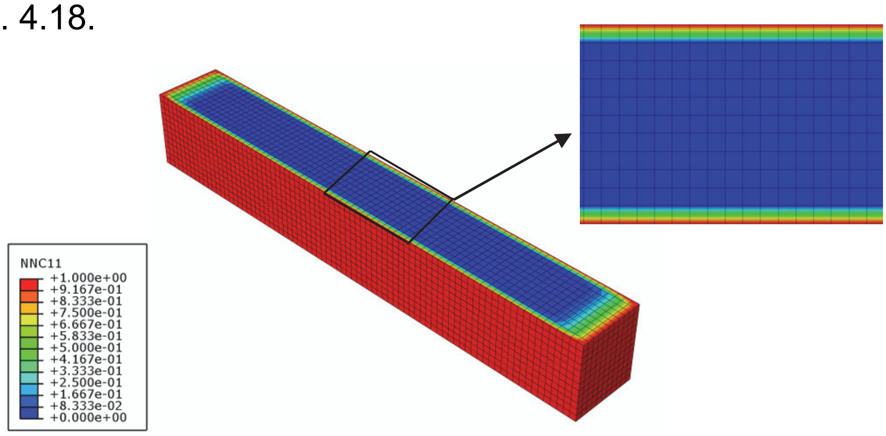

Fig. 4.23 Moisture concentration distribution across the mid-plane of the FRP specimen with 30% moisture uptake content (time= 26 hours)

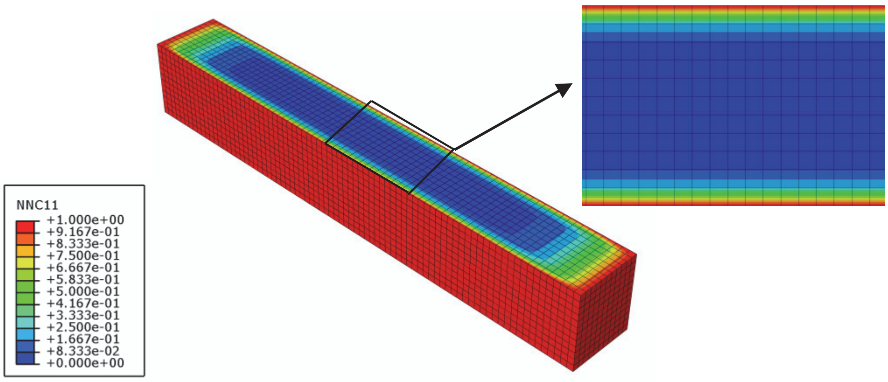

Fig. 4.24 Moisture concentration distribution across the mid-plane of the FRP specimen with 50% moisture uptake content (time= 107 hours)

Comparison between FE results and test data of S-30%-20°C specimens and S-50%-20°C specimens is shown in Fig. 4.25a) and Fig. 4.25b) respectively. Good agreements on slopes of load-displacement curves are achieved for these two groups of specimens, which prove that the predictive equation 4.18 is accurate enough to simulate the stiffness of FRP specimens with other moisture contents.

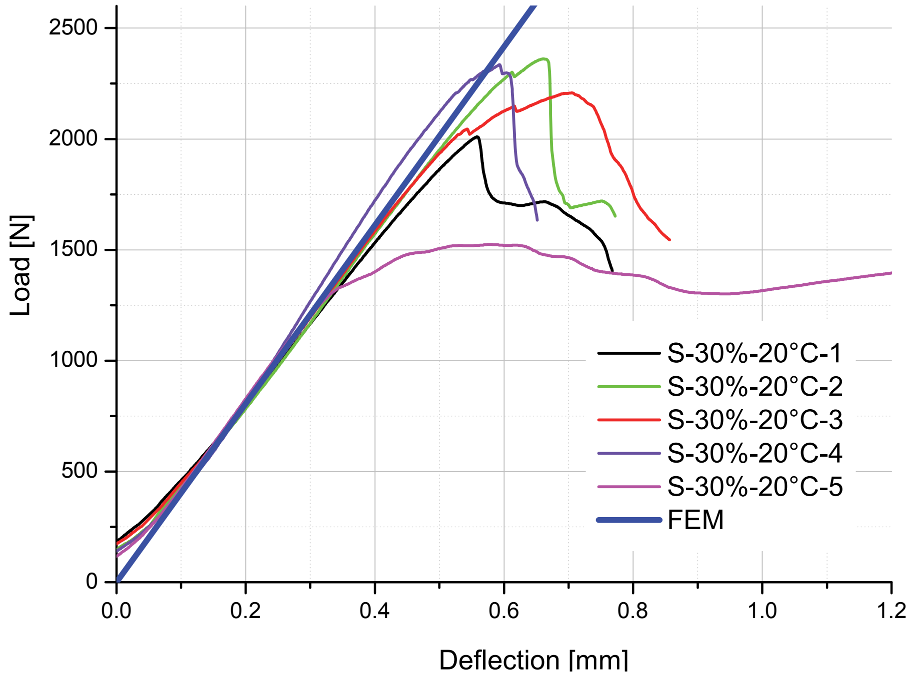

a) S-30%-20°C

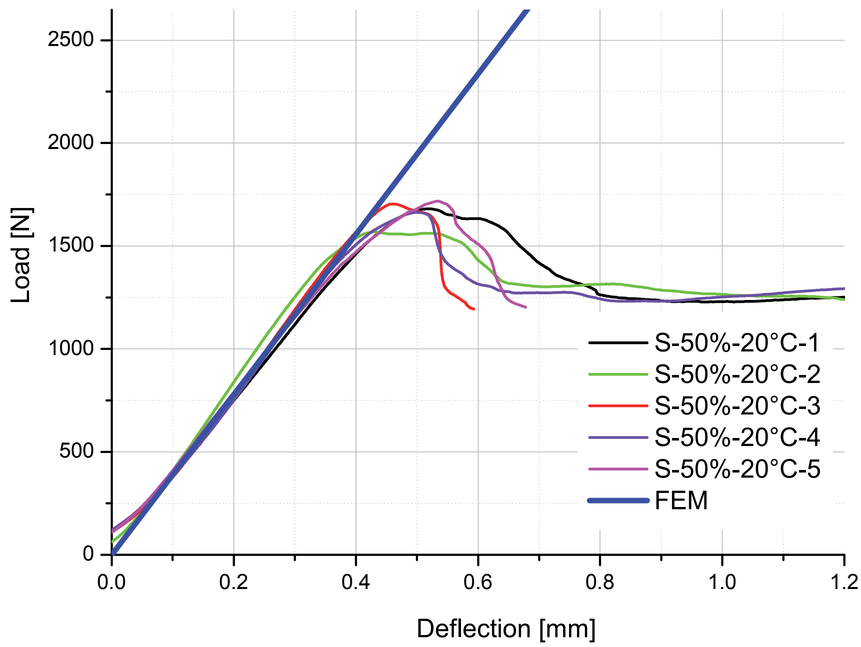

b) S-50%-20°C

Fig. 4.25. Comparison of load-deflection curves between FE analysis and test results of S-30%-20°C specimens and S-50%-20°C specimens

For the FRP specimens tested at 20°C and in the moisture desorption process, the same inverse parameter identification method is employed to detemine the environment-dependent interlaminar shear modulus. The predictive equation is developed and validated by the middle two exposure time intervals, as follows:

$$G_{23} = G_{13} = -50 \times M_t / M_\infty + 850 \tag{4.19}$$

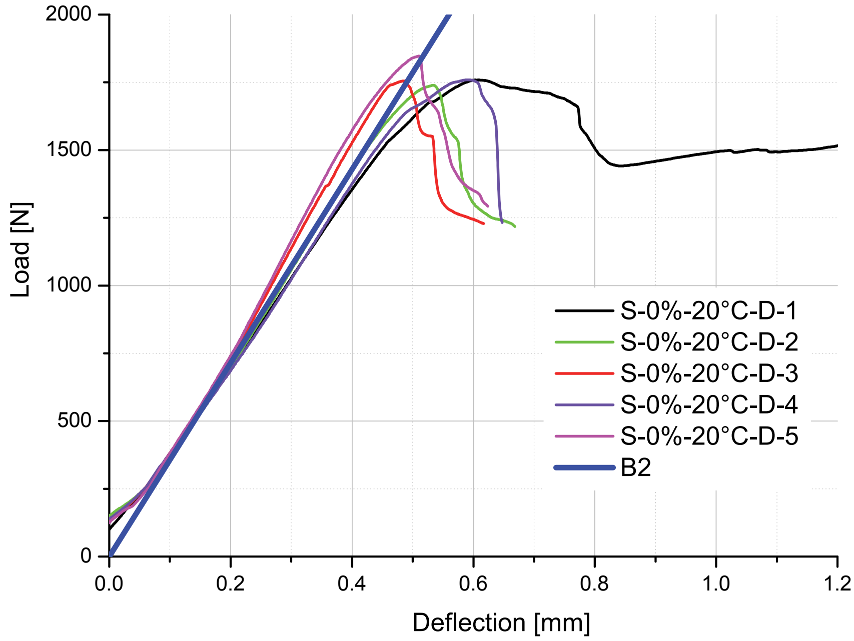

Fig. 4.26. a) S-0%-20°C-D

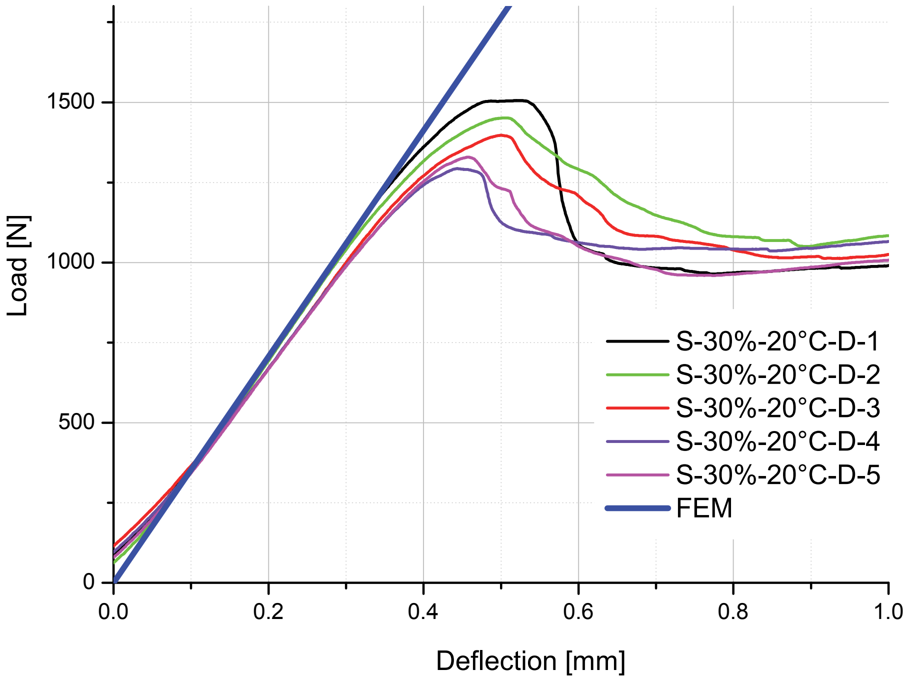

Fig. 4.26. b) S-30%-20°C-D

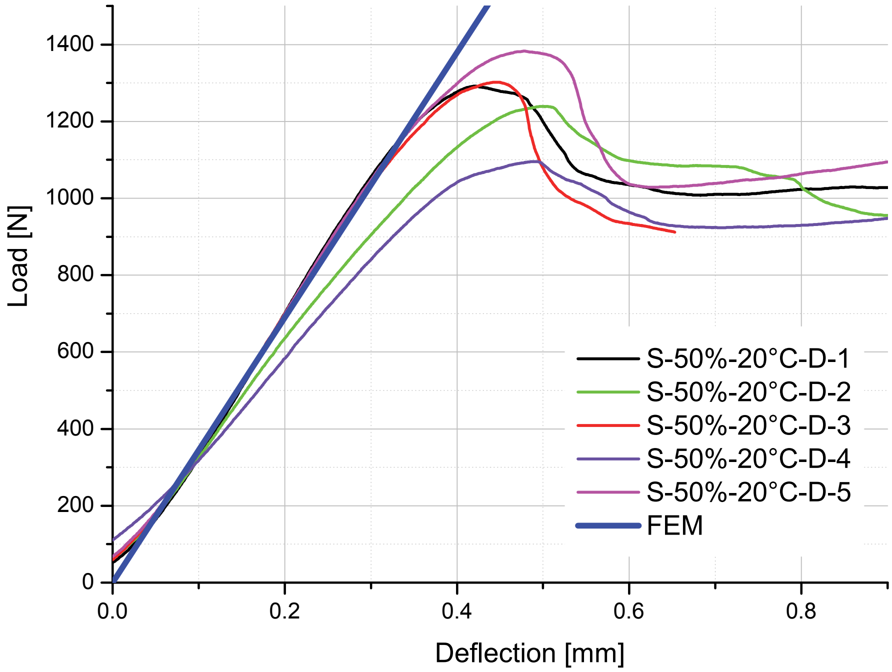

c) S-50%-20°C-D

Fig. 4.26. Comparison of load-deflection curves between FE analysis and test results of specimens tested at 20°C and in the moisture desorption process

For the FRP specimens tested at 40°C and in the moisture absorption process, the predictive equation is as follows:

$$G_{23} = G_{13} = -450 \times M_t/M_\infty + 1050 \tag{4.20}$$

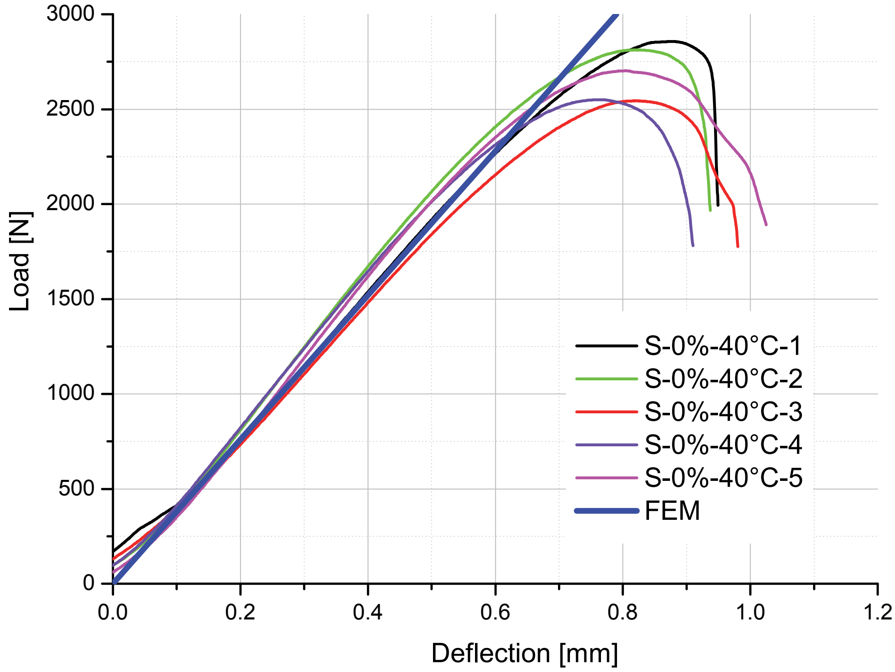

Fig. 4.27. a) S-0%-40°C

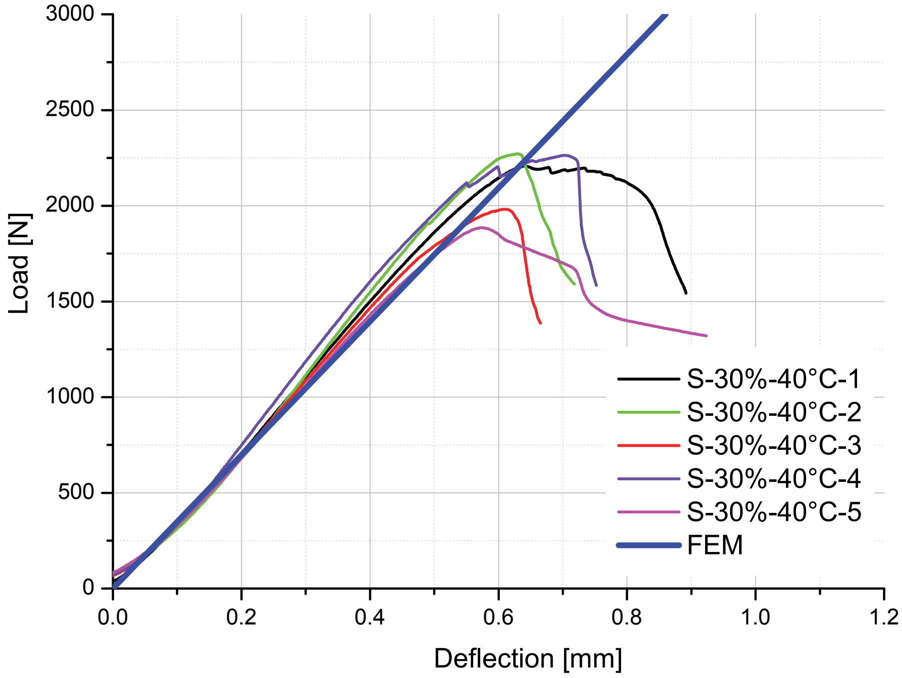

Fig. 4.27. b) S-30%-40°C

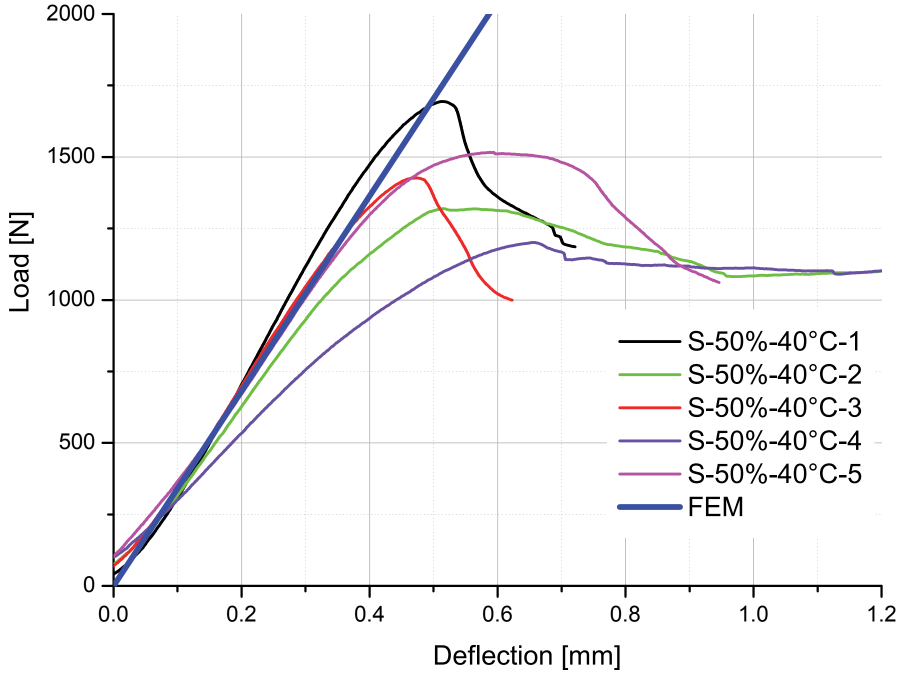

Fig. 4.27. c) S-50%-40°C

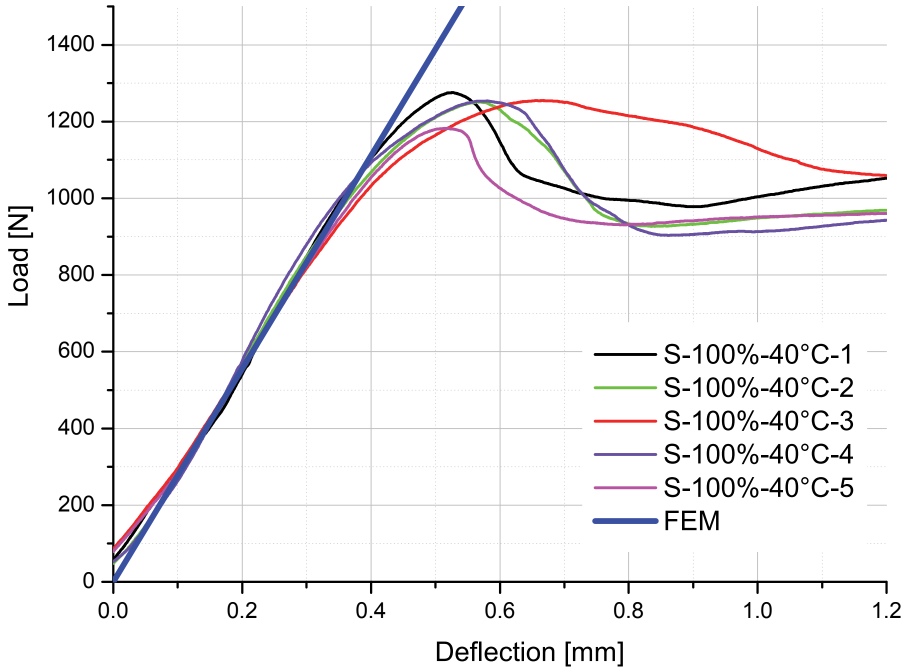

d) S-100%-40°C

Fig. 4.27. Comparison of load-deflection curves between FE analysis and test results of specimens tested at 40°C and in the moisture absorption process

For the FRP specimens tested at 40°C and in the moisture desorption process, the predictive equation is as follows:

$$G_{23}= G_{13}= -250\times M_t/M_\infty+850 \tag{4.21}$$

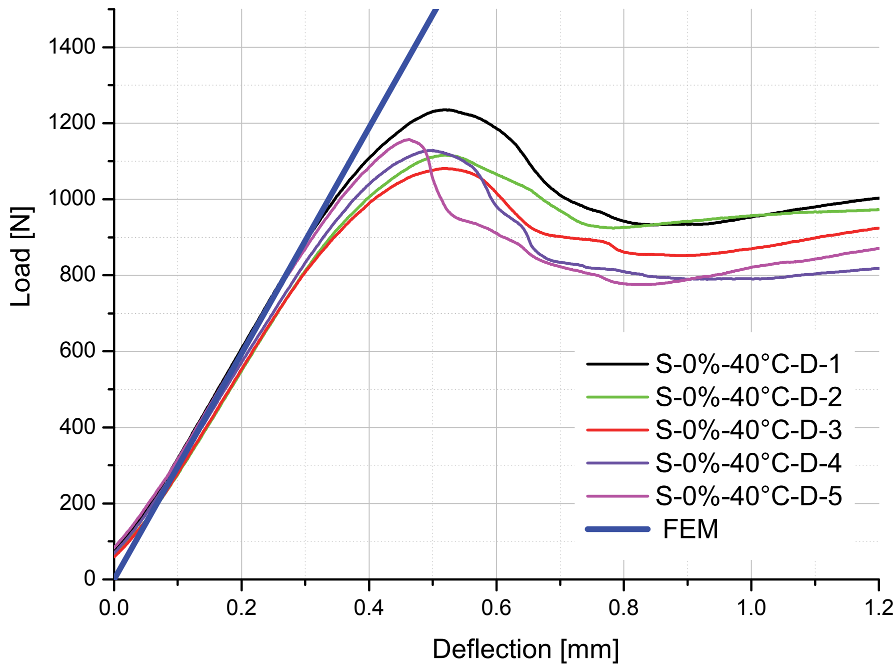

Fig. 4.28. a) S-0%-40°C-D

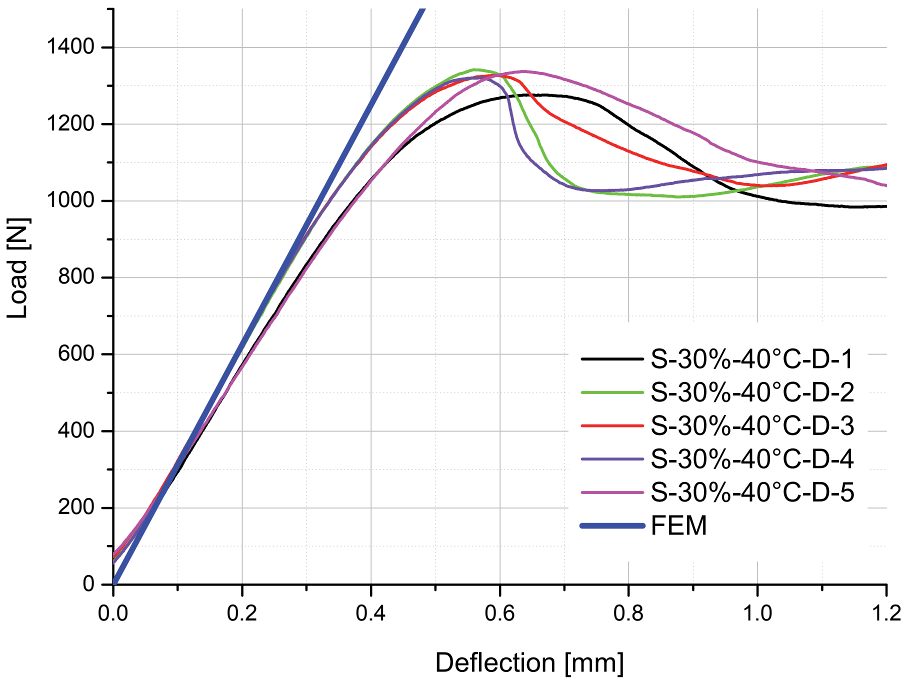

b) S-30%-40°C-D

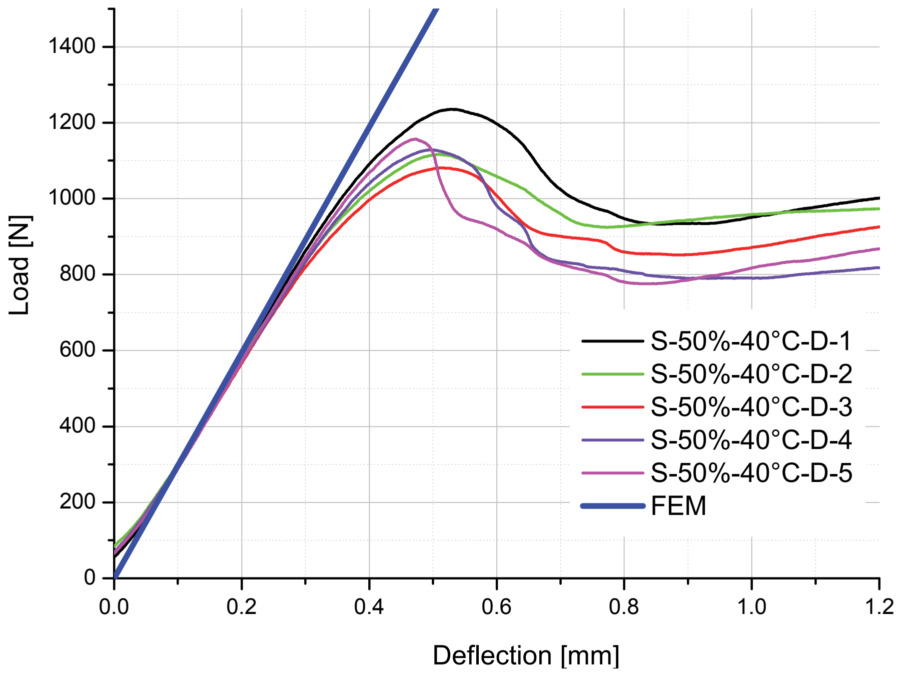

c) S-50%-40°C-D

Fig. 4.28. Comparison of load-deflection curves between FE analysis and test results of specimens tested at 40°C and in the moisture desorption process

As shown in Figs. 4.26, 4.27 and 4.28, good agreement on the stiffness of specimens is evident between the FE predicted curves and test results. However, there are some exception (S-50%-20°C-2, S-50%-20°C-4, S-50%-40°C-2 and S-50%-40°C-4), which significantly deviate from other specimens in the same test group. It can be attributed to non-homogenity of FRP laminate specimens, which influence the stiffness of the material. It also influences the moisture absorption property and correspondingly degrades the material stiffness. Excluding these exceptions, the predictive equations of moisture-dependent interlaminar shear modulus are acceptably reliable. Hence, they can be employed as the input material properties of an FE model to analyse the enviroment-dependent mechanical behaviours of FRP joints and FRP structures.

Fig. 4.29 illustrates these four predictive equations. For the specimens tested at 20°C, a dramatic drop of interlaminar shear modulus is found from the unconditioned dry specimen (1200MPa) to the moisture saturated specimen (800MPa). Then, after the moisture desorption process, a slight recovery is found for the shear modulus of S-0%-20°C-D specimens (850MPa). In total 29.2% decrease of interlaminar shear modulus is obtained for the specimens enduring one cycle of moisture absorption-desorption process. For the specimens tested in 40°C, a similar tendency of interlaminar shear modulus loss is obtained, with a 42.9% decrease from the unconditioned dry specimens (1050MPa) to the fully saturated specimens (600MPa) and a 19% decrease for the specimens enduring one cycle of moisture absorption-desorption process.

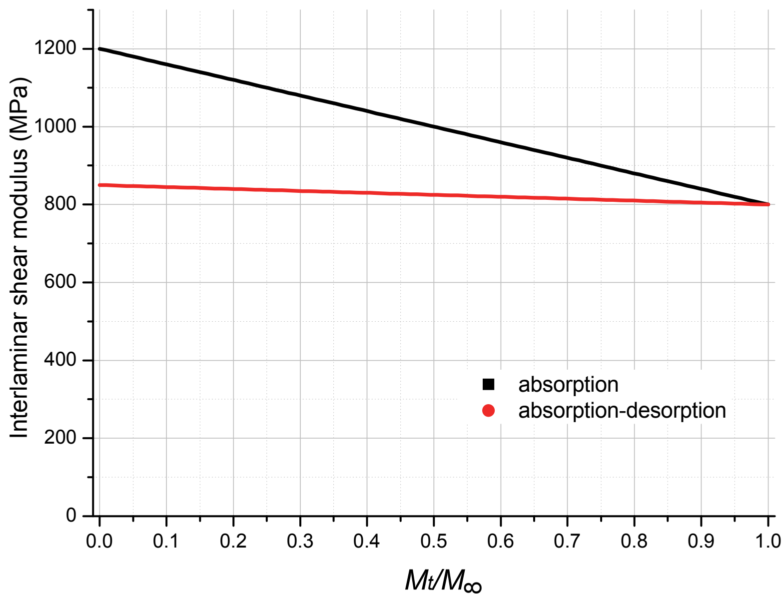

Fig. 4.29. a) 20°C

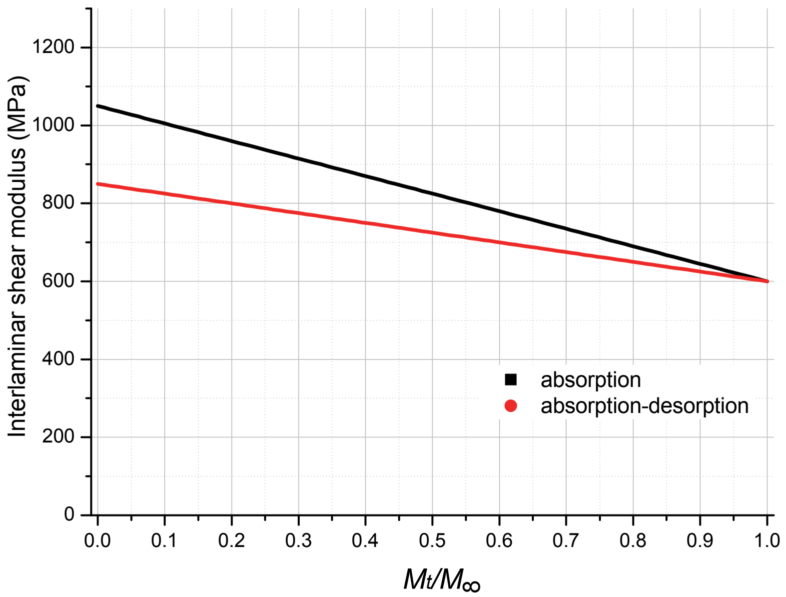

b) 40°C

Fig. 4.29. Degradation on the short-beam shear strength of FRP laminates

4.4 Conclusions

This chapter describes the investigation of the environment-dependent mechanical properties (flexural and interlaminar shear properites) of the FRP laminate material, which is achieved by the flexural tests and short-beam shear tests according to the ASTM test code D790-10 and D2344/2344M-00. The hydrothermal aging condition is a typical hot/wet aging environment (40°C-water) for the application of FRP bridge decks. The test conditions vary in terms of test temperature, moisture uptake content and absorption/desorption process. Experimental results confirm that the combination of moisture and temperature effects sincerely deteriorates the mechanical properties of FRP laminates, on both strength and stiffness.

Furthermore, a coupled hygro-mechanical FE modeling method was developed to analyse the enviroment-dependent mechanical behaviours of FRP lanimates. This FE model is firstly validated by the test results of flexural tests. Subsequently, the coupled hygro-mechanical FE model is employed in an inverse parameter identification method to determine the elastic interlaminar shear modulus of FRP laminates. The basis of this method is to minimize the difference between the experimentally measured and numerically determined material response by varying the interlaminar shear modulus of the FE model.

Finally, the predictive equations for environment-dependent mechanical properites of FRP laminates are sustained by using the least square method for the curve fitting. These predictive equations can be used as the input parameters for a coupled hygro-mechanical FE model, as well as a contribution to the design code as far as the long-term performance of FRP structures is concerned.

References:

[1] D790-10 A. Standard Test Methods for Flexural Properties of Unreinforced and Reinforced Plastics and Electrical Insulating Materials. PA, United States: ASTM International; 2010.
[2] Gellert EP, Turley DM. Seawater immersion ageing of glass-fibre reinforced polymer laminates for marine applications. Compos Part a-Appl S. 1999;30(11):1259-65.
[3] Loh WK, Crocombe AD, Wahab MMA, Ashcroft IA. Modelling anomalous moisture uptake, swelling and thermal characteristics of a rubber toughened epoxy adhesive. Int J Adhes Adhes. 2005;25(1):1-12.
[4] Ashcroft IA, Hughes DJ, Shaw SJ, Wahab MA, Crocombe A. Effect of temperature on the quasi-static strength and fatigue resistance of bonded composite double lap joints. J Adhesion. 2001;75(1):61-88.
[5] Ashcroft IA, Wahab MMA, Crocombe AD, Hughes DT, Shaw SJ. The effect of environment on the fatigue of bonded composite joints. Part 1: testing and fractography. Compos Part a-Appl S. 2001;32(1):45-58.
[6] Barjastech E, Nutt SR. Moisture absorption of unidirectional hybrid composites Compos Part a-Appl S. 2012;43:158-64.
[7] Bank LC, Gentry TR, Barkatt A. Accelerated Test Methods to Determine the Long-Term Behavior of Frp Composite Structures - Environmental-Effects. J Reinf Plast Comp. 1995;14(6):559-87.
[8] Muliana A, Nair A, Khan KA, Wagner S. Characterization of thermo-mechanical and long-term behaviors of multi-layered composite materials. Compos Sci Technol. 2006;66(15):2907-24.
[9] Davies P, Evrard G. Accelerated ageing of polyurethanes for marine applications. Polym Degrad Stabil. 2007;92(8):1455-64.
[10] Moulzakis DE, Zoga H, Galiotis C. Accelerated environmental ageing study of polyester/glass fiber reinforced composites (GFRPCs). Compos Part B-Eng. 2008;39(3):467-75.
[11] Crocombe AD, Ashcroft IA, Abdel Wahab MM. Chapter 8 Environmental Degradation. Modeling of Adhesively Bonded joints: Springer-Verlag Berlin Heidelberg; 2008.
[12] D2344/2344M-00 A. Standard Test Methods for Short-Beam Strength of Polymer Matrix Composite Materials and Their Laminates. PA, United States: ASTM International; 2006.
[13] Staab GH. Laminar Composites. Oxford: Butterworth-Heinemann; 1999.
[14] Chan A, Chiu WK, Liu XL. Determining the elastic interlaminar shear modulus of composite laminates. Compos Struct. 2007;80(3):396-408.

Chapter 5

Mechanical behaviour of FRP-to-steel adhesively-bonded joints before and after hydrothermal aging*

5.1 Introduction

The research presented in this chapter is focusing on mechanical behaviours (load-displacement behaviours and failure modes) of the adhesively-bonded joint between FRP sandwich decks and steel girders before and after hydrothermal aging. As stated in Chapter 1, there are two typical stress states in the adhesively-bonded joint (Fig. 5.1): shear and tensile stress, and combinations of both.

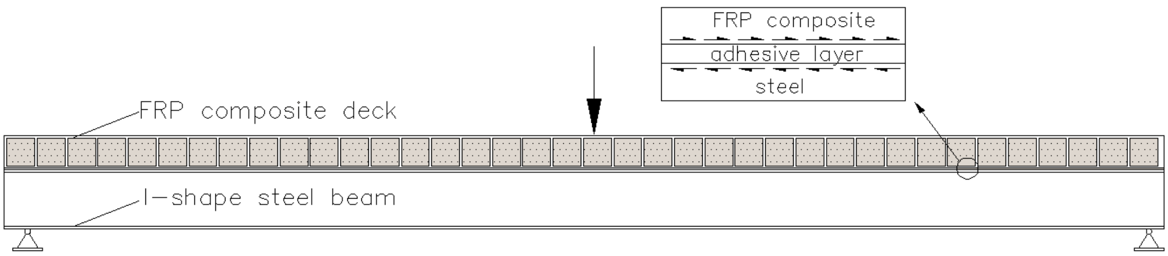

a) Shear stress in the longitudinal direction

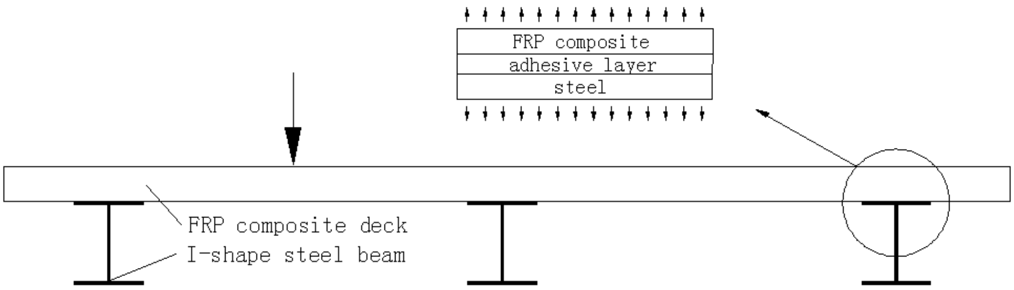

b) Tensile stress in the transverse direction

Fig. 5.1. Typical stress states in adhesively-bonded joint of FRP-steel composite bridge

---

* The content of this chapter is partially published in [1] Jiang X, Kolstein MH, Bijlaard FSK. Study on mechanical behaviors of FRP-to-steel adhesively-bonded joint under tensile loading. Compos Struct. 2013;98:192-201. and [2] Jiang X, Kolstein MH, Bijlaard FSK. Experimental and numerical study on mechanical behavior of an adhesively-bonded joint of FRP-steel composite bridge under shear loading. Compos Struct. 2014;108:387-399.

To realize these stress states in the adhesively-bonded joint in the test specimen, a specific loading device is developed to provide six different loading angles, which are 0°(pure tension), 18°, 36°, 54°, 72° and 90°(pure shear). This loading device is described in detail in section 5.2.1. Firstly, the adhesively-bonded joint is investigated experimentally under pure shear and pure tensile loading, considering the influence of different surface pretreatments on the FRP sandwich deck and the steel girder. The interfacial bonding quality of different surface pretreatment methods is studied. Subsequently, a three-dimensional FE model of tested specimens is developed by employing ABAQUS 6.8, and validated by comparing the relative deformation between FRP sandwich deck and steel support of the adhesively-bonded joint with experimental results. Linear elastic simulations are performed to characterize the stress distribution throughout the adhesively-bonded joint. The mesh-dependency of the FE model is addressed in the longitudinal, transverse and through-thickness direction of the adhesive joint. The preferable mesh configuration is confirmed for the further FE analysis of adhesive joints under other loading conditions. Secondly, a continuous study is conducted on the adhesively-bonded joint under the combination loading of tension and shear. Four combining ratios are employed. Failure modes of adhesive-bonded joints are experimentally investigated. Depending on the test results of six angle loading conditions, a tensile/shear failure criterion of the adhesive-bonded joint before hydrothermal aging is obtained. Based on the FE model, developed for the pure shear and pure tensile loading condition, the three-dimensional stress state is characterized through the interface between FRP sandwich deck and adhesive layer for four combining loading conditions. To study the environmental effects on the durability of adhesively-bonded joints, a further research is focusing on mechanical behaviours of adhesively-bonded joints after hydrothermal aging. The adhesive joint specimens have been hydrothermally aged in water of 40°C for a period of four months. Test results address a tensile/shear failure criterion of the adhesively-bonded joint after hydrothermal aging. To better understand the different mechanical performances of the adhesively-bonded joint before and after hydrothermal aging, a systematic comparison on experimental results of un-aged specimens and hydrothermal aged specimens is conducted. The discussion includes the ultimate failure load, failure mode and stiffness. The hydrothermal aging effects on the mechanical degradation of adhesive joints are discussed. Furthermore, the post curing mechanism induced by the elevated temperature of hydrothermal aging environment is discussed, which significantly influences the interfacial bonding quality of adhesive joints.

5.2 Experiment

5.2.1 Tensile-shear loading device

It is noted that, for the application of adhesively-bonded joints in aerospace engineering, single-lap joints or double-lap joints were usually employed to investigate the mechanical properties of joints under shear loading [3, 4]. However, it is not convincing to directly extend the experimental data and results from the aerospace industry to the civil engineering field. FRP composites used for civil infrastructures have essential differences as compared to the FRP composites used in aerospace and aircraft applications, which include geometries, types of fibres and matrix, fabrication methods, curing process and service environmental conditions. For instance, the FRP composite profiles and adhesive layers for aerospace/aircraft structures are usually thin (0.1–1 mm); while for bridge and building structures adherents and adhesive layers are usually comparatively much thicker (2–20 mm). Thus, with the thicker adhesive layers, the single-lap or double-lap adhesive joints will lead to a considerable additional bending moment around the adhesive tips, which can result in a significant increase of the peeling stress at that location (as shown in Fig. 5.2) [5-9]. Sheppard et al. [9] confirmed that the peeling stress at the end of a double-lap adhesive joint was relatively lower than that of the single-lap adhesive joint, by using a damage zone FE model. Finally, the failure of adhesive joints is initiated by the peeling stress rather than by the shear stress.

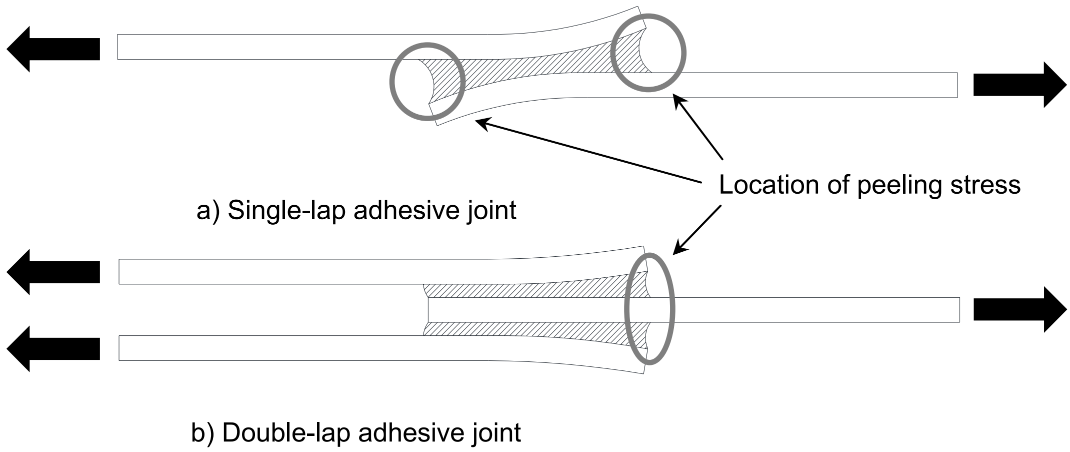

Fig. 5.2. Locations of peeling stress in single-lap and double-lap adhesive joints

For the application of adhesive joints in the FRP-steel composite bridge, the adherents (FRP decks and steel beams) are usually thick profiles. Thus, the deformation in single-lap or double-lap adhesive joints (as shown in Fig. 5.2) is not realistic. In this research, to simulate the real stress state of the adhesively-bonded joint for the application of FRP-steel composite bridges as well as reduce the scale of the peeling stress, a specific loading device is designed as shown in Fig. 5.3. The circular steel plates are separated into two pieces. Two parts of the central area of circular steel plates are cut off to save some space for putting up displacement sensors. The two steel blocks are fastened to the circular steel plates by 8 bolts. The adhesively-bonded joints are located in the middle of the loading device. Several bolt holes on the circular steel plates are proposed to force the whole loading device by different angles. Three bolts are employed to transfer the loading uniformly to the circular steel plates. Dimensions of the tested adhesively-bonded joint (more details are presented in the following section) are intentionally designed to locate the centroid of adhesive layer exactly in line with the shear loading axis. In this way, the additional bending moment can be avoided.

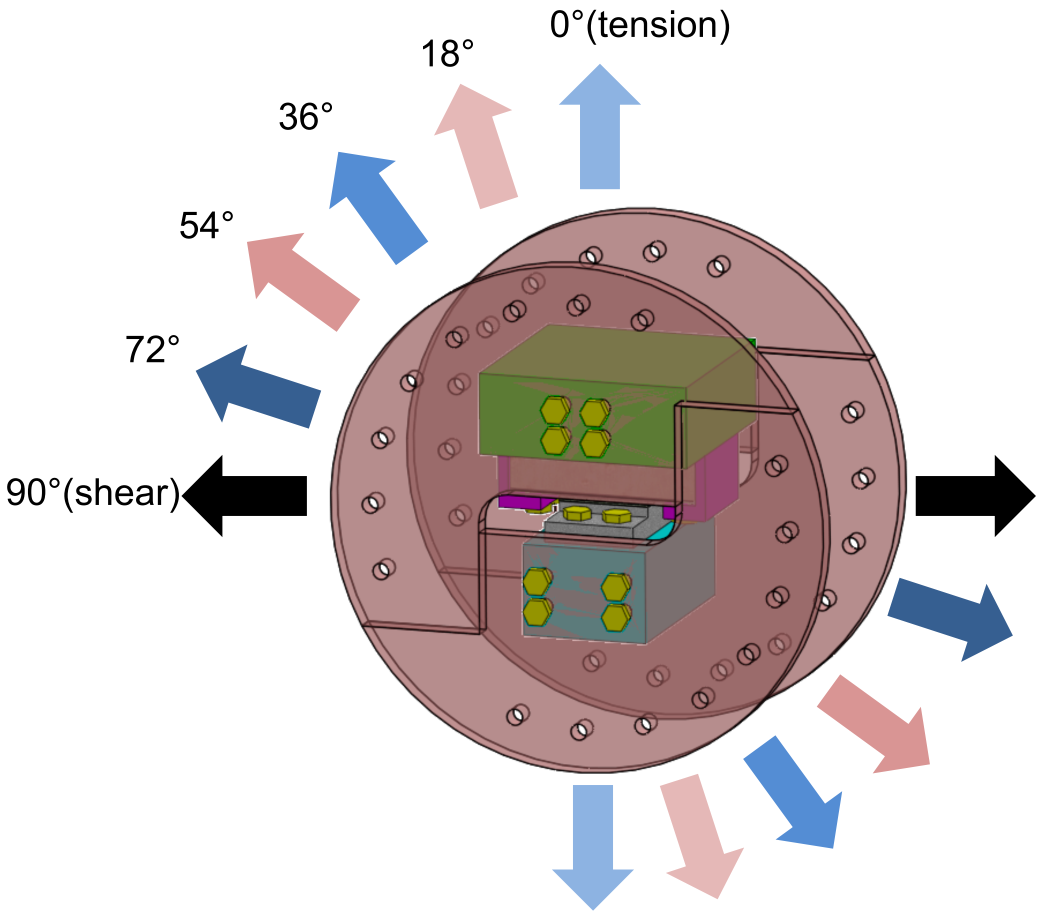

Fig. 5.3. Tensile/shear loading device

Besides the pure shear loading condition, this specific tensile/shear loading device can provide other loading conditions, such as a pure tensile loading condition and four combinations of shear and tensile loading. Accordingly, in total six loading conditions are feasible through this tensile/shear loading device. The angle step between each loading direction is 18°.

5.2.2 Test specimen

5.2.2.1 Un-aged specimen

To be adaptable to the loading device, the adhesively-bonded joint between FRP deck and steel girder is extracted for experimental investigation as shown in Fig. 5.4.

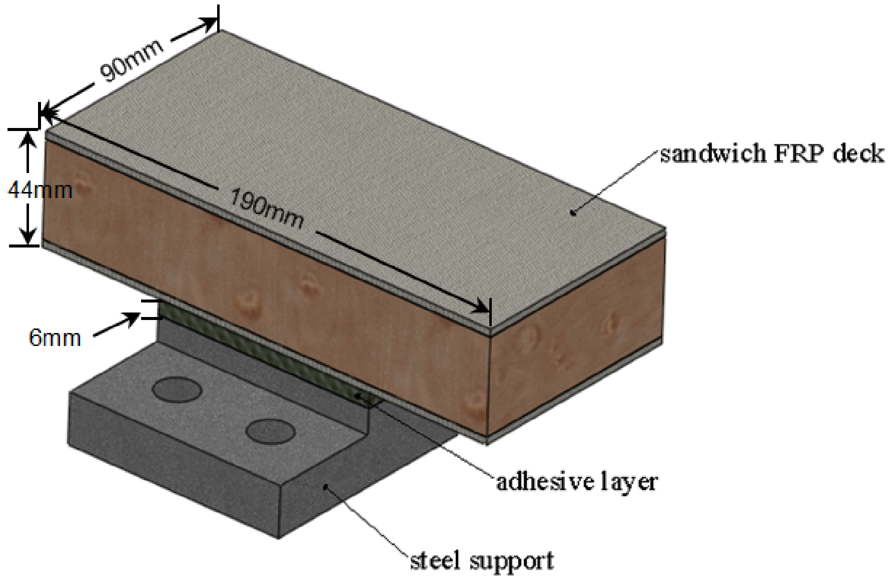

Fig. 5.4. FRP-to-steel adhesively-bonded joint

Considering the dimensional limitation of loading device and installation convenience, the specimen geometries are determined as follows: a 190mm×90mm piece of FRP sandwich bridge deck (supplied by Infra Composites B.V.[10]) is adhesively bonded to the steel support. The area of adhesively bonding surface on the steel support is a 90mm×90mm square. The bottom steel part is 190mm×90mm, with four holes for bolting it to the loading device. In the middle of the FRP sandwich deck, there is a Balsa SB150 wood layer with a thickness of 38.1mm, which is a core material produced from certified kiln-dried Balsa wood in the 'end-grain' configuration. The surface layer of the FRP sandwich deck is composed of three plies of 0.94mm thick EQX1200, which are the glass-fibre reinforced laminated polymer composites (54% glass content by weight). The layup configuration of EQX1200 is given in Table 5.1.

Table 5.1. FRP laminate properties (supplied by manufacturer)

Product name	Total weight (g/m^2)	Weight uniformity (g/m^2)				
		Yarn roving				Knit yarn
		0^o	$+45^o$	90^o	-45^o	
EQX 1200	1193	283	300	300	300	10

The sandwich profiles are manufactured by resin vacuum infusion. The gluing of FRP sandwich deck to steel support is executed and subsequently cured in a specific climate room, with the constant condition of 20 ^oC and 50%RH. The nominal thickness of the adhesive layer is controlled to be

6mm using spacers, as shown in Fig. 5.5. 6mm adhesive thickness is supposed to be a practical value, as far as installation tolerance and easy operation in the on-situ situation of bridge construction is concerned. The spacers are made of Teflon, which are those for easy demoulding from the adhesive layer after fully curing of adhesive joints. The commercial structural adhesive used herein is BUFA-BONDING PASTE 740-0110, which is a two-component adhesive material, based on toughened vinyl ester resin.

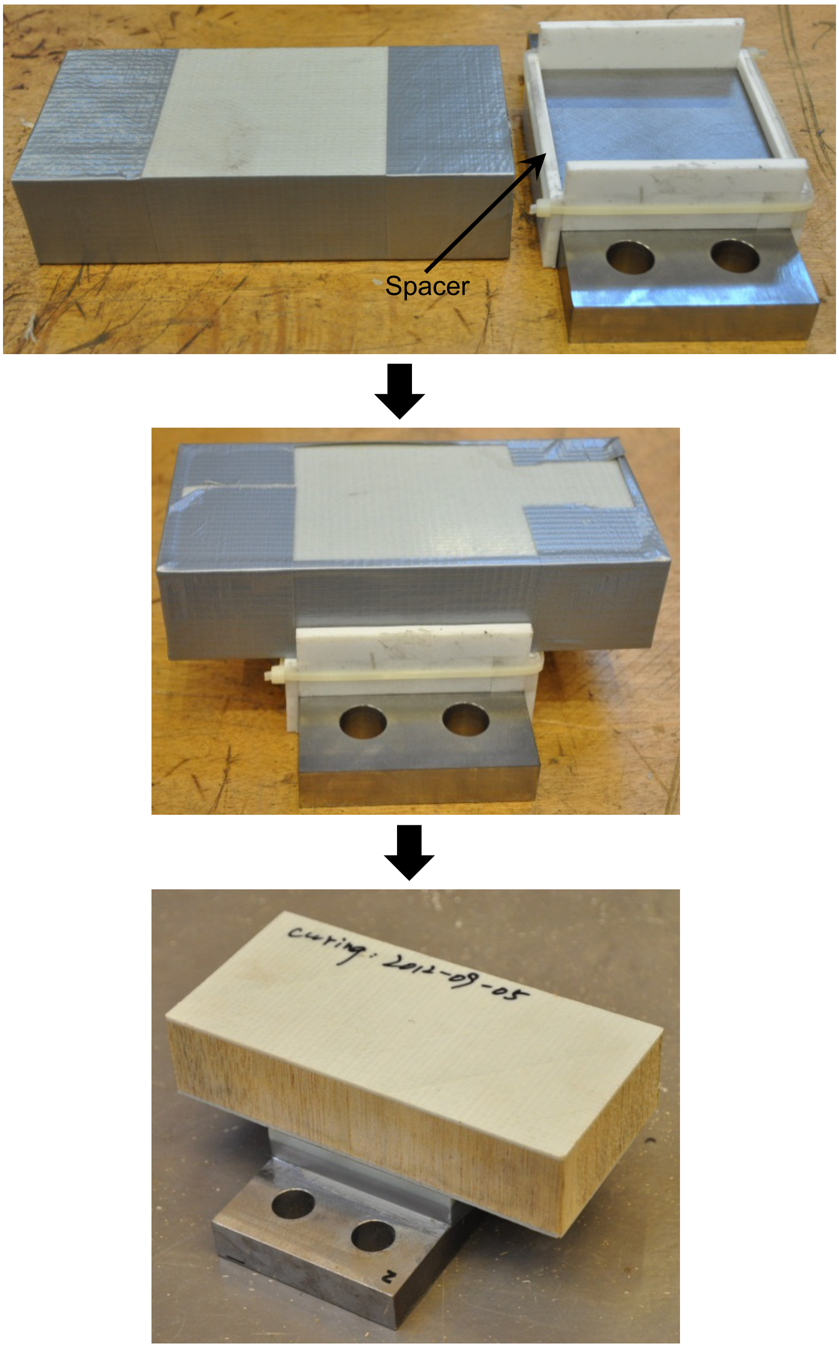

Fig. 5.5. Preparation process of adhesive joint specimens

Table 5.2. Adhesive properties (supplied by manufacturer)

Property	Value
Viscosity (MPa.s)	1,800,000
Solid content (%)	9
Elongation at break, steel (%)	3.7
E-modulus (MPa)	3400
Tensile strength, steel (MPa)	14.5
Heat deflection temperature (°C)	70
Geltime (min)	60
Curing time (min)	85

Adhesive material properties are listed in Table 5.2. The preparation process of the specimens is shown in Fig. 5.5. To investigate the influence of surface pretreatment methods on the interfacial bonding quality, three different surface pretreatment methods are conducted on the surfaces of FRP sandwich deck and steel support for the pure tensile and shear loading conditions. The first method is the simplest one, which is only degreasing and cleaning of the surfaces with acetone. The second one is conducted by using sandpaper. It starts with the wiping of specimen surfaces with acetone to eliminate any presence of oil used in the machining process. Then, the surfaces are abraded with sandpaper to remove any impurities and oxide layer which can potentially exist. After that, a re-degreasing and re-cleaning of the surface is done with acetone to remove any particles that can remain after sanding. The last surface pretreatment method is by using a sand blasting machine. The whole process is similar to the second one, except for using the sand blasting to remove the impurities and oxide layer. For each surface pretreatment method, three replicated specimens are prepared. In the following sections of this chapter, for the identification of specimens (as listed in Table 5.3), specimens pretreated using the first method (acetone) are indicated as AC for short, the second method (sand paper) as SP and the last method (sand blasting) as SB. For specimens tested under the combination of shear and tensile loading, the surface pretreatment method is limited to the sand blasting method, based on the test results under the pure shear and pure tensile loading. As listed in Table 5.3, in total 30 pieces of adhesive joint specimens are prepared for the tests before hydrothermal aging.

Table 5.3. Adhesively-bonded joint specimens

Specimen identification	Loading condition	Surface pretreatment method	Hydrothermal aging	Numder of specimens
S-AC-01~03	90° angle (shear)	acetone	no	3
S-SP-01~03	90° angle (shear)	sand paper	no	3
S-SB-01~03	90° angle (shear)	sand blasting	no	3
T-AC-01~03	0° angle (tension)	acetone	no	3
T-SP-01~03	0° angle (tension)	sand paper	no	3
T-SB-01~03	0° angle (tension)	sand blasting	no	3
18°-SB-01~03	18° angle	sand blasting	no	3
36°-SB-01~03	36° angle	sand blasting	no	3
54°-SB-01~03	54° angle	sand blasting	no	3
72°-SB-01~03	72° angle	sand blasting	no	3
S-SB-A-01~03	90° angle (shear)	sand blasting	yes	3
T-SB-A-01~03	0° angle (tension)	sand blasting	yes	3
18°-SB-A-01~03	18° angle	sand blasting	yes	3
36°-SB-A-01~03	36° angle	sand blasting	yes	3
54°-SB-A-01~03	54° angle	sand blasting	yes	3
72°-SB-A-01~03	72° angle	sand blasting	yes	3

In order to fix the adhesive joint to the loading system, some accessorial components are designed as shown in Fig. 5.6 a) and b). As mentioned above, the steel support is fastened directly by four bolts to the bottom steel block. However, for the FRP sandwich decks no holes are proposed, since the discontinued part in decks can cause more stress distribution distortions, which is not the case in applications of FRP composite bridges. To fix the FRP sandwich deck part, it is designed to be fastened with two L-shape steel profiles by four bolts to the top steel block, as shown by the purple coloured parts in Fig. 5.6 a). In this way, the two L-shape steel plates are holding the FRP sandwich deck specimen. The pure shear loading condition is realized by applying force to the L-shape steel profile, and the load is transferred through interacted contact-surfaces from the lateral plate to the adhesive joint. The pure tensile loading condition is realized by forcing the bottom plate of the L-shape steel profile. The combining loading conditions are realized by the combination of the above two loading conditions. As shown in Fig. 5.3, the forces of six loading conditions are applied exactly via the center line of the adhesive layer. In this way, no additional bending moment is expected. All the accessorial components are made of steel. Compared to the FRP composites and adhesive materials, the deformation of steel components can be neglected during tests, due to the high stiffness of steel material.

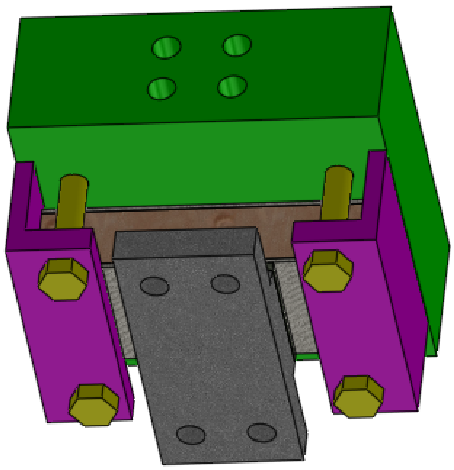

a) FRP Deck fixed configuration

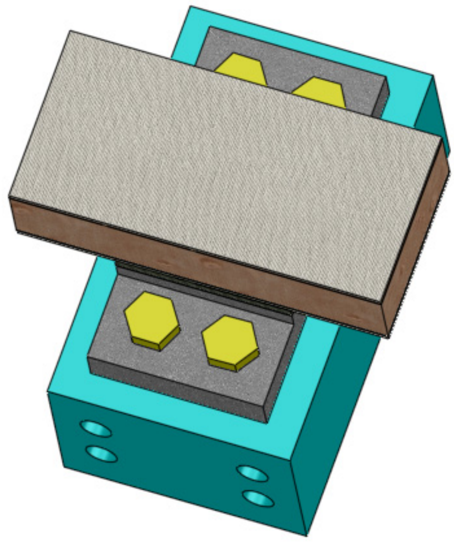

b) Steel support fixed configuration

Fig 5.6 Fastening system for fixing the adhesively-bonded joint to the loading device

5.2.2.2 Hydrothermal aged specimen

The preparation process of FRP-to-steel adhesively-bonded joints is the same as stated in section 5.2.2.1. The surface pretreatment method is the sand blasting (SB) method. Based on test results under the pure tensile and pure shear loading, this pretreatment method is considered to be the preferable and easy method to obtain the best bonding quality and controllable quality of adhesive layer of an FRP-to-steel adhesively-bonded joint. The identification of specimens is given in Table 5.3. The "A" character is added to the numbering of specimens, indicating that the specimens are tested after aging. In total 18 pieces of specimens are prepared for the tests after hydrothermal aging.

After the curing of the adhesively-bonded joints at the environment of 20°C and 50%RH, they are immersed in the water with a temperature of 40°C, which is considered as a typical hot/wet environment regrading the actual service environment of FRP-steel composite bridges. This environmental aging condition is simulated by putting specimens in a water filled container, which is kept in an oven in which the temperature is set at 42°C. In this way, the water temperature is 40°C. The total aging time is four months. To simulate the real in-situ condition of FRP sandwich decks, prior to putting specimens into the environmental aging condition, the four surrounding surfaces of the FRP sandwich deck specimen are sealed by a commercial coating Sikafloor 156. After fully curing of the first layer of coating, another layer of water-proof adhesive tape is applied on the coating to doubly ensure that no water can penetrate through the surrounding surfaces of FRP sandwich decks. Because, the tested FRP sandwich deck is cut from the whole piece of the bridge deck. In the service-life of these FRP sandwich bridge decks, the edge surfaces are sealed to be water-resistant. Thus, most of the moisture content should diffuse through the top and bottom surfaces into the FRP sandwich deck specimens. The moisture uptake of core material (Basal wood) should not directly absorb from the environment, but absorb from the FRP laminates. Hence, during the hydrothermal aging, the core material (Basal wood) should not be exposed to the water aging condition.

The adhesively-bonded joint specimen after the hydrothermal aging is shown in Fig. 5.7. To simplify the manufacturing process of the steel support, it is made of two parts and then assembled together by 9 bolts for testing, see Fig. 5.7.

Fig.5.7 Hydrothermal aged adhesively-bonded joint and its assembling process

5.2.3 Experimental procedure

The series of experiments are carried out in the Stevin II laboratory of the Faculty of Civil Engineering and Geosciences at Delft University of Technology. All the aged and un-aged specimens are tested by the specific tensile/shear loading device under the ambient environment. The whole test set-up is shown in Fig. 5.8. The tensile/shear loading device can provide six loading conditions by forcing the different angles of semi-circle steel plates. A SCHENCK Hydropuls testing machine with a loading capacity of 600 kN in tension is employed and controlled by the INSTRON 8400 controller, which can provide both load- or displacement-controlled test procedures. The whole tensile/shear loading device is loaded by jacks by means of two hinged joints, which avoid the additional bending moment due to the eccentric loading from the specimen misalignment. Two LVDTs are fixed on each side of the loading system, as shown in Fig. 5.9, to measure the displacement between the top and bottom semi-circle loading device, for checking equal distribution of the load. The measuring range of the LVDT is 0~10mm. The quasi-static experiments of adhesively-bonded joints are displacement controlled by LVDTs (linear variable differential transformer) at a rate of 0.001mm/sec. When the adhesive joint specimen is installed in the loading device, the four bolts connecting the L-shape steel profiles (see Fig.5.6 a)) are not fully fastened firstly. A preload of 1kN is applied to make every loading component touch each other. In this way, the load can transfer smoothly from the loading device to the adhesive joint. After that, these four bolts are fully fastened and then the preload is unloaded. The tests start at a load of 0kN. All the measured test data can be found in the Stevin II lab report.

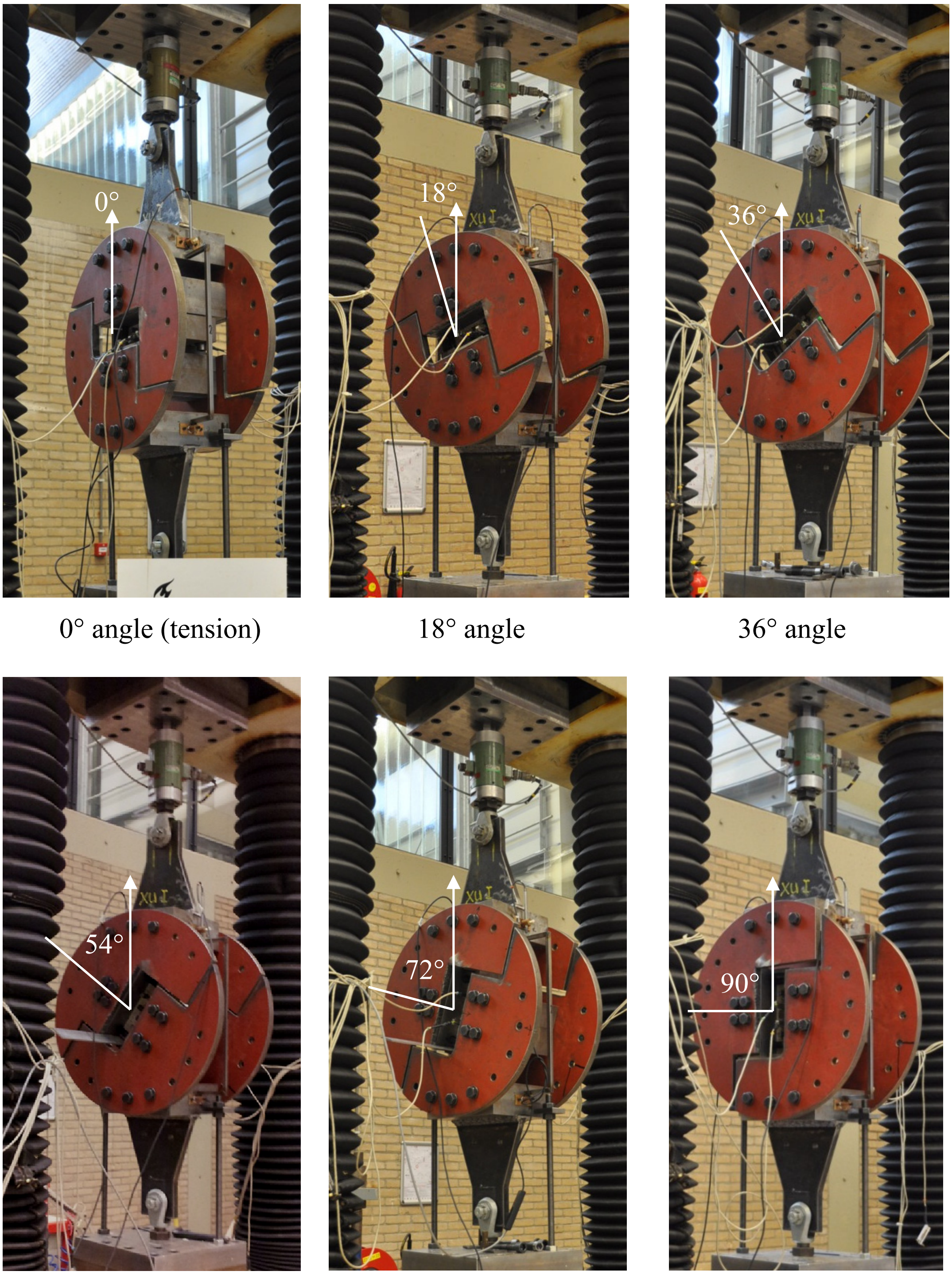

0° angle (tension) 18° angle 36° angle

54° angle 72° angle 90° angle (shear)

Fig. 5.8. Six loading angles of the tensile/shear loading device

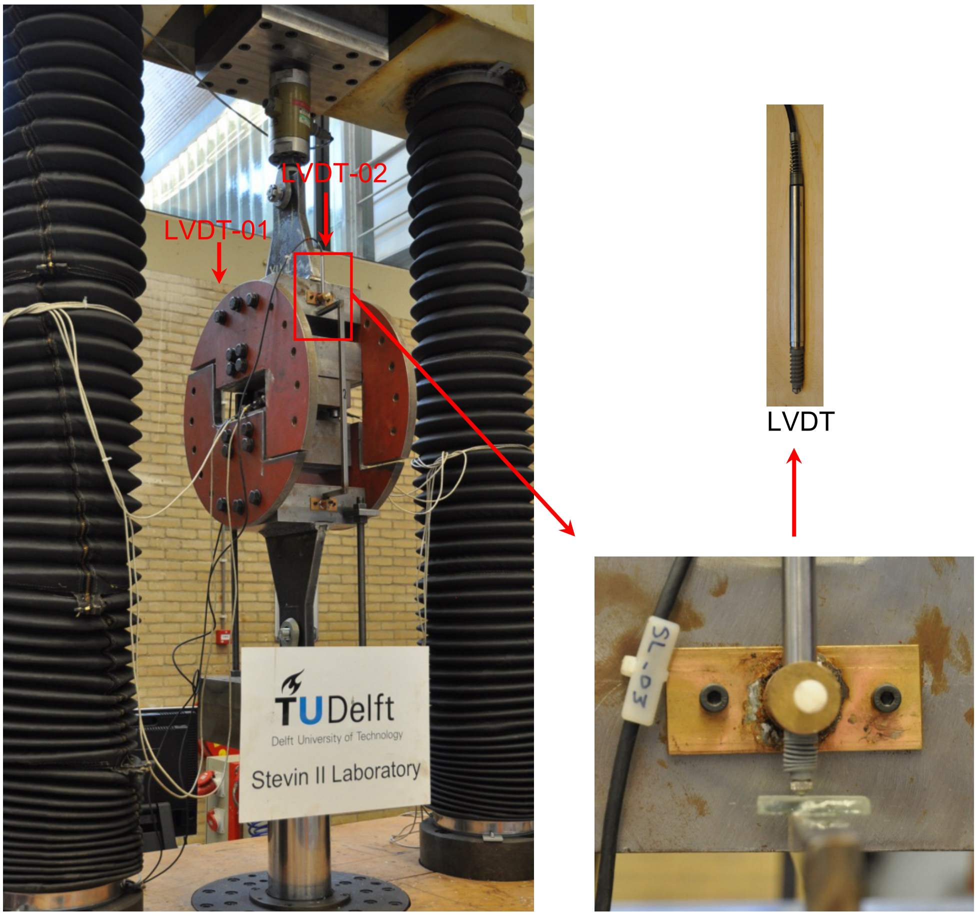

Fig. 5.9. Test set-up for the shear loading condition

For the shear loading condition, two displacement sensors are secured on both sides of adhesive joints, as shown in Fig. 5.10, to track the relative deformation between FRP sandwich deck and steel support (indicating the shear deformation in the adhesive layer) during the whole test process. The measuring range of the displacement sensor is 0~2mm. For the tensile loading condition, the locations of displacement sensors are illustrated in Fig. 5.11. Two displacement sensors are secured on each side of adhesive joint, to track the vertical deformation between FRP sandwich deck and steel support during the whole test process.

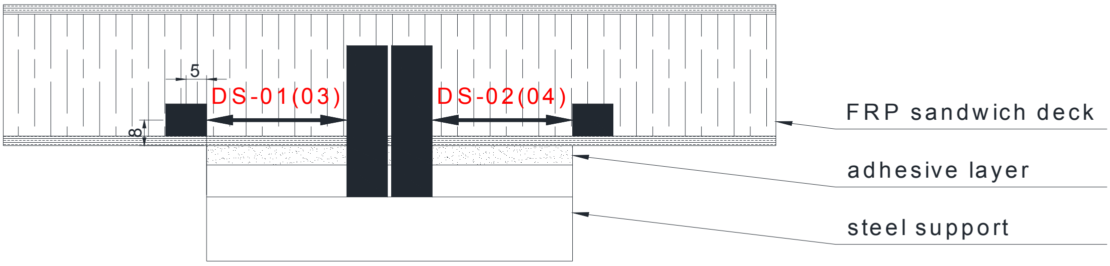

a) Schematic representation of the displacement sensor location

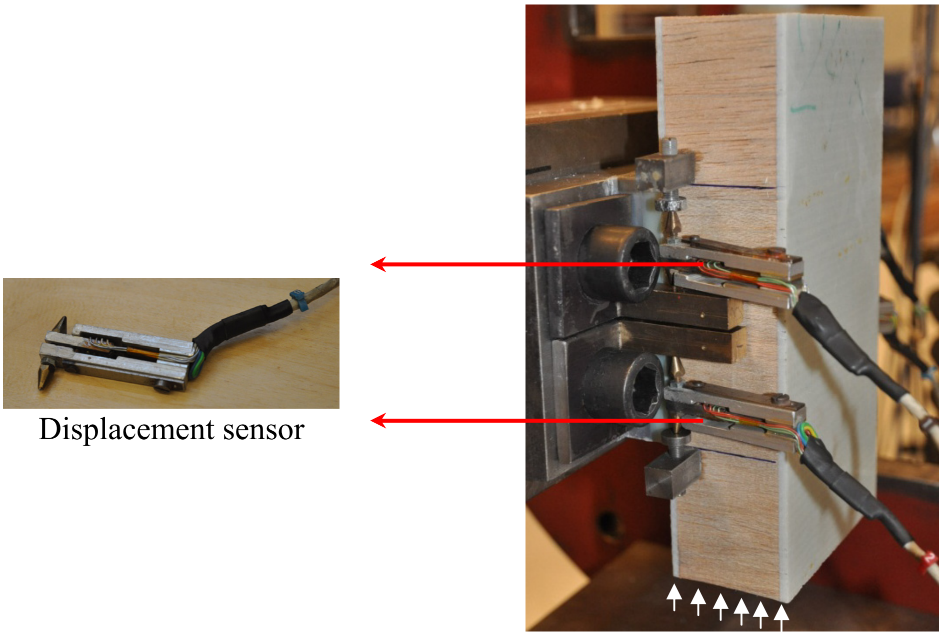

b) Lateral view of the displacement sensor location

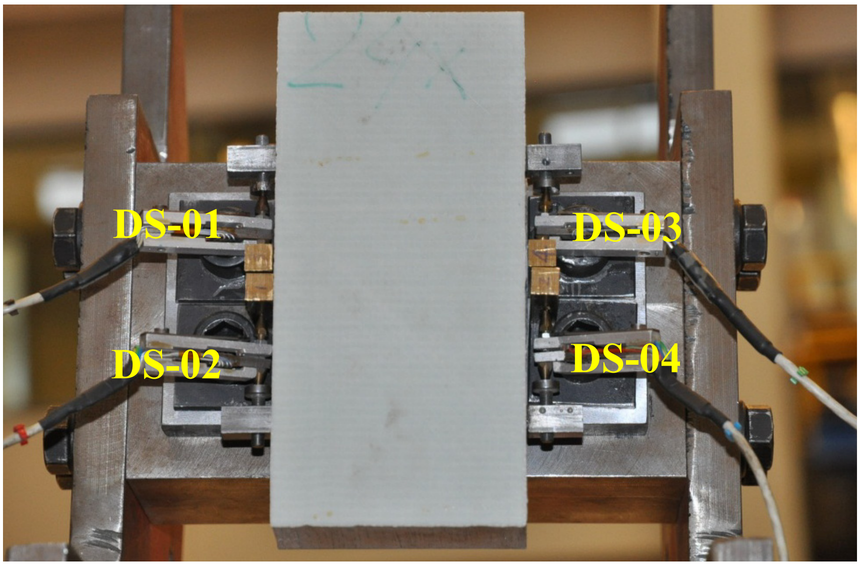

c) Front view of the displacement sensor location

Fig. 5.10. Location of four displacement sensors for the adhesive joint under the pure shear loading (DS=displacement sensor)

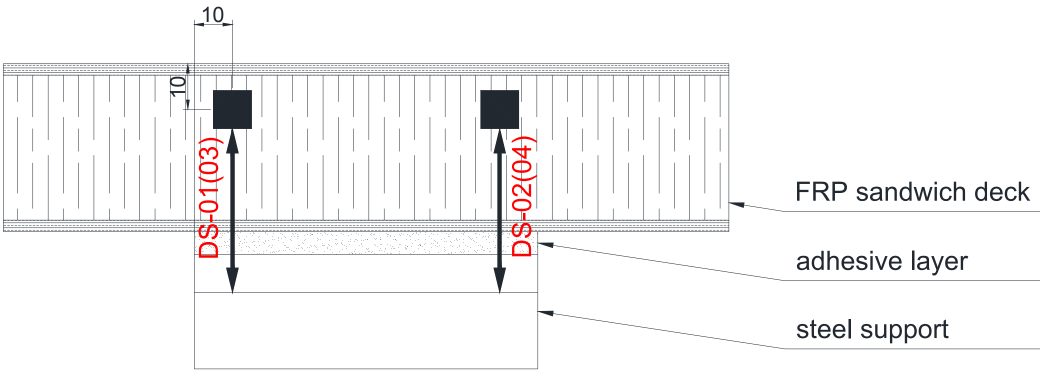

a) Schematic representation of the displacement sensor location

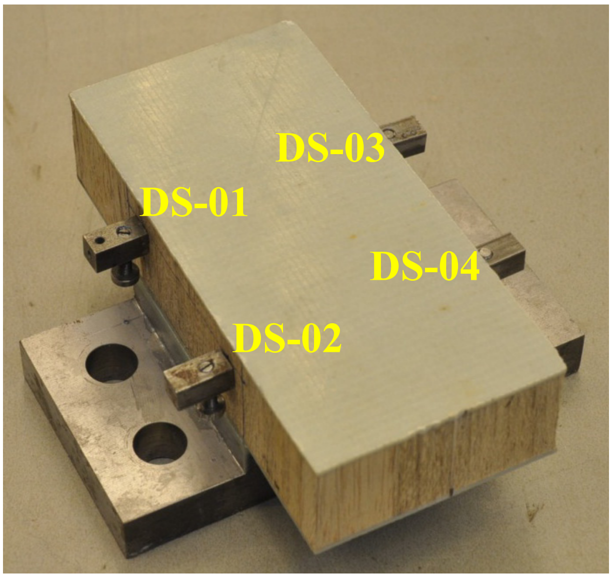

b) Top view of the displacement sensor location

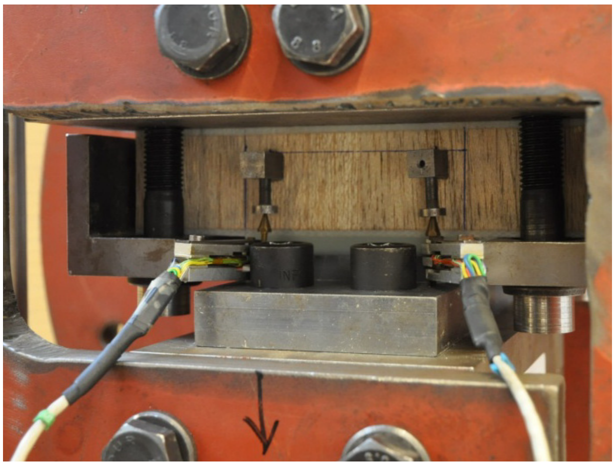

c) Lateral view of the displacement sensor location

Fig. 5.11. Location of four displacement sensors for the adhesive joint under the pure tensile loading (DS=displacement sensor)

Fig. 5.12 shows the location of displacement sensors for the combination loading condition. The ones on the left (DS-01 and 03) measure the vertical deformation between FRP sandwich deck and steel support, which indicates the tensile deformation, while the ones on the right (DS-02 and 04) measure horizontal deformation, which indicates the shear deformation.

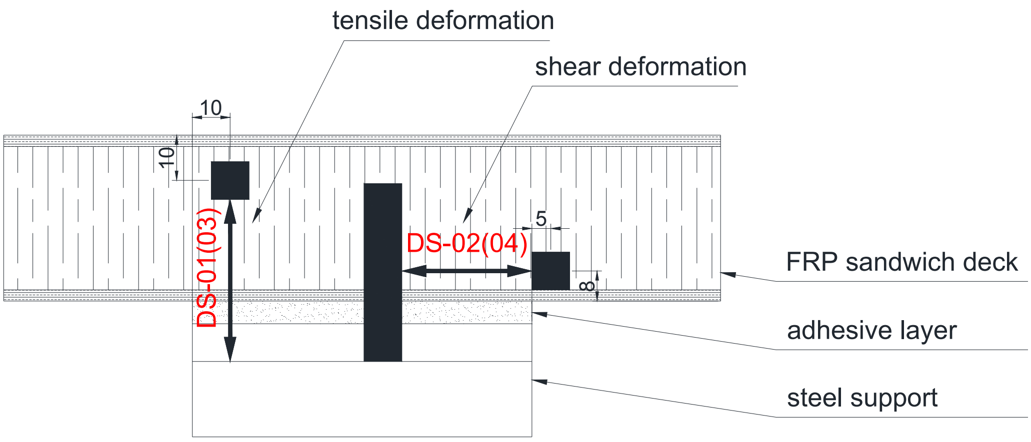

a) Schematic representation of the displacement sensor location

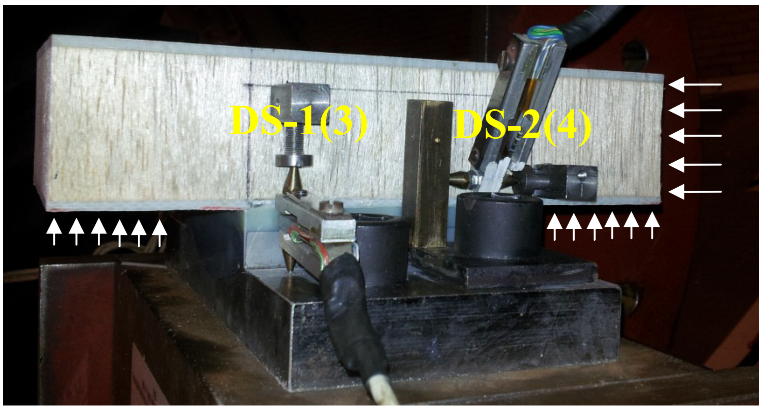

b) Lateral view of the displacement sensor location

Fig. 5.12. Location of four displacement sensors for the adhesive joint under the combination loading of shear and tension (DS=displacement sensor)

Before testing, all instrumentations (LVDTs and displacement sensors) are calibrated. Experimental data is recorded per second by a PC. In the tests, the local strain through the adhesive layer and FRP laminates is difficult to be measured by the strain gauges. Hence, the stress-strain distribution in the adhesive joint is analysed by a three-dimensional FE analysis as discussed hereafter.

5.3 Mechanical behaviour of adhesively-bonded joints before hydrothermal aging

5.3.1 Shear loading

5.3.1.1 Experimental results and discussion

For the S-AC-specimens, S-SP-specimens and S-SB-specimens, the load increase is almost linear up to failure. The ultimate failure of the adhesive joints always occurs in a brittle and sudden manner, without any visible signs or sound warning from fibre breaking. Fig. 5.13 shows the load-displacement curves of all nine specimens under the pure shear loading condition, which are the average values measured by the LVDTs. It can be found that, at the initial stage of the test process, a large deviation is observed. This is because at the beginning of the loading process, the shear load is transferred by the friction between the L-shape steel profile and the FRP deck. As the load increases, it is beyond the friction and then the adhesive joint starts to move under the constant loading until the FRP deck touches the L-shape steel profile. Subsequently, the shear load is transferred by the interacted contact-surfaces. The friction between the L-shape steel profile and the FRP deck cannot be controlled during the tests, which causes the deviations at the initial stage of loading. It is also found that, when the load is below the friction, the slope of the curve is higher than that beyond the friction. This is because the friction between the L-shape steel profile and the FRP deck makes the deformation of joint distributing uniformly. After the load beyond the friction, the shear load is transferred mainly by the vertical contact surface of L-shape steel profiles. Then, the deformation on the load directly applied side dominates the global deformation of the adhesive joint.

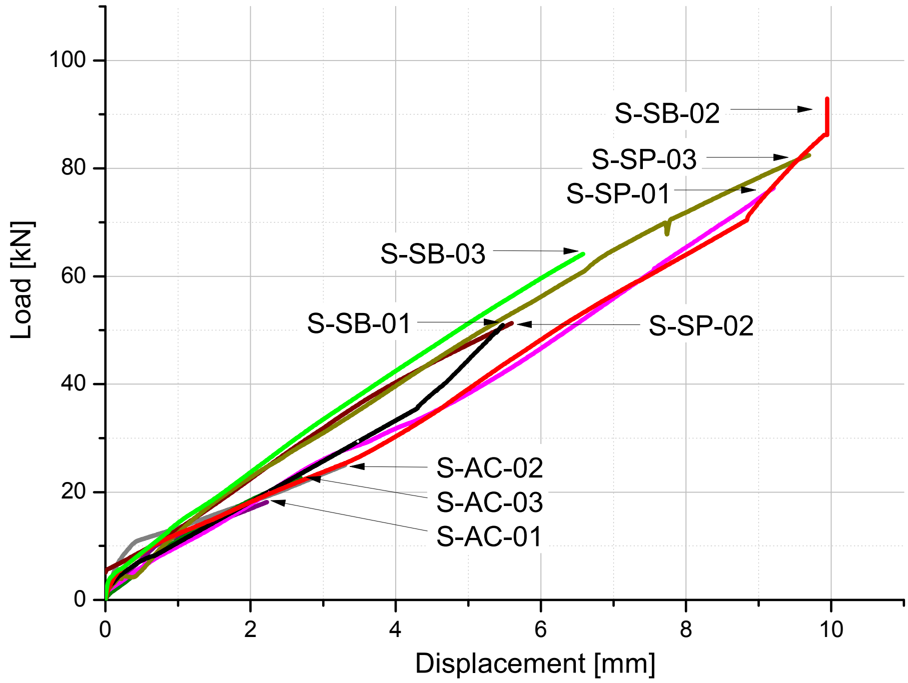

Fig. 5.13. Load-displacement curves based on average values of LVDT-01 and LVDT-02 measurements

The average shear stress-displacement curves are shown in Fig.5.14. The average shear stress is calculated by eq. (5.1) as follows:

$$\tau_{average} = \frac{F_{shear}}{A} \tag{5.1}$$

where $\tau_{average}$ is the average shear stress, F_{shear} is the shear load applied on the adhesive joint, and A is the adhesively-bonding area.

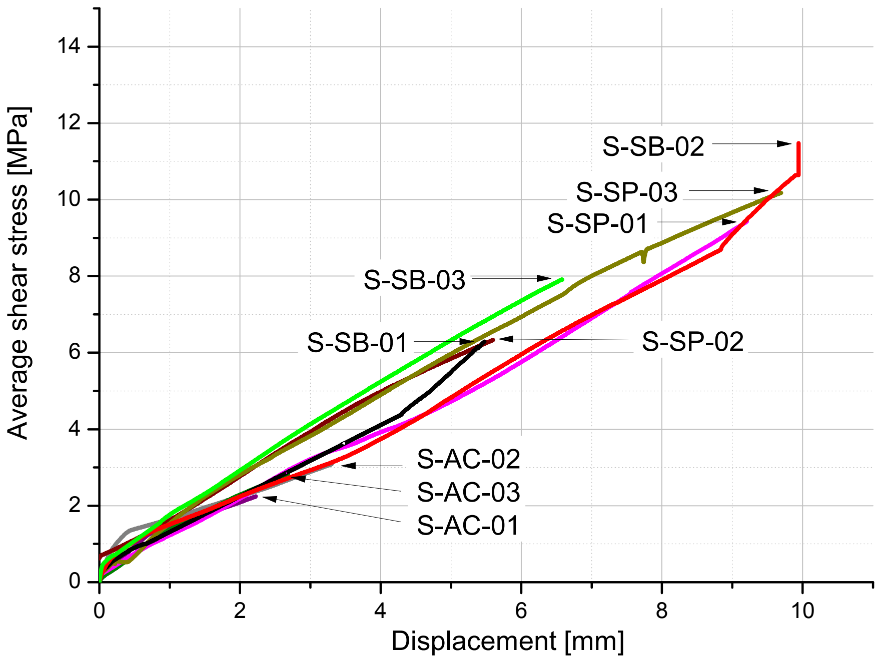

Fig. 5.14. Average shear stress-displacement curves

Fig. 5.14 shows that specimens with different surface pretreatment methods agree well with each other for the slopes of curves, which indicates that the stiffness of adhesive joints under shear loading hardly relates to surface pretreatment methods. For the ultimate failure loads, as listed in Table 5.4, the average ultimate failure loads of S-SP-specimens and S-SB-specimens obtain almost the same value of about 70 kN, which is more than three times of that of AC-specimens. The deviation of test results is established by Eq. (5.2):

$$deviation = \frac{max\begin{Bmatrix} |max\ failure\ load - average\ failure\ load| \\ |min\ failure\ load - average\ failure\ load| \end{Bmatrix}}{average\ failure\ load} \quad (5.2)$$

Here, the deviation indicates the spread of the test data. It can be found from Table 5.4, a relatively large deviation of test results is obvious, especially for the S-SP-specimens and S-SB-specimens, which is due to the artificial surface pretreatment and porosity in the adhesive layer. The bonding quality is not easily controlled. More test results are needed to gain a better statistical determination of characteristic values. According to EN 1990 “Eurocode 0: Basis of structural design”-Annex D: Design assisted by testing [11], for the test data of only three specimens, the value of K_n (characteristic fractile factor) is 3.37. This will decrease to 1.73, if the number of specimens increases to 30. The value of K_n will continue decreasing to 1.64, if the number of specimens is infinite.

Moreover, Table 5.4 also implies that there is no significant difference on load-bearing capacities of adhesive joints between the surface pretreatment methods using the sandpaper and the sand blasting technique. Both these methods achieve a similar bonding quality between adhesive layer and steel support. As compared to S-AC-specimens, the failure plane of S-SP-specimens and S-SB-specimens move from the interface between adhesive layer and steel support to the adhesive layer, which is discussed in detail hereafter.

Table 5.4. Ultimate failure loads of nine adhesive joints

S-AC-specimen	01	02	03	Average	Deviation
Failure load (kN)	18.1	25.0	22.7	21.9	17.5%
S-SP-specimen	01	02	03	Average	Deviation
Failure load (kN)	76.4	51.2	82.4	70.0	26.9%
S-SB-specimen	01	02	03	Average	Deviation
Failure load (kN)	51.0	92.9	64.1	69.3	34.0%

Figs. 5.15, 5.16 and 5.17 show the failure modes of all adhesive joints. As to the S-AC-specimens, there is no damage occurring in the adhesive layer. The failure of adhesive joints take place through the interface between the adhesive layer and the steel support, as presented in Fig. 5.18 a). This failure mechanism is due to the lack of sufficient surface pretreating on the surface of steel support, in this way losing the reliable bonding quality between adhesive layer and steel support. From the failure surface of the adhesive layer, as shown in Fig. 5.15, it can be clearly seen that the residual rust (dark-colour stuff) is torn away from the steel surface and left on the adhesive surfaces, which is not observed on the failure surfaces of S-SP-specimens and S-SB-specimens. For S-SP-specimens and S-SB-specimens, the failure modes are the same, which are cohesive fractures (near the interface between adhesive layer and steel support) in the adhesive layer, as clearly shown in Figs. 5.18 b) and c). The failure modes of S-SP-specimens and S-SB-specimens also indicate that the fracture initiates at the edge zone (about 10mm away from the end of adhesively-bonding area) of the adhesive layer, and then propagates to trigger the final failure of the whole adhesive joint. The 10mm distance is indicated in Fig.

5.16 and Fig. 5.17, where the fracture initiated lines (white-colour lines) on the adhesive layer are visible. However, the S-SP-02 specimen is an exception. There is no obvious slowly fracturing area on the surface of the steel support, where cracks gradually develop. Instead, some relatively large cracks can be found at the area close to the adhesive layer edge (Fig. 5.16, middle picture). It can be attributed to the fact that cracks are initiated by the stress concentration at the non-homogeneous area of adhesive material, which induces the premature failure of the adhesive joint. Accordingly, the S-SP-02 specimen obtains the lower load-bearing capacity (51.2kN) as compared to the other two S-SP-specimens.

S-AC-01 S-AC-02 S-AC-03

Fig. 5.15. Failure mode of S-AC-specimens

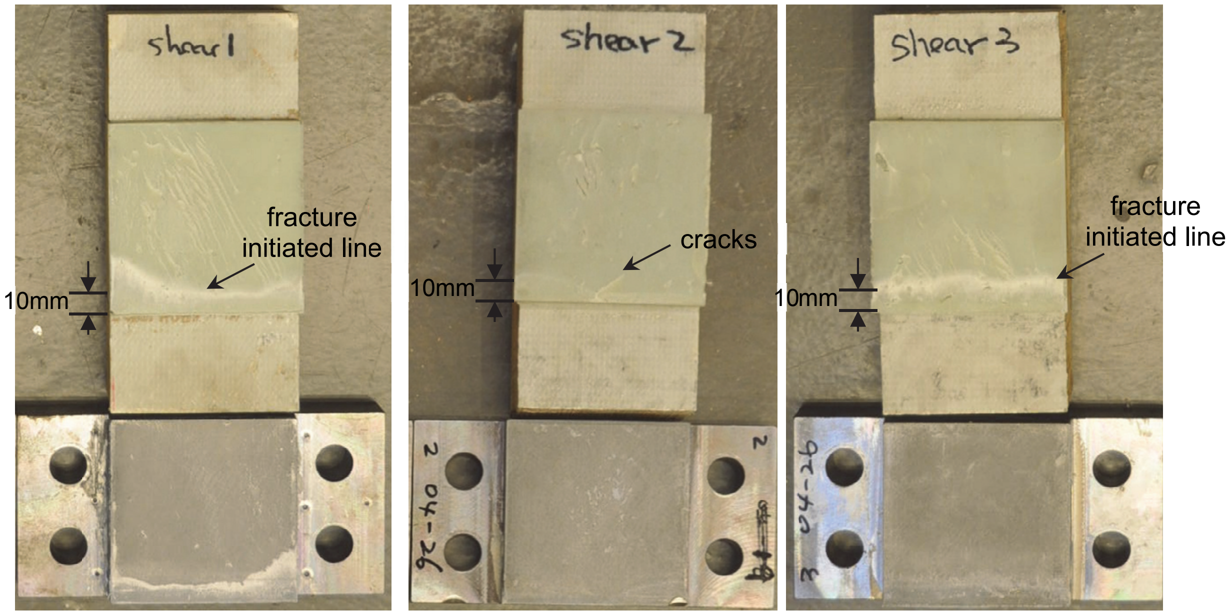

S-SP-01 S-SP-02 S-SP-03

Fig. 5.16. Failure mode of S-SP-specimens

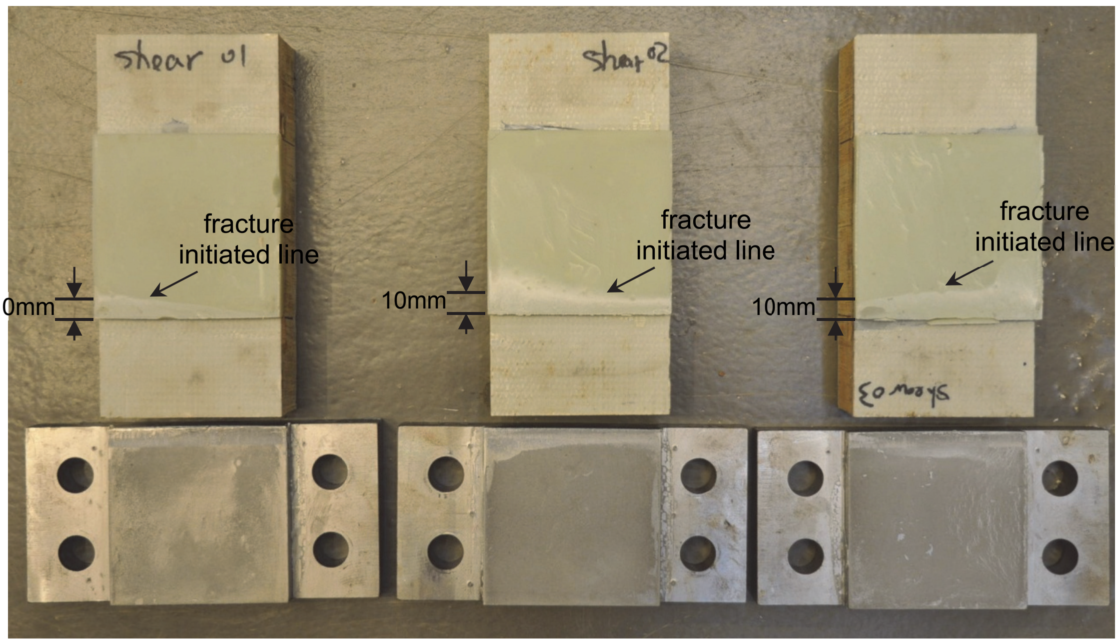

S-SB-01 S-SB-02 S-SB-03

Fig. 5.17. Failure mode of S-SB-specimens

Fig. 5.18 clearly shows the different failure modes among the S-AC-specimens, S-SP-specimens and S-SB-specimens, from views of the steel support surfaces. The adhesive joints without surface pretreatment (S-AC-specimens) fail at extremely lower values of ultimate failure loads, as mentioned before, less than one-third of S-SP-specimens and S-SB-specimens. Consequently, it is of great importance to execute the sufficient surface pretreatment on both FRP sandwich deck and steel girder in practice to ensure reliable mechanical performance of the adhesive joints between them.

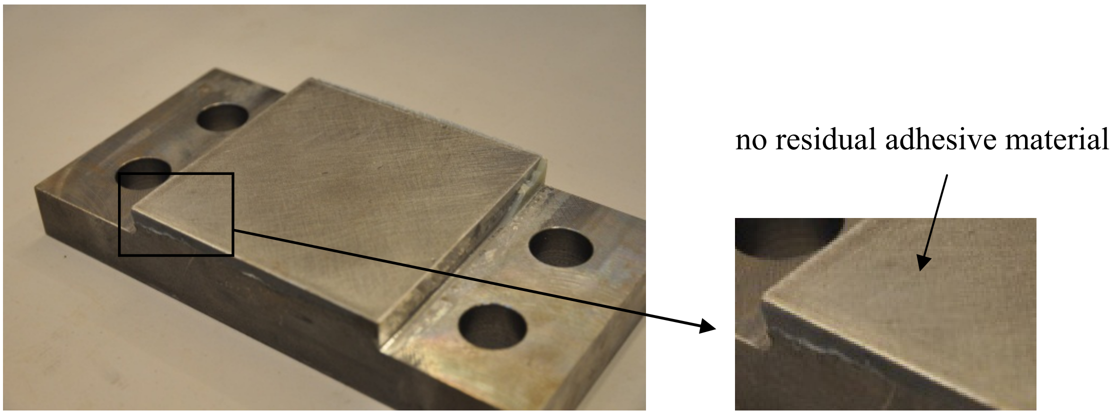

a) Failure mode “interfacial failure” of S-AC-specimen

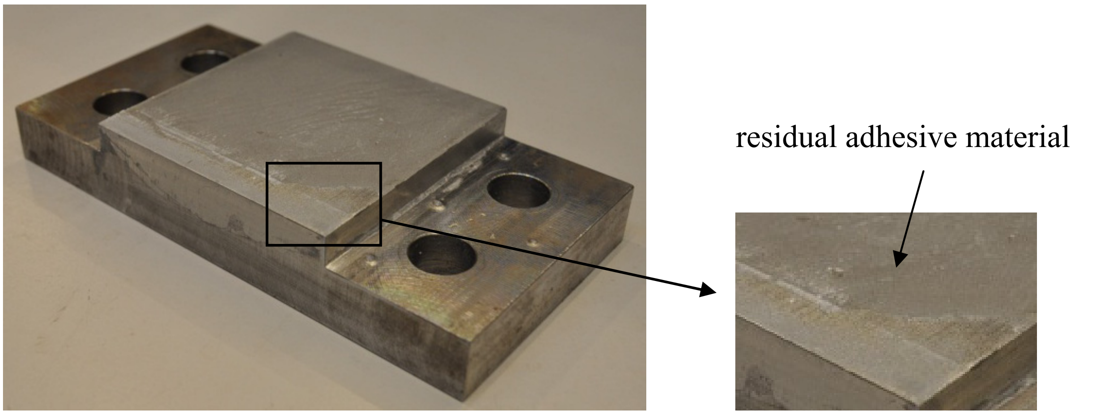

b) Failure mode “adhesive failure” of S-SP-specimen

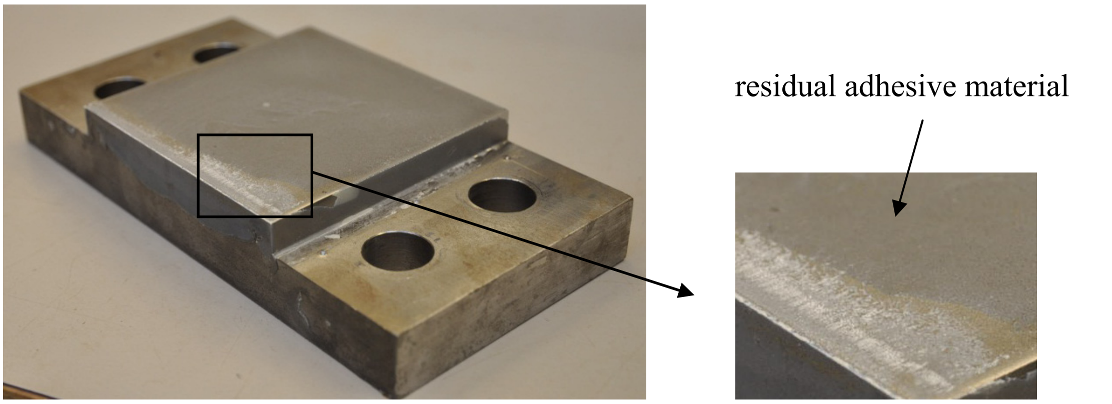

c) Failure mode “adhesive failure” of S-SB-specimen

Fig. 5.18. Different failure modes from the view of steel support surfaces

Fig. 5.19 shows the measurement of relative deformation between FRP sandwich deck and steel support on the S-SB-specimens from four displacement sensors. In this respect, reference is made to the location of displacement sensors (Fig. 5.9). The measured test data from the DS-02 and DS-04 displacement sensors are negative values, since these sensors are under compression during the tests. The test data from the DS-01 and DS-03 displacement sensors, on the other hand, are positive, since they are extending during the tests. However, the shear deformation in the adhesive layer is in the same direction. The positive/negative test data from displacement sensors are only due to their opposite locations. It can be seen that the measured deformation from DS-02 and DS-04 significantly deviate from each other, which indicates that the shear force is not loaded perfectly centrally. Besides this, the non-homogeneous characteristic of the adhesive layer can also make the load distribution non-uniformly. However, for the displacement sensors DS-01 and DS-03, the measured deformations match each other well, indicating that the load is balanced on both sides of the specimen at the far end of the adhesive joint from the loading edge. The absolute values of displacement are less than half of those from DS-02 and DS-04. Moreover, all the load-deformation curves are not increasing linearly, since the stresses in the adhesive layer keep redistributing during the whole test process, which is supposed to be due to the non-homogeneous property of the adhesive layer. Porosity of the adhesive layer is not avoidable during the preparation process of the adhesive joint. Test results on S-AC-specimens and S-SP-specimens present similar mechanical behaviours regarding the relative deformation between the FRP sandwich deck and the steel support. The eccentric loading cannot be avoided in such a small scale test. Even the load is compelled to be exactly centric; afterwards, it will be eccentric as the load is increasing. This is because the stress in the adhesive joint keeps redistributing during the whole loading process.

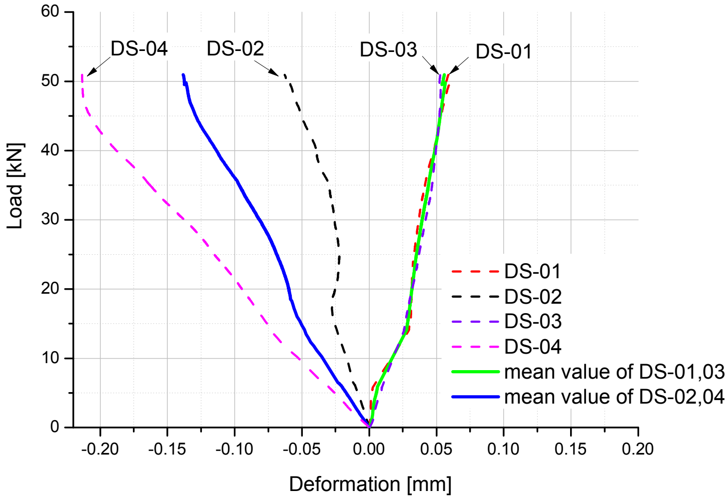

a) S-SB-01

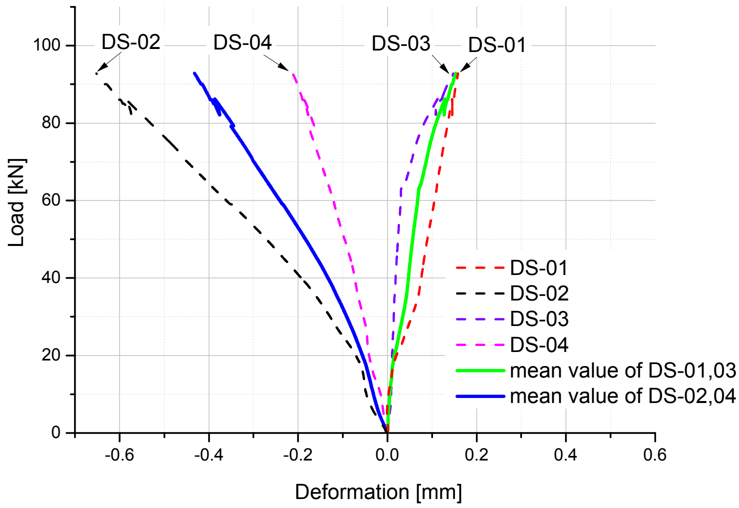

b) S-SB-02

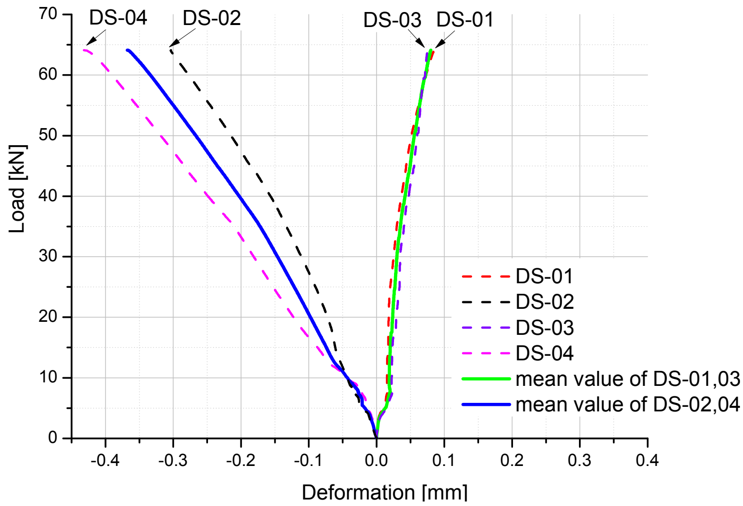

c) S-SB-03

Fig. 5.19. Load-deformation curves measured from four displacement sensors on the S-SB-specimens (DS=displacement sensor)

5.3.1.2 FE analysis

1) FE model

As mentioned before, the experimental investigations usually present limitations to obtaining the stress-strain distribution throughout the adhesive joint. While the FE analysis of adhesive joints can provide more information about the stress-strain state. Compared with the two-dimensional (2D) plane strain analysis, three-dimensional analysis results can reveal the existence of a complex multi-axial stress/strain state at the ends of the overlap in the bondline. Thus, the 3D FE model of the adhesive joint loaded under shear loading is developed by employing the FE package ABAQUS 6.8, as shown in Fig. 5.20 and Fig. 5.21.

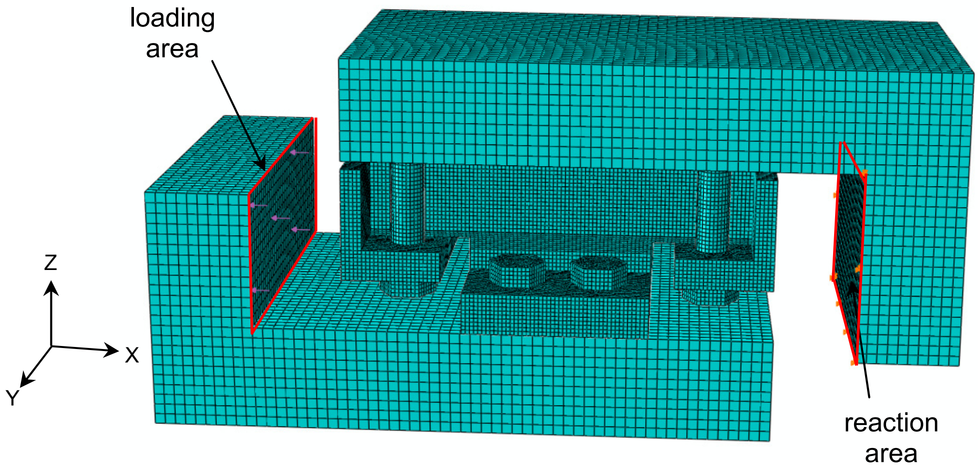

Fig. 5.20. Loading and boundary condition of FE model

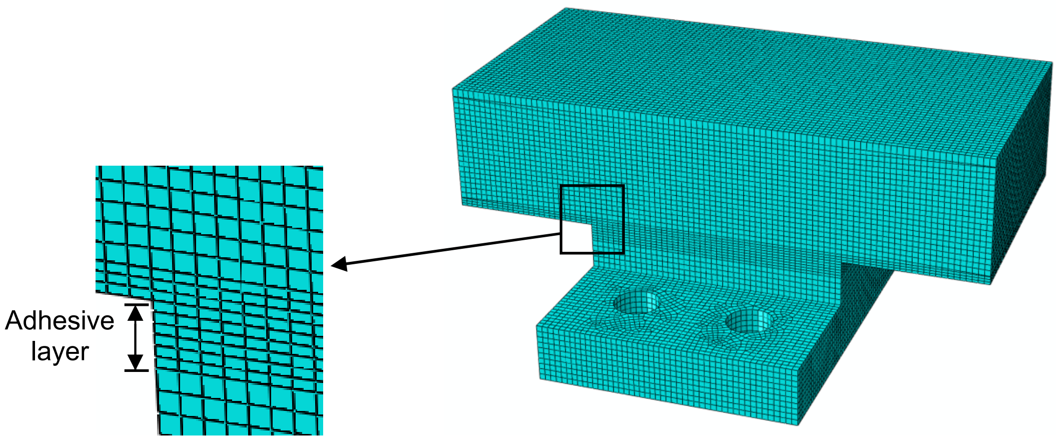

Fig. 5.21. FE model of adhesive joint

As shown in Fig. 5.20, to simplify the FE model and save computational time, only the L-shape steel parts and bolts for fastening the adhesive joint are included in the FE model. Other accessorial load transferring devices are equivalently replaced by two “big-size” stiff blocks. Eight-node linear brick elements with reduced integration and hourglass control (C3D8R) are employed for all the components. The total number of elements is 284593. With regard to the adhesive layer, a six-layer discretization is used in the through-thickness direction to guarantee accurate stresses and flexible deforming capacity, as well as a three-layer discretization for the FRP laminates close to the adhesive layer, as shown in Fig. 5.21. There is no specific element defined at the interphase between the FRP sandwich deck and the adhesive layer, or between the adhesive layer and the steel support. All these surfaces are fixed to each other, assuming that no cracks or relative slip occur during the loading procedure. As shown in Fig. 5.20, dimensions of the loading area and the reaction area (three-direction fully restricted as a boundary condition) are intentionally designed, with the center of these two areas exactly in the middle plane of the adhesive layer to avoid an additional bending moment. The total loading of 50kN is applied by the surface tractions on the loading area. The contact pairs are created between the L-shape steel part and the sandwich FRP deck. Eight bolts are fixed to the top and bottom stiff blocks by TIE command. The material properties of FRP laminates and core material are anisotropic, while adhesive and steel are assumed to be isotropic. The input material properties supplied by manufacturers are listed in Table 5.5. The value of E_{11}, E_{22}, G_{13} and G_{23} is from the test results of Chapter 4.

Table 5.5. Mechanical properties of materials for FE model

Property	FRP laminates
Elastic Modulus 11 (MPa)	16609
Elastic Modulus 22 (MPa)	16609
Elastic Modulus 33 (MPa)	11000
Poisson Ratio 12	0.33
Poisson Ratio 23	0.3
Poisson Ratio 13	0.18
Shear Modulus 12 (MPa)	6986
Shear Modulus 23 (MPa)	1200
Shear Modulus 31 (MPa)	1200
	adhesive
Elastic Modulus (MPa)	3400
Poisson Ratio	0.37
	core material
Elastic Modulus (MPa)	5759
Poisson Ratio	0.35
Shear Modulus (MPa)	309
	steel
Elastic Modulus (MPa)	206000
Poisson Ratio	0.3

The whole analysis process is linear elastic. No geometric non-linearity or elastic-plastic material properties are included in FE analysis. Thus, the FE results can be amplified by specific factors to be comparable with the experimental results. The automatic incrementation scheme is active to make the analysis easily convergent as well as optimize the increment sizes based on computational efficiency [12].

2) Validation of FE model

To validate the FE model, the FE results of relative deformation between FRP sandwich and steel support at the locations of experimental displacement sensors are presented in Fig. 5.22 for comparison with test results. The FE results are amplified to make the comparison much clearer. The FE results from two symmetric locations of DS-01 and DS-03 are almost the same (the same case goes for the locations of DS-02, DS-04), since the FE model is perfectly symmetric, centrally loaded and there is no experimental installation inaccuracy. When the FE result is compared with the mean value of experimental results from DS-01, 03 and DS-02, 04, good agreements are achieved. The experimental curves are not ideally linear, which is attributed to the stress redistribution occurring during the tests. But the experimental curve still revolves around the linear FE curve. Based on the above comparison between FE modeling and experimental results, it can be confirmed that the FE model is reasonably accurate for predicting the mechanical behaviours of the adhesive joint under shear loading. Hence, further analysis and discussion depending on this FE model are reliable.

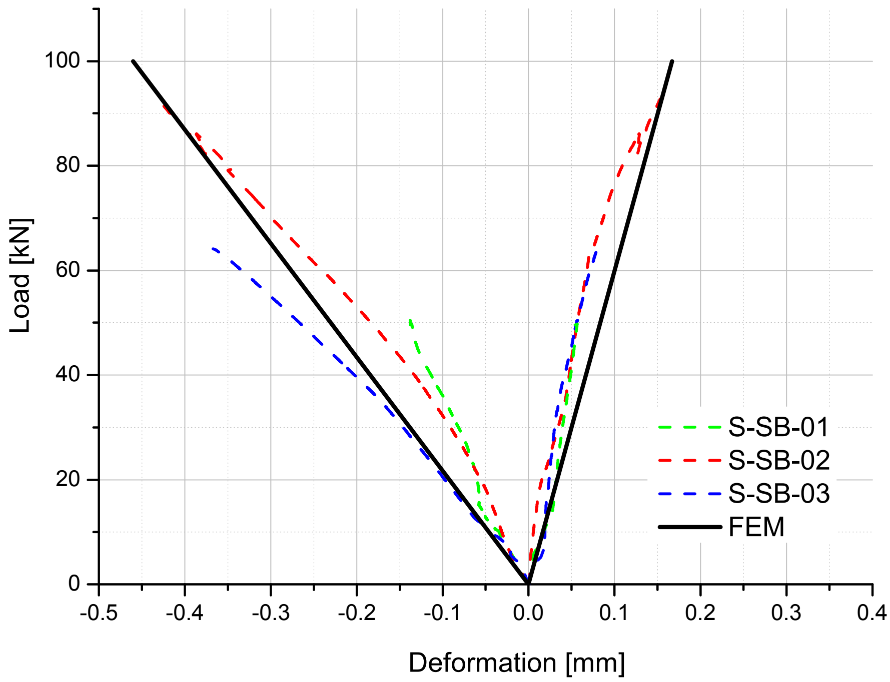

Fig. 5.22 Comparison with experimental results and FE analysis at the locations of displacement sensors

3) FEA results and discussion

Based on the failure mode of specimens, it is of interest to further investigate the stress distribution across the interface between the steel support and the adhesive layer, which is supposed to be the weakest plane of the adhesive joint. Contour maps of shear stress and tensile stress are drawn through this plane, as shown in Fig. 5.23 and Fig. 5.24. The X-axis is along the longitudinal direction of the FRP sandwich deck, as indicated in Fig. 5.20, while the Y-axis is in the transverse direction. These two specific contour maps are drawn by employing the MATLAB software (R2011b version), using the FE results from ABAQUS 6.8.

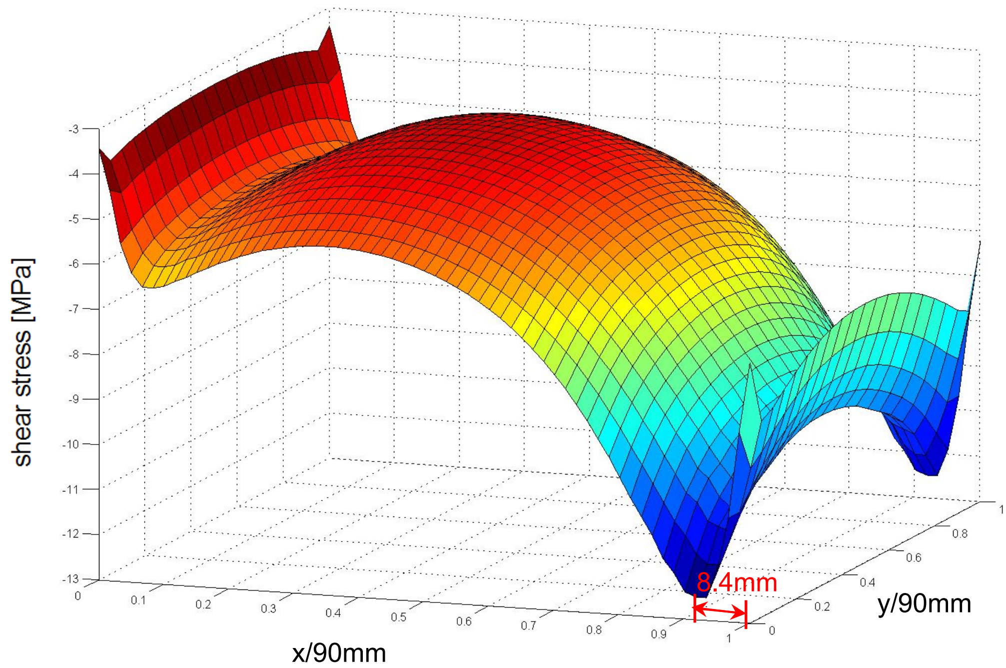

Fig. 5.23. Contour map of shear stress on the interface between steel support and adhesive layer of the adhesive joint under the shear load of 50kN

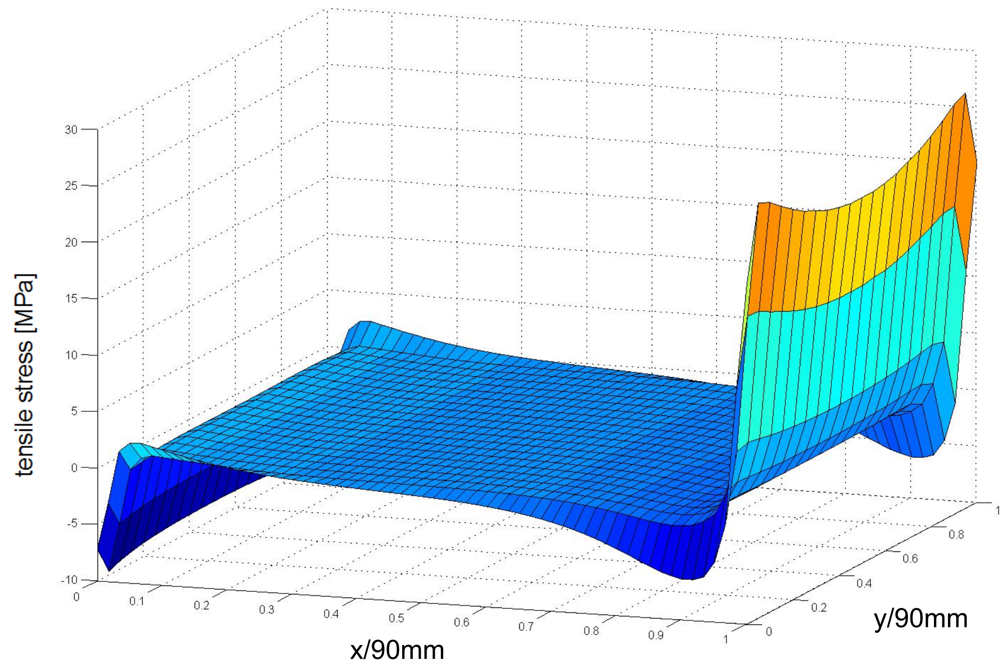

Fig. 5.24. Contour map of tensile stress on the interface between steel support and adhesive layer of the adhesive joint under the shear load of 50kN

For the shear stress distribution along the longitudinal direction, there are two stress peaks throughout the interface, with the one on the right side (loaded side) considerably higher (absolute value) than the left side. The locations of stress peaks are not exactly at the ends of the adhesive overlap, but 8.4mm away from the ends, which is approximately the same place of adhesive fracture initiated lines for S-SP-specimens and S-SB-specimens, as shown in Fig. 5.16 and Fig. 5.17. In the transverse direction, the shear stress is distributed in a saddle shape, with a less steeper gradient. The stress peaks occur at the transverse edges. For the tensile stress distribution in the X direction, it is more stable with the values around zero, except that at the edge zone of the interface the stress increases steeply, which results in very high tensile stress at the end of the adhesive overlap. With regard to the transverse direction, stress distributes at a rather steady gradient. The maximum absolute values of stress are not located exactly at the ends of interface, but a small distance away from the corners.

Further investigation is conducted on mesh-dependency of this FE model. The part concerned is the adhesive layer in both longitudinal direction and transverse direction, as shown in Fig. 5.25. Herein, four mesh configurations are selected with mesh scales (length and width of elements) of 2.00mm, 1.50mm and 1.25mm and 1.00mm.

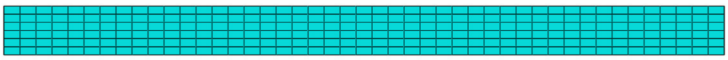

a) Mesh scale = 2.00mm

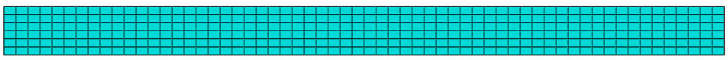

b) Mesh scale =1.50mm

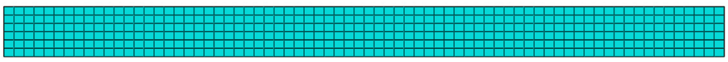

c) Mesh scale = 1.25mm

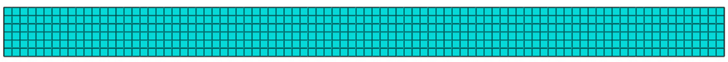

d) Mesh scale = 1.00mm

Fig. 5.25. Different mesh configurations at the adhesive layer

The shear and tensile stress distributions are extracted for a comparison from a longitudinal path, as shown in Fig. 5.26. The location of the longitudinal path is through the interface between the adhesive layer and the steel support.

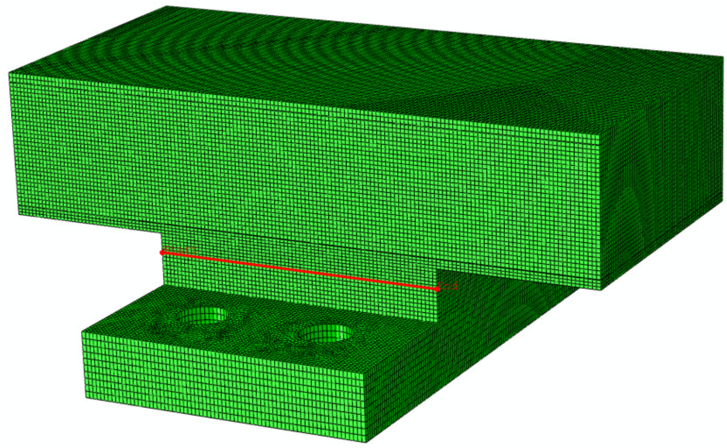

Fig. 5.26. Longitudinal path for analysing the stress distribution

For the shear stress distribution (Fig. 5.27), a large deviation is evident between the FE results of 2.00mm mesh scale and the other three mesh-refined FE models. For the FE model with the 2.00mm scale mesh, the elements defined along the longitudinal path are not enough, which tend to constrain the deformation in the adhesive layer, in this way making the adhesive layer much stiffer. Thus, the elements in the adhesive layer cannot deform appropriately to release the stress concentration on the left side of the adhesive layer. Due to the “additional” load-carrying capacity of the left side of the adhesive layer, the absolute value of stress peak on the right side (directly forced side) is relatively lower than expected. On the contrary, the other three FE models with 1.50mm, 1.25mm and 1.00mm mesh scales have sufficient deformation ability in the adhesive layer. The stress peak on the right side (directly forced side) is significantly higher than that of the left side, and these three curves overlap each other along the whole longitudinal path, except the end nodes, where the mesh refined FE models tend to slightly decrease the absolute stress values. It does not influence the shear stress peak value. The peak value of shear stress is 12.52 MPa (under the total loading of 50kN).

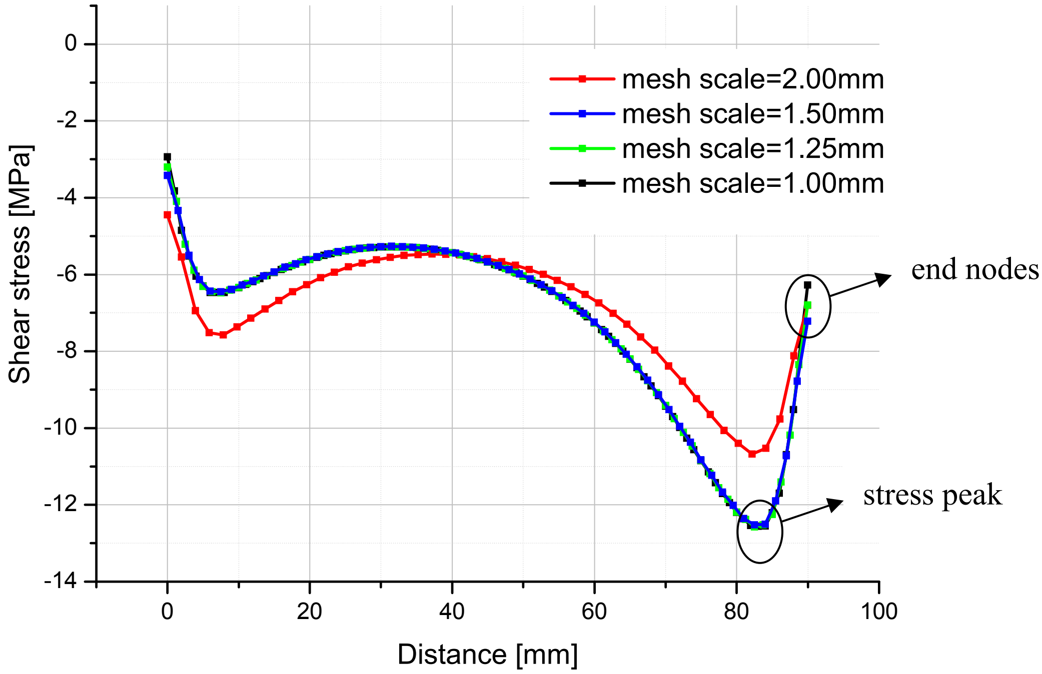

Fig. 5.27. Shear stress distribution along the longitudinal path depending on mesh scale

For the tensile stress distribution along the longitudinal path (Fig. 5.28), deviation between FE results of 2.00mm mesh scale and the other three mesh-refined FE models occurs again. Due to limitation of deformation ability in the adhesive layer, the FE curve of 2.00mm mesh scale develops a lower absolute value of compressive stress on the right side (directly forced side) of adhesive layer. Nodes at the right end of the longitudinal path (as shown in Fig. 5.28), lead to different tensile values. The tensile stress of 1.50mm, 1.25mm and 1.00mm scale mesh FE models is 20.07MPa, 21.37MPa and 22.88MPa respectively. This mesh dependent stress singularity at the end of adhesively bonding overlap was also found by the researches [13, 14]. The smaller mesh scale used, the higher tensile stress was obtained, until FE analysis cannot converge at the location of end nodes.

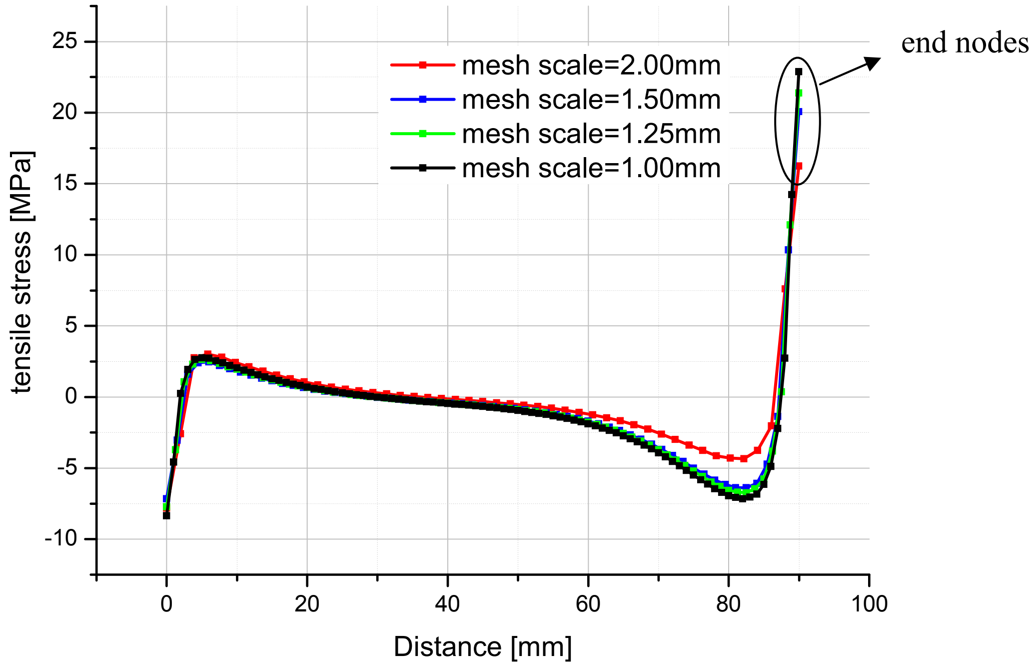

Fig. 5.28. Tensile stress distribution along the longitudinal path

Further investigation on mesh dependency of FE model through the thickness of the adhesive layer is carried out. Eight-layer discretization is defined in the adhesive layer to be compared with the six-layer discretization, as illustrated in Fig. 5.29.

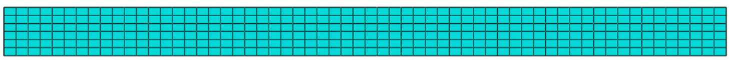

a) six-layer discretization

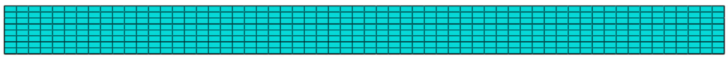

b) eight-layer discretization

Fig. 5.29. Mesh configuration through the thickness of adhesive layer

Comparison of the stress distribution between six-layer discretization mesh and eight-layer discretization mesh is presented in Fig. 5.30 and Fig. 5.31. Two curves are in conformity with each other, which mean the refined mesh configuration (eight-layer discretization) through the thickness of the adhesive layer does not make any difference in the stress distribution along the concerned longitudinal path. Thus, the six-layer discretization mesh is enough to obtain reasonably accurate FE results.

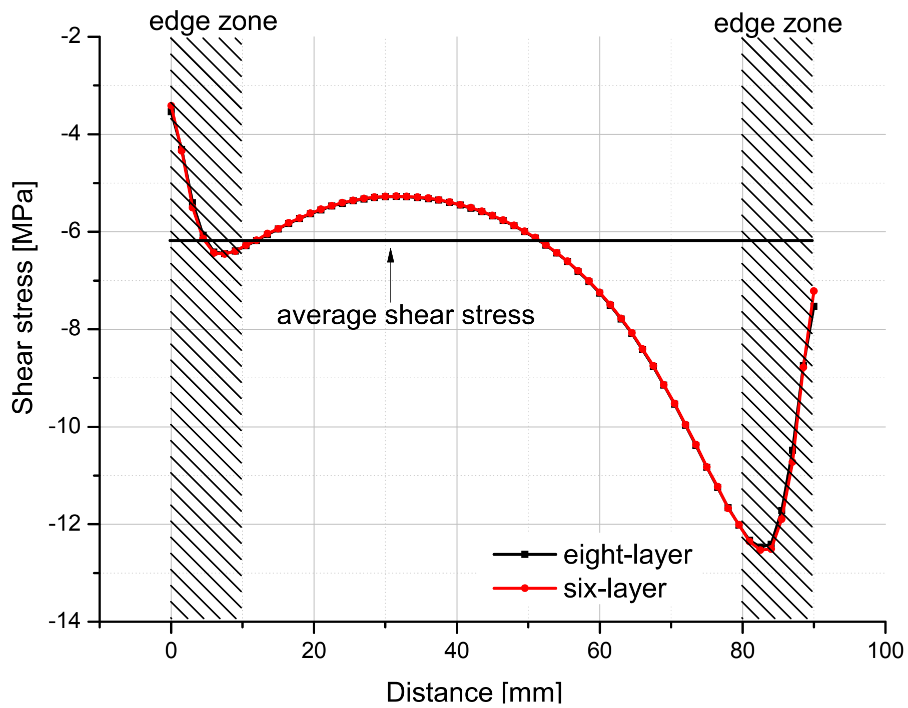

Fig. 5.30. Shear stress distribution along the longitudinal path depending on the different through-thickness meshes

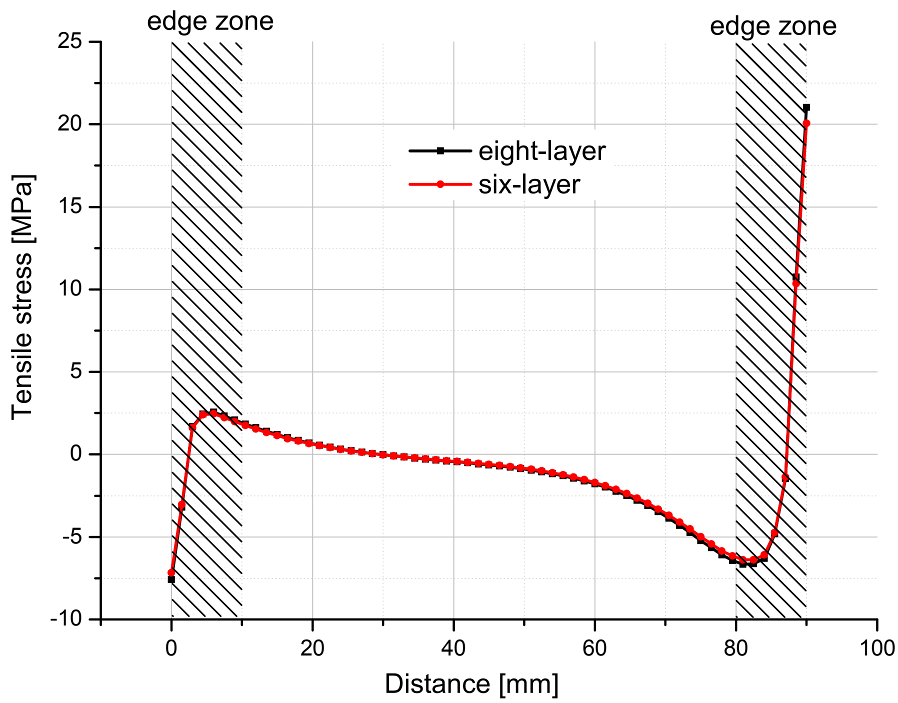

Fig. 5.31. Tensile stress distribution along the longitudinal path depending on the different through-thickness meshes

As shown in Fig. 5.30 and Fig. 5.31, the shear stress and tensile stress distribute relatively stable in the middle part of the bondline, but dramatically bend over at the edge zone (approximately 10mm from the ends of adhesive layer). The shear stress peak is approximately twice the average shear stress (calculated by Eq. 5.1). It implies that the failure of the adhesive joint is triggered by the stress concentration at the edge zone of the directly forced part (right side in Fig. 5.30 and Fig. 5.31). It can be found that, even under the proposed “pure shear” loading condition, the failure of an adhesive joint is attributed to a combination of shear stress and tensile stress. Furthermore, the singularity of tensile stress is relatively larger than the peak of shear stress and they are located at different places of the edge zone. The FE results also indicate that the bonding quality at the edge zone of adhesive layer calls for more attention to avoid premature failure of the adhesive joint under shear condition.

5.3.2 Tensile loading

5.3.2.1 Experimental results and discussion

The ultimate failure loads of nine adhesive joints are given in Table 5.6. It can be found that the average failure load of T-SP-specimens is close to that of T-SB-specimens, with a value of about 17.5kN. For T-AC-specimens, the failure load is slightly lower at 16.05kN, which means the additional surface pretreatments (using sandpaper or sand blasting) cannot significantly increase the load-bearing capacity of an adhesive joint under tensile loading (only 9% higher). However, as stated in Section 5.3.1 under shear loading condition, both sandpaper and sand blasting surface pretreatments increase the failure load of adhesive joints more than twice under shear loading condition. With regard to deviations of test results (calculated by Eq. 5.2), T-SP-specimens show the largest deviation of all. It is due to that, the surface pretreatment quality of sandpaper method is difficult to be controlled. The roughness of surfaces after pretreating is not uniform throughout the whole section. It definitely influences the bonding quality between adhesive and adherent, and accordingly deviates the ultimate failure load and even failure modes (this is discussed in more detail hereafter). Failure modes of nine adhesive specimens are shown in Fig. 5.32. For all the T-AC-specimens, the loads increase almost linearly up to failure. The ultimate failure of three specimens always occurs in a brittle and sudden manner, through the bondline between FRP laminates and adhesive layer, without any visible signs or sound warning from fibre breaking, as shown in Fig. 5.32 a). For T-SP-specimens and T-SB-specimens, there is always some sound warning from fibre breaking when the applied load approaches the ultimate failure load. Failure modes of these are a combination of fibre breaking and interfacial failure between adhesive layer and FRP laminations. The typical failure mode is shown in Fig. 5.33. Also, FRP delamination failure is observed on the T-SP-01 (Fig. 5.34), which achieves the highest failure load (19.37kN) of adhesive joints. This indicates that the failure threshold of FRP delamination is a little higher than that of interfacial failure between adhesive layer and FRP laminates. Furthermore, from Fig. 5.32 it can be found that the areas of fibre breaking or FRP delaminating parts are different among T-SP-specimens and T-SB-specimens. The T-SP-01 specimen attains the largest FRP delaminated area which almost covered the whole bonding area. Therefore, it achieves the highest load-bearing capacity of adhesive joints. Thus, it can be found that the area of fibre breaking and FRP delamination is the direct factor influencing the final strength of an adhesive joint under tensile loading.

Table 5.6. Ultimate failure loads of nine adhesive joints under tensile loading

T-AC-specimen	01	02	03	Average	Deviation
Failure load (kN)	15.69	16.43	16.04	16.05	2.37%
T-SP-specimen	01	02	03	Average	Deviation
Failure load (kN)	19.37	17.93	15.57	17.62	11.63%
T-SB-specimen	01	02	03	Average	Deviation
Failure load (kN)	17.53	16.05	18.72	17.43	7.94%

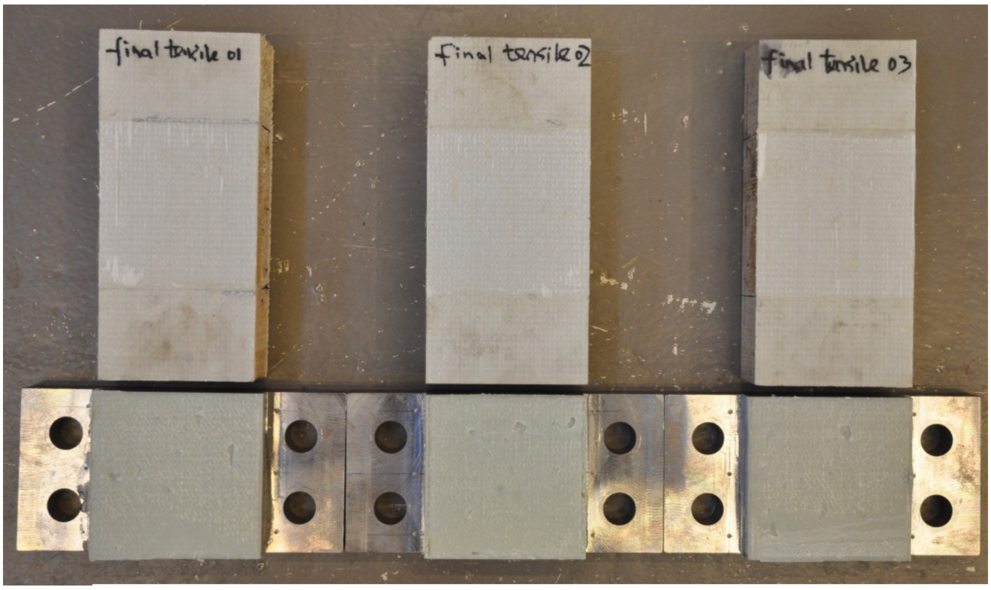

T-AC-01 T-AC-02 T-AC-03

Fig. 5.32. a) Failure mode of T-AC-specimens

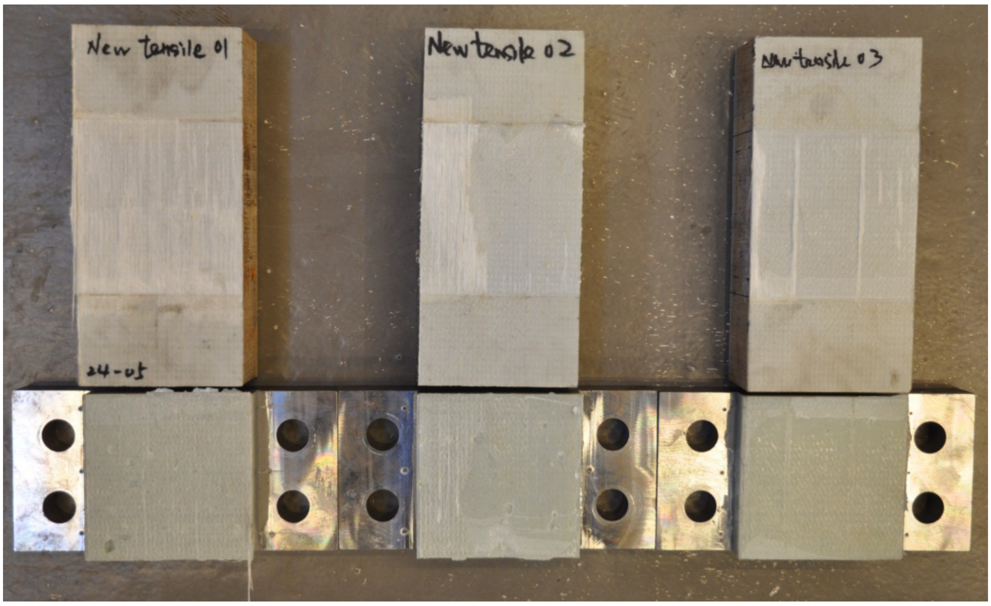

T-SP-01 T-SP-02 T-SP-03

b) Failure mode of T-SP-specimens

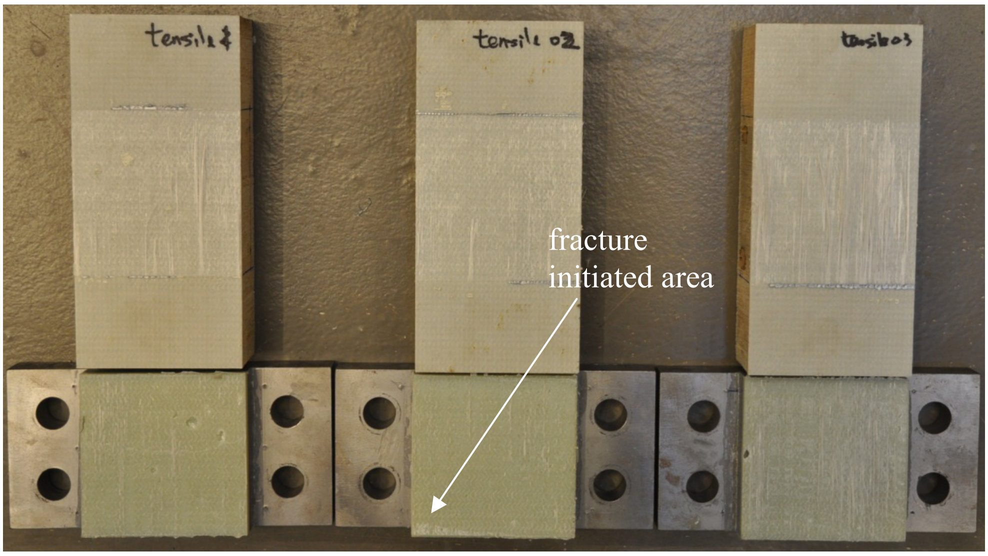

T-SB-01 T-SB-02 T-SB-03

c) Failure mode of T-SB-specimens

Fig. 5.32. Failure modes of adhesive joints

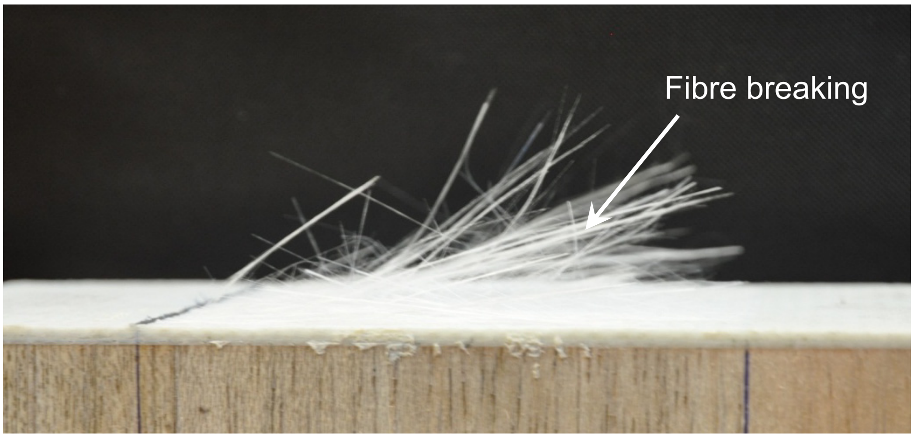

Fig. 5.33. Combination of fibre breaking and interfacial failure between adhesive layer and FRP laminates (T-SB-03)

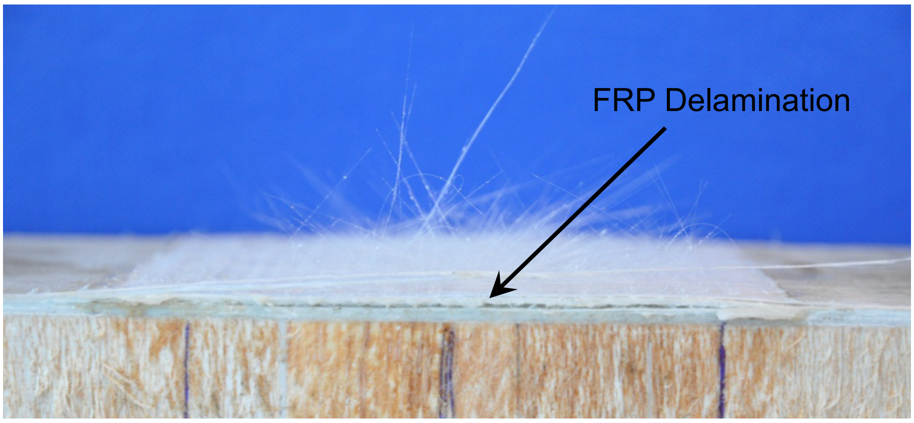

Fig. 5.34. Delamination failure in FRP laminates (T-SP-01)

Fig. 5.35 shows the load-displacement curves of nine adhesive joint specimens under tensile loading, which are measured by the LVDTs. Fig. 5.36 shows the average tensile stress-displacement curves of these specimens. The average tensile stress is calculated by Eq. 5.3. It is obvious that curves are almost parallel to each other in the stable load increasing stage. However, for the initial part slopes of nine curves are different. It can be explained that at the beginning of loading, the friction between each component of loading device makes the initial stiffness of specimens different from each other. However, when the loading is large enough beyond the friction, the deformation measured by LVDTs is dominated by the adhesive joint specimen and the stiffness of adhesive joints is approximately the same. For the T-SP-specimens and T-SB-specimens, there is a certain extent of residual load-bearing capacity achieved after reaching the maximum loading, especially for the T-SP-01 and T-SB-03. It is contributed by the mechanism of fibre breaking and FRP delamination, of which the failure process is not brittle but gradual until fibres from the whole bonding area disconnect from the fracture interface. As already proven for the adhesive joints under the shear loading condition (section 5.3.1), the surface pretreatments cannot significantly influence the stiffness of the adhesive joint, whereas they change the failure modes and subsequently increase the load-bearing capacity.

$$\sigma_{average} = \frac{F_{tension}}{A} \tag{5.3}$$

where $\sigma_{average}$ is the average tensile stress. $F_{tension}$ is the tensile load applied to the adhesive joint.

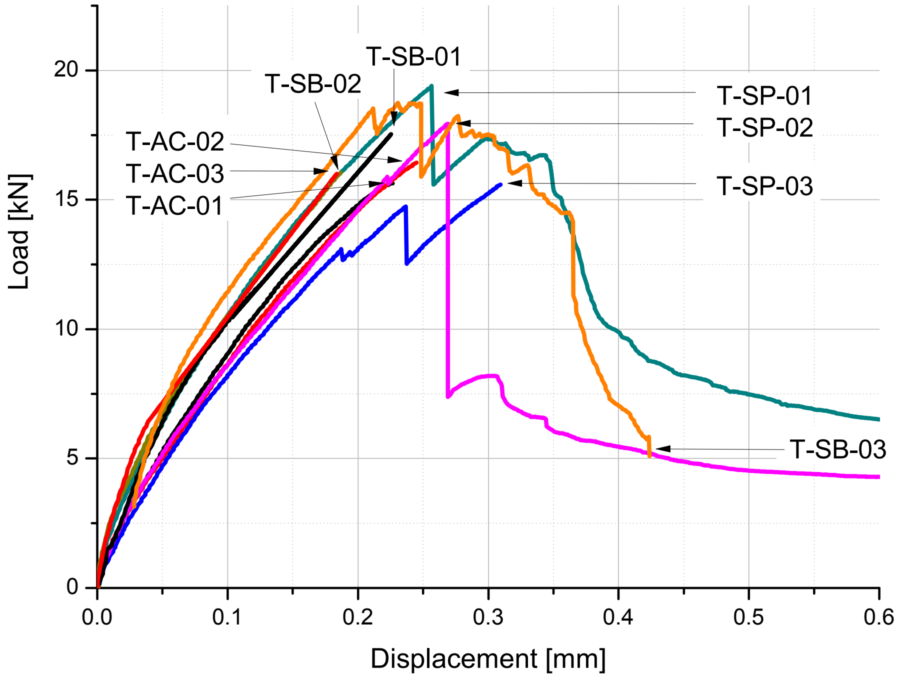

Fig. 5.35. Load-displacement curves measured from LVDTs

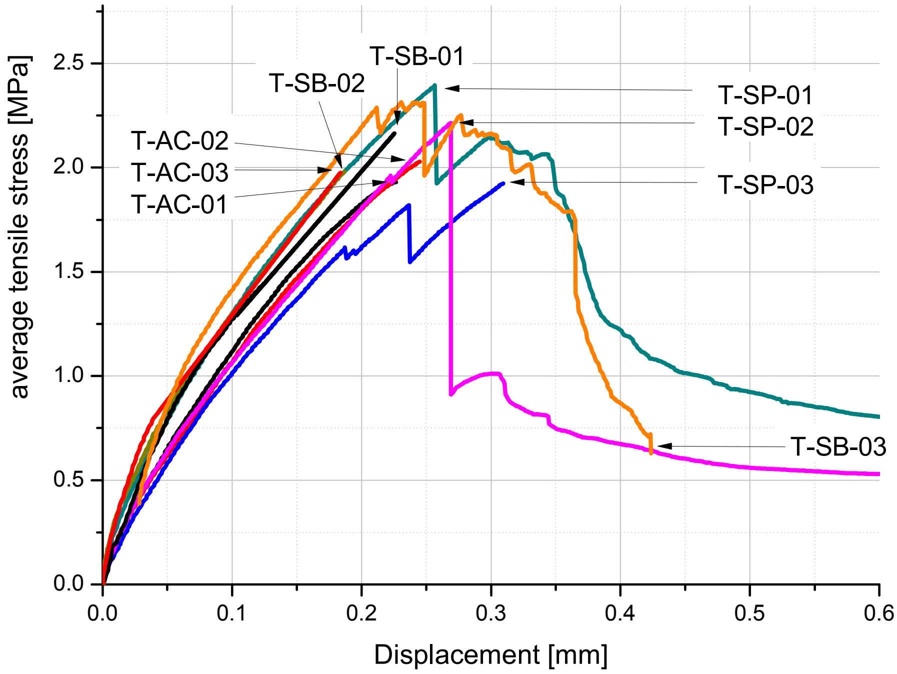

Fig. 5.36. Average tensile stress-displacement curves

Fig. 5.37 shows the measurement of vertical deformation between FRP sandwich deck and steel support on the T-SB-specimens from four displacement sensors. It can be clearly seen that the measured data from displacement sensors DS-01, DS-02, DS-03 and DS-04 are different from each other, which implies that the loads are not centrally applied. The relative deformation between FRP sandwich deck and steel support measured by displacement sensors is rather small, on the order of magnitude of 0.01mm. With this loading device, the unexpected eccentric loading cannot be avoided. Even the load is compelled to be exactly centric on the adhesive joint (as illustrated at the initial stage of the curve of Fig. 5.37 (c)). Afterwards it will be eccentric as the load increased. Fig. 5.37 also indicates, besides the pure tensile loading, a certain amount of additional bending moment is also applied during the whole testing process in both longitudinal and transverse directions of the adhesive joints. Test results on other specimens present similar mechanical behaviours regarding the vertical deformation of adhesive joints. Furthermore, the vertical deformation between FRP sandwich deck and steel support is not increasing linearly during the whole test. It indicates that the stress redistribution occurs through the adhesive joint when the applied load is approaching the failure load. As shown in Fig. 5.32c), it can be found that on the fracture surface of adhesive layer there are some fracture initiated areas at the edge zone, which reconfirms that the stress redistribution takes place due to the partially fractured area of the adhesive layer. Until the remaining part of the adhesively-bonded area cannot carry the total loading anymore, the adhesive joint fails in a brittle mode.

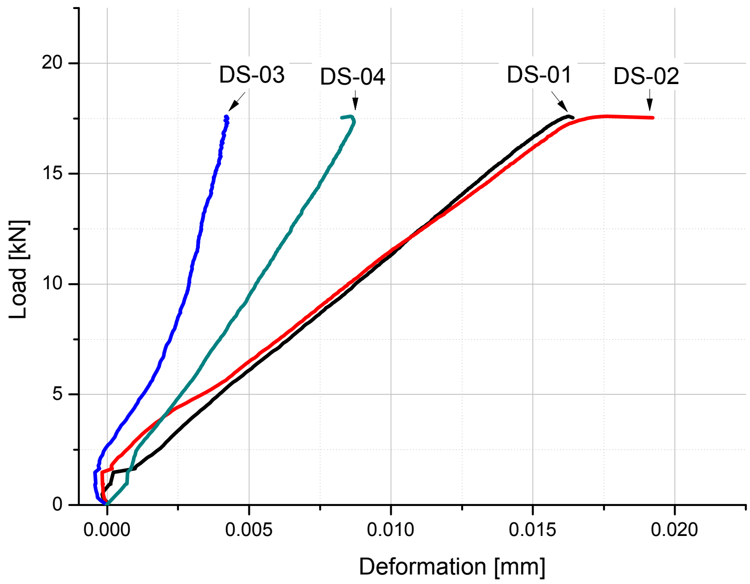

5.37. a) T-SB-01

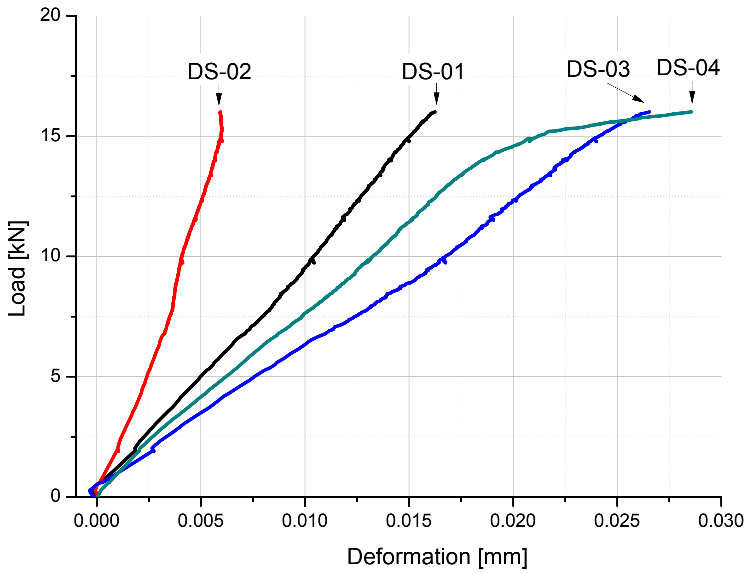

5.37. b) T-SB-02

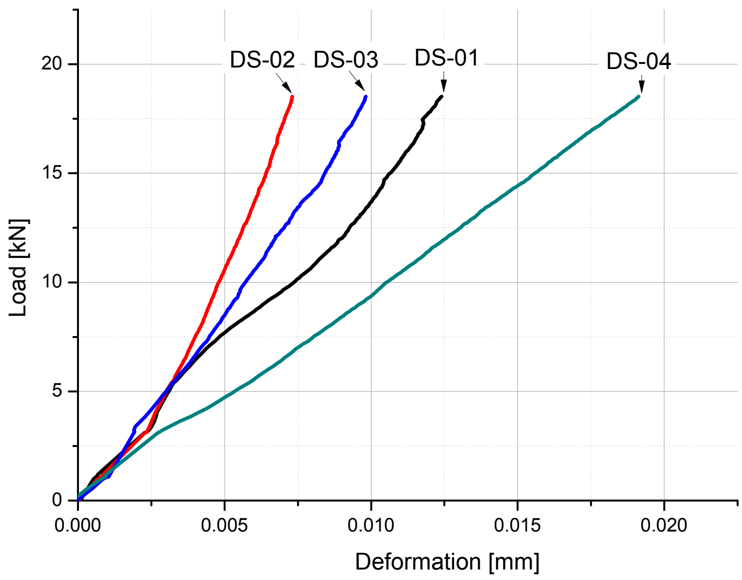

c) T-SB-03

Fig. 5.37. Load-deformation curves measured from four displacement sensors on the T-SB-specimens (DS=displacement sensor) under tensile loading

5.3.2.2 FE analysis

1) FE model

Similar to what is stated in section 5.3.1, the 3D FE model is more preferable for the stress-strain analysis on the adhesive joint than the two-dimensional FE model. By employing the three-dimensional FE models, the behaviour outside the plane can be addressed in a more reliable way. As shown in Fig. 5.38, the 3D FE model is built up by using ABAQUS 6.8 software. To simplify the FE model and save computational time, only the L-shape steel parts and four bolts for fastening the sandwich deck are involved in the FE model. Other accessorial steel parts are equivalently replaced by the corresponding boundary conditions. Eight node linear brick elements (C3D8R) with reduced integration and hourglass control are employed for all the modeling works. The total number of elements is 189828. Regarding the adhesive layer, a six-layer discretization is used in the through-thickness direction to provide accurate stresses and flexible deforming capacity as well as a three-layer discretization for the FRP laminates close to the adhesive layer. There is no specific element defined at the interphase between FRP sandwich deck and adhesive layer, or between adhesive layer and steel support. All these surfaces are fixed to each other, assuming that no cracks or relative slip occur during the loading procedure. For the boundary condition of the FE model, as shown in Fig. 5.38, all degrees of freedom on the cross-section of four bolts are restricted, and the loading of 15kN is applied by the surface tractions through the four bolt holes on the bottom steel support. The contact pairs are created between L-shape steel parts and sandwich FRP deck. Four bolts are fixed to the bolt hole surfaces of L-shape steel parts by TIE command, since it is assumed that no relative slip occurred between bolts and L-shape steel parts during the whole loading process. The properties of materials involved in the FE model are the same as presented in section 5.3.1 (Table 5.5). The whole analysis process is linear elastic. No geometrical non-linearity or elastic-plastic material properties are involved in FE analysis. The FE results can be easily amplified to a suitable value to compare with the test results. The automatic incrementation scheme is active to make the analysis easily convergent as well as to optimize the increment sizes based on computational efficiency [12].

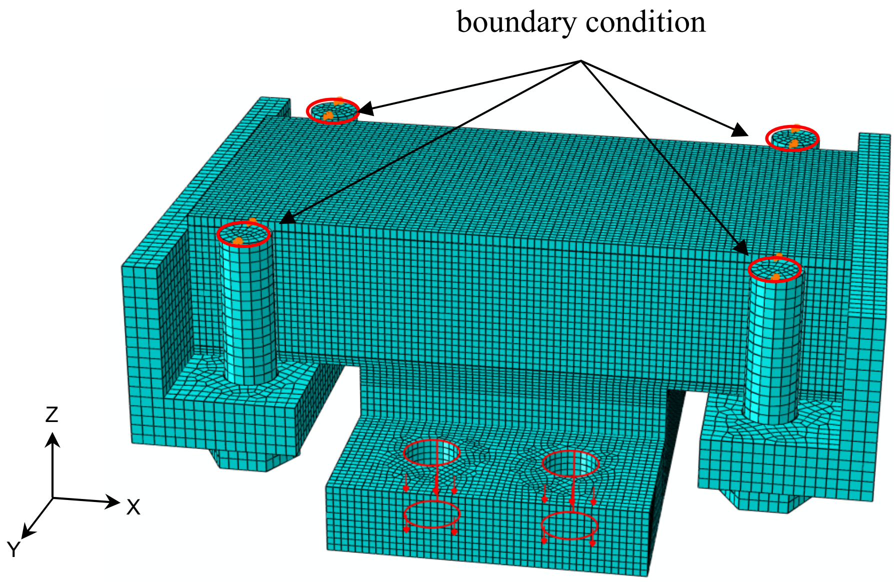

Fig. 5.38. Mesh, loading and boundary conditions of FE model under tensile loading

2) Validation of FE model

To validate the FE model, the FE results of vertical displacement between FRP sandwich and steel support at the locations of experimental displacement sensors are shown in Fig. 5.39, comparing these with experimental results. The FE results from four locations of DS-01, 02, 03 and 04 deviate much less from each other, since the FE model is perfectly symmetric, centrally loaded and there is no experimental installation inaccuracy. When it is compared with experimental results of T-SB-specimens, good agreement is obtained. The T-SB-01 and T-SB-02 curves are close to each other, with a higher stiffness than that of FE model. While the T-SB-03 curve develops lower than the FE curve. This deviation from experimental results can be due to the non-homogeneity of adhesive layer, bonding quality of interphases, as well as additional bending moment induced by inevitable eccentric loading. But still, the FE results are acceptably accurate for predicting the mechanical behaviours of the adhesive joint under tensile loading. Further FE analysis and discussion depending on this FE model is convictive.

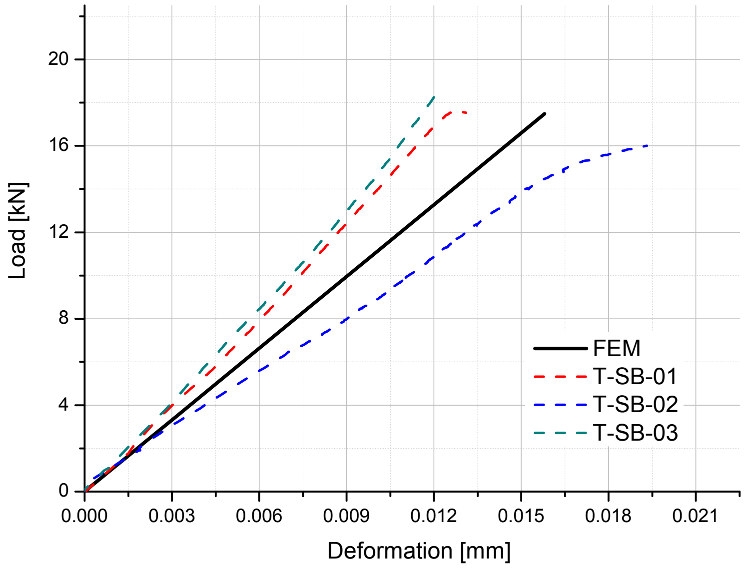

Fig. 5.39. Comparison with FE analysis and experimental results at the locations of displacement sensors

3) FEA results and discussion

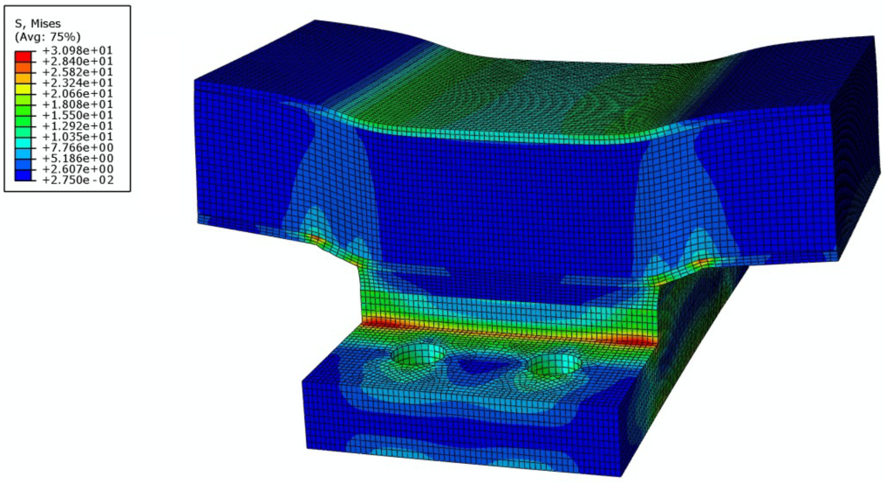

Fig. 5.40. Von Mises stress distribution and deformation throughout the adhesive joint

Fig. 5.40 shows the global Von Mises stress distribution and deformation throughout the adhesive joint. The Von Mises stress σ_v is calculated by the equation (5.4), where σ_1, σ_2 and σ_3 are principal stresses in three directions. Deformation is amplified to 50 times of the original value, the purpose of which is to clearly present the local deformation at the corners of the adhesive layer. A large portion of deformation is evident in the FRP sandwich deck as well as at the edges of the adhesive layer. There is, however, no visible deformation occurring in the steel supports, since the stiffness of steel material is non-comparatively higher than that of other composed materials. With regard to the adhesive layer, stress concentrates at the ends against the surface of FRP laminates, where stress singularity takes place and cracks initiate.

$$\sigma_v = \sqrt{\frac{(\sigma_1 - \sigma_2)^2 + (\sigma_2 - \sigma_3)^2 + (\sigma_1 - \sigma_3)^2}{2}} \tag{5.4}$$

In order to better understand the stress distribution across the interface between FRP laminates and adhesive layer, contour maps of tensile stress and shear stress are drawn through this plane, as shown in Fig. 5.41 and Fig. 5.42. The X-axis is along the longitudinal direction of the FRP sandwich deck (the ordinate is shown in Fig. 5.38), while the Y-axis is in the transverse direction. In the longitudinal direction, as can be predicted, the tensile and shear stress concentrates at the ends of the interface. The variation rate of the stress field is rough at the edge zone, whereas both tensile and shear stress distribution in the central part of interface is more stable, with the values round zero. This means that the load is dominantly carried through the two highly loaded end zones, separated by a lightly loaded trough. This result confirms the conclusion that increasing the length of overlap of adhesively-bonded joints cannot always result in the strength improvement of the whole adhesive joint. There is an upper limit of the joint strength as a function of overlap length. Thus, the conclusion can be drawn that the bonding defect in the central zone of adhesive layers does not significantly influence the ultimate failure loads of joints. On the contrary, the bonding quality at the edge zone of the adhesive layer calls for more attention to avoid premature failure of the adhesive joint.

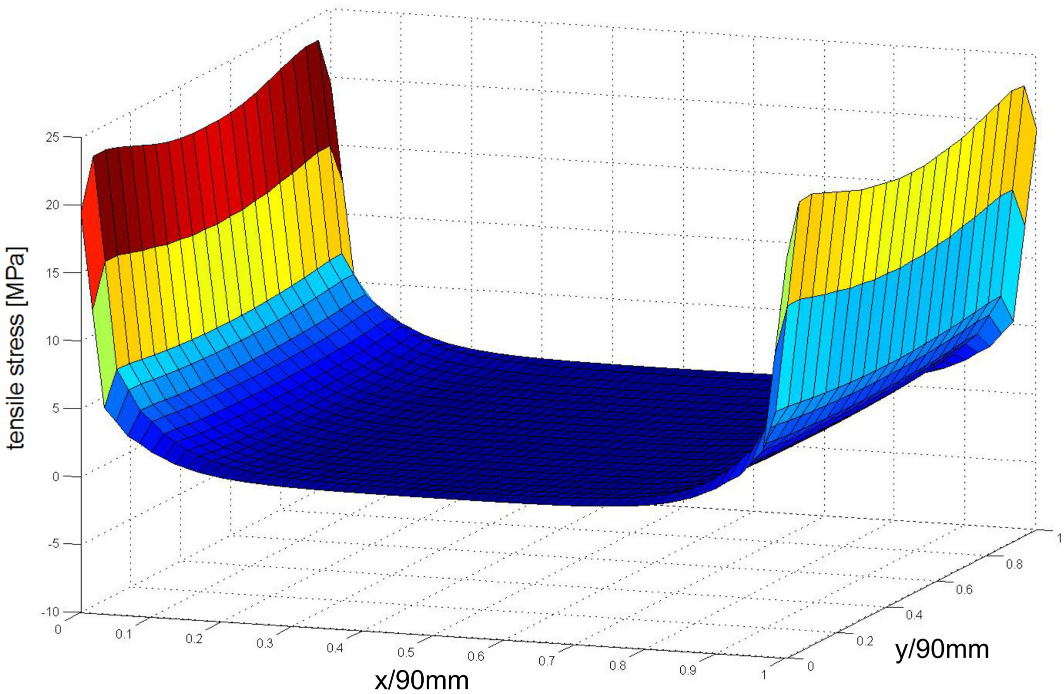

Fig. 5.41. Contour map of tensile stress on the interface between FRP laminates and adhesive layer under the tensile loading of 15kN

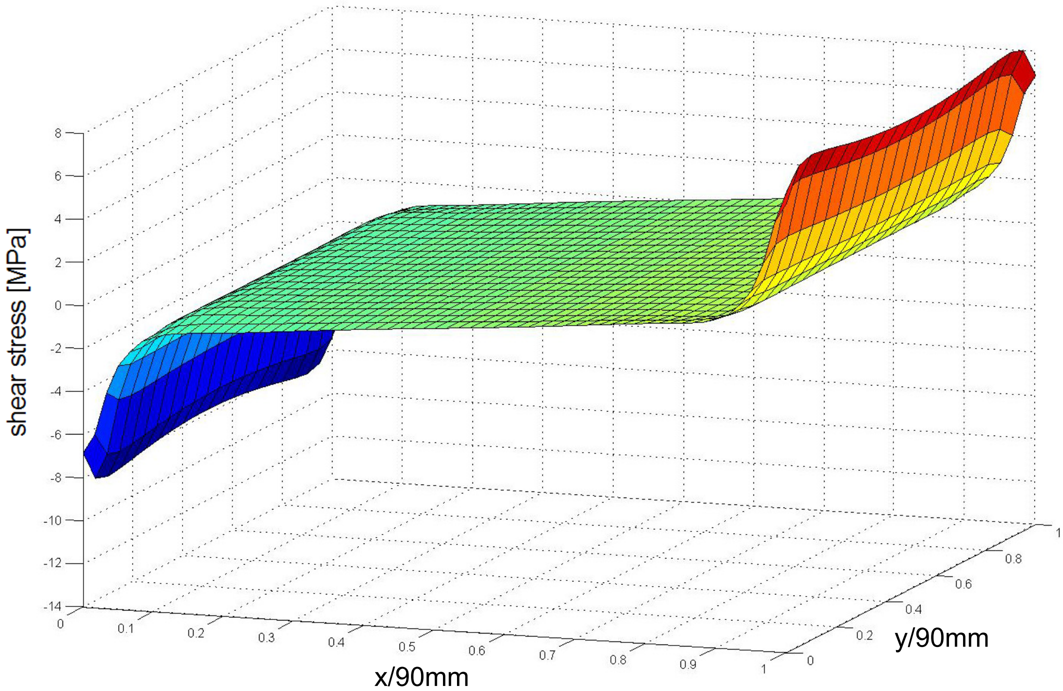

Fig. 5.42. Contour map of shear stress on the interface between FRP laminates and adhesive layer under the tensile loading of 15kN

Regarding the transverse direction, both tensile and shear stress are distributed at a rather steady gradient. Worthy mentioning here is that the maximum absolute values of stress are not located exactly at the ends of the adhesive layer, but a small distance away from the corners. Comparing Fig. 5.42 with Fig. 5.41, shows that even under the “pure tensile” loading condition there still is a comparative scale of shear stress distributed across the interface between FRP laminates and adhesive layer, which implies that the failure of adhesive joints in the experiments is induced by the combination of tensile stress and shear stress, but not only the tensile stress.

Further investigation was conducted on mesh-dependency of the FE model under tensile loading. The same condition as the shear loading, the part concerned is the adhesive layer in both longitudinal direction and transverse direction, as shown in Fig. 5.43. Four mesh configurations were selected with mesh scales of 2.00mm, 1.50mm and 1.25mm and 1.00mm.

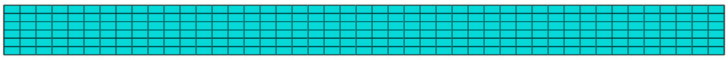

a) Mesh scale = 2.00mm

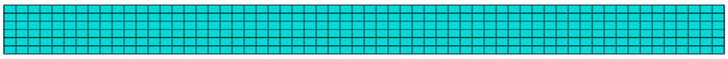

b) Mesh scale =1.50mm

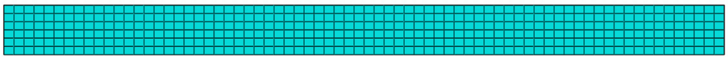

c) Mesh scale = 1.25mm

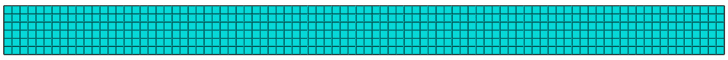

d) Mesh scale = 1.00mm

Fig. 5.43. Different mesh configurations in the adhesive layer

Based on the failure modes of tested adhesive joints under tensile loading, the concerned location of the longitudinal path is on the interface line between adhesive layer and steel support. As shown in Fig. 5.44, the shear and tensile stress distributions are extracted for comparison from the longitudinal path.

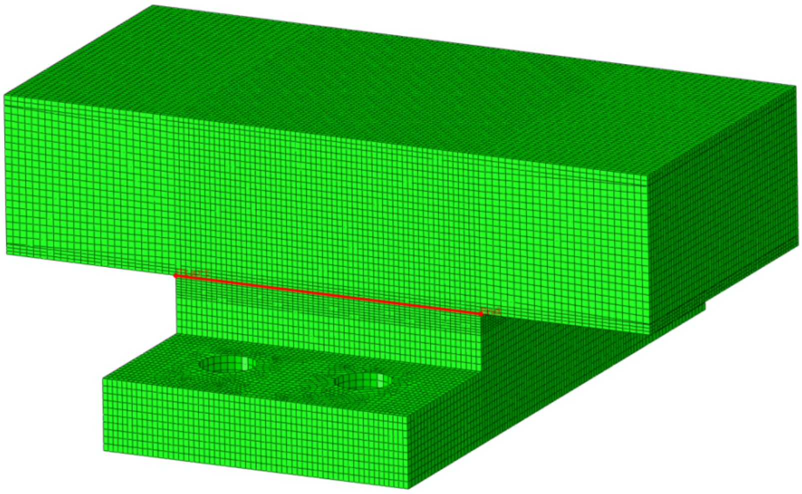

Fig. 5.44. Longitudinal path for analysing the stress distribution

Tensile stress and shear stress distributed along the longitudinal path are shown in Fig. 5.45 and Fig. 5.46. For the tensile stress distribution, mesh refined FE models do not show a highly effective improvement, which means the 2.00mm scale mesh can offer sufficient deformation flexibility of the adhesive layer. But at the ends of the adhesive layer, the small scale mesh tends to increase the tensile stress singularity, with a value of the 1.00mm scale mesh (21.58 MPa) 19.5% higher than that of the 2.00mm scale mesh (18.06 MPa). It can be predicted that the stress singularity will go to higher values when much smaller elements are proposed at the ends of the adhesive layer. But based on the former researches [13, 14], this stress singularity is not realistic. For the shear stress distribution (Fig. 5.46), the curves of 1.00mm, 1.25mm and 1.5mm scale mesh are almost the same along the whole longitudinal path, even at the ends of the adhesive layer. A slight deviation is evident for the 2.00mm scale mesh FE model. However, differences between the 2.00mm scale mesh curve and the other three curves are very limited.

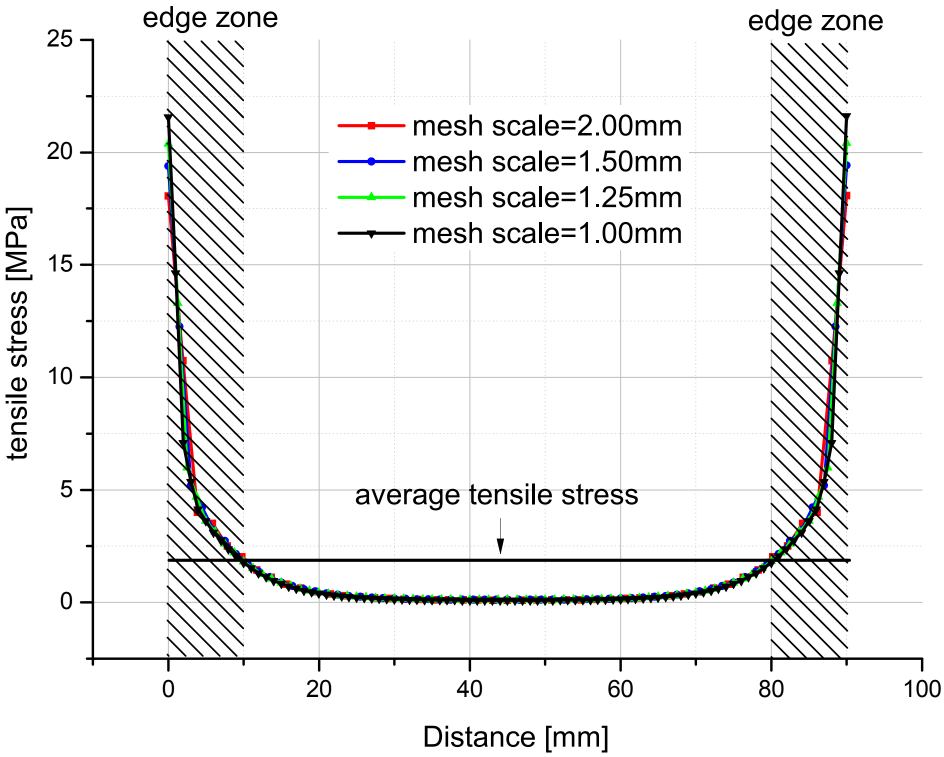

Fig. 5.45. Tensile stress distribution along the longitudinal path

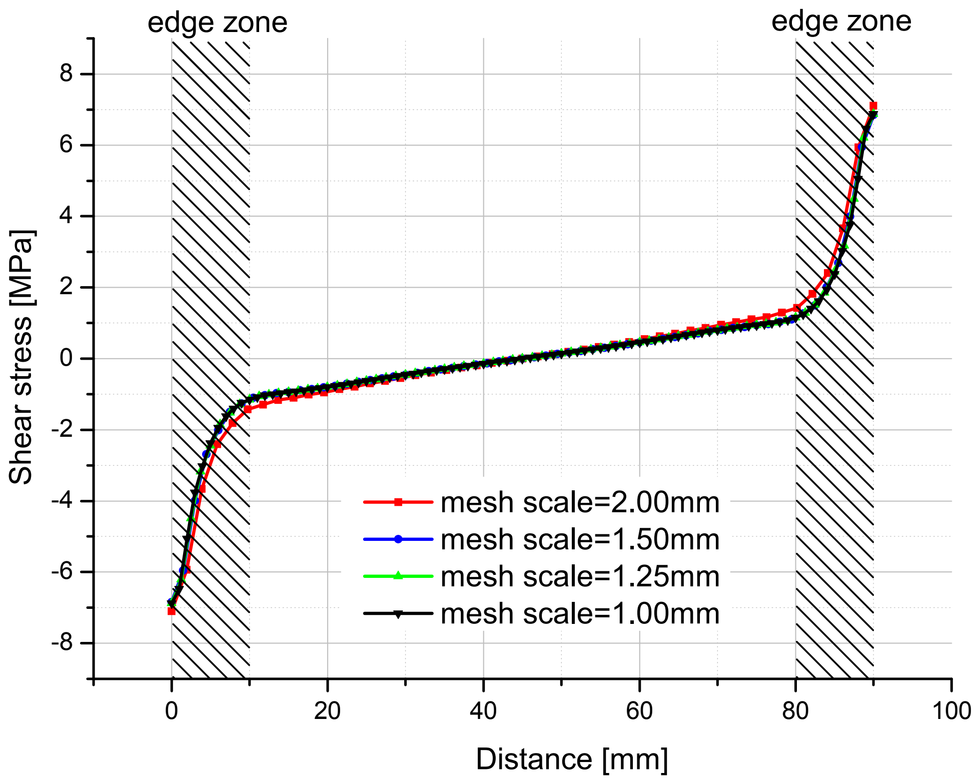

Fig. 5.46. Shear stress distribution along the longitudinal path

To fully investigate the mesh dependence of the FE model, mesh configurations through the thickness of the adhesive layer are also considered. As shown in Fig. 5.47, six-layer discretization and eight-layer discretization are selected for the study. The FE results are presented in Fig. 5.48 and Fig. 5.49. Similar to what is stated in section 5.3.1, the FE model with eight-layer elements in the through-thickness direction develops almost the same curve as that of the six-layer discretization mesh, except a slight deviation at the ends of the adhesive layer. Depending on the investigations of mesh dependency of FE model, the preferable mesh configuration is the 1.5mm element scale with six-layer discretization through the thickness of the adhesive layer, which can present the satisfactory solution and meanwhile optimize the computational time. Thus, this mesh configuration is used for further FE analysis on adhesive joints under monotonic loading in combination of shear and tension, which is addressed in the following section.

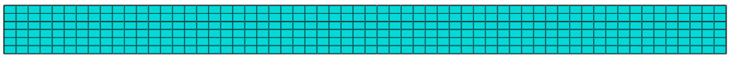

a) six-layer discretization

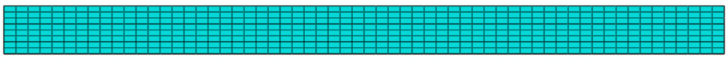

b) eight-layer discretization

Fig. 5.47. Mesh configuration through the thickness of adhesive layer

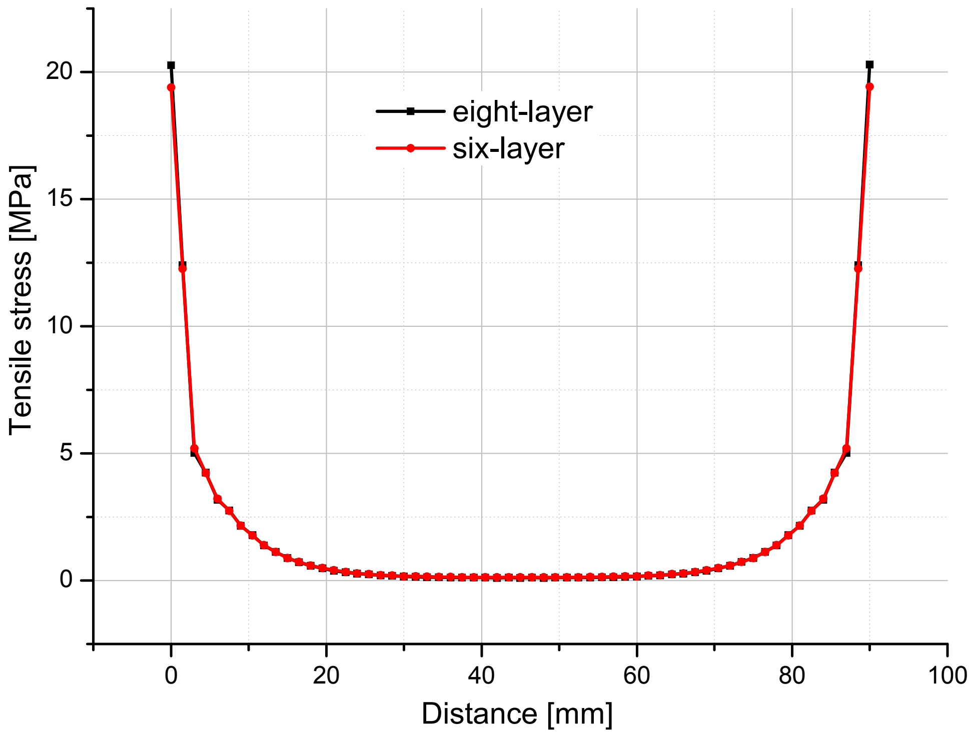

Fig. 5.48. Tensile stress distribution along the longitudinal path (through-thickness mesh)

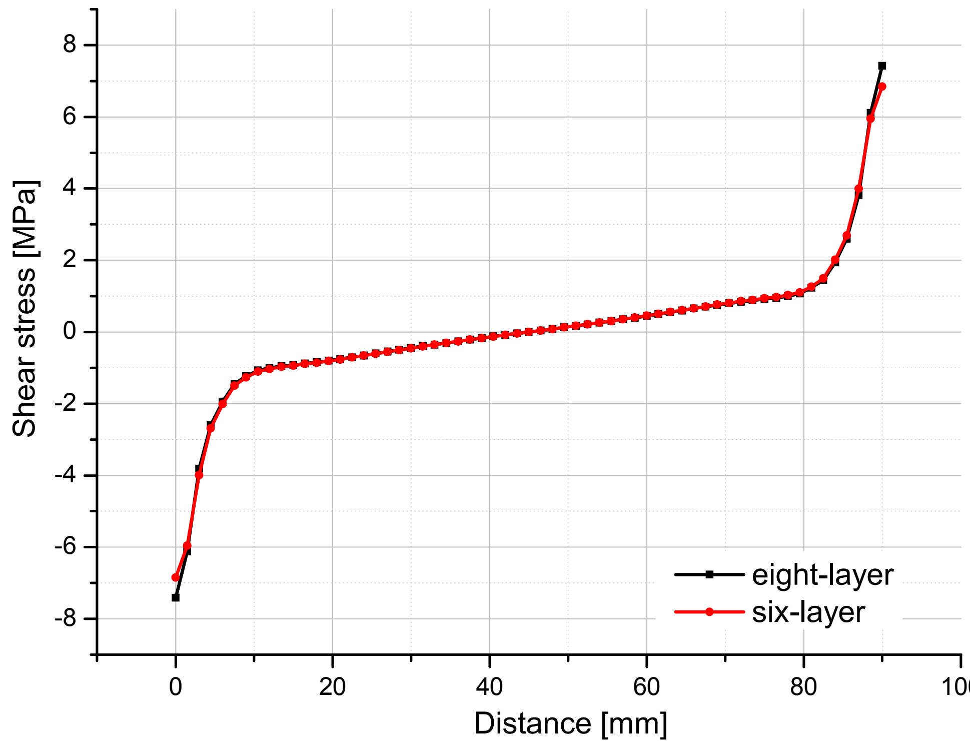

Fig. 5.49. Shear stress distribution along the longitudinal path (through-thickness mesh)

5.3.3 Combination of shear and tension loading

5.3.3.1 Experimental results and discussion

Table 5.7 lists failure loads of adhesive joints under four load angles (18°, 36°, 54° and 72°). For comparison, test results of adhesive joints (S-SB-specimens and T-SB-specimens) under pure tensile and pure shear loading conditions are also listed in Table 5.7. The lowest load-bearing capacity of adhesive joints is obtained under the 18° angle loading condition, with an average failure load of 11.9kN. The load-bearing capacity is gradually increasing from 11.9kN to 23.27kN as the loading angle increases from 18° to 72°. The largest deviation obtained by Eq. 5.2 is 16.5% under the 36° loading angle, while the smallest deviation obtained is 5.55% under the 54° loading angle.

Table 5.7. Ultimate failure loads of adhesive joints under six loading conditions

Pure tensile	01	02	03	Average	Deviation
Failure load (kN)	17.53	16.05	18.72	17.43	7.94%
18° angle	01	02	03	Average	Deviation
Failure load (kN)	12.7	11.2	11.8	11.9	6.72%
36° angle	01	02	03	Average	Deviation
Failure load (kN)	11.2	14.6	11.8	12.53	16.5%
54° angle	01	02	03	Average	Deviation
Failure load (kN)	16.5	17.7	16.1	16.77	5.55%
72° angle	01	02	03	Average	Deviation
Failure load (kN)	26.6	20.0	23.2	23.27	14.3%
Pure shear	01	02	03	Average	Deviation
Failure load (kN)	51.0	92.9	64.1	69.3	34.0%

To easily recognize the load combining effects, the total failure load is vectorially separated into shear load and tensile load, with regard to the loading angle of each loading condition, as shown in Fig. 5.50. The horizontal axis represents the shear load applied to the adhesive joint, while the vertical axis is the tensile load. It is apparent that, under combination of tensile and shear loading, the load-bearing capacity of adhesive joints decreases as compared to that of pure tensile and pure shear loading conditions. From Fig. 5.50, the failure load of adhesive joints under pure shear loading (69.3kN) is considerably higher than other loading conditions, due to the different failure mode, which is discussed in detail hereafter. It is manifest that the failure load of an adhesive joint under different combined loading conditions is more sensitive to the ratio of tensile load vectorially separated from the resultant force.

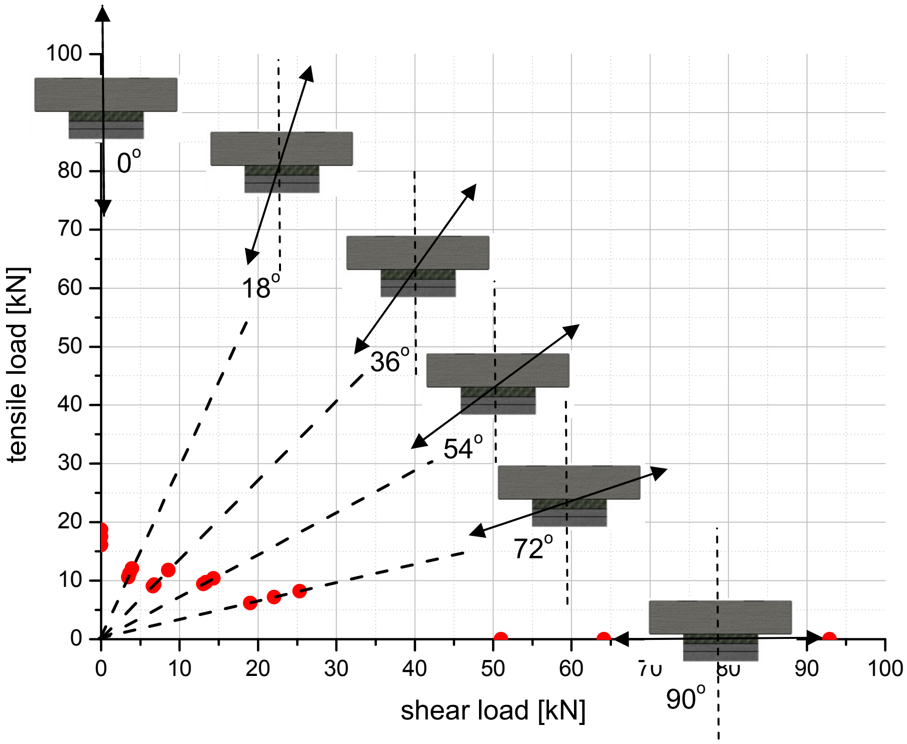

Fig. 5.50. Failure loads of adhesive joints under the combining loading of tensile and shear

To investigate the failure criterion of adhesive joints, an ellipsoid function is employed for the curve fitting by the least square method. Firstly, considering all the test results of six loading conditions, the predictive curve (Eq. 5.5) is obtained and indicated as a solid line in Fig. 5.51. It can be found that the agreement between the test results and the predictive equation is very bad. All the test data of four combining loading conditions are below the predictive curve, which implies that the predictive equation is not conservative for the design of adhesive joints. To solve this issue, only the test results of four combinations of shear and tensile loads are selected to perform as the basic curve fitting data, since involving the test results of the pure tensile and pure shear loading conditions will make the predictive curve deviate too much from the four combination loading conditions. The modified predictive equation is expressed by Eq. 5.6, and indicated as a dashed line in Fig. 5.51. In this way, the failure criterion is more conservative and practical, since in the real application of an adhesive joint between FRP decks and steel girders, the joint mainly serves under the combination loading of tension and shear.

Predictive curve:

$$\left(\frac{\sigma}{1.54}\right)^2 + \left(\frac{\tau}{9.59}\right)^2 = 1 \qquad (5.5)$$

Modified predictive curve: $$\left(\frac{\sigma}{1.41}\right)^2+\left(\frac{\tau}{3.18}\right)^2=1 \qquad (5.6)$$

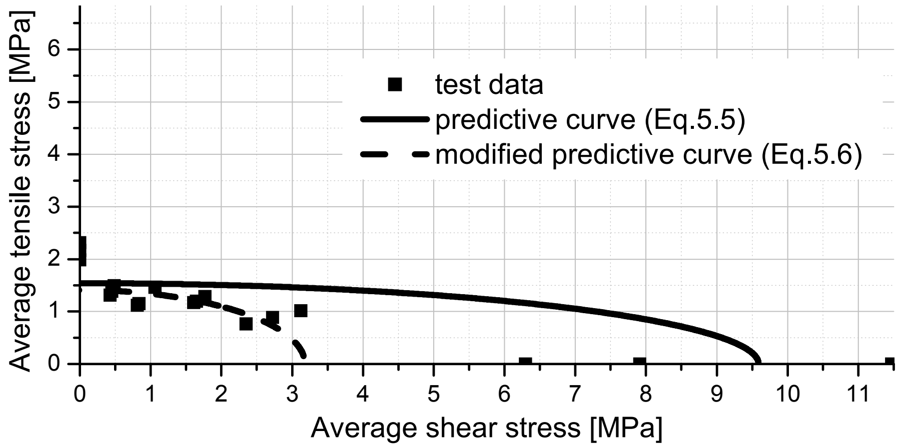

Fig. 5.51 Shear-tensile failure criterion for the adhesively-bonded joint

It is known that the stress distribution is not uniform either through the interface between the adhesive layer and the steel support or through the interface between the FRP sandwich deck and the adhesive layer. Regularly, the stress concentrates at the ends of the adhesive layer. Thus, the shear-tensile failure criterion needs to be modified with the stress non-uniform distribution factor, which needs to be determined by the FE parametric study of adhesive joints in future work.

The failure modes of adhesive joints under four combinations of tensile and shear loads are illustrated in Fig. 5.52. All the fracture planes are through the interface between the FRP sandwich deck and adhesive layer, which is the same as that observed for the adhesive joint under pure tensile loading (section 5.3.2). Some area of fibre breaking or FRP delamination is evident from the view of the FRP laminate failure surface. But these areas do not fully cover the adhesively-bonding area. This failure mode can be defined as the combination of fibre breaking (or FRP delamination) and interfacial adhesion failure between FRP sandwich deck and adhesive layer. It is worthwhile mentioning that, for the 72° angle loading condition, there are cracks observed in the adhesive layer of the 72°-SB-01 and propagate through the interface between adhesive layer and steel support, as illustrated in Fig. 5.53. It indicates that the failure plane almost switches to the interface between adhesive layer and steel support, which occurred for the adhesive joints under the pure shear loading condition. This phenomenon suggests that the upper and lower interfaces between adhesive layer and FRP laminates or steel support almost achieve the failure homogenously. However, for the other two specimens under the 72° loading angle, cracks in the adhesive layer are not visible. Instead, a large portion of FRP delamination or fibre breaking area is evident in Fig. 5.54. Once again, the test results confirm that the controllable adhesively-bonding technique is essential to guarantee the mechanical performance of the adhesive joints.

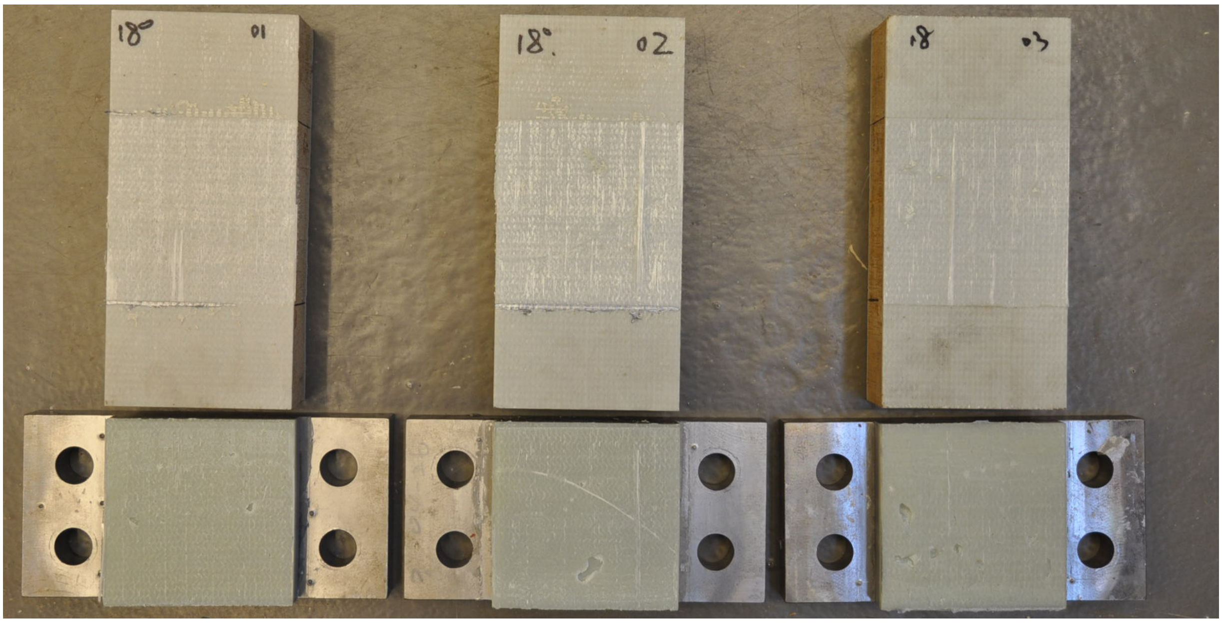

18°-SB-01 18°-SB-02 18°-SB-03

Fig. 5.52. a) 18° angle

36°-SB-01 36°-SB-02 36°-SB-03

Fig. 5.52. b) 36° angle

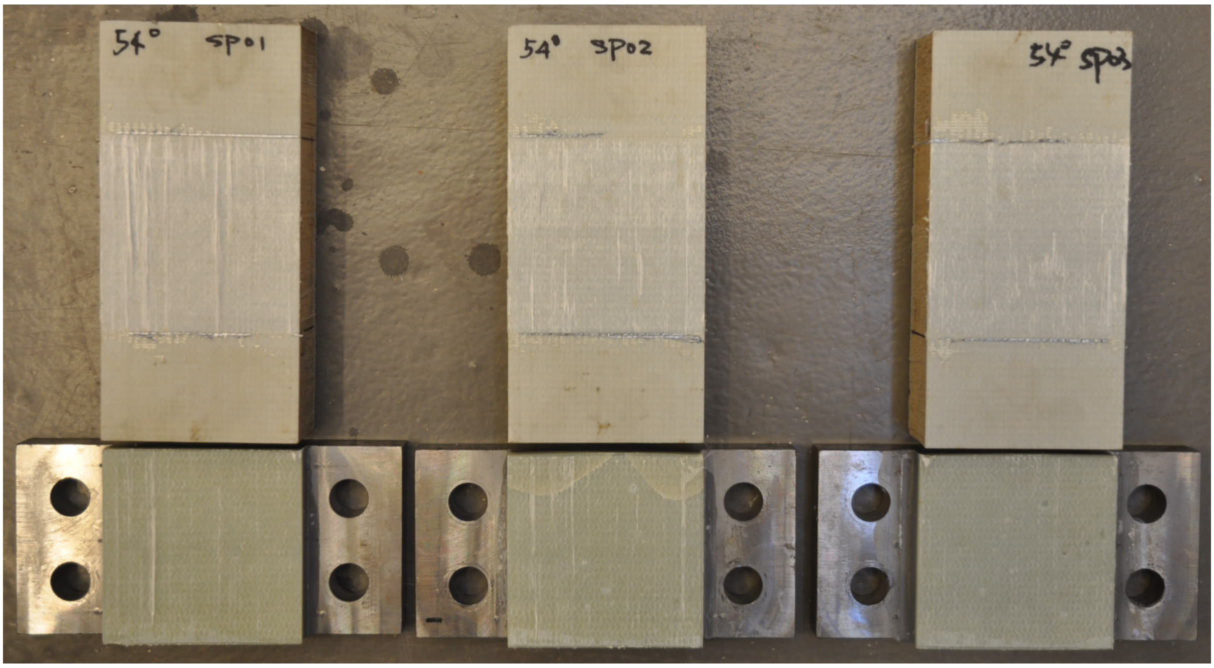

54°-SB-01 54°-SB-02 54°-SB-03

c) 54° angle

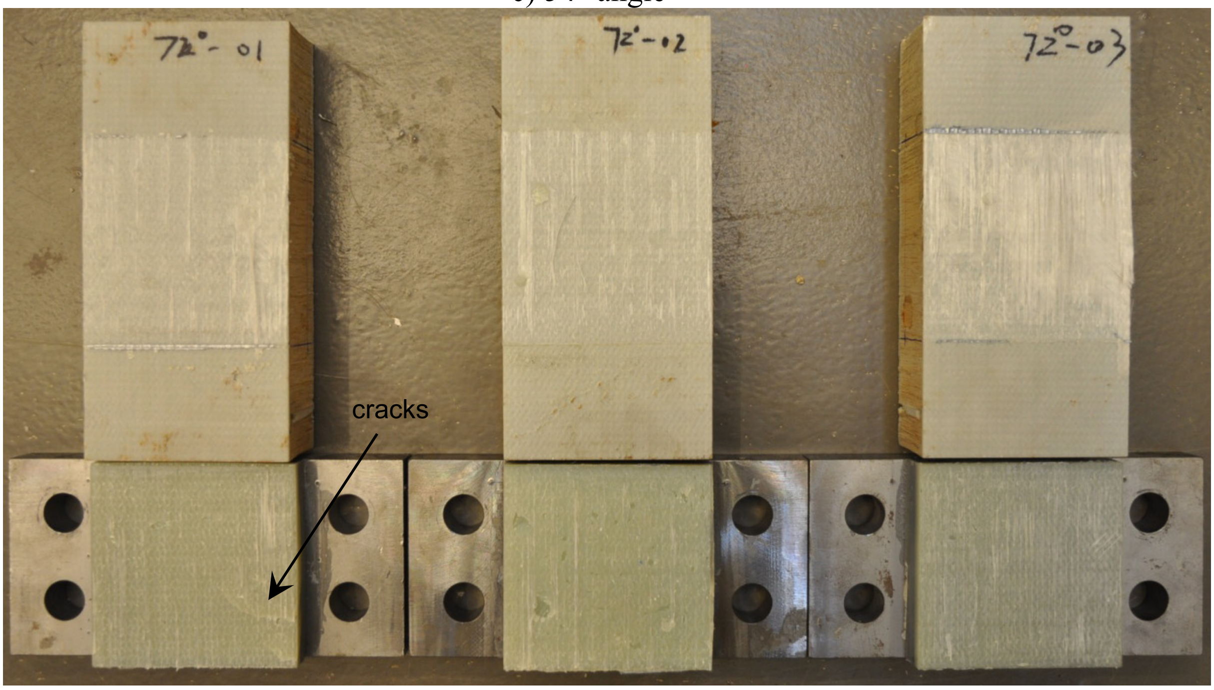

72°-SB-01 72°-SB-02 72°-SB-03

d) 72° angle

Fig. 5.52. Failure modes of adhesive joints under four loading angles

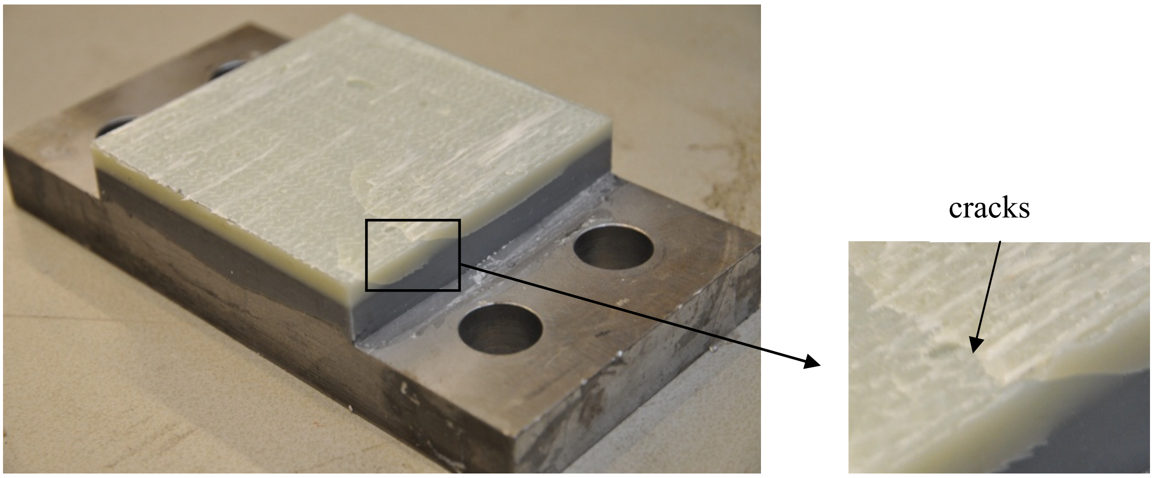

Fig. 5.53. Cracks in the adhesive layer of 72°-SB -01 under the 72° angle loading

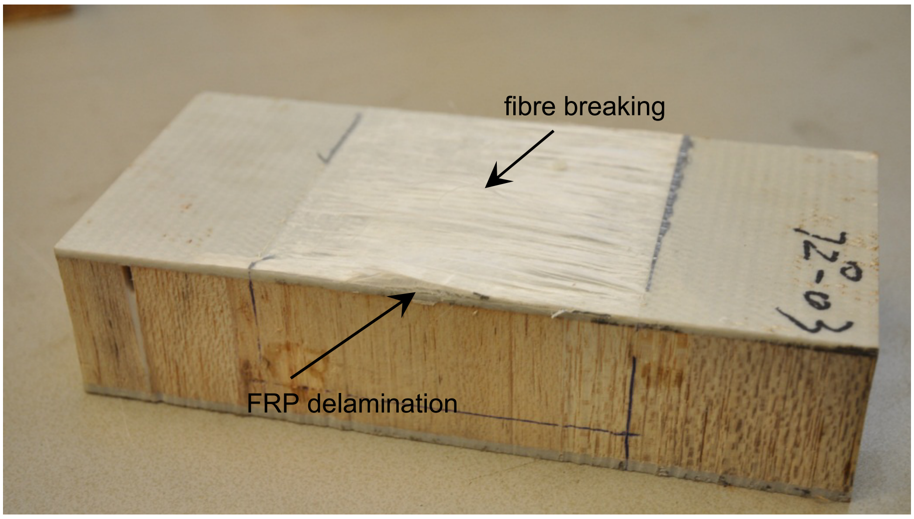

Fig. 5.54. FRP delamination and fibre breaking in the FRP sandwich deck of 72°-SB-03 under 72° angle loading

5.3.3.2 FE analysis

1) FE model

The FE model of adhesive joints under the combination of tensile and shear loads is developed by using ABAQUS 6.8. The simplification of an FE model is the same as that of the shear loading condition (section 5.3.1.2), except the loading and boundary condition definition. As shown in Fig. 5.55, the shear and tensile loads are applied by the surface tractions on the loading area respectively, while all the degrees of freedom are restricted for the reaction area. The center of shear and tensile load is exactly through the centroid of the adhesive layer, in such a way as to confirm that the resultant force is also through the centroid of the adhesive layer and no additional bending moment is proposed. Subsequently, four loading angles can be realized by varying the ratio between shear load and tensile load with specific tangent values. Depending on the investigations of mesh dependence of an FE model under shear and tensile loading conditions (sections 5.3.1 and 5.3.2), the FE model with 1.50mm mesh scale and six-layer discretization through the thickness of the adhesive layer is preferable to achieve reasonable accuracy as well as to save computational time. Thus, this mesh configuration is continuously employed for FE analysis in this section, as shown in Fig. 5.56 and Fig. 5.57. All the elements used are C3D8R. No geometric non-linearity or elastic-plastic material properties are involved in the FE analysis. The input of material properties is the same as listed in Table 5.5. The resultant force of 15kN (vectorial combination of tensile and shear load) is applied on the FE model. The FE results can be amplified with any ratio to be comparable with test results.

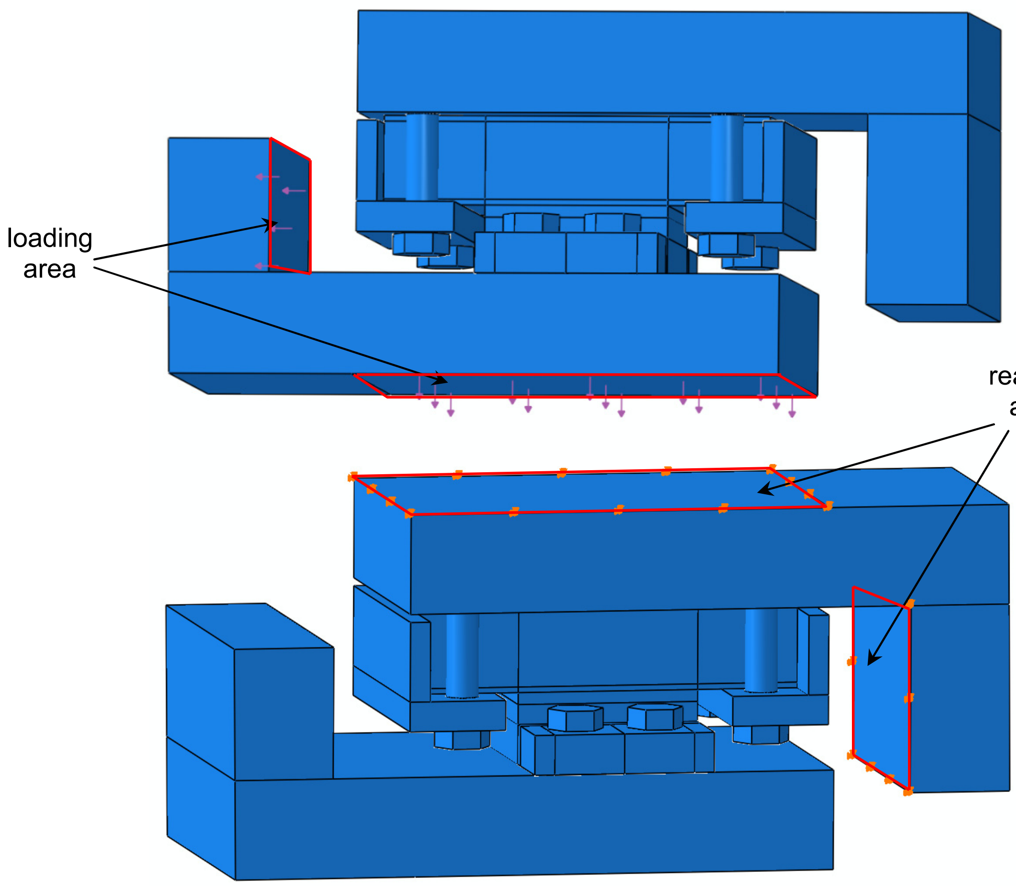

Fig. 5.55. Loading and boundary condition of FE model

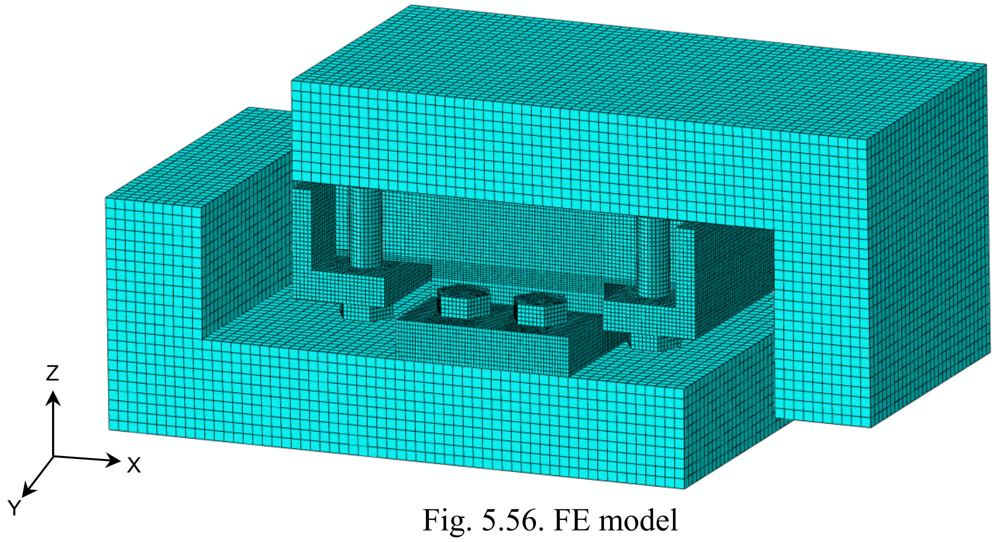

Fig. 5.56. FE model

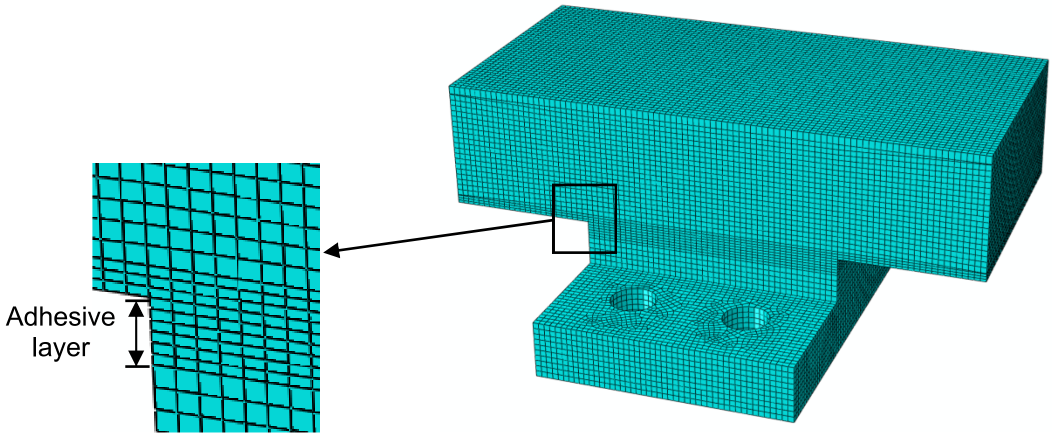

Fig. 5.57. Mesh configuration of adhesive joint

2) Validation of FE model

Fig. 5.58 illustrates the FE results of relative deformation between FRP sandwich deck and steel support at the locations of experimental displacement sensors under four loading angles, compared with the mean value of experimental results. The deformation values in the minus area represent the mean value of measured deformation from DS-02 and DS-04, while the positive area represents the mean value of measured deformation from DS-01 and DS-03. The location of displacement sensors is illustrated in Fig. 5.12. For the 54°-SB-02 of the 54° angle loading condition, DS-01 and DS-03 displacement sensors are not installed firmly and they drop off during the test. Thus, the test data are absent in Fig. 5.58 c). From Fig. 5.58 it can be found that at the initial stage of loading process good agreement is obtained between FE results and experimental data. However, as the test proceeds, some deviations occur for both tensile and shear deformation.

The curves of test results are nonlinear, especially for the mean values of DS-02 and DS-04. This is due to the inhomogeneity of adhesive material and Basal wood. During the whole test, the stress in the adhesive joint is not ideally distributed, but keeps redistributing depending on the stiffness of the components. The three test curves of each loading angle do not exactly match with each other, since the extent of porosity in the adhesive layer and Basal wood deviate from each other. Based on the above discussion, considering the manufacture tolerance, inhomogeneity of materials involved and the scale of measured deformation, the agreement obtained between FE results and experimental data is reasonably acceptable. The FE model is therefore reasonably acceptable to be used in further analysis.

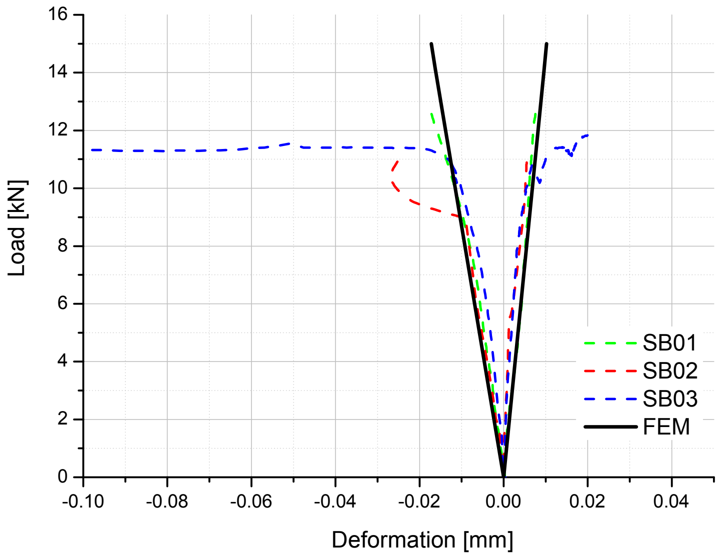

Fig. 5.58. a) 18° angle

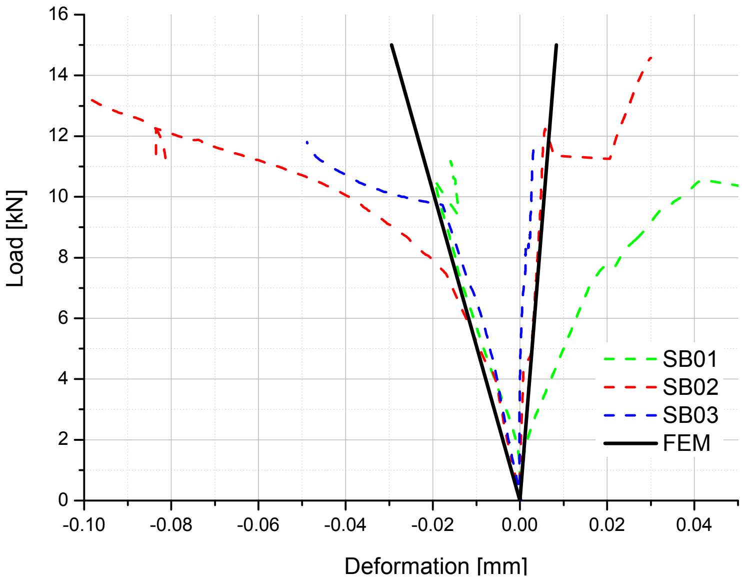

Fig. 5.58. b) 36° angle

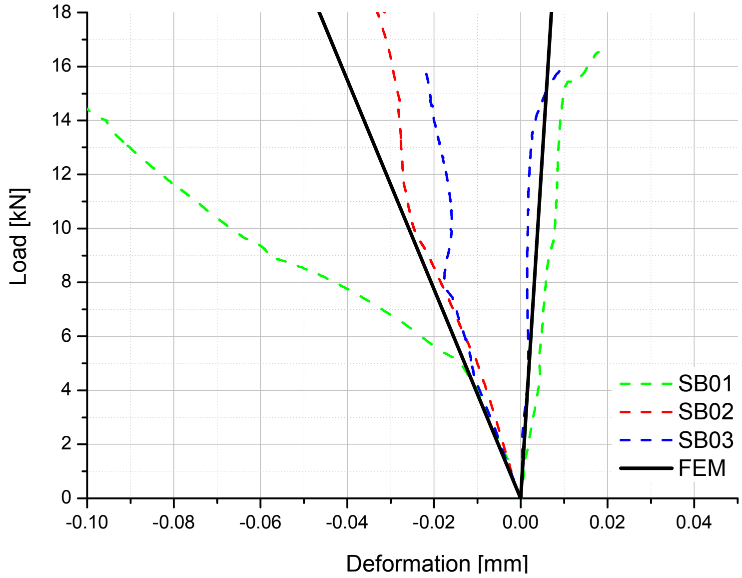

c) 54° angle

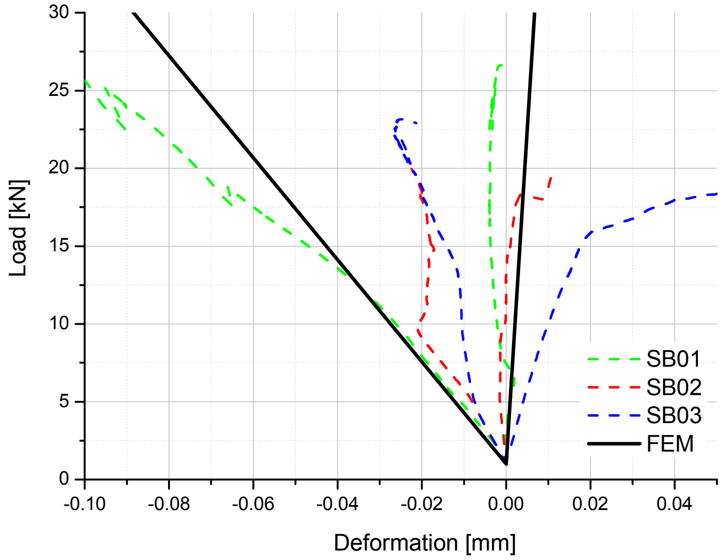

d) 72° angle

Fig. 5.58. Comparison on experimental results and FE analysis at the locations of displacement sensors

3) FE results and discussion

Fig. 5.59 and Fig. 5.60 illustrate the contour map of tensile and shear stress on the interface between FRP laminates and adhesive layer under four loading angles. For comparison, the tensile and shear stress states under the shear and tensile loading conditions are also included. For all the six angle loading conditions, in the transverse direction (the Y axis as indicated in Fig. 5.56), tensile and shear stress are distributed more uniformly. The maximum absolute stress values are not located exactly at the ends of the interface, but at 9mm distance from the end. To further investigate the stress distribution in the longitudinal direction (the X axis as indicated in Fig. 5.56), the tensile and shear stress is extracted through the longitudinal path at the location of 9mm distance from the end, as shown in Fig. 5.61 and Fig. 5.62.

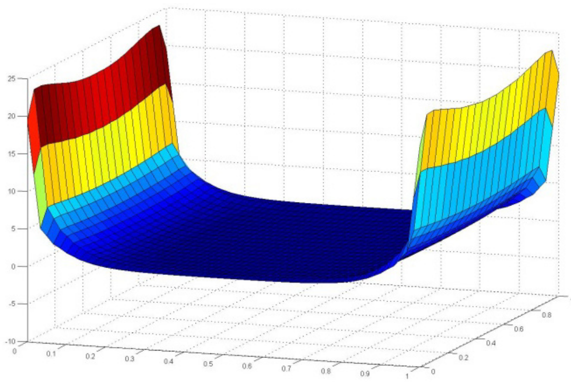

a) 0° angle loading (tensile)

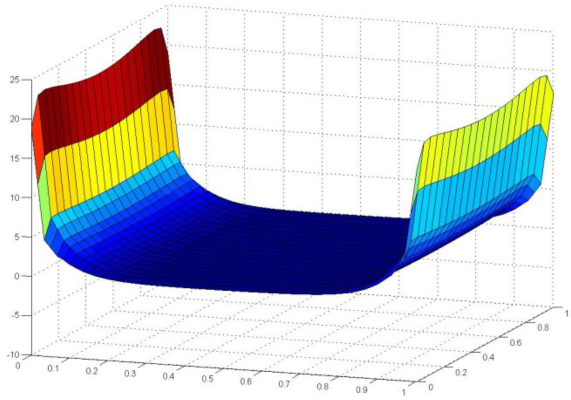

b) 18° angle loading

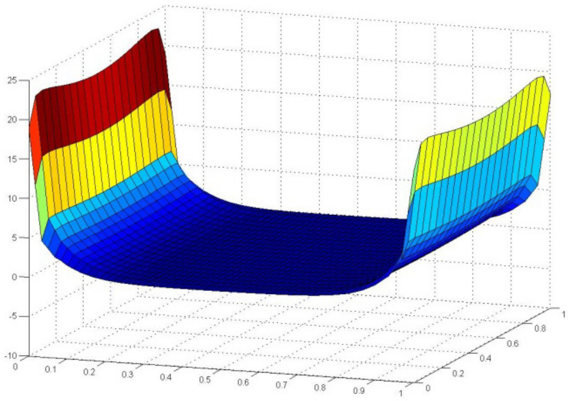

c) 36° angle loading

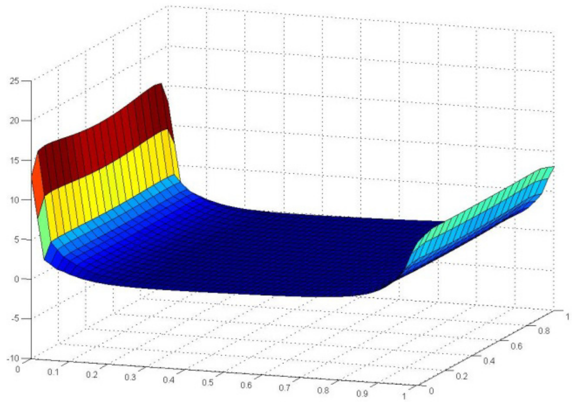

d) 54° angle loading

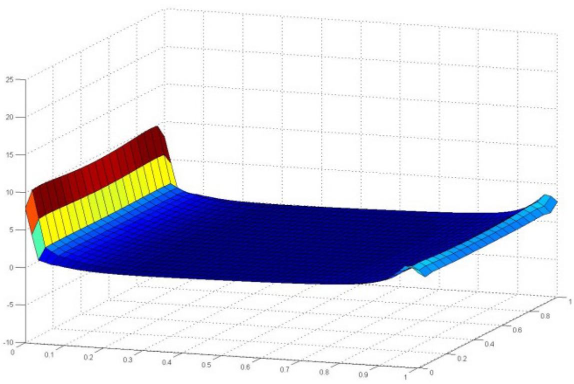

e) 72° angle loading

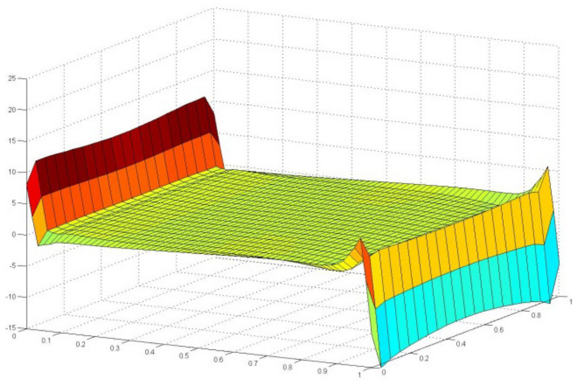

f) 90° angle loading (shear)

Fig. 5.59. Contour map of tensile stress on the interface between FRP laminates and adhesive layer under six loading conditions

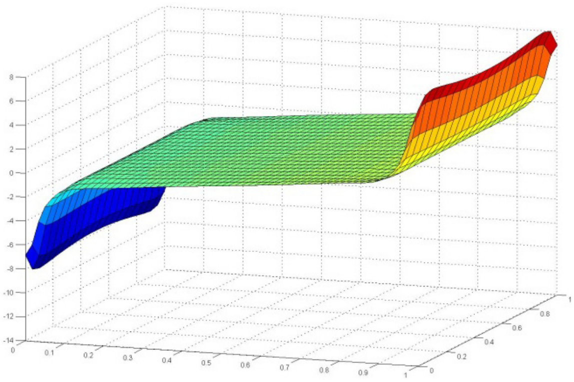

a) 0° angle loading (tensile)

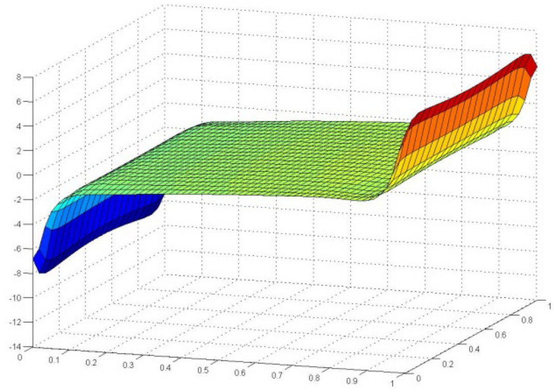

b) 18° angle loading

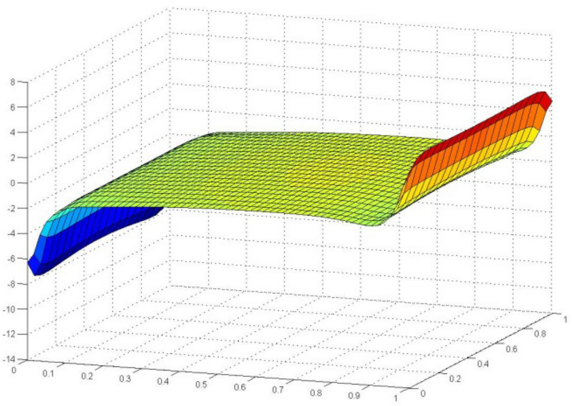

c) 36° angle loading

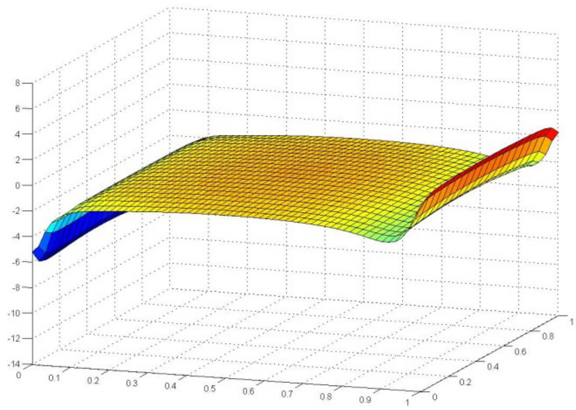

d) 54° angle loading

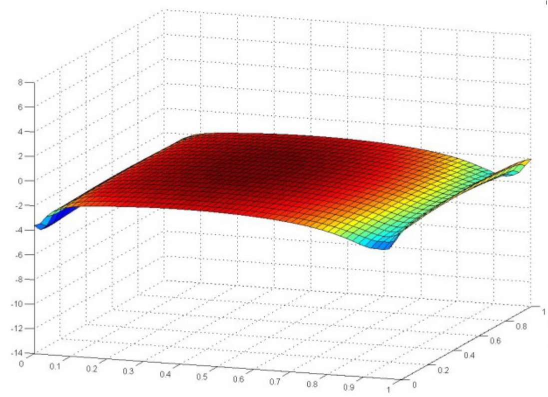

e) 72° angle loading

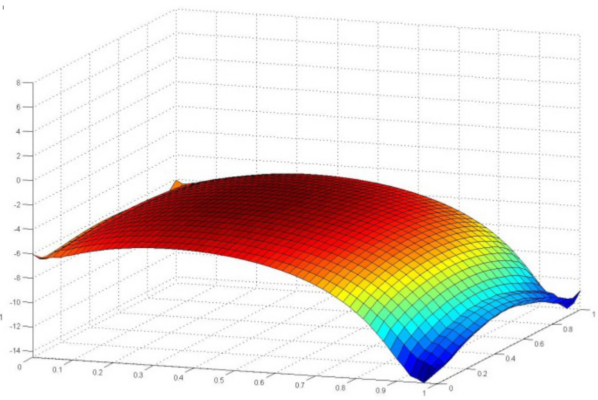

f) 90° angle loading (shear)

Fig. 5.60. Contour map of shear stress on the interface between FRP laminates and adhesive layer under six loading conditions

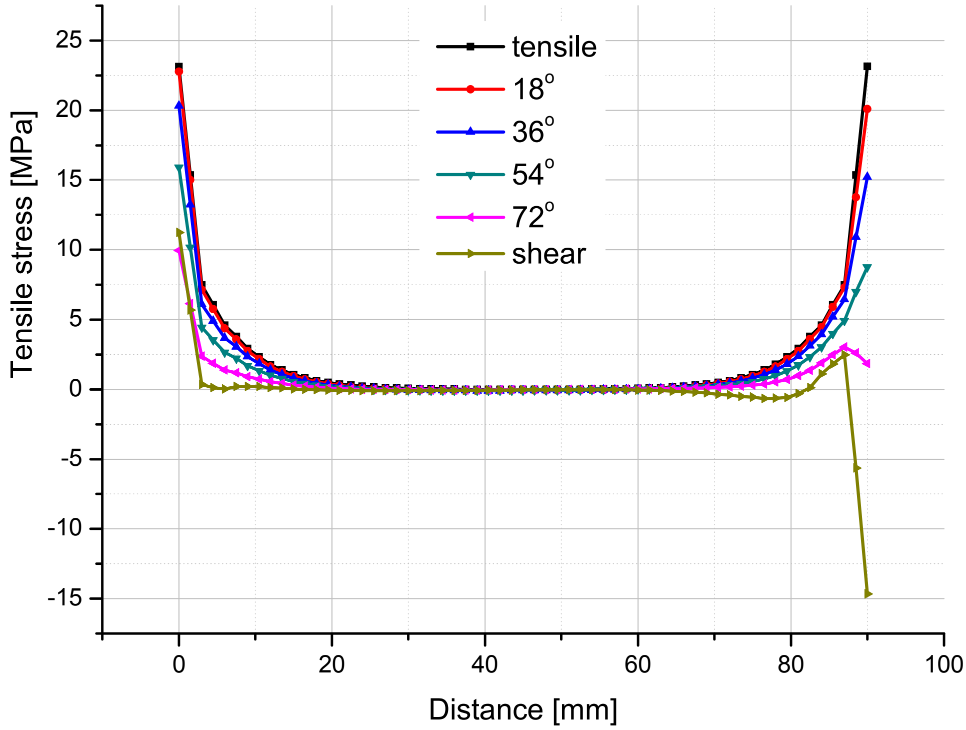

Fig. 5.61. Tensile stress distribution in the longitudinal path at a location 9mm from the end of the interface

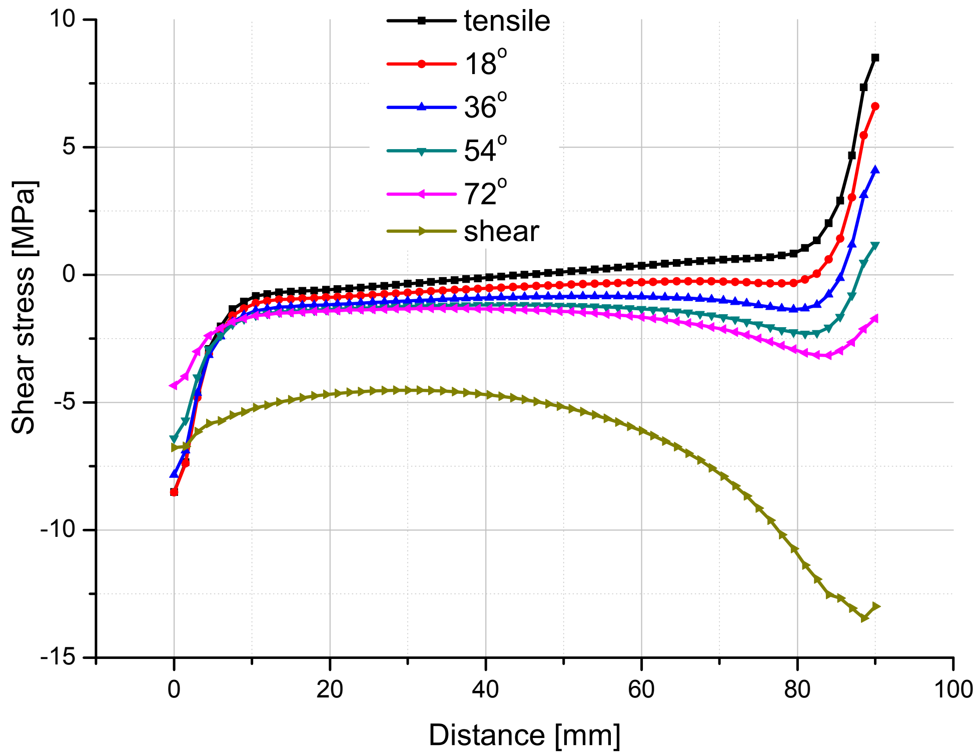

Fig. 5.62. Shear stress distribution in the longitudinal path at a location 9mm from the end of the interface

From Fig. 5.61, it can be found that for all six loading conditions the tensile stress is approximately zero in the central part of the interface in the longitudinal direction (the X axis as indicated in Fig. 5.56). However, in the vicinity of adhesive layer ends, the tensile stress concentration is evident. As the loading angle rotates from 0° (tensile) to 90° (shear), the tensile stress singularity decreases at both ends of the interface, since the vectorially separated tensile load applied on the FE model of adhesive joint decreases. For the right end (shear load applied side), the extent of tensile stress decreasing is more significant than that on the left side, which introduces an asymmetrical tensile stress state throughout the longitudinal path. Subsequently, the tensile stress singularity at the right end drops to the minus zone for the shear loading condition.

Fig. 5.62 illustrates the shear stress distribution along the longitudinal path. The tensile and shear loading condition achieve the two extreme shear stress states. The shear stress distributions of the other four angle loading conditions regularly transit from tensile loading condition to shear loading condition. In the central part of the interface, the shear stress values of four loading angles are not zero anymore, the absolute values of which are increasing with the vectorially separated shear load increased from the 18° angle loading to 72° angle loading. Without any doubt, the absolute value of shear stress achieves the maximum for the shear loading condition (90° angle). For the right end (shear load applied side), the variation of the shear stress state is more significant than that on the left side, since the shear stress at the load directly forced side is more sensitively influenced. To the contrary, the shear stress distribution at the left side does not vary too much among six loading conditions. The three curves of 0° (tensile), 18° and 36° loading conditions almost cover each other.

5.4 Mechanical behaviour of adhesively-bonded joints after hydrothermal aging

5.4.1 Shear loading

For the aged adhesive joints under shear loading, the failure mode is brittle, without any visible signs or sound warning from fibre breaking. The load-displacement curves of three specimens are shown in Fig. 5.63. Similar to what was discussed in section 5.3.1.1 for the un-aged specimens under shear loading, the initial stage with a higher slope is due to the friction between the L-shape steel profile and the FRP sandwich deck. Fig. 5.63 also indicates that the slopes of the two-stage load-displacement curves are close to each other. Only the friction of each specimen test is a bit different, which compels the test curves to bend at different locations.

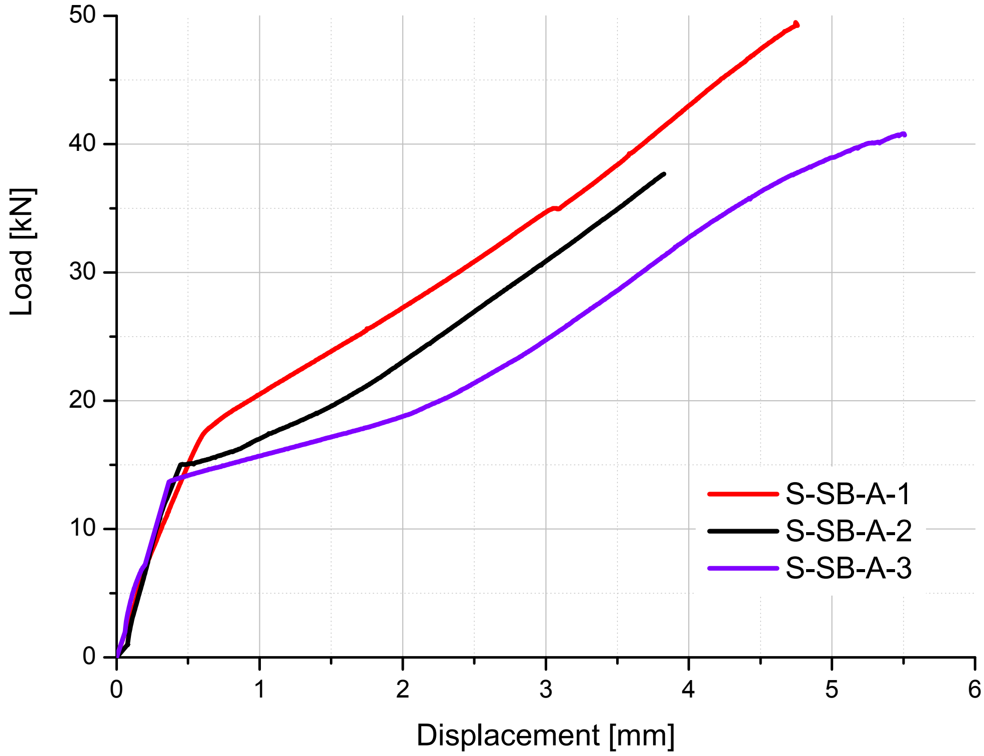

Fig. 5.63. Load-displacement curves of aged specimens under shear loading

As shown in Fig. 5.64, the failure of adhesive joints is a cohesive fracture (adjacent to the interface between the adhesive layer and the steel support) in the adhesive layer, which confirms that the sand blasting surface pretreatment method results in a good quality bonding between the adhesive layer and the steel surface, even in the hydrothermal aging environment. The failure mode also indicates that the absorbed moisture in the hydrothermal aging environment does not significantly degrade the interfacial strength between the adhesive layer and the steel support.

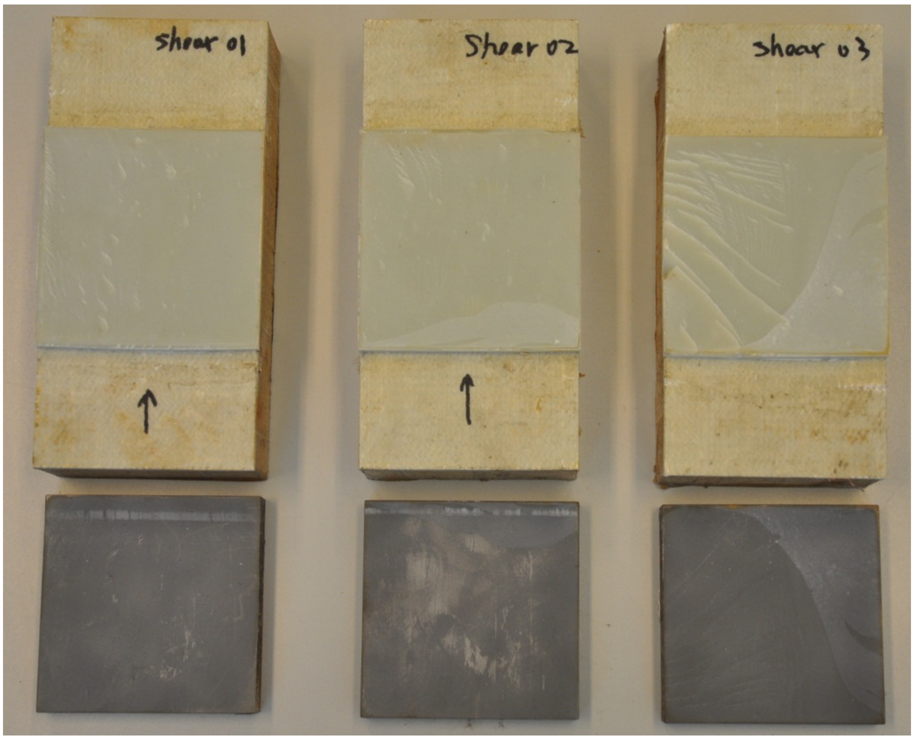

S-SB-A-01 S-SB-A-02 S-SB-A-03

Fig. 5.64. Failure mode of the aged adhesively-bonded joint under shear loading

Table 5.8 lists the ultimate failure loads of three adhesive joint specimens. Their average value of them is 41.9 kN with the deviation (calculated by Eq. 5.2) of 18.1%.

Table 5.8. Ultimate failure loads of three aged adhesive joints under shear loading

S-SB-A-specimen	01	02	03	Average	Deviation
Failure load (kN)	49.5	37.7	38.4	41.9	18.1%

Fig. 5.65 shows the failure modes from the view of steel supports. From Fig. 5.65 a) it can be easily found that there is a fracture initiated line (white colour) locating a small distance from the edge of the steel support. As indicated by the FE analysis of stress distribution on the interface between steel support and adhesive layer (section 5.3.1.2), the shear stress peak is more or less at the same location as this yielding line. This means the failure of the whole adhesive joint is initiated at this spot and develops to the vicinity to trigger the final failure of the joint. However, significantly different from the S-SB-A-01 specimen, there is no visible fracture initiated line on the surface of the S-SB-A-03 specimen (see Fig. 5.65c)). Instead, there is a big adhesive fracture initiated area at the right corner of the whole adhesive-bonding area, which suggests that cracks firstly occur at the right corner and

gradually propagate into the middle of adhesive layer as the load increases until the rest of the adhesively-bonding area cannot carry the load anymore. Then, the whole adhesive joint fails in a sudden way. The failure mode of the S-SB-A-03 specimen may be due to the local non-homogeneity of the adhesive layer, where the stress concentration is located and subsequently changes the stress distribution across the section and induces the premature failure of the adhesive joint. As can be seen in Fig. 5.63, the load-displacement curve of the S-SB-A-03 specimen is a little more flexible than that of the other two specimens, which can be attributed to its specific failure mode. Furthermore, for the S-SB-A-02 specimen (Fig. 5.65b)), both the fracture initiated line and fracture initiated area are visible on the surface of the steel support. This failure mode can be considered to be a combination of the S-SB-A-01 specimen and the S-SB-A-03 specimen. Clearly, the failure mode of the S-SB-A-01 specimen is more preferable, which results in the highest load-carrying capacity (49.5kN) of the three adhesive joints under shear loading.

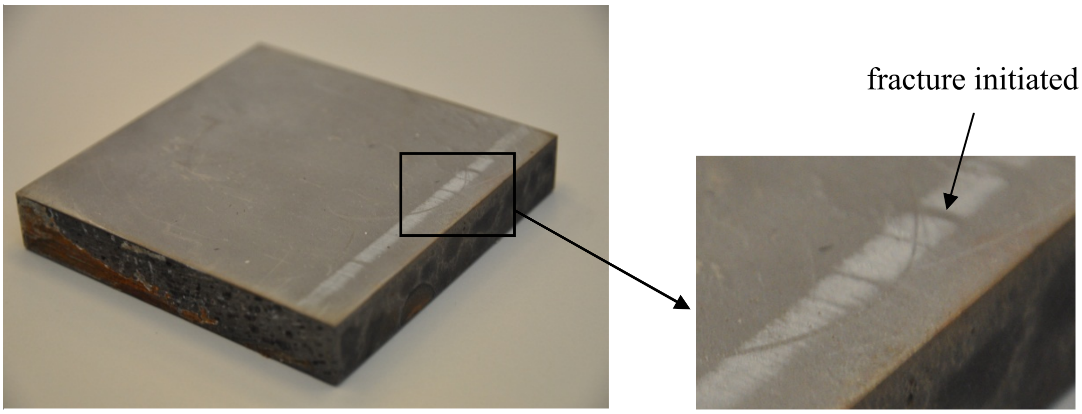

a) S-SB-A-01

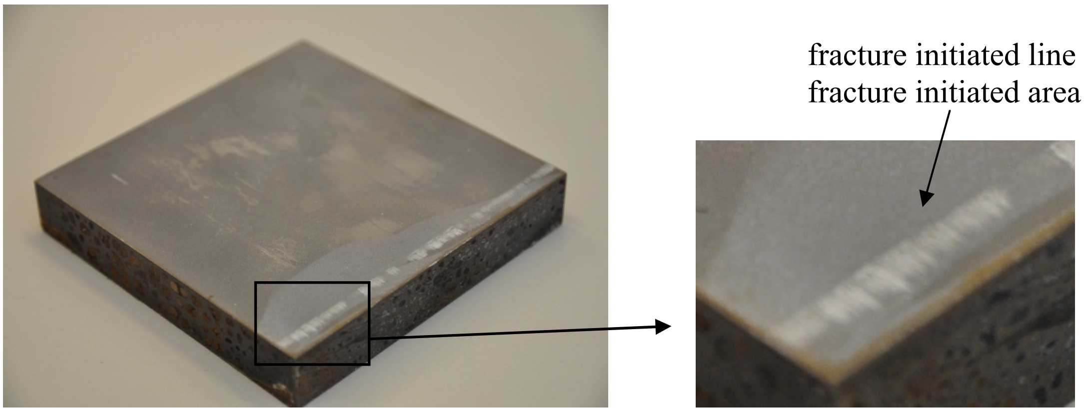

b) S-SB-A-02

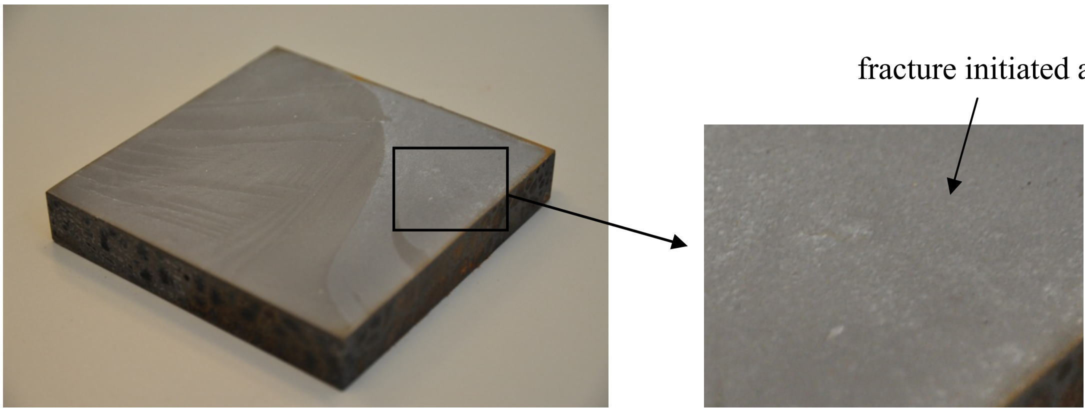

c) S-SB-A-03

Fig. 5.65. Failure modes of aged specimens from the view of steel surfaces

5.4.2 Tensile loading

Load-displacement curves of aged adhesively-bonded joints under tensile loading are shown in Fig. 5.66. It can be seen that the curves of the T-SB-A-2 and T-SB-A-3 specimens are very close to each other both for slopes and maximum loads. However, the T-SB-A-1 specimen develops a rather flexible curve and the maximum load obtained is also quite low. This may be attributed to the non-homogeneity of FRP laminates and adhesive materials. The ultimate failure loads of three aged adhesive joints under tensile loading are summarized in Table 5.9. Their average value is 11.0 kN with a deviation of 16.4% (calculated by Eq.5.2). The average tensile strength is 1.36MPa (calculated by Eq.5.3).

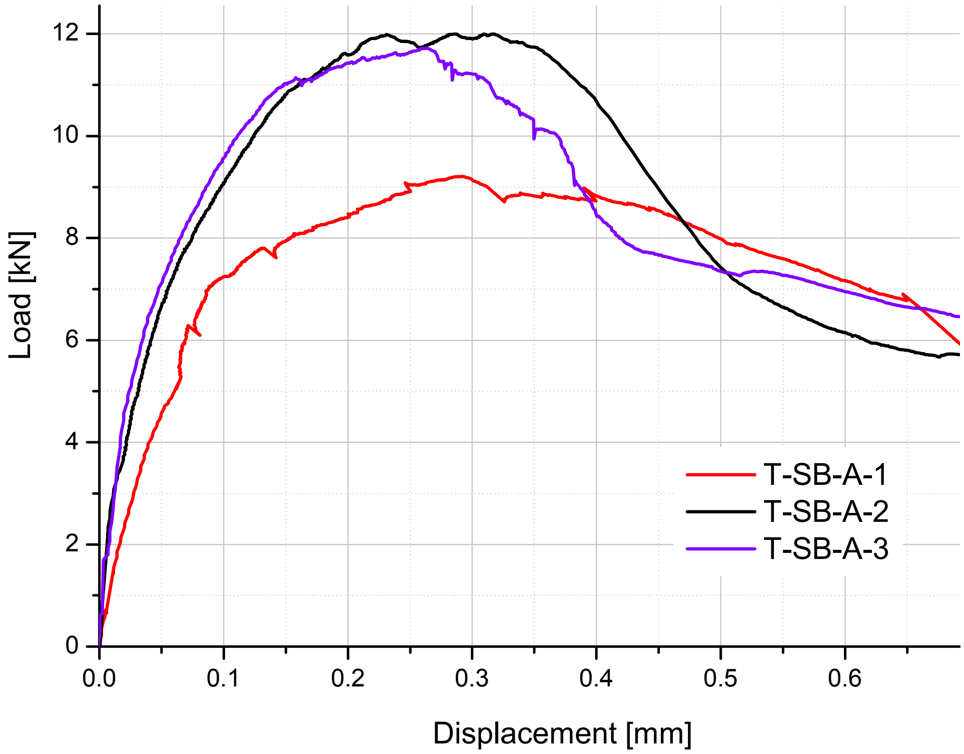

Fig. 5.66. Load-displacement curves of aged specimens under tension loading

Table 5.9. Ultimate failure loads of three aged adhesive joints under tensile loading

T-SB-A-specimen	01	02	03	Average	Deviation
Failure load (kN)	9.2	11.7	12.0	11.0	16.4%

The failure mode of the aged adhesively-bonded joint under tensile loading is shown in Fig. 5.67. It is the combination of FRP delamination and fibre breaking on the surface of an FRP sandwich deck, as illustrated in Fig. 5.68. The ultimate failure of these three specimens does not occur suddenly, but there is always some sound warning from fibre breaking or FRP delamination when the applied load is approaching the ultimate failure load. After achieving the ultimate failure load, there is still some residual load-bearing capacity of the adhesive joints (as indicated by the load-displacement curves in Fig. 5.66), due to the gradual delamination of FRP laminates. From Fig. 5.67 it can be seen that the fibre breaking area is uniformly distributed and almost covers the whole adhesively-bonding area.

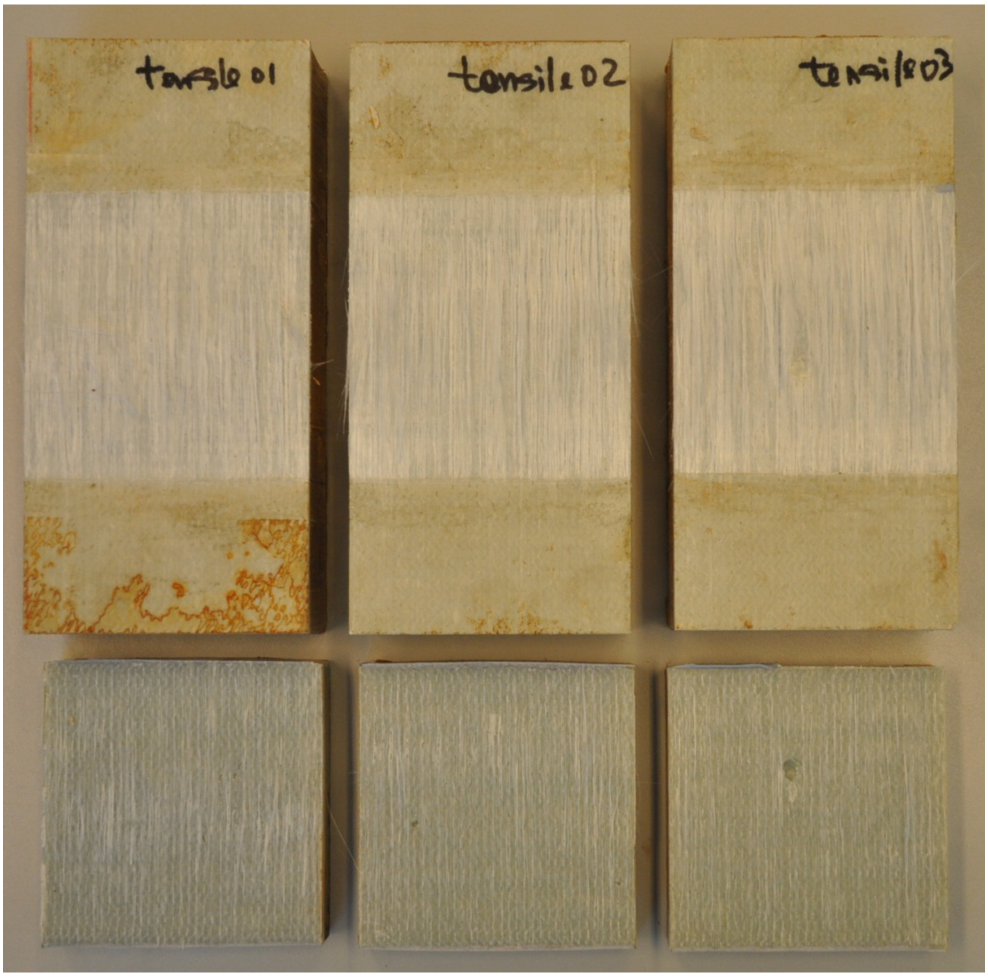

T-SB-A-01 T-SB-A-02 T-SB-A-03

Fig. 5.67. Failure mode of the aged adhesively-bonded joint under tensile loading

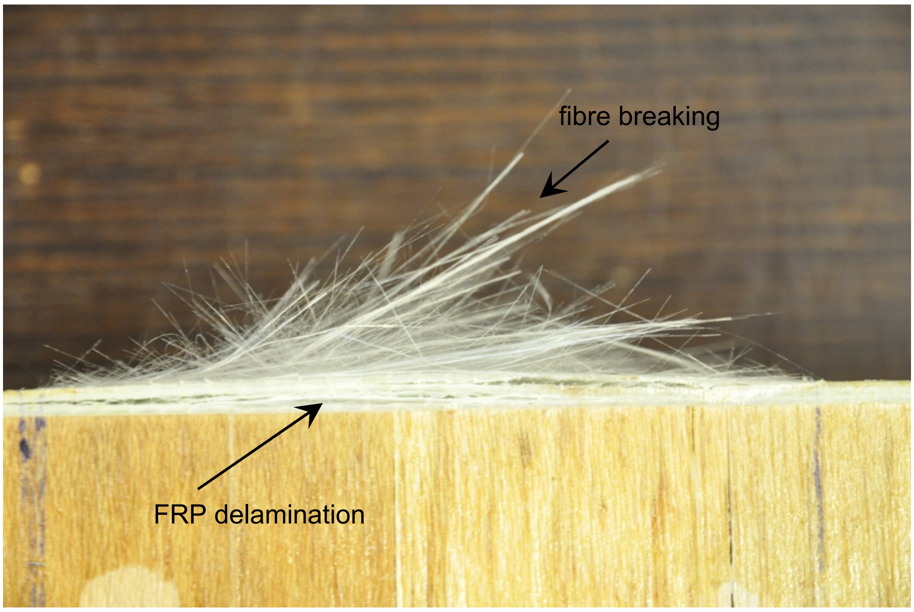

Fig. 5.68. FRP delamination and fibre breaking in the FRP sandwich deck of the aged specimen under tensile loading

5.4.3 Combination loading of shear and tension

Failure loads of adhesive joints under four load angles (18°, 36°, 54° and 72°) are listed in Table 5.10. For comparison, the test results of shear and tensile loading conditions are also involved. During the test of the 54°-SB-A-03 specimen, some operation mistakes occur. Hence, the test result of the 54°-SB-A-03 specimen is not valid and excluded from the Table 5.10. Beside the tensile loading condition, the lowest load-bearing capacity of adhesive joints after hydrothermal aging is obtained under the 18° angle loading condition, with the average failure load of 11.5kN. The load-bearing capacity is increasing from 11.5kN to 25.6kN as the loading angle increases from 18° to 72°. The deviations (calculated by Eq. 5.2) of all these four groups of specimens are within 10%, which indicates that the test results are repeatable and reliable.

Table 5.10. Ultimate failure loads of aged adhesive joints under four loading conditions

T-SB-A-specimen	01	02	03	Average	Deviation
Failure load (kN)	9.2	11.7	12.0	11.0	16.4%
18°-SB-A-specimen	01	02	03	Average	Deviation
Failure load (kN)	12.1	11.5	10.8	11.5	6.1%
36°-SB-A-specimen	01	02	03	Average	Deviation
Failure load (kN)	13.5	14.9	13.7	14.0	6.4%
54°-SB-A-specimen	01	02	03	Average	Deviation
Failure load (kN)	13.9	14.6	-	14.3	2.8%
72°-SB-A-specimen	01	02	03	Average	Deviation
Failure load (kN)	26.5	26.4	23.8	25.6	7.0%
S-SB-A-specimen	01	02	03	Average	Deviation
Failure load (kN)	49.5	37.7	38.4	41.9	18.1%

To easily recognize the combining effects of tensile and shear loading, the total failure load is vectorially separated into shear load and tensile load, with regard to the loading angle of each loading condition, as shown in Fig. 5.69. The horizontal axis represents the shear load applied to the aged adhesive joint, while the vertical axis represents the tensile load. It can be found that the vectorially separated tensile loads are close to each other for the aged specimens tested under tensile, 18° angle and 36° angle loading. This implies that under these three loading conditions, the vectorially separated tensile load dominates the failure load. For the other two loading conditions (54° and 72°), it is the combination of both tensile and shear loading that triggers the final failure of aged adhesive joints, but not only the vectorially separated tensile load.

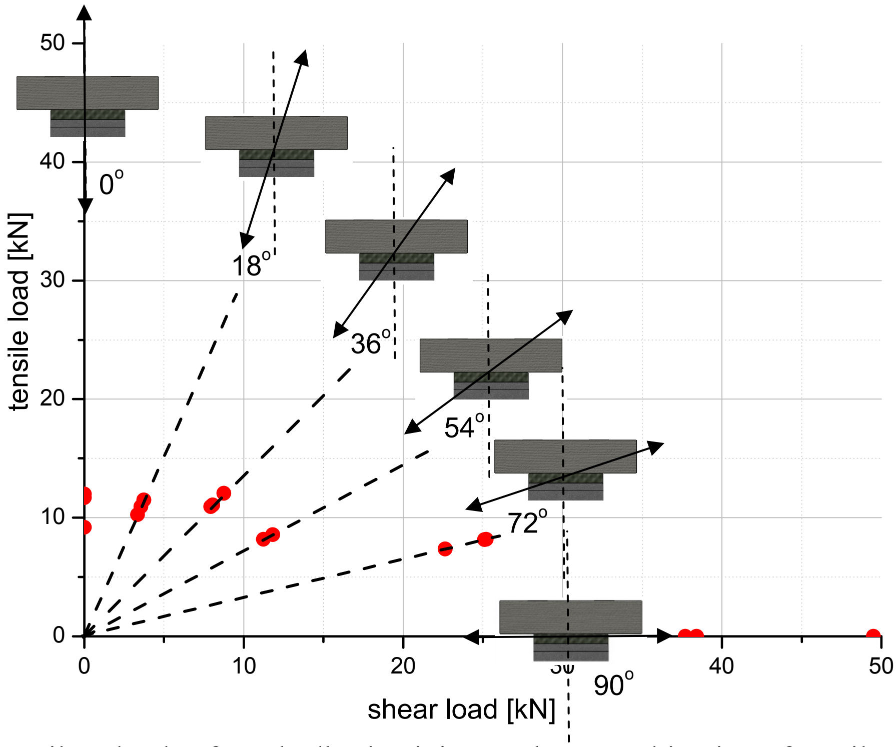

Fig. 5.69. Failure loads of aged adhesive joints under a combination of tensile and shear loading

To investigate the failure criterion of aged adhesive joints, an ellipsoid function is employed for the curve fitting by the least square method. All the test results of the aged specimens are included to perform as the basic curve fitting data. The average shear stress is calculated by Eq. 5.1, while the average tensile stress is calculated by Eq. 5.3. The best fit shear-tensile failure criterion of the aged adhesive joints is as follows:

$$\left(\frac{\sigma}{1.3}\right)^2 + \left(\frac{\tau}{4.6}\right)^2 = 1 \tag{5.7}$$

Fig. 5.70 shows the predictive curve of the shear-tensile failure criterion of the aged adhesive joints together with the test results.

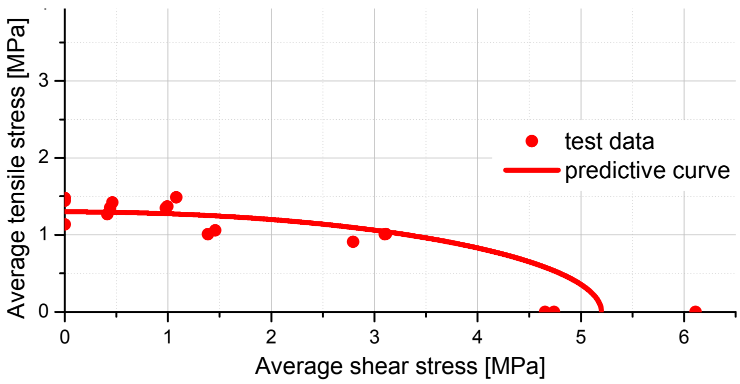

Fig. 5.70. Shear-tensile failure criterion for the aged adhesively-bonded joint

The failure modes of adhesive joints under four combinations of tensile and shear loads are illustrated in Fig. 5.71. The failure mode of the aged adhesive joint under 18°, 36° and 54° angle loading conditions is the combination of FRP delamination and fibre breaking, which is the same as that of specimens under tensile loading. The fibre breaking area always fully covers the whole adhesively bonded area. For the 72° angle loading condition, the failure mode of the 72°-SB-A-01 specimen is the cohesive failure in the adhesive layer, which is as the same as that of specimens under shear loading. It indicates that the failure plane switches from the FRP delamination to the cohesive fracture in the adhesive layer. The vectorially separated shear load dominates the failure load of the 72°-SB-A-01 specimen. Fig. 5.72 clearly shows the cohesive failure in the adhesive layer and residual adhesive material left on the surface of the steel support. The other two aged specimens tested under the 72° angle loading condition fail in the same mode (FRP delamination and fibre breaking) as other loading angles. This phenomenon suggests that the 72° angle loading condition is approximately the marginal loading angle of the tensile-shear combining ratio, which switches the failure mode from the typical tensile-loading failure mode (FRP delamination and fibre breaking) to the typical shear-loading failure mode (cohesive facture in the adhesive layer).

18°-SB-A-01 18°-SB-A-02 18°-SB-A-03

Fig. 5.71. a) 18° angle

36°-SB-A-01 36°-SB-A-02 36°-SB-A-03

Fig. 5.71. b) 36° angle

54°-SB-A-01 54°-SB-A-02

c) 54° angle

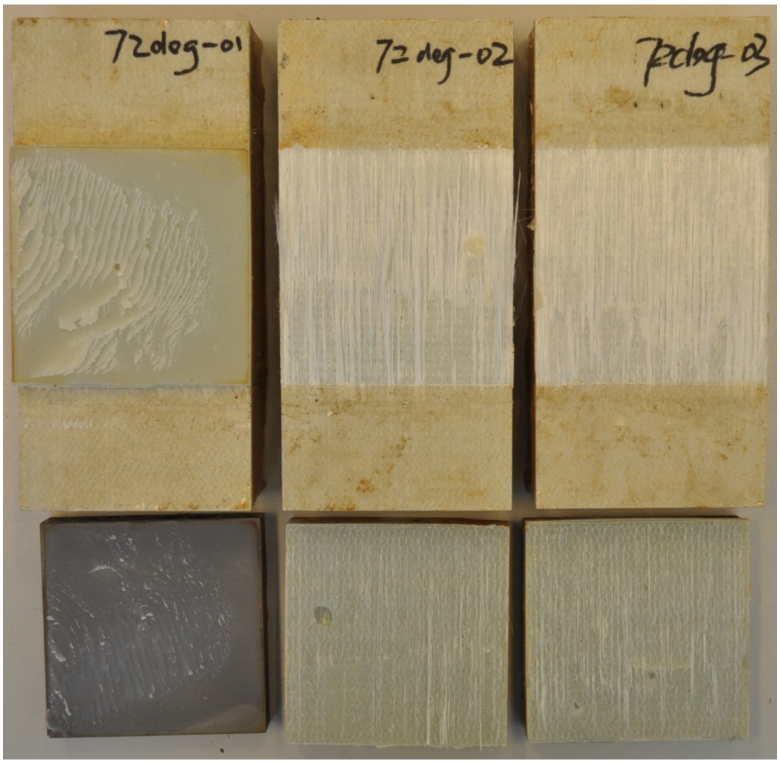

72°-SB-A-01 72°-SB-A-02 72°-SB-A-03

d) 72° angle

Fig. 5.71. Failure modes of aged adhesive joints under four load angles

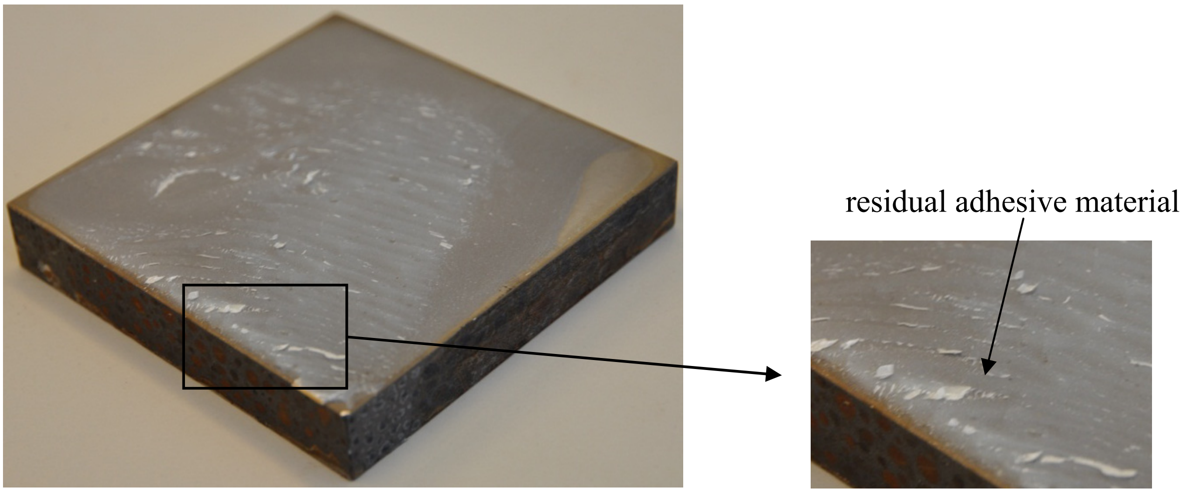

Fig. 5.72. Cohesive failure in the adhesive layer of 72°-SB-A-01 specimen

5.5 Comparison of mechanical behaviours of FRP-to-steel adhesively-bonded joints before and after hydrothermal aging

5.5.1 Ultimate failure load and shear-tensile failure criterion

Ultimate failure loads of the un-aged and aged specimens under six angle loading conditions are listed in Table 5.11. For the tensile and shear loading conditions, the failure loads achieved by the un-aged adhesive joint specimens are definitely higher than those of the aged specimens, 58.2% higher for tensile loading and 65.4% higher for shear loading. This indicates that the absorbed moisture content in FRP laminates and adhesive layer tend to deteriorate the mechanical performance of the adhesively-bonded joints. However, for the tensile/shear combining loading conditions, the un-aged and aged specimens achieve almost the same failure loads. For some cases (36° and 72° angle loading), the failure loads of aged specimens are even a little higher than those of un-aged specimens. Unlike the tensile and shear loading, the hydrothermal aging does not dramatically decrease the failure loads of adhesive joints under the combining loading of tensile and shear, but to the contrary, it slightly increases the load-bearing capacity of joints under 36° and 72° angle loading. These results can be due to the post curing mechanism. Post curing is the process of exposing polymeric materials to elevated temperatures to accelerate the curing process and to maximize some of the material's physical properties by expediting the crosslinking process and properly aligning the polymer's molecules. This is usually done after the material has cured at room temperature. In general, post curing is employed to achieve the full cure of polymeric materials, which cannot be easily realized at room temperature. As stated in researches [15, 16], the post curing can produce significant improvements on the mechanical properties of polymeric materials. Here, the hydrothermal aging environment (40°C-water) offers the elevated temperature to post-cure the FRP laminates and adhesive layer, in this way increasing the load-bearing capacity of adhesive joints. For the shear loading condition, the post-curing efforts are not that obvious. It may be due to the fact that, under shear loading, the failure mode of adhesive joints is the cohesive fracture in the adhesive layer. As compared to the improvement by the post curing, the absorbed moisture is more dramatic in degrading the mechanical properties of adhesive materials.

Also, deviations of test results of the aged specimens are significantly lower than those of un-aged specimens in almost all loading conditions except the tensile loading, which also indicates that the post curing mechanism improves the bonding quality of adhesive joints to minimize the test result deviations.

Table 5.11. Comparison of ultimate failure loads of un-aged and aged adhesive joints

Loading condition	Un-aged specimen		Aged specimen	
	Failure load (kN)	Deviation	Failure load (kN)	Deviation
Tensile	17.4	7.9%	11.0	16.4%
18° angle	11.9	6.7%	11.5	6.1%
36° angle	12.5	16.5%	14.0	6.4%
54° angle	16.8	5.6%	14.3	2.8%
72° angle	23.3	14.3%	25.6	7.0%
Shear	69.3	34.0%	41.9	18.1%

Fig. 5.73 illustrates the vectorially separated tensile and shear failure loads of un-aged and aged adhesive joints under six loading conditions. Fig. 5.74 shows the comparison of the shear-tensile failure criterions for un-aged and aged adhesively-bonded joints. In the tensile load dominated area, the predictive failure criterion curve of un-aged specimens is slightly higher than that of the aged specimens. To the contrary, in the shear load dominated area, the predictive failure criterion curve of aged specimens is higher than

the modified predictive curve of un-aged specimens. In general, the four-month hydrothermal aging does not significantly deteriorate the load-carrying capacity of adhesive joints. However, in Chapter 4, a relatively larger loss of strength of FRP laminates after hydrothermal aging is observed. In conclusion, the absorbed moisture content tends to degrade the mechanical properties of FRP laminates and adhesives, while the post curing process tends to upgrade the mechanical properties of FRP laminates and adhesives, as well as the interfacial bonding quality. These two mechanisms occur homogeneously when the adhesive joints are exposed to the hydrothermal aging environment (40°C-water). The failure load-bearing capacity as well as failure modes of adhesive joints are controlled by whichever mechanism (moisture absorption or post curing) is dominant. Further discussion about this is to be found hereafter in section 5.5.3 of Failure mode.

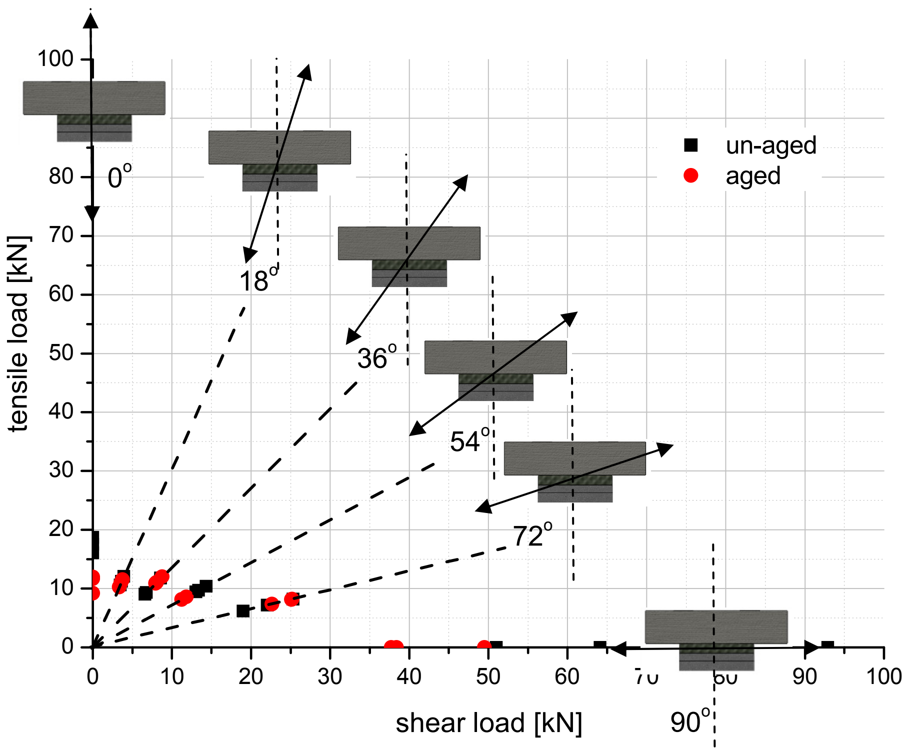

Fig. 5.73. Comparison on vectorially separated failure loads of un-aged and aged adhesive joints under six loading conditions

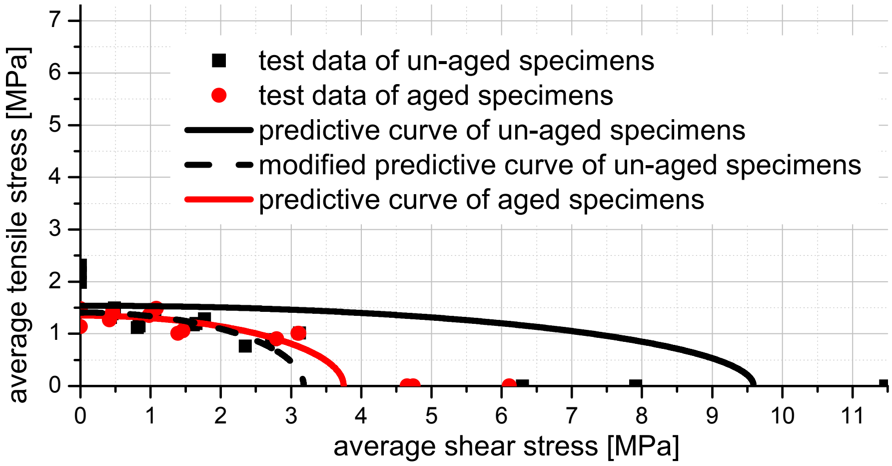

Fig. 5.74. Comparison on the shear-tensile failure criterions for un-aged and aged adhesively-bonded joints

5.5.2 Failure mode

For the aged and un-aged adhesive joints tested under shear loading, the failure mode is the cohesive failure in the adhesive layer, located close to the steel support surface (Fig. 5.75). The locations of the fracture initiated lines are close to each other. As already discussed in section 5.5.1, the failure load of aged specimens is significantly lower than that of un-aged specimens, which means that for the adhesive material, the mechanical degradation due to the absorbed moisture content is much larger than the property improvement by the post curing process.

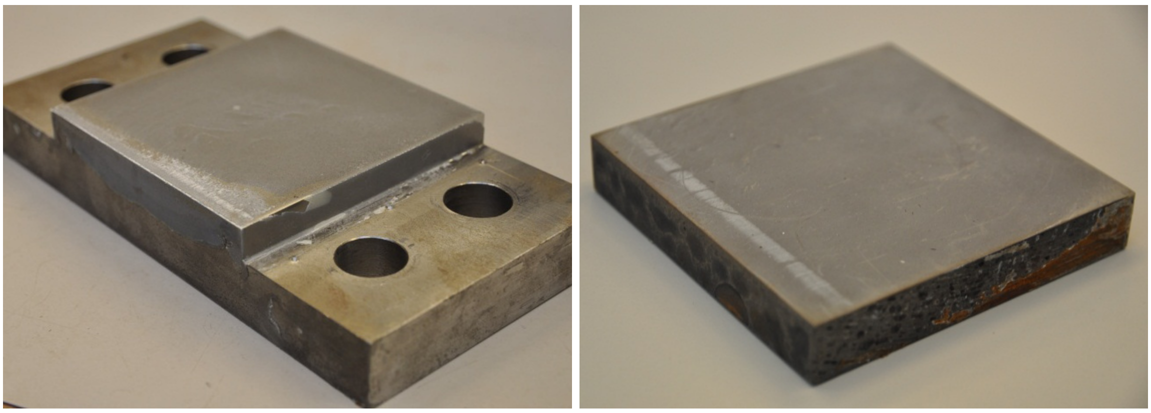

a) Un-aged specimen b) Aged specimen

Fig. 5.75. Failure mode of un-aged and aged adhesive joints under shear loading from the view of the steel support surface

For the other five angle loading conditions, the failure mode is different between the aged and un-aged specimens. The failure mode of un-aged adhesive joints is the combination of partial fibre breaking or local FRP delamination and interface failure between FRP laminates and adhesive layer, as shown in Fig. 5.76 a). The interfacial fracture is due to the insufficient bonding quality between FRP laminates and adhesive layer. However, for the adhesive joints after four-month hydrothermal aging, the weakest plane of adhesive joints moves to the FRP laminates. The failure mode of aged specimens is definitely the FRP delamination through the thickness of FRP laminates combined with fibre breaking on the surface ply. The area of the FRP delamination and fibre breaking distributes more uniformly and almost covers the whole adhesively bonding area, as shown in Fig. 5.76 b). As stated in Section 5.5.1, the load-bearing capacity of aged adhesive joints does not significantly decrease, and even slightly increases for the 36° and 72° angle loading conditions. This implies that the elevated temperature of the hydrothermal aging environment makes the adhesive joint post-cured and in turn significantly improves the bonding quality between FRP laminates and adhesive layer, while the absorbed moisture is less inclined to deteriorate this bonding line. In this way, the failure plane of aged specimens switches to the FRP laminates. Furthermore, the secondary reason for the aged specimens undergoing this failure mode is because the absorbed moisture content degrades the through-thickness mechanical property of FRP laminates, which propels the FRP plies to delaminate.

a) Un-aged specimen b) Aged specimen

Fig. 5.76. Failure mode of un-aged and aged adhesive joints under tensile loading

It is worthwhile mentioning here that, for the 72° angle loading condition, there is one exceptional failure mode both for the un-aged specimens and the aged specimens. They are the 72°-SB-01 specimen (Fig. 5.77 a)) and 72°-SB-A-01 specimen (Fig. 5.77 b)).

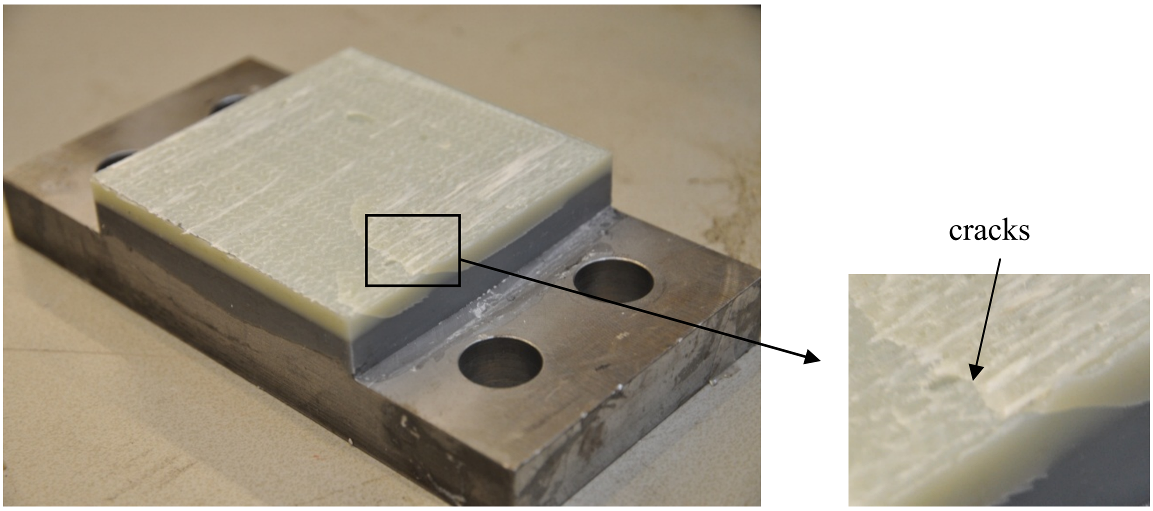

a) 72°-SB-01 specimen

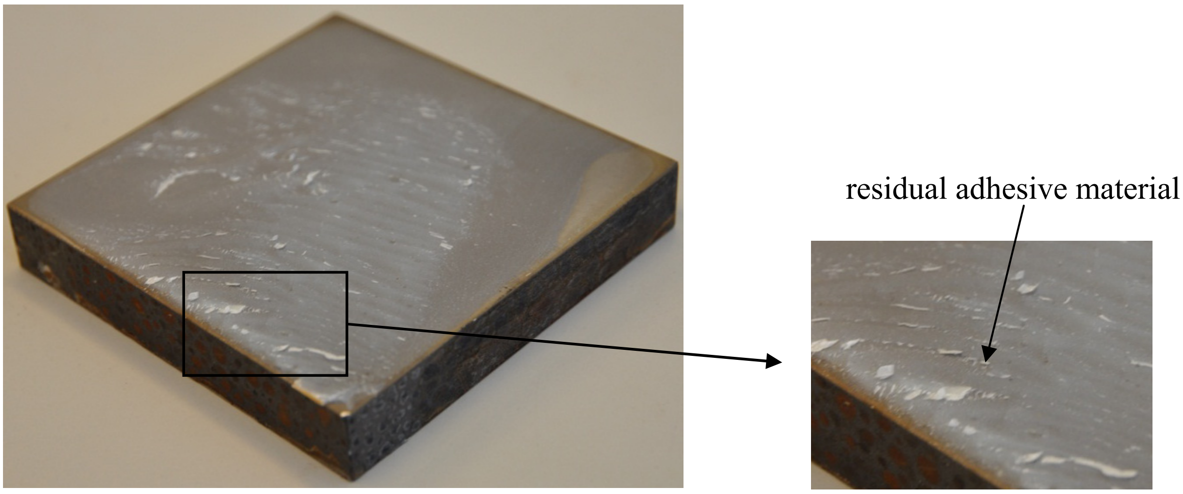

b) 72°-SB-A-01 specimen

Fig. 5.77. Different failure modes of adhesive joints under the 72° loading condition

From Fig. 5.77 a) it can be found that, beside the common failure mode of the adhesive joints tested under other tensile/shear combining loading, several cracks are observed in the adhesive layer of the 72°-SB-01 specimen and propagate through the interface between adhesive layer and steel support. It indicates that the failure plane almost switches to the cohesive failure in the adhesive layer located close to the steel support, which occurred for the adhesive joints under the shear loading condition. For the 72°-SB-A-01 specimen (Fig. 5.77 b)), the failure mode of the aged adhesive joint is the same as that observed for the aged specimens under shear loading. This means that the absorbed moisture degrades the mechanical property of adhesive materials, which in turn influences the failure mode of adhesive joints. Clearly, the 72° loading angle offers the critical combining ratio of tensile and shear load. Under a larger (than 72°) angle loading, the failure of the adhesive joint may occur in the adhesive layer but not in the FRP laminates. However, only one exceptional failure mode is observed both for the un-aged specimens and the aged specimens. Hence, the current test results are too limited to draw further conclusions.

5.5.3 Stiffness

Fig. 5.78 and Fig. 5.79 show the load-displacement curves (measured by LVDTs) of un-aged and aged specimens. It seems that the stiffness of adhesive joints does not decrease significantly under the influence of hydrothermal aging. However, it should be noted that the displacement measured by the LVDTs includes the deformation of the whole loading device and not only the deformation of the adhesive joint. Thus, to further understand the hydrothermal aging effects on the stiffness of the adhesive joint, more comparison should be made on the local deformation of adhesive joints measured by the displacement sensors.

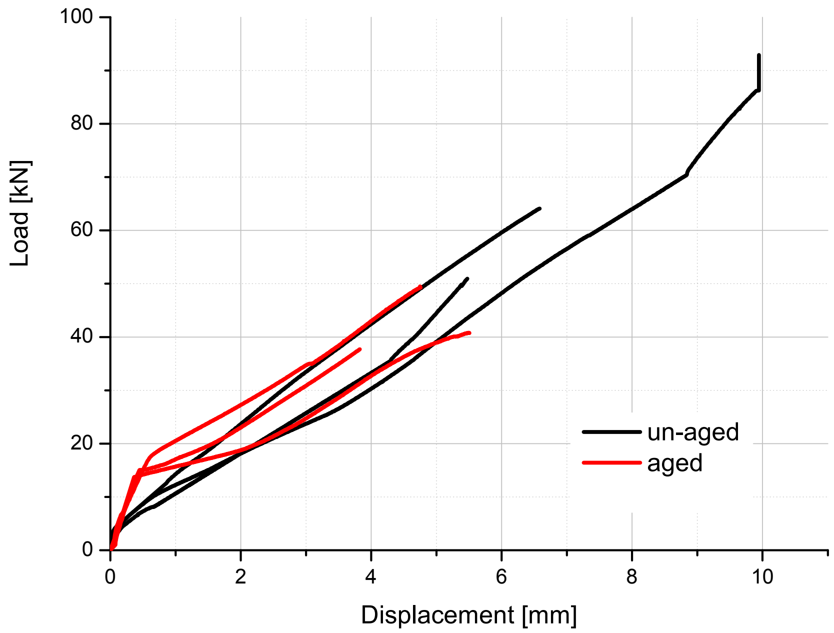

Fig. 5.78. Comparison of load-displacement curves of un-aged specimens and aged specimens under shear loading

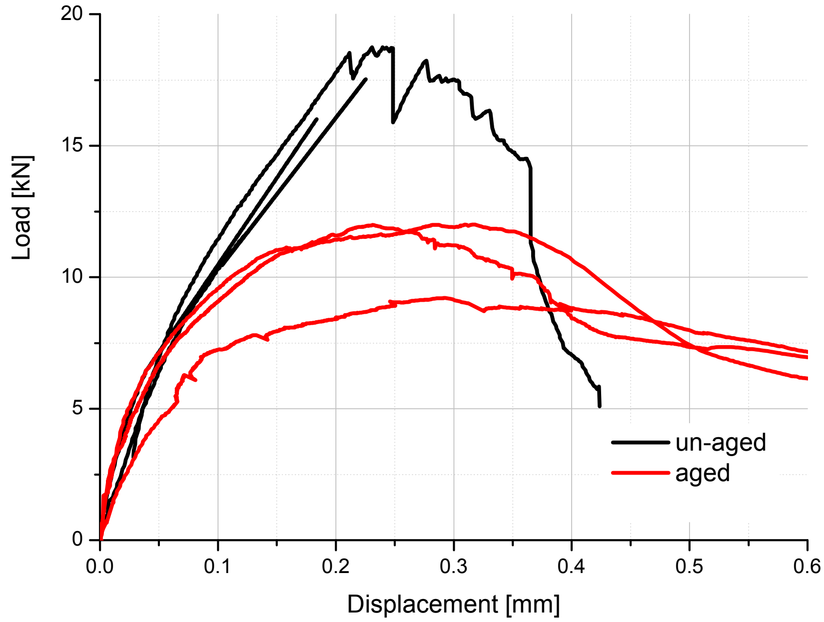

Fig. 5.79. Comparison of load-displacement curves of un-aged specimens and aged specimens under shear loading

Fig. 5.80 shows the comparison of load-deformation curves measured by four displacement sensors on the un-aged and aged specimens under six angle loading conditions. For the tensile loading condition, each load-deformation curve of Fig. 5.80 a) represents the average test result of four displacement sensors. The location of the displacement sensors is illustrated in Fig. 5.11. It can be found that the stiffness of aged adhesive joints is significantly lower than that of the un-aged specimens. After the failure load has been achieved, the curves of aged specimens do not drop immediately but continue with a plateau and then gradually go down. This phenomenon is due to the failure mode of FRP delamination. For the tensile/shear combining loading conditions (Fig. 5.80 b), c), d) and e)), the minus values of displacement sensors represent the average horizontal relative deformation between the FRP sandwich deck and the steel support (DS-2(4), as indicated in Fig. 5.12). The positive value, however, is the average vertical deformation (DS-1(3), as indicated in Fig. 5.12). It is clear that the curves of aged specimens are always more flexible than the un-aged specimen curves. For 18° angle loading condition, the stiffness difference in the vertical direction (positive zone) between un-aged and aged specimens is more significant than the horizontal direction, since the load is separated more in the tensile direction. For the 72° angle loading condition, the situation is quite opposite. The stiffness difference in the horizontal direction (minus zone) between un-aged and aged specimens is more significant than that in the vertical direction, since the load is separated more in the shear direction. For all these four loading conditions, the vertical deformation curves of aged adhesive joints experience a plateau after reaching the failure load. This confirms that these aged joints experienced the same failure mode (FRP delamination) as mentioned in section 5.5.2. For the shear loading condition, the displacement sensors are located as shown in Fig. 5.10. In Fig. 5.80 f), the minus deformation curves represent the average horizontal deformation between the FRP sandwich deck and the steel support at the loading directly applied side (DS-02(04)). Once again, the stiffness of aged specimens is lower than that of un-aged specimens. What is more, for the un-aged adhesive joints, the absolute value of minus deformation is dramatically larger than the positive deformation, which indicates that the deformation distribution along the adhesive layer is very different and the loading directly applied side carries more load than the other side. However, for the aged specimens, the slopes of minus and positive deformation curves are relatively close to each other, which suggests that the deformation distribution in the aged adhesive joints is much more balanced. Further, it indicates that the stiffness of the adhesive layer is decreased by the absorbed moisture content, which makes the adhesive layer rather flexible and subsequently the load is easily transferred from the loading directly applied side to the other side.

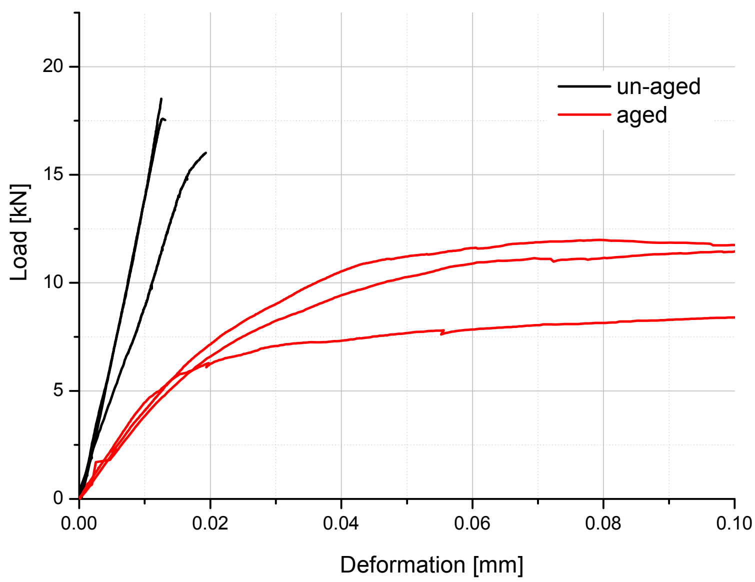

Fig. 5.80. a) Tensile

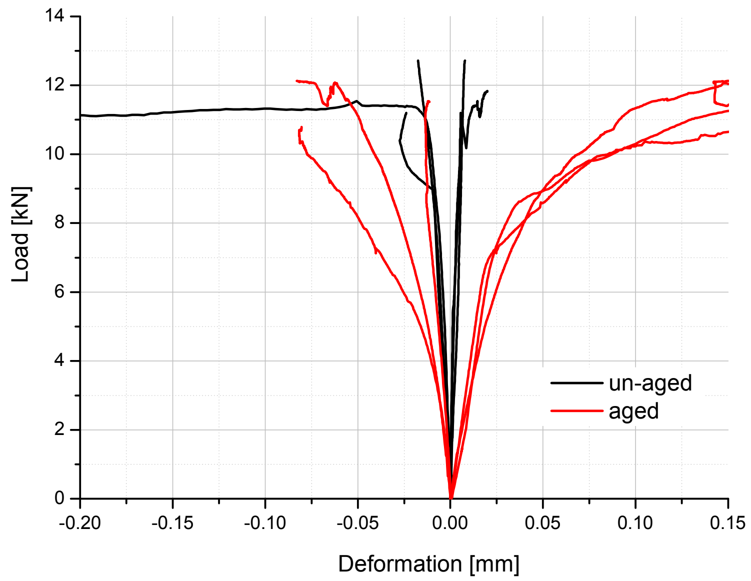

Fig. 5.80. b) 18° angle

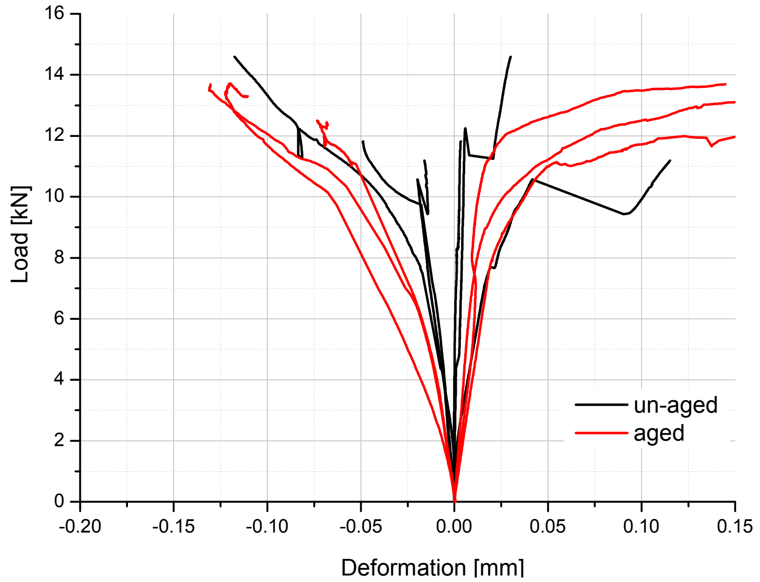

Fig. 5.80. c) 36° angle

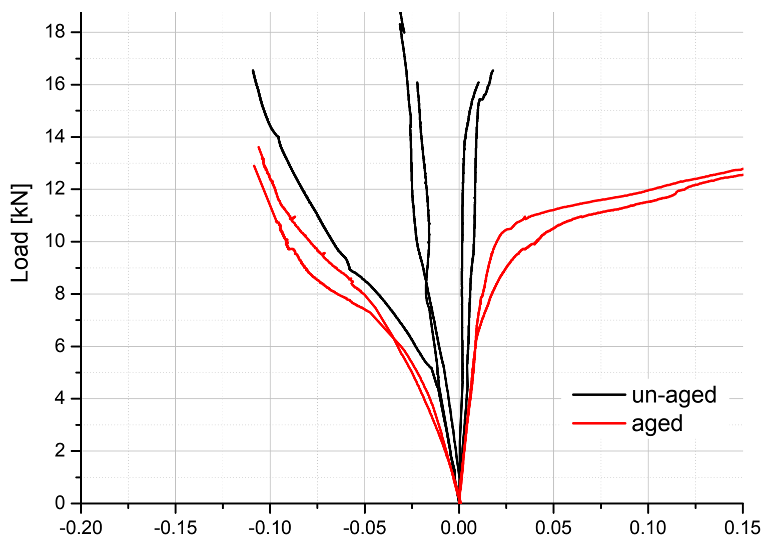

Fig. 5.80. d) 54° angle

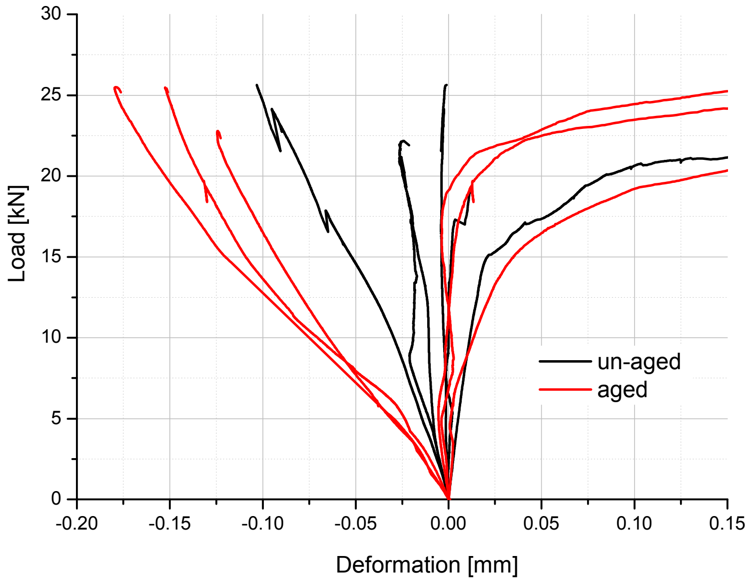

e) 72° angle

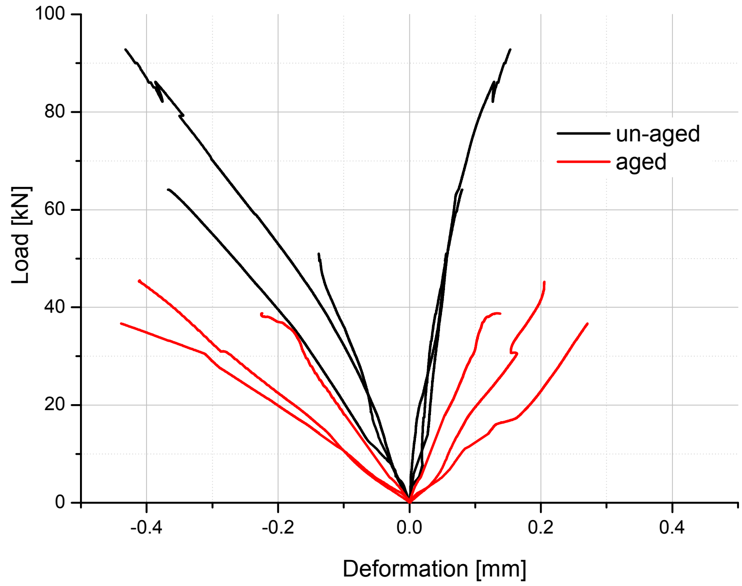

f) Shear

Fig. 5.80. Comparison of load-deformation curves measured by four displacement sensors on the un-aged and aged specimens

5.6 Conclusions

In this chapter, mechanical behaviours of FRP-to-steel adhesively-bonded joints are studied before and after the hydrothermal aging. A specific tensile-shear loading device was designed and then employed to offer six different angle loading conditions. The FE model of the adhesive joint was developed by using ABAQUS 6.8 and subsequently employed to better understand the stress distribution throughout the adhesive joint. Finally, comparison between the experimental results of un-aged joints and hydrothermal aged joints was conducted, with regard to the ultimate failure load, failure criterion, failure mode and stiffness. The following conclusions are drawn:

- For un-aged adhesively-bonded joints under shear and tensile loading, three types of surface pretreatment methods were investigated: acetone (AC), sand paper (SP) and sand blasting (SB). The surface pretreatment cannot improve the stiffness of the adhesive joint. However, for the shear loading condition, the surface pretreatment methods using sand paper (SP) and sand blasting (SB) increase the ultimate failure load of specimens by more than twice of specimens pretreated only using acetone (AC), while for the tensile loading condition the corresponding increase of the ultimate failure load is 9.5%;
- Under shear loading, the un-aged adhesively-bonded joints fail in a brittle way. The failure of S-SP-specimens and S-SB-specimens occurs in the adhesive layer, at a location close to the steel support, while the S-AC-specimens fail through the interface between the adhesive layer and steel support;
- Under tensile loading, the un-aged adhesively-bonded joints pretreated by using sand paper (SP) and sand blasting (SB) fail in a gradual failure process, due to the FRP delamination and fibre breaking. The failure load of the adhesive joints is closely related to the FRP delaminated area or the fibre breaking area. The larger the area is, the higher load-bearing capacity that is achieved, while the T-AC-specimens fail in a brittle and sudden manner, and the failure mode is the interfacial fracture between the FRP laminates and the adhesive layer;
- In practice, the sufficient and quality-controllable surface pretreatment on FRP sandwich decks and steel girders is required to improve the mechanical performance of the adhesively-bonded joints. The sand blasting method is considered to be a preferable surface pretreatment method, based on the researches in this thesis;
- The three-dimensional FE model of un-aged adhesive joints is developed by using ABAQUS 6.8, and validated by the experimental results of relative deformation between the FRP sandwich deck and the steel support. The stress distribution in the adhesive joint proves that the failure is induced by the combination of both tensile and shear stress peaks, but not only the

shear stress or normal tensile stress, even under the expected "pure shear" or "pure tension" loading condition. The edge zone (approximately 10mm from the ends of the adhesive layer) is the most sensitive area to initiate the failure, where both the shear stress peak and the tensile stress singularity are located;

- Investigations on mesh dependency of the FE model confirm that the 1.50mm mesh scale model with six-layer discretization through the thickness of adhesive layer is reasonably accurate and optimizes the computational time;
- For the un-aged adhesive joints under the combing loading of shear and tension, the failure mode is the combination of fibre breaking (or FRP delamination) and interfacial adhesion failure between FRP sandwich deck and adhesive layer, except the 72°-SB-specimen-01, the failure of which combines the cracks in the adhesive layer and propagation through the interface between adhesive layer and steel support. The shear-tensile failure criterion of the un-aged adhesive joints is addressed;
- For the hydrothermal aged adhesive joints, under shear loading, the adhesive joint specimens fail in a brittle mode, with the failure mode of cohesive fracture in the adhesive layer. For the tensile loading and shear/tensile combining condition, the failure mode of aged adhesive joints is a combination of FRP delamination and fibre breaking and it occurs gradually, except for the 72°-SB-A-01 specimen, which fails in the cohesive fracture of the adhesive layer. The shear-tensile failure criterion of the aged adhesive joints is addressed;
- Comparison of the mechanical behaviours of adhesively-bonded joints before and after a four-month hydrothermal aging shows that the hydrothermal aging significantly decreases the ultimate failure loads of aged adhesive joints under shear and tensile loading. However, for the tensile/shear combining loading conditions, the environmental degradation is not that obvious, which is due to the post curing mechanism, improving the bonding quality between the FRP sandwich deck and the adhesive layer. The failure criterion curves of un-aged and aged adhesive joints are close to each other. However, the stiffness of adhesive joints is significantly influenced by the hydrothermal aging;

• With regard to the failure modes, for the tensile and tensile/shear combing loading conditions, the hydrothermal aging switches the failure mode of adhesive joints, from the partial interfacial failure between the FRP sandwich deck and the adhesive layer to the full FRP delamination in FRP laminates and fully covered fibre breaking area. For the shear loading condition, the same failure mode (cohesive fracture in the adhesive layer) is obtained before and after the four-month hydrothermal aging.

References:

[1] Jiang X, Kolstein MH, Bijlaard FSK. Study on mechanical behaviors of FRP-to-steel adhesively-bonded joint under tensile loading. Compos Struct. 2013;98:192-201.
[2] Jiang X, Kolstein MH, Bijlaard FSK. Experimental and numerical study on mechanical behavior of an adhesively-bonded joint of FRP-steel composite bridge under shear loading. Compos Struct. 2014;108:387-399.
[3] da Silva LFM, das Neves PC, Adams RD, Wang A, Spelt JK. Analytical models of adhesively bonded joints-Part II: Comparative study. Int J Adhes Adhes. 2009;29(3):331-41.
[4] da Silva LFM, das Neves PJC, Adams RD, Spelt JK. Analytical models of adhesively bonded joints-Part I: Literature survey. Int J Adhes Adhes. 2009;29(3):319-30.
[5] Diaz J, Romera L, Hernandez S, Baldomir A. Benchmarking of three-dimensional finite element models of CFRP single-lap bonded joints. Int J Adhes Adhes. 2010;30(3):178-89.
[6] He XC. A review of finite element analysis of adhesively bonded joints. Int J Adhes Adhes. 2011;31(4):248-64.
[7] Vallee T, Correia JR, Keller T. Probabilistic strength prediction for double lap joints composed of pultruded GFRP profiles part I: Experimental and numerical investigations. Compos Sci Technol. 2006;66(13):1903-14.
[8] Zhang Y, Vassilopoulos AP, Keller T. Effects of low and high temperatures on tensile behavior of adhesively-bonded GFRP joints. Compos Struct. 2010;92(7):1631-9.
[9] Sheppard A, Kelly D, Tong LY. A damage zone model for the failure analysis of adhesively bonded joints. Int J Adhes Adhes. 1998;18(6):385-400.
[10] http://www.infracomposites.com.
[11] EN 1990:2002(E) Eurocode - Basis of structural design. Brussels2002.
[12] Abaqus Analysis User's Manual, 6.8 version.
[13] Sancaktar E, Narayan K. Substrate volume and stress gradient concepts in mechanical adhesion: analysis of single straight sections. J Adhes Sci Technol. 1999;13(2):237-71.
[14] Gleich DM, van Tooren MJL, Beukers A. Analysis of bondline thickness effects on failure load in adhesively bonded structures. Int Sampe Tech Conf. 2000;32:567-79.
[15] Ferracane JL, Condon JR. Postcure Heat-Treatments for Composites - Properties and Fractography. Dent Mater. 1992;8(5-6):290-5.
[16] Soares CJ, Pizi ECG, Fonseca RB, Martins LRM. Mechanical properties of light-cured composites polymerized with several additional post-curing methods. Oper Dent. 2005;30(3):389-94.

Chapter 6

Conclusions and recommendations

This research work is divided into two parts: material level research (Part I) and joint level research (Part II). The following sections present the main outcome of each part, while the final section provides some recommendations for future research work.

6.1 Conclusions

6.1.1 Part I: Material level research

The main aim of this part is to study the moisture diffusion characteristics of two types of FRP composite materials and the environmental degradation on mechanical properties of FRP laminates. The following brief conclusions can be drawn:

• Moisture diffusion coefficients are determined using the test data fitting method based on the one-dimensional Fickian diffusion theory for pultruded FRP composites and three-dimensional Fickian diffusion theory for resin-infusion FRP laminates. Using these moisture diffusion coefficients as input values for material properties, the FE model was developed for simulating the moisture diffusion process in FRP composite materials and structures and subsequently validated by the gravimetric experimental data and analytical solution. It can be considered as a first step towards the coupled hygro-thermal mechanical FE analysis;

• For the two FRP composite materials studied in this thesis, the resin-infusion FRP laminates obtain much lower values for both moisture diffusion rates and saturated contents than those of the pultruded FRP composites, which indicates good corrosion resistance from environmental effects;

• It is confirmed that the elevated temperature could speed up the moisture diffusion process, and the maximum moisture equilibrium contents are dominated by the humidity of aging environments;

- For the pultruded FRP composites, no significant variations on moisture diffusion characteristic of specimens from different parts of the FRP deck profile exist;
- For the resin-infusion FRP laminates, the mass loss mechanism is observed for Square and Rectangular specimens under 40°C-water aging condition;
- Three-point bending test results of FRP lamiantes confirm that the combination of moisture and temperature effects seriously deteriorates the mechanical properties of FRP laminates on both strength and stiffness;
- A coupled hygro-mechanical FE model was developed to analyse the enviroment-dependent mechanical behaviours of FRP lanimates. This FE model was first validated by the test results of flexural tests and subsequently employed in an inverse parameter identification method to determine the elastic interlaminar shear modulus of FRP laminates;
- The predictive equations for environment-dependent mechanical properties (flexural and interlaminar) of FRP laminates were sustained by using the least square method for the curve fitting.

6.1.2 Part II: Joint level research

In Part II, mechanical behaviours of FRP-to-steel adhesively-bonded joints are studied before and after the hydrothermal aging. A specific tensile-shear loading device was designed and then employed to offer six different angle loading conditions. A comparison between the experimental results of un-aged joints and hydrothermal aged joints is made with regard to the ultimate failure load, failure criterion, failure mode and stiffness. The following brief conclusions can be drawn:

- For un-aged adhesively-bonded joints under shear and tensile loading, three types of surface pretreatment methods were investigated: acetone (AC), sand paper (SP) and sand blasting (SB). The surface pretreatment cannot improve the stiffness of the adhesive joint. However, for the shear loading condition, the surface pretreatment methods using sand paper (SP) and sand blasting (SB) increase the ultimate failure load of specimens by more than twice of specimens pretreated only using acetone (AC), while for the tensile loading condition the corresponding increase of the ultimate failure load is 9.5%;

- Under shear loading, the un-aged adhesively-bonded joints fail in a brittle way. The failure of S-SP-specimens and S-SB-specimens occurs in the adhesive layer, at a location close to the steel support, while the S-AC-specimens fail through the interface between the adhesive layer and steel support;
- Under tensile loading, the un-aged adhesively-bonded joints pretreated by using sand paper (SP) and sand blasting (SB) fail in a gradual failure process, due to the FRP delamination and fibre breaking. The failure load of the adhesive joints is closely related to the FRP delaminated area or the fibre breaking area. The larger the area is, the higher load-bearing capacity that is achieved, while the T-AC-specimens fail in a brittle and sudden manner, and the failure mode is the interfacial fracture between the FRP laminates and the adhesive layer;
- In practice, the sufficient and quality-controllable surface pretreatment on FRP sandwich decks and steel girders is required to improve the mechanical performance of the adhesively-bonded joints. The sand blasting method is considered to be a preferable surface pretreatment method, based on the researches in this thesis;
- The three-dimensional FE model of un-aged adhesive joints is developed by using ABAQUS 6.8, and validated by the experimental results of relative deformation between the FRP sandwich deck and the steel support. The stress distribution in the adhesive joint proves that the failure is induced by the combination of both tensile and shear stress peaks, but not only the shear stress or normal tensile stress, even under the expected “pure shear” or “pure tension” loading condition. The edge zone (approximately 10mm from the ends of the adhesive layer) is the most sensitive area to initiate the failure, where both the shear stress peak and the tensile stress singularity are located;
- Investigations on mesh dependency of the FE model confirm that the 1.50mm mesh scale model with six-layer discretization through the thickness of adhesive layer is reasonably accurate and optimizes the computational time;
- For the un-aged adhesive joints under the combing loading of shear and tension, the failure mode is the combination of fibre breaking (or FRP delamination) and interfacial adhesion failure between FRP sandwich deck

and adhesive layer, except the 72°-SB-specimen-01, the failure of which combines the cracks in the adhesive layer and propagation through the interface between adhesive layer and steel support. The shear-tensile failure criterion of the un-aged adhesive joints is addressed;

- For the hydrothermal aged adhesive joints, under shear loading, the adhesive joint specimens fail in a brittle mode, with the failure mode of cohesive fracture in the adhesive layer. For the tensile loading and shear/tensile combining condition, the failure mode of aged adhesive joints is a combination of FRP delamination and fibre breaking and it occurs gradually, except for the 72°-SB-A-01 specimen, which fails in the cohesive fracture of the adhesive layer. The shear-tensile failure criterion of the aged adhesive joints is addressed;
- Comparison on the mechanical behaviours of adhesively-bonded joints before and after a four-month hydrothermal aging shows that the hydrothermal aging significantly decreases the ultimate failure loads of aged adhesive joints under shear and tensile loading. However, for the tensile/shear combining loading conditions, the environmental degradation is not that obvious, which is due to the post curing mechanism, improving the bonding quality between the FRP sandwich deck and the adhesive layer. The failure criterion curves of un-aged and aged adhesive joints are close to each other. However, the stiffness of adhesive joints is significantly influenced by the hydrothermal aging;
- With regard to the failure modes, for the tensile and tensile/shear combing loading conditions, the hydrothermal aging switches the failure mode of adhesive joints, from the partial interfacial failure between the FRP sandwich deck and the adhesive layer to the full FRP delamination in FRP laminates and fully covered fibre breaking area. For the shear loading condition, the same failure mode (cohesive fracture in the adhesive layer) is obtained before and after the four-month hydrothermal aging.

6.2 Recommendations for future research work

The following recommendations for future work can be given as follows:

- For material level researches, more test data are needed contribute to the statistical determination of characteristic values and appropriate safety factors of material properties considering the moisture and temperature effects;

- Further research work is needed to study more moisture absorption/ desorption cycles, to understand how the residual damage develops and what is the maximum scale of it;
- The brittle character of FRP composite materials and adhesive joints need to be better understood, especially under the colder temperature and freezing condition;
- Researches presented in this thesis are limited in types of FRP composite and adhesive materials used for composing the adhesively-bonded joints. Other types of FRP composite and adhesive materials can lead to different failure modes, stiffness, load-bearing capacity of adhesive joint and workability, due to different material properties and interfacial bonding quality;
- The post curing mechanism is evident for adhesive joints exposed to the hydrothermal aging environment. It can definitely be used in practice to improve the interfacial bonding quality between FRP decks and adhesive layers. Future work can be conducted on how to realize the post-curing process in the in-situ condition of FRP-steel composite bridges;
- Environmental effects on the fatigue and creep performance of adhesively-bonded joints need to be investigated in the future. On the one hand, fatigue cracks can enable moisture penetration. On the other hand, the absorbed moisture content can result in the stress redistribution and in turn influence the fatigue performance. Meanwhile, the absorbed moisture content and elevated temperatures can influence the viscoelastic properties of FRP composite and adhesive materials, which accordingly influence the creep behaviours of adhesive joints;
- Based on the research results of material level and joint level researches obtained in this thesis, full-scale tests on the FRP-steel composite bridge should be proposed in future research work, to investigate environmental effects on the degree of composite action between FRP decks and steel girders as well as the effective width of FRP decks;
- Parametric studies are of interest to be conducted on the dimensions of the adhesively-bonded joint and full-scale FRP-steel composite bridge with regard to the thickness of the adhesive layer, FRP laminates and core

materials, to study their influence on the stress distribution, stiffness, degree of composite action and effective width.

Acknowledgements

After five years of studying, researching and living in Delft, I am going to defend my PhD thesis. At this moment, I would like to give my gratitude to my supervisors, colleagues and friends, for their technical suggestions, encouragement and accompanying.

First and foremost, I would like to thank my supervisors Prof. Frans Bijlaard and Dr. Henk Kolstein, for their patient guidance and cordial encouragement. The most research freedom they offered is highly appreciated, which fully explored my research interests and independent research ability. Before I come to the Netherlands, I never heard of FRP bridge decks. In the first one or two years, they always encourage me to be patient on literature study and explore the interesting research points in this field. It is really my great fortune to conduct my PhD research under their supervisions.

Furthermore, I would like to acknowledge the valuable discussions from the committee members. Special appreciation goes to Prof. Airong Chen, Prof. Philippe Van Bogaert and Prof. Dick Hordijk, for their careful review and helpful comments.

The experimental research in this thesis was carried out in Delft University of Technology, at Stevin II Macrolab and Delft Aerospace Structures and Materials Laboratory. I would like to give my gratitude to Arjen van Rhijn, John Hermsen, Kees van Beek, Fred Schilperoort and Bob de Vogel. They realized my imagination in fantastic ways. The test works would not have been so successful without their help. Moreover, I would like to thank Infra Composite B.V. for test specimen manufacture and financial support.

I would also like to thank my colleagues Sofia Teixeira de Freitas, Maarten Mulder, Richard Pijpers, Carmen Sandhaas, Ayse Nesen Surmeli-Anac, Wolfgang Gard, Roland Abspoel, Geert Ravenshorst, Peter de Vries for their help, patience in academic discussion, culture talk, group excursion, city tour organization, lunch time and coffee break. Special gratitude goes to Caspar Groot, who brings me into the world of art, share life attitude and treat me in a Chinese way. Caspar, I feel very lucky to meet you in the Netherlands, and hopefully we will extend our museum journey in the future.

What is more, I would like to extend my faithful thanks to my dear friends Mingliang Li, Ning Li, Zhuqing Yu, Tingting Jiang, Yue Xiao, Jitang Fan, Jinlong Li, Zhan Zhang, Hailing Zhang, Yuan Zhang, Gang Liu, Zhiyi Chen, Ming Liu, Hui Yu, Yunan Gao etc. I enjoy the great time with you by cooking, drinking, talking, kidding, sporting and travelling.

Finally, I am deeply grateful to my parents for their love, patience, encouragement and understanding. Their amiable smiles always easily refresh me from massive test data and complicated equations. Special thanks goes to my beloved Xuhong Qiang, who shares my sorrow and happiness forever.

Xu Jiang

Delft, the Netherlands

Curriculum vitae

Personal Information

Name	Xu Jiang
Date of birth	August 8th, 1982
Gender	Male
Nationality	China
Email	jxcooool@gmail.com

Education Background

Sep. 2001 - July 2005	Bachelor in Civil Engineering with honors Dalian University of Technology Dalian, Liaoning Province, China
Sep.2005 – Mar. 2008	MSc in Structural Engineering with honors Major in Steel Structures Tongji University Shanghai, China

Work Experience

Apr. 2008 – Oct. 2008	Structural engineer East China Architectural Design & Research Institute Shanghai, China
Nov. 2008 – Oct. 2013	PhD researcher in Structural Engineering Research on mechanical performance and durability of the adhesively-bonded joint between FRP bridge deck and steel girder Delft University of Technology Delft, the Netherlands

List of Publications

I. Journal publications:

1) **Xu Jiang**, Henk Kolstein, Frans S.K. Bijlaard. Moisture Diffusion and Hygrothermal Aging in Pultruded Fibre Reinforced Polymer Composites of Bridge decks. **Materials & Design**, 2012, 37: 304-312.
2) **Xu Jiang**, Henk Kolstein, Frans S.K. Bijlaard. Moisture diffusion in glass-fiber-reinforced polymer composite bridge under hot/wet environment. **Composites Part B-Engineering**, 2013, 45: 407-416.
3) **Xu Jiang**, Henk Kolstein, Frans S.K. Bijlaard. Study on mechanical behaviors of FRP-to-steel adhesively-bonded joint under tensile loading. **Composite Structures**, 2013, 98: 192- 201.
4) **Xu Jiang**, Henk Kolstein, Frans S.K. Bijlaard. Experimental and Numerical Study on Mechanical Behavior of an Adhesively-bonded joint of FRP-steel Composite Bridge under Shear Loading. **Composite Structures**, 2014, 108: 387-399.
5) **Xu Jiang**, Henk Kolstein, Frans S.K. Bijlaard. Effects of hygrothermal aging on glass-fibre reinforced polymer laminates and adhesive of FRP composite bridge: Moisture diffusion characteristics. **Composite Part A - Applied Science and Manufacturing**, 2014, 57: 49-58.
6) Xuhong Qiang, Frans S.K. Bijlaard, Henk Kolstein, **Xu Jiang**. Behaviour of beam-to-column high strength steel endplate connections under fire conditions - Part 1: Experimental study. **Engineering Structures**. (minor revision)
7) Xuhong Qiang, Frans S.K. Bijlaard, Henk Kolstein, **Xu Jiang**. Behaviour of beam-to-column high strength steel endplate connections under fire conditions - Part 1: Numerical study. **Engineering Structures**. (minor revision)

II. Conference Publications

1) **Xu Jiang**, Henk Kolstein and Frans S.K. Bijlaard. Coupled Hygro-mechanical Stress Analysis on Adhesive Material under Hot/wet Environments. In Proceeding of the 4th International Conference on Structural Engineering, Mechanics and Computation, 2010, Cape Town, South Africa.
2) **Xu Jiang**, Henk Kolstein, Frans Bijlaard. Moisture Diffusion in FRP Adhesively-Bonded Joints under Hot/wet Environments. Proc. of the 5th International Conference on FRP Composites in Civil Engineering. 2010, Beijing, China.
3) **Xu Jiang**, Henk Kolstein and Frans S.K. Bijlaard. Study on Moisture Fickian Diffusion Process of a Pultruded FRP Composite Material under Hot/wet Environment. In Proceeding of the Fourth International Conference on Durability & Sustainability of Fibre Reinforced Polymer (FRP) Composites for Construction and Rehabilitation. 2011, Quebec, Canada.
4) **Xu Jiang**, Henk Kolstein, Frans S.K. Bijlaard. Experimental Investigation on FRP to Steel Adhesively-bonded Joint under Tensile Loading. Proceedings of the 6th International Composites Conference (ACUN-6): COMPOSITE & NANOCOMPOSITES IN CIVIL, OFFSHORE AND MINING INFRASTRUCTURE. 2012, Melbroune, Australia.（**BEST PAPER AWARD**）
5) **Xu Jiang**, Henk Kolstein and Frans S.K. Bijlaard. Numerical Analysis and Parametric Study on Composite Action Between Fiber-reinforced Polymer Bridge Decks and Steel Girder. ASCCS: 10th International Conference on Advances in Steel Concrete Composite and Hybrid Structures, 2012, Singapore.
6) **Xu Jiang**, Henk Kolstein and Frans S.K. Bijlaard. Mechanical Behaviour of Adhesive Joint under Tensile and Shear Loading. IABSE, 2013, Rotterdam, the Netherlands.